



UNIVERSITY OF

LIVERPOOL

**Probing Structure and Dynamics in Advanced Molecular
Materials by Solid State Nuclear Magnetic Resonance**

Thesis submitted in accordance with the requirements of the
University of Liverpool for the degree of Doctor in Philosophy

by

Ashlea Robyn Hughes

Department of Chemistry

February 2021

Probing Structure and Dynamics in Advanced Molecular Materials by Solid State Nuclear Magnetic Resonance

Ashlea Hughes

Abstract

Probing and determining the structure and dynamics of advanced molecular materials is crucial to aid our understanding of their properties. Solid state NMR is capable of probing short-range order and dynamics. Therefore this analytical technique (often used in conjunction with computational studies) is able to provide structural characterisation at the atomic level as well as probing local order and therefore has great potential to study these motions. In this thesis, advanced solid state NMR approaches have been used to access the temperature dependence site-selective dynamics of guest-free and -adsorbed tubular covalent cages and pillar[n]arenes, accessing understanding of their flexibility behaviours, and determine the structures of a new class of amorphous paramagnetic hybrid perovskites glasses. Firstly, ^2H static NMR spectra has identified tubular covalent cages as ultra-fast molecular rotors and smart materials capable of adsorbing iodine and its release upon the application of an external stimuli. Secondly, correlation times and proton detected local field NMR experiments found that the extruding ethoxy group of perethylated pillar[n]arenes has significant dynamics when compared to the dynamics associated within the core. Using these techniques we also show the strong dipolar coupling present between *para*-xylene and the EtP6 host, providing insights into the guest's location inside the host. Finally, spectral analysis of paramagnetic hybrid perovskites was completed and NMR methods were able to confirm that the materials studied melt at low temperatures and can be quenched into a glass form. It is the dynamics and flexibility of these structures that controls the selectivity of molecules in the voids located in the frameworks and hence enable them to be used for molecular separation.

Thesis Overview

Chapter 1 covers some of the basic principles of NMR along with an introduction to the solid state NMR methods used within this thesis.

Chapter 2 provides a general introduction to host-guest chemistry and some selected NMR techniques often used within this field.

Chapter 3 comprises of a published paper concerning “Ultra-Fast Molecular Rotors within Porous Organic Cages” with ^2H NMR being the predominant technique utilised to study the dynamics of the supramolecular tubular covalent cages.

Chapter 4 is based on a manuscript which has recently been sent for publication entitled “Dynamics in flexible pillar[n]arenes probed by solid-state NMR” as well as having inserts of work published in a collaborative paper on pillar[n]arenes; “Near-Ideal Xylene Selectivity in Adaptive Molecular Pillar[n]arene Crystals” . This section focuses on both structural characterisation as well as assessing dynamics of the assemblies exploiting the dipolar interaction and correlation times.

Chapter 5 encompasses the NMR work completed by A. Hughes which went towards the manuscript entitled “Melting of Hybrid Organic-Inorganic Perovskites” encompassing the detailed structural analysis of these paramagnetic materials.

Chapter 6 gives an overall conclusion and outlook for the project.

Note: All chapters which have been based on publication have been amended to include the supporting information into the main text.

Acknowledgements

After finally making it so close to the end (I think there is a light somewhere over there?!) I want to say thank you to all those who have helped me through this PhD. Firstly, my main supervisor: Dr. Frédéric Blanc. I cannot thank him enough for this opportunity, and all the help and support he has given me, for the constant corrections, persistence, and encouragement to strive for the best I can achieve.

I would formally like to acknowledge the University of Liverpool and the Engineering and Physical Sciences Research Council for a Doctoral Training Studentship. The Nottingham DNP MAS NMR Facility where low temperature MAS NMR experiments were performed on pillar[n]arenes which was funded by the University of Nottingham and EPSRC (EP/L022524/1 and EP/R042853/1). The UK 850 MHz solid-state NMR Facility used in this research for high field data and very fast MAS data was funded by EPSRC and BBSRC, as well as the University of Warwick including *via* part funding through Birmingham Science City Advanced Materials Projects 1 and 2 supported by Advantage West Midlands (AWM) and the European Regional Development Fund (ERDF). Assistance from the 850 MHz facility Manager, Dr Dinu Iuga, is also appreciated. I would also like to thank Prof. Andrew I. Cooper for access to his laboratory and my sincere thanks to the various people for their synthesis work used in this thesis, Dr. Michael E. Briggs and Dr. Anna G. Salter for the tubular covalent cages; Dr. Ming Liu and Dr. Kecheng Jie for the pillar[n]arenes and Dr. Bikash K. Shaw and Dr. Thomas D. Bennett for the hybrid perovskites.

Nick, Ken and Dong were my first guides throughout this process, being already a few years into it themselves, they taught me what I needed to do to get by and picked me up after a few breakdowns (did I not put a cap on the rotor before I put it in?!). Nick gave me a great intro to NMR with his help on the ^2H work and Dong patiently sat down and went through the dreaded PDLF pulse program with me.

Andrea, Ben and George have been there through my last few years and have provided just the support I needed. We have been through a lot together, grown much closer as a group and even though separated at the end by Covid-19 they were always there to help and occasionally gossip with, when I just couldn't hold back. I

hope they know that my sanity would not have held together for so long if it wasn't for them and that I'm always there to return the favour if needed.

I also want to thank my family. My mum, who couldn't even tell you what a PhD was, let alone what I am doing in mine, would always make an effort to ask and sit there whilst I tell her and dad what had gone wrong that week with Scrabbles on my lap for additional comfort. My dad, always there to reduce my MOT costs and make money issues minimal, was a great support with keeping my home life as stress-free as possible. My sisters and our constant weight loss goals kept my life as normal as it could be, and the occasional babysitting (I should probably say child-minding now that they have grown up so much over the past few years) duties just to keep me busy! – I loved it most of the time, but I don't think it's my vocation.

I also have to acknowledge my future in-laws and certain friends (Rowan, Tay and Mike), I want to thank them for all their effort and patience throughout this rollercoaster ride, reading through my various reports and presentations giving as much advice as possible, attempting to convince me I am nearly at the finishing line, and mostly just being there for a chat. It has been a great help.

Our cats, Flux and Tesla have been more of a hindrance rather than a help, always sitting on the textbook wanting attention whilst trying to study and particularly when working from home during Covid-19 just sitting in front of the computer screen making thesis writing exceptionally difficult. But at least they always let me know I'm loved as they try to convince me that this thesis isn't the most important thing in the world; they are!

Finally, I wish to thank future husband, Chris Taylor. He entered his third year of his own PhD just as I started mine, convinced I was crazy to want to go through it after I had seen what he had endured. But he supported me none the less and it was the highlights of his years at Manchester and the many friends he made along the way that convinced me to return to university. I owe this all to him and wouldn't have been here, never mind written a thesis, without all of his love and support.

Awards, Presentations and Publications

Awards

2019 The UK 850 MHz Solid-state NMR facility PhD travel fund for Alpine Conference on Solid-State NMR.

2018 Runner-up prize for Oral presentation and poster at RSC Annual NMR Discussion Group Postgraduate Meeting.

Presentations

2019 Round Table Talk at Alpine Conference on Magnetic Resonance in Solids.

2019 Poster at the RSC Annual NMR Discussion Group Postgraduate Meeting.

2019 Oral presentation at UK 850 MHz solid-state NMR facility annual symposium.

2018 Oral presentation at Supramolecular Chemistry in Functional Materials Discovery symposium.

2018 Oral presentation at 7th EuCheMS Chemistry Congress.

2018 Poster at RSC Northwest Symposium.

2018 Oral presentation and poster at RSC Annual NMR Discussion Group Postgraduate Meeting (*runner-up prize*).

2017 Poster at RSC Annual NMR Discussion Group Postgraduate Meeting.

Publications

“Recent Advances in Probing Host-Guest Interactions with Solid State Nuclear Magnetic Resonance”. **Ashlea R. Hughes**, Frédéric Blanc, *CrystEngComm*, **2021**, 23, 2491–2503. (contains the contents of **Chapter 2** of this thesis)

“Ultra-Fast Molecular Rotors within Porous Organic Cages”. **Ashlea R. Hughes**, Nick J. Brownbill, Rachel C. Lalek, Michael E. Briggs, Anna G. Slater, Andrew I. Cooper, Frédéric Blanc, *Chem. Eur. J.*, **2017**, 23, 17217–17221. (contains the contents of **Chapter 3** of this thesis)

“Near-Ideal Xylene Selectivity in Adaptive Molecular Pillar[n]arene Crystals”. Kecheng Jie, Ming Liu, Yujuan Zhou, Marc A. Little, Angeles Pulido, Samantha Y. Chong, Andrew Stephenson, **Ashlea R. Hughes**, Fumiyasu Sakakibara, Tomoki Ogoshi, Frédéric Blanc, Graeme M. Day, Feihe Huang, and Andrew I. Cooper, *J. Am. Chem. Soc.*, **2018**, 140, 6921–6930. (selected parts are shown in **Chapter 4** of this thesis)

“Dynamics in flexible pillar[n]arenes”. **Ashlea R. Hughes**, Ming Liu, Subhradip Paul, Andrew I. Cooper, Frédéric Blanc, *J. Phys. Chem. C.*, **2021**, <https://doi.org/10.1021/acs.jpcc.1c02046>. (contains the contents of most of **Chapter 4** of this thesis)

“Melting of Hybrid Organic-Inorganic Perovskites”. Bikash Kumar Shaw, **Ashlea R. Hughes**, Maxime Ducamp, Stephen Moss, Anup Debnath, Adam F. Sapnik, Michael F. Thorne, Lauren McHugh, Andrea Pugliese, Dean Keeble, Philip Chater, Juan M. Bermudez-Garcia, Xavier Moya, Shyamal K. Saha, David A. Keen, Francois-Xavier Coudert, Frédéric Blanc and Thomas D. Bennett, *Nat. Chem.*, **2021**, <https://doi.org/10.1038/s41557-021-00681-7>. (selected parts are shown in **Chapter 5** of this thesis)

List of Abbreviations

2D	Two-dimensional
3D	Three-dimensional
API	Active pharmaceutical ingredient
ASD	Amorphous solid dispersion
ATR-FTIR	Attenuated total reflectance Fourier transform infrared spectrometry
CIS	Complexation induced shifts
COF	Covalent organic framework
CP	Cross polarisation
CSA	Chemical shift anisotropy
CSP	Crystal structure prediction
dca	Dicyanamide
DFT	Density functional theory
DipShift	Dipolar chemical shift correlation
DNP	Dynamic nuclear polarisation
DSC	Differential scanning calorimetry
EFG	Electric field gradient
EtP5	Perethylated pillar[5]arene
EtP6	Perethylated pillar[6]arene
EXSY	Exchange spectroscopy
FID	Free induction decay
FT-IR	Fourier transform infrared spectrometry
HOIPs	Hybrid organic-inorganic perovskites
HPDec	High-power decoupling
HTS	High throughput screening
INADEQUATE	Incredible natural abundance double quantum experiment
IR	Infrared
MAS	Magic angle spinning
MD	Molecular dynamics
MOF	Metal organic framework
MTH	Methanol-to-hydrocarbon
<i>mX</i> @EtP6	<i>meta</i> -xylene in EtP6
NIF	Nifedipine
NMR	Nuclear magnetic resonance
NOESY	Nuclear overhauser effect spectroscopy
<i>oX</i> @EtP6	<i>ortho</i> -xylene in EtP6
PAF	Polyaromatic framework
PDLF	Proton detected local field
PFG	Pulsed field gradient
POC	Porous organic cage
POF	Porous organic framework
PRE	Paramagnetic relaxation enhancement
PRESTO	Phase shifted recoupling effects a smooth transfer of order

PVP	Polyvinylpyrrolidone
<i>pX</i> @EtP6	<i>para</i> -xylene in EtP6
PXRD	Powder X-ray diffraction
REDOR	Rotational echo, double resonance
RESPDOR	Resonance-echo saturation-pulse double resonance
RF	Radio frequency
SHAP	Short high-powered adiabatic pulse
SLF	Separated local field
TCC	Tubular covalent cage
TEDOR	Transferred echo double rotation
TPrA	Tetrapropylammonium
wPDLF	Windowed proton detected local field
XRD	X-ray diffraction
ZIF	Zeolitic imidazolate framework

Contents

Probing Structure And Dynamics In Advanced Molecular Materials By Solid State Nuclear Magnetic Resonance	1
Abstract	1
Thesis Overview	2
Acknowledgements	3
Awards, Presentations and Publications	5
Awards	5
Presentations	5
Publications	6
List of Abbreviations	7
Chapter 1: Introduction to Nuclear Magnetic Resonance Spectroscopy	14
1.1 Overview	14
1.2 Nuclear Magnetic Resonance (NMR) spectroscopy	15
1.2.1 NMR Introduction	15
1.2.2 Solid State NMR	19
1.2.2.1 Chemical shift anisotropy	21
1.2.2.2 Dipolar coupling	23
1.2.2.3 Quadrupolar interaction	24
1.2.2.4 Paramagnetic NMR	26
1.2.2.5 Magic angle spinning	27
1.2.3 NMR Experiments	29
1.2.3.1 Observing NMR signal	30
1.2.3.2 Spin-lattice relaxation	31

1.2.3.3 Saturation recovery	34
1.2.3.4 Echo	35
1.2.3.5 Heteronuclear decoupling	37
1.2.3.6 ^{13}C NMR	38
1.2.3.6.1 Cross polarisation	38
1.2.3.6.2 Phase shifted recoupling effects a smooth transfer of order	40
1.2.3.6.3 ^{13}C T_1	41
1.2.3.7 Short high-powdered adiabatic pulses	42
1.2.3.8 Transferred echo double rotation	44
1.2.3.9 Two-dimensional NMR	45
1.2.3.9.1 Inadequate	46
1.2.3.9.2 Proton detected local field	47
1.3 Systems and materials used in this thesis	48
1.4 Conclusion	49
1.5 References	50
Chapter 2: Recent Advances in Probing Host-Guest Interactions with Solid State NMR	53
2.1 Overview	53
2.2 Abstract	54
2.3 Introduction to host guest interactions and supramolecular chemistry	55
2.4 Widely used approaches to probe host-guest interactions	57
2.5 Solid state NMR and NMR interactions as probes to study supramolecular materials	58
2.5.1 Complexation induced shift	59
2.5.2 Lineshape analysis	61

2.5.3 NMR relaxometry	67
2.5.4 Spin diffusion	68
2.5.5 Xenon NMR	71
2.5.6 Cross polarisation	73
2.5.7 Rotational echo double resonance	76
2.5.8 Separated local field NMR	78
2.6 Conclusion	80
2.7 References	81
Chapter 3: Ultra-Fast Molecular Rotors within Porous Organic Cages	87
3.1 Overview	87
3.2 Abstract	88
3.3 Introduction	89
3.4 Materials and Methods	91
3.4.1 General synthesis consideration for the syntheses of the chiral tubular covalent cages	91
3.4.2 Synthesis of the aldehyde precursors	91
3.4.2.1 Synthesis of 2,2'-([D4]1,4-phenylene)bis(4,4,5,5-tetramethyl-1,3,2-dioxaborolane)	91
3.4.2.2 Synthesis of (([D4]1,4-phenylene)bis(ethyne-2,1-diyl))bis(trimethylsilane)	92
3.4.2.3 Synthesis of [D4]1,4-diethynylbenzene-2,3,5,6	92
3.4.2.4 Synthesis of [1,1':4',1''-terphenyl]-3,3''5,5''-tetracarbaldehyde	93
3.4.2.5 Synthesis of 1,4-bis(3,5-diformylphenyl)phenylethynylbenzene	93
3.4.3 Synthesis of the chiral tubular covalent cages	94
3.4.3.1 Synthesis of solvated cage compound [D ₁₂]TCC2-R	94

3.4.3.2 Synthesis of solvated cage compound [D ₁₂]TCC3- <i>R</i>	94
3.4.3.3 Preparation of all the desolvated cages	95
3.4.3.4 Iodine loading into the cages	95
3.4.3 Solid State NMR methods	96
3.5 Results and Discussion	97
3.5.1 Synthesis of TCC(X) cages	97
3.5.2 ² H NMR Studies	101
3.5.3 Iodine Loading	108
3.5.4 Relaxation rates	116
3.6 Conclusion	118
3.7 References	119
Chapter 4: Dynamics in flexible pillar[n]arenes probed by solid state NMR	123
4.1 Overview	123
4.2 Abstract	124
4.3 Introduction	125
4.4 Materials and Methods	129
4.4.1 Materials synthesis	129
4.4.2 Powder X-ray diffraction	129
4.4.3 Differential scanning calorimetry	129
4.4.4 NMR experiments	129
4.4.5 Solid state NMR calculations	132
4.5 Results and Discussion	134
4.5.1 NMR structural analysis	134

4.5.2 Temperature dependent motional averaged site-selectivity in guest-free pillar[n]arenes	166
4.5.3 Temperature dependent motional averaged site-selectivity in xylene-loaded pillar[6]arenes	175
4.5.4 Host-guest interaction probed by dipolar coupling in xylene-loaded pillar[6]arenes	179
4.5.5 Temperature dependent relaxation studies of guest-free and loaded pillar[n]arenes	183
4.6 Conclusion	205
4.7 References	207
Chapter 5: Melting of Hybrid Organic-Inorganic Perovskites	216
5.1 Overview	216
5.2 Abstract	217
5.3 Introduction	218
5.4 Materials and Methods	221
5.4.1 Synthesis of Hybrid Organic-Inorganic Perovskites	221
5.4.2 Solid State NMR	221
5.5 Results and Discussion	223
5.5.1 Synthesis of amorphous glasses	223
5.5.2 Delineating Decoordination and Decomposition	224
5.6 Conclusion	234
5.7 References	235
Chapter 6: Conclusions and Further Work	238
6.1 Conclusions	238
6.2 Further work	240
6.3 References	243

Chapter 1: Introduction to Nuclear Magnetic Resonance Spectroscopy

1.1 Overview

Chapter 1 is a condensed introduction to general nuclear magnetic resonance (NMR), the interactions which occur in solid state NMR, some general NMR techniques and pulse sequences which are used along with the materials studied throughout the results chapters of this thesis.

1.2 NMR spectroscopy

1.2.1 NMR introduction

Most nuclei possess a nuclear spin quantum number I (or a spin) that gives rise to angular momentum. Nuclear Magnetic Resonance (NMR) spectroscopy is a very powerful and versatile technique which can probe the chemical environment of nuclei that have a spin greater or equal to a half. The majority of elements in the periodic table have at least one NMR active isotope that satisfies this rule; hence, NMR is a widely used technique for a range of applications including the study of materials. A nucleus with a spin of I , has $2I + 1$ energy levels within the range of $+I$ and $-I$ in increments of ± 1 . In the absence of a magnetic field, these energy levels are all degenerate, however in the presence of an external magnetic field, this degeneracy is lifted and the spin of a nucleus generates a nuclear magnetic moment, μ , and in turn creates a Boltzmann distribution of populations between the various energy levels. It is the transitions between these non-degenerate nuclear spin states that we observe in NMR spectroscopy. The magnetic moment produced is proportional to both the spin, I , and the gyromagnetic ratio, γ , as can be seen in **equation 1.1**.

$$\mu = \gamma I \tag{1.1}$$

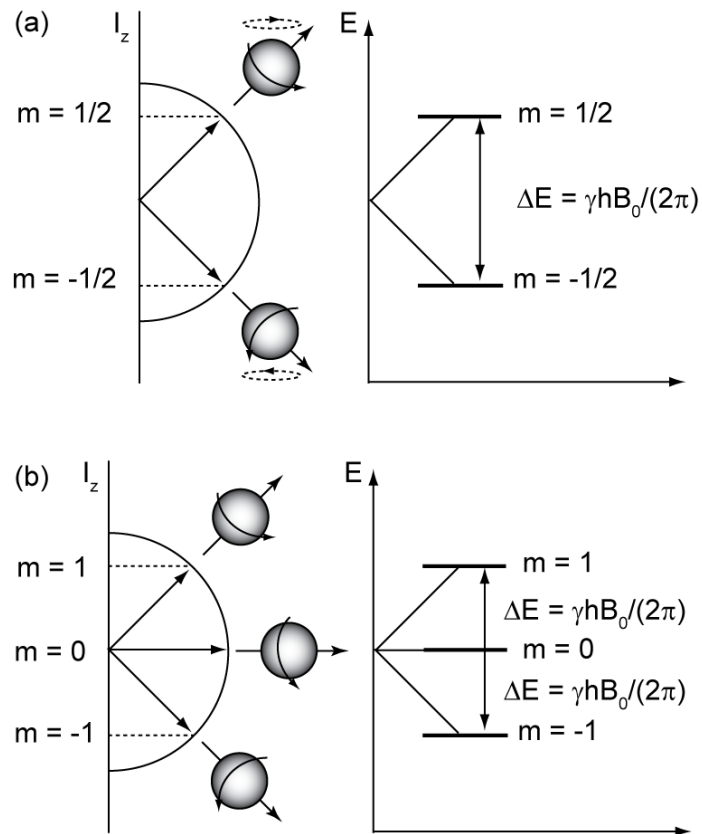


Figure 1.1. The splitting of spin states in an external magnetic field, B_0 , with a corresponding energy level diagram, where I_z is parallel to B_0 , to show the transition of electrons between the nuclear spin states for (a) spin, $I = 1/2$ nucleus and (b) $I = 1$ nucleus. ΔE is the energy difference between the states, B_0 is the external magnetic field, and γ is the gyromagnetic ratio for the relevant nucleus.

It is demonstrated within **Figure 1.1(a)** that the nuclear spins also precess within a magnetic field. The rate (frequency) of precession is known as the Larmor frequency, ν_0 , (expressed in **equation 1.2**) and is dependent on B_0 , and γ . The gyromagnetic ratio, γ , is a constant which differs only with the nucleus observed, resulting in a Larmor frequency, which is also nucleus specific.

$$\nu_0 = \gamma B_0 / 2\pi \quad (1.2)$$

Signal intensity is dependent on the population difference between the energy levels. This can be expressed using the Boltzmann equation (**equation 1.3**), where k_B is the Boltzmann constant, ΔE is the energy difference between the energy levels and T is temperature. This population difference is inherently small (for a ^1H nucleus, at room temperature and 9.4 T, the population difference is 1/20000) and so, larger external magnetic field strengths and/or lower temperatures are often used to maximise the energy difference, ΔE , resulting in a larger ratio of $n_{\text{upper}}/n_{\text{lower}}$.

$$\frac{n_{\text{upper}}}{n_{\text{lower}}} = e^{-\Delta E/k_B T} \quad (1.3)$$

NMR spectroscopy can provide insights into both structure and a nuclei's surroundings because it is very sensitive to the local electronic environment of particular sites. The electron density surrounding the nucleus induces its own magnetic field when subjected to the external magnetic field. This induced field opposes the external magnetic field. It is proportional to the external magnetic field and dependent on the chemical shielding, σ which gives information regarding the surrounding electron density and electronic structure. Therefore, this localised magnetic field, B_{loc} , in turn alters the frequency at which a nucleus will appear on an NMR spectrum and is defined as:

$$B_{\text{loc}} = B_0(1-\sigma) \quad (1.4)$$

This causes a change to the energy level splitting causing nuclei within different environments (i.e. different electronic structures) to resonate at different frequencies, ν .

$$\nu = \frac{\gamma B_{\text{loc}}}{2\pi} \quad (1.5)$$

As frequencies are dependent on field strength, values are converted into chemical shift in parts per million due to the difference in frequency being very small, using **equation 1.6** below, eliminating the field strength dependency. Chemical shifts, δ , are calculated using **equation 1.6**, where ν_{sample} is the resonance frequency of the observed signal, and $\nu_{\text{reference}}$ is the resonance frequency of the reference compound: Resonance frequencies are most often referenced to a known compound, for example, trimethylsilane for ^1H .

$$\delta = 10^6 \frac{\nu_{\text{sample}} - \nu_{\text{reference}}}{\nu_{\text{reference}}} \quad (1.6)$$

1.2.2 Solid State NMR

NMR signals are a sum of multiple interactions, given in **Table 1.1** below. These interactions are responsible for the lineshape and positioning of the NMR signals.

Table 1.1. NMR interactions, their corresponding magnitudes and brief equations. ¹

Hamiltonian	Interaction	Magnitude	Equation
\hat{H}_z	Zeeman Splitting	MHz	$\hat{H}_z = -\gamma B_0 \hat{I}_z$
\hat{H}_{CS}	Chemical Shift	kHz	$\hat{H}_{CS} = -\gamma \hat{I}_z B_0 \sigma$
\hat{H}_D	Dipolar Coupling	kHz	$\hat{H}_{DHetero} = d_{ij}(3\cos^2 - 1)\hat{I}_z\hat{S}_z$ $\hat{H}_{DHomo} = d_{ii}(3\cos^2 - 1)3\hat{I}_{1z}\hat{I}_{2z} - \hat{I}_{1z}\hat{I}_{2z}$
\hat{H}_J	J Coupling	Hz	$\hat{H}_J = -J_{12}\hat{I}_{1z}\hat{I}_{2z}$
\hat{H}_Q	Quadrupolar Coupling	MHz	$\hat{H}_Q = f\hat{I}_z\hat{S}_z\left[\frac{g(iso)}{\omega_0} + h(aniso)3\cos^2 - 1 + i(aniso)35\cos^4 - 30\cos^2 + 3\right]$
\hat{H}_{para}	Paramagnetic Coupling	MHz	$\hat{H}_{para} = \hat{H}_0 + \hat{H}_z + (\hat{H}_{contact} + \hat{H}_D)$

Where \hat{I}_z/\hat{S}_z is the angular momentum operator which represents the z component of magnetisation for the respective spins, σ is a second rank shielding tensor which describes the electronic distribution surrounding the nucleus and d_{ij} is the dipolar coupling constant defined in **equation 1.9**.

In brief, the Zeeman interaction refers to the energy level difference between the two spin states determined by how the spins align in relation to the magnetic field. The remaining Hamiltonians typically perturb the Zeeman interaction. The chemical shift Hamiltonian relates to the nuclear spin interaction with the surrounding electrons. Without rapid molecular tumbling, this interaction differs depending on the orientation of the sample, see section 1.2.2.1. The dipolar interaction relates to the interaction of two dipoles with each other, either of the same nuclei

(homonuclear) or differing nuclei (heteronuclear). Distance and geometry between the two nuclei affect the dipolar coupling Hamiltonian. J Coupling is similar to the dipolar Hamiltonian as it occurs between two spins, however it is a through-bond interaction. Quadrupolar coupling, \hat{H}_Q , is only relevant to nuclei with $I > 1/2$ due to the electronic charge distribution not being spherically symmetrical, which allows the electric field gradient to interact with the nucleus perturbing the energy levels as shown in **Figure 1.3**. Finally, the paramagnetic Hamiltonian describes the effect caused by paramagnetic metal ions to the NMR spectrum and further detail can be found in section 1.2.2.4.

Many of these interactions contain an orientation dependent term $(3\cos^2\theta-1)$. Such terms are averaged to zero in the liquid state, due to rapid molecular tumbling, which is absent in the solid state. Without this rapid tumbling, the Hamiltonians for anisotropic chemical shift, dipolar coupling and quadrupolar interactions are not averaged out, resulting in broad lines within the solid state spectrum.

1.2.2.1 Chemical Shift Anisotropy (CSA)

Chemical Shift Anisotropy (CSA) is derived from the fact that the sample can have different orientations (**Figure 1.2(a)**) with respect to the external magnetic field, hence a broad powder pattern made of multiple lines all at slightly different chemical shifts is observed (**Figure 1.2(b)**). This arises due to the charge distribution around the nuclei not being spherical, this will give a range of chemical shifts for different nuclear orientations with respect to the external magnetic field is described by the principle components, δ_{11} , δ_{22} and δ_{33} , shown in **Figure 1.2**. The most likely orientation of the chemical shift tensor is perpendicular to the external magnetic field, therefore this signal is seen as the most intense, δ_{22} , with the edges of the powder pattern, δ_{11} and δ_{33} , representing less likely orientations, resulting in a similar example powder pattern to that shown for a typical carbonyl in **Figure 1.2(c)**. Using these three values, the isotropic chemical shift can be calculated using **equation 1.7**

$$\delta_{\text{iso}} = \frac{\delta_{11} + \delta_{22} + \delta_{33}}{3} \quad (1.7)$$

If any of these principle components are equal to each other the line shape is uniaxial. The deviation from this line shape is given by the asymmetry parameter, η

$$\eta = \frac{\delta_{22} - \delta_{11}}{\delta_{33} - \delta_{\text{iso}}} \quad (1.8)$$

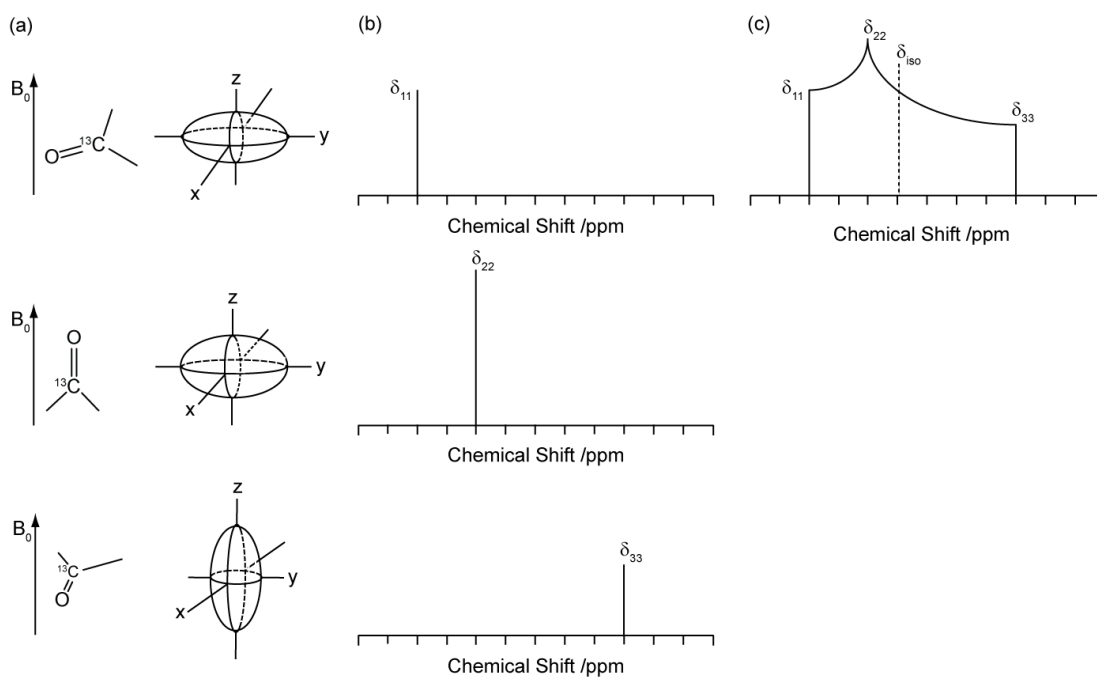


Figure 1.2. (a) Three possible arrangements of a carbonyl group with respect to B_0 and a depiction of their corresponding chemical shift tensor. (b) The signal produced at varying chemical shift for this compound. (c) Typical powder pattern created from an infinite number of lines due to every orientation of the sample with respect to B_0 being possible.

1.2.2.2 Dipolar coupling

As mentioned previously in this chapter, each nuclear spin possesses a magnetic or dipole moment. These dipoles can interact with each other through space, termed dipolar coupling. This interaction is orientation dependent, and hence is not observed in traditional solution state NMR, however, it is observed in the solid state. The magnitude of dipolar coupling follows **equation 1.9**.¹

$$d_{ij} = -\frac{\mu_0}{4\pi} \frac{\hbar\gamma_i\gamma_j}{r_{ij}^3} \quad (1.9)$$

Where d_{ij} is the dipolar coupling constant between an i and j nuclei in rad s^{-1} , μ_0 is the vacuum permittivity, \hbar is the reduced Planck's constant, γ_i and γ_j are the gyromagnetic ratios for i and j respectively and r_{ij} is the distance between the i and j nuclei. Due to its dependence on both orientation (see **Table 1.1**) and internuclear distance (**equation 1.9**), dipolar couplings are often a rich source of structural information.

1.2.2.3 Quadrupolar interaction

This thesis only deals with Spin $\frac{1}{2}$ and Spin 1 nuclei. Since spin 1 nuclei are quadrupolar the quadrupolar interactions are present. In liquid state NMR, a singlet is expected due to molecular tumbling as the first order quadrupolar interaction has been averaged to zero, leaving only the Zeeman interaction and chemical shift interaction to be visible in the NMR spectrum. However, in solid state NMR under static conditions it is expected to look like the classical Pake doublet (shown in **Figure 1.3(a)** below) due to the Zeeman interactions (+1 - 0 and 0 - -1) as well as the quadrupolar interactions in the sample which are not averaged out without rapid tumbling or spinning of the sample.

The energy level diagram must take into consideration \hat{H}_Q , causing the two transitions, between the +1 and 0 and the 0 and -1 energy levels, to have slightly different energies as shown in **Figure 1.3(b)**. Therefore, these transitions appear at slightly different chemical shifts in the NMR spectrum with each peak being a mirror image, as illustrated in **Figure 1.3** below. From the equation for the quadrupolar Hamiltonian in **Table 1.1** we can see that the first order term has angular dependence (contains the geometric term $3\cos^2\theta-1$) and hence the powder pattern appears as shown in **Figure 1.3(a)**. Powder patterns are often sensitive to motions which occur at rates comparable to their linewidth, and such motions will cause a change in the shape of the Pake doublet when monitored under static conditions.² This line shape change can be simulated by a number of programs and a rate of rotation can be extracted.^{3,4}

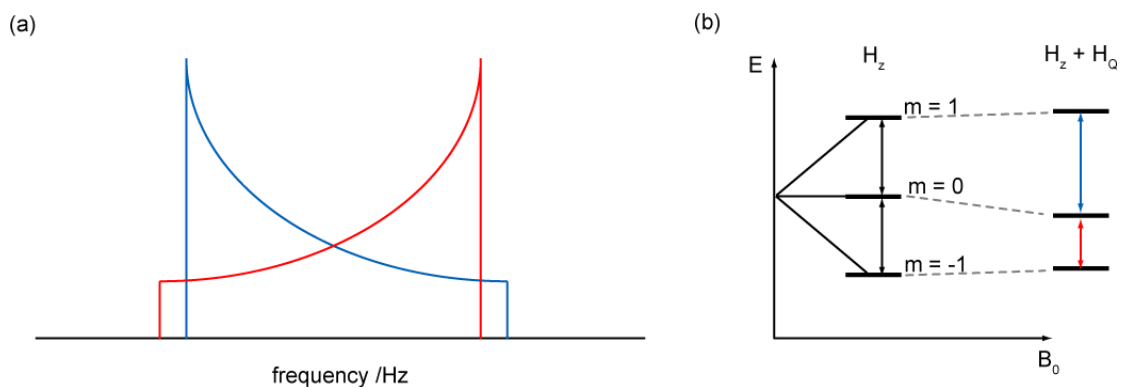


Figure 1.3. (a) Pake doublet. Red spectrum is this typical spectrum observed for an NMR transition. Blue spectrum is a reflection of the red spectrum, owing to the other transition from $+1 - 0$ seen due to ^2H being spin $I = 1$. (b) Energy level diagram from $I = 1$ with contribution of quadrupolar Hamiltonian, causing a larger energy gap (due to addition of quadrupolar interaction) for the blue transition and smaller for the red transition (due to subtraction of quadrupolar interaction).

1.2.2.4 Paramagnetic NMR

Paramagnetic materials are ones which have an unpaired electron (often from a transition metal). This unpaired electron interacts with surrounding nuclei, producing a range of interactions summed up in the Hamiltonian, \hat{H}_{para} as shown in **equation 1.10**.⁵

$$\hat{H}_{para} = \hat{H}_0 + \hat{H}_Z + (\hat{H}_{contact} + \hat{H}_D) \quad (1.10)$$

Where, \hat{H}_0 is the field- and nuclear spin-free electronic part which contains interactions that arise from kinetic energy and electrostatic interactions involving electrons and fixed nuclei, \hat{H}_Z refers to the Zeeman effect of the nuclear spins, and $\hat{H}_{contact} + \hat{H}_D$ (Fermi contact and dipolar effects) together describe a very strong interaction called the electron-nucleus hyperfine coupling interaction, which dominates solid state NMR spectra. $\hat{H}_{contact}$ causes partial transfer of unpaired electrons by direct delocalisation and spin polarisation, resulting in a shift in the “usual” peak position, whereas, \hat{H}_D couples the average dipole moment of the electronic distribution to the surrounding nuclear spins resulting in a large increase in the CSA.

These two factors can cause a ^1H spectrum which usually spans from 0 - 10 ppm for small organic molecules in a diamagnetic spectrum to span 1000s of ppm in paramagnetic materials. The use of fast magic angle spinning (rates exceeding 50 kHz – see section 1.2.2.5) has become widely accepted as part of the solution to overcome the difficulties of NMR of paramagnetic compounds and is routinely used because of its availability and relative ease to set up. Short high-powered adiabatic pulses (SHAPs)⁶ have been developed as described in section 1.2.3.8 below to overcome the broadband pulses required to excite the entire chemical shift range/required.

1.2.2.5 Magic angle spinning

CSA and dipolar coupling are major contributors to the broad lines observed in solid state spectra. Often the broadness of the spectra is undesirable due to lack of resolution, and multiple techniques have been developed which can be utilised to provide resolution enhancement. The most common technique is magic angle spinning (MAS). The Hamiltonians for \hat{H}_Q , \hat{H}_D and $\hat{H}_{CS\text{aniso}}$ all contain both a spin part as well as a geometric part which contains the term $3\cos^2\theta-1$ as seen in **Table 1.1**. By spinning the sample angled at $\theta = 54.74^\circ$ (well known as the 'magic angle' as illustrated in **Figure 1.4(c)**) the geometric term $3\cos^2\theta-1$ averages to zero, and the 1st order quadrupolar interactions, dipolar interactions and CSA can be eliminated from the spectrum. At high spinning speeds the anisotropic interactions in the sample start to be averaged and the spectrum starts to resemble the high resolution spectrum of solution state NMR, shown in **Figure 1.4(d)**. Without sufficient spinning speed the modulation of the interaction frequencies at the rotor frequency results in the CSA being manifested within spinning side bands, at a distance relating to the spinning speed of either side of the isotropic peak.

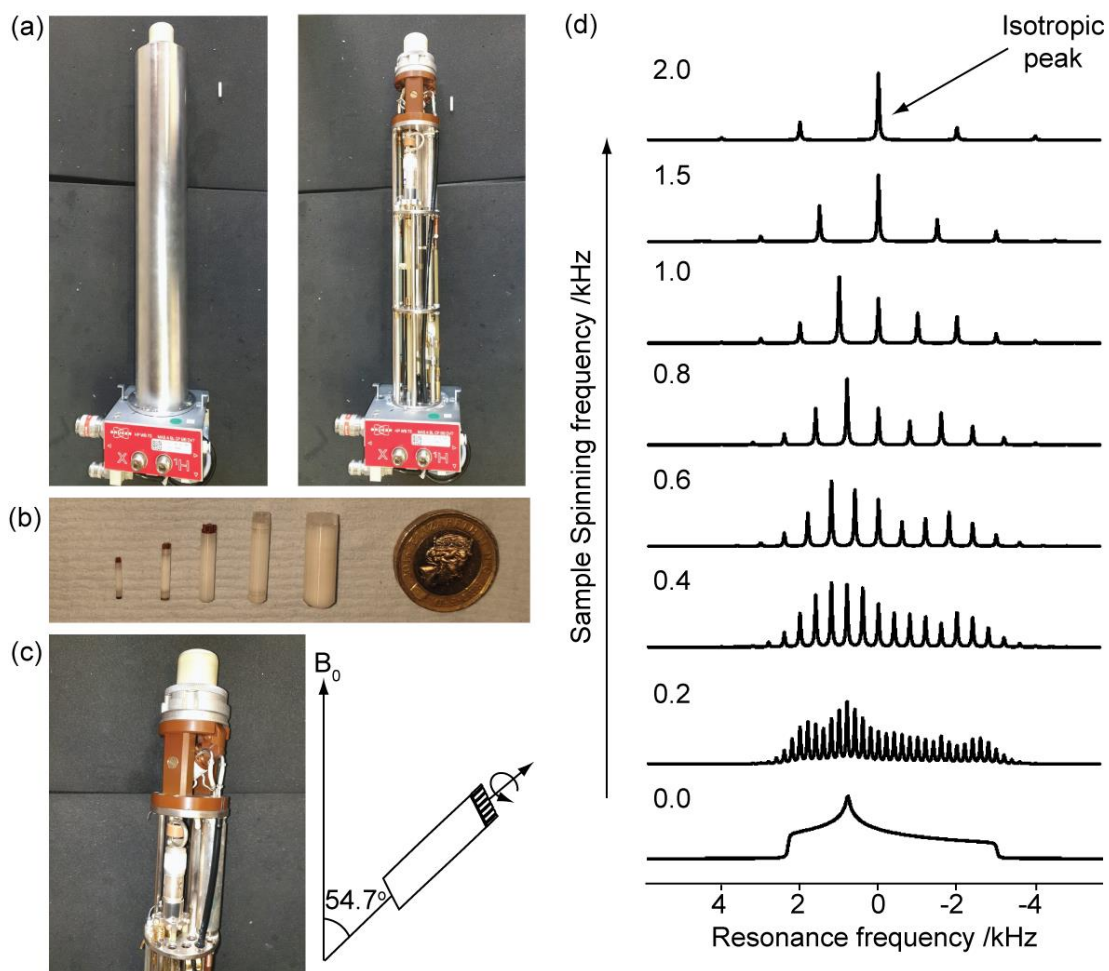


Figure 1.4. (a) Image of 4 mm probe with and without cover beside a 4 mm rotor. (b) Image of selection of rotors of differing sizes, from left to right 1.3, 1.9, 3.2, 4 and 7 mm rotor. (c) A close up image of the stator where the rotor sits in the probe and a schematic of MAS rotation. (d) NMR spectra vs MAS frequencies showing how CSA can be averaged out by MAS with increasing spinning speed increasing resolution.

1.2.3 NMR experiments

The following NMR experiments are used throughout this thesis and their understanding is crucial to ensure these are performed correctly in order to obtain results and translate them into meaningful data.

1.2.3.1 Observing NMR Signal

To observe signal in an NMR spectrum, the nuclei first need to become magnetized, by arranging themselves parallel with the magnetic field, this is a process known as relaxation. This alignment is referred to as the bulk magnetization vector. In the simplest NMR experiment, a “one pulse” also known as “pulse-acquire”, a single radio frequency (RF) pulse is applied to tilt this magnetisation factor away from the z axis into the transverse plane as shown in **Figure 1.5** below. A π pulse rotates the magnetisation factor 180°, whereas a $\pi/2$ pulse rotates it 90°.

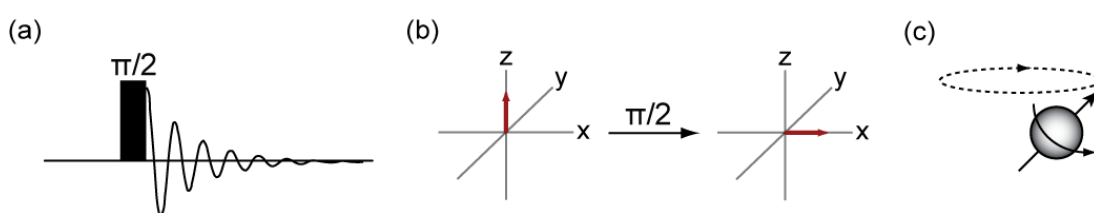


Figure 1.5. (a) Schematic representation of a one pulse experiment. (b) Vector model (red) representation of what happens to the bulk magnetization vector during the pulse sequence. (c) Schematic of nuclei precession within magnetic field.

As noted earlier, nuclei precess within the magnetic field (**Figure 1.5(c)**). When in the transverse plane, the precession of the nuclei induces a current at the resonating frequency of the nucleus. As the magnetization vector relaxes, less signal is detected on the x axis. This current is recorded over time and forms the free induction decay (FID). The FID can be Fourier transformed converting it into a frequency domain NMR spectrum.

1.2.3.2 Spin-lattice relaxation⁷

To observe signal, RF pulses perturb magnetization away from the z axis into the transverse plane, where signal is acquired, then the nuclei relax back to the z axis (to the standard Boltzmann distribution of states) over time. In order to do this, they must lose energy, and the route by which they lose that energy defines the relaxation pathway. Losing energy to the “lattice”, i.e. the nuclei’s surroundings, is known as spin-lattice relaxation and results in a growth of the z component of magnetization, as the Boltzmann equilibrium is restored. This is in contrast to Spin-Spin relaxation which corresponds to decoherence of magnetization in the transverse plane.

Relaxation is due molecular motion and results in the fluctuation of local magnetic fields in the sample and in solids typically the dipolar mechanism dominates. The correlation time, τ_c , is the time taken for the molecule to rotate by a radian and can be estimated when T_1 reaches a minimum using the following equation:

$$\omega_{0,H}\tau_c \approx 0.62 \quad (1.11)$$

Correlation times can be used to in conjunction with the Arrhenius theory to extract activation energies to provide further details about the motion of molecules.

Awareness of spin lattice relaxation is also required for NMR measurements. Prior to performing multiple scans in an experiment, we need to ensure that all nuclei are fully relaxed in order to obtain maximum signal in any NMR experiment. Therefore, their spin-lattice relaxation time, T_1 , is often measured using the inversion recovery experiment.

The inversion recovery experiment follows the pulse sequence shown in **Figure 1.6(a)** below, which can be visualised using the vector model shown in **Figure 1.6(b)**. Briefly, this sequence works by a π pulse inverting the magnetisation to the $-z$ axis. This magnetisation is then allowed recover during the delay period, τ , followed by a final read-out pulse prior to detection. The array of τ delay results in a range of various signal intensities. If $\tau = 0$, a maximum negative intensity is observed, whereas if τ is

long, a maximum positive intensity is seen. Using this sequence multiple times with increasing delay values results in increasing signal intensities which can be plotted, and eventually shows a plateau seen in **Figure 1.6(c)** which signifies $5 \cdot T_1$. $5 \cdot T_1$ is used as the recycle delay time to ensure full relaxation has occurred to attempt to get quantitative spectra.¹

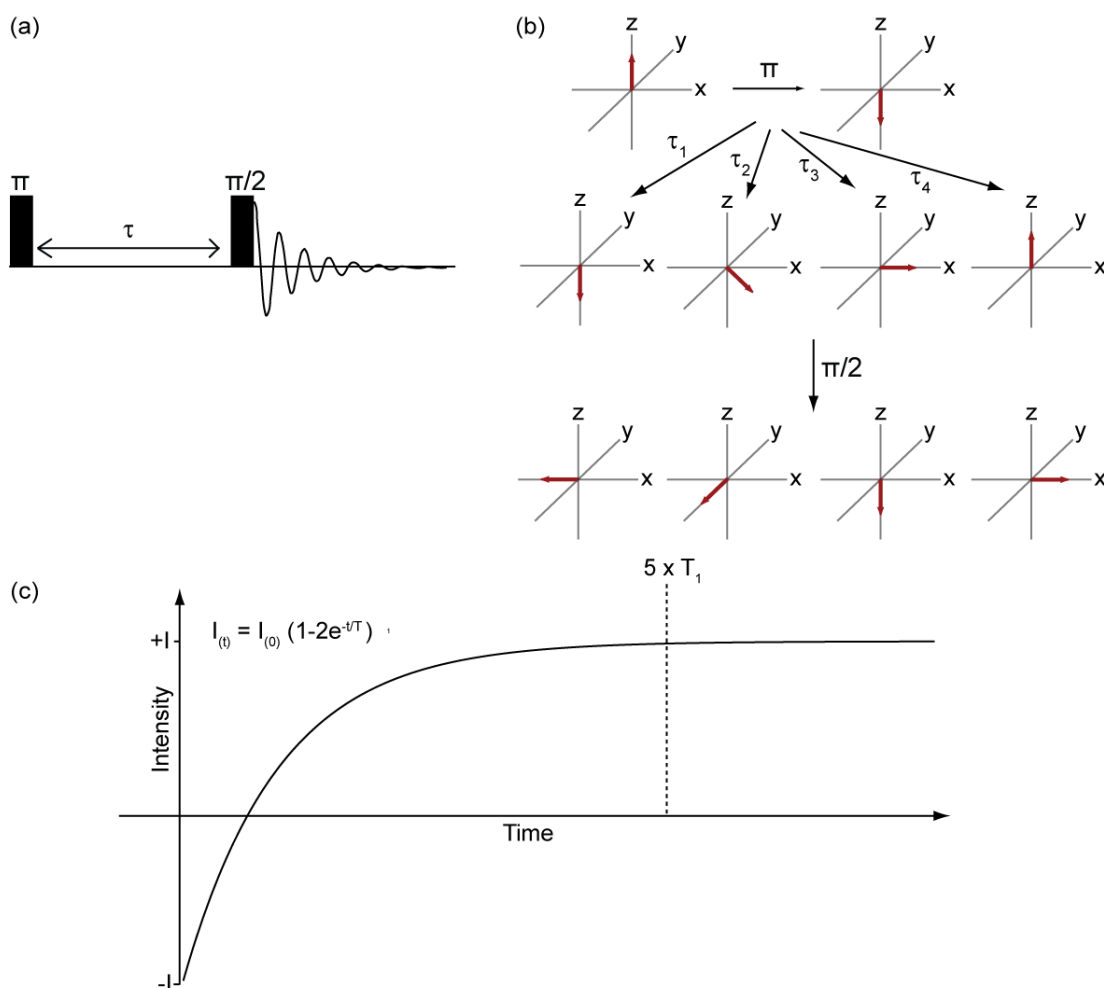


Figure 1.6. (a) Pulse sequence for inversion recovery experiment where τ is the polarisation build-up time. (b) Vector representation of what is happening throughout pulse sequences, length of τ increasing from $\tau_1 - \tau_4$ (c) Plot of intensity vs time to find value for T_1 .

Relaxation rates differ depending on many factors including the paramagnetic mechanism, quadrupolar relaxation mechanism, dipolar mechanism, and CSA, with the two latter relaxation mechanisms being the most dominant.⁸ Analysis of T_1 values can give information regarding the correlation times of motion in the order of the Larmor frequency. These correlation times can give insights into the motional

processes, the overall size of molecules as well as provide information on dynamics occurring in the systems.

If a paramagnetic centre is present, dipolar interactions between the unpaired electrons and the paramagnetic centre causes the spin-lattice (longitudinal) relaxation times and spin-spin (transverse) relaxation times (T_2) of surrounding NMR-active nuclei to reduce, shortening the time for excitation to decay. This phenomenon is known as paramagnetic relaxation enhancement (PRE) and accounts for the major relaxation mechanism within paramagnetic solids. These extremely short relaxation times experienced can lead to difficulties in obtaining signal for paramagnetic compounds.

1.2.3.3 Saturation recovery

Saturation recovery is another experiment which enables the measurement of T_1 . It is often the technique of choice over the inversion recovery method due to being less time consuming as well as only requiring $\frac{\pi}{2}$ degree pulses, which allows quadrupolar nuclei which cannot invert their magnetisation to also be observed. A saturation train causes saturation of the bulk magnetization to zero, the time delay, τ , permits relaxation on the z axis, followed by the $\frac{\pi}{2}$ pulse back into the transverse plane and signal acquisition (**Figure 1.7**). This method results in a build-up curve of magnetization, eventually recovering all magnetization resulting in a plateau at $5 \cdot T_1$. From this a T_1 time can be determined and it is this T_1 method that has been used for all ^1H T_1 determinations of diamagnetic materials throughout this thesis.

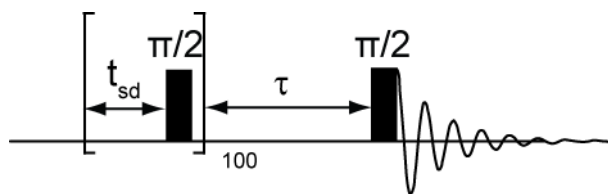


Figure 1.7. Pulse sequence for Saturation recovery experiment. t_{sd} is the saturation delay between $\pi/2$ pulses. The saturation block is repeated 100 times in this instance to ensure full saturation of the magnetisation. τ is the polarisation build-up time.

1.2.3.4 Echo

The decay of the NMR signal over time due to both relaxation and inhomogeneous effects which result in each nuclei present in the samples to precess at varying rates. By applying an inversion (π) pulse after a time τ , any dephasing experienced is “refocused” back to the opposite axis resulting in all signals being refocused at the end of the second τ period and signal is typically obtained after τ as shown in **Figure 1.8** below. The additional benefit to this effect is that the dead time required after the π pulse-acquire will no longer result in a lack of signal as there is sufficient time between the π pulse and the top of the echo where the signal should be recorded from. This pulse sequence can be used to measure T_2 relaxation by increasing the τ interval.

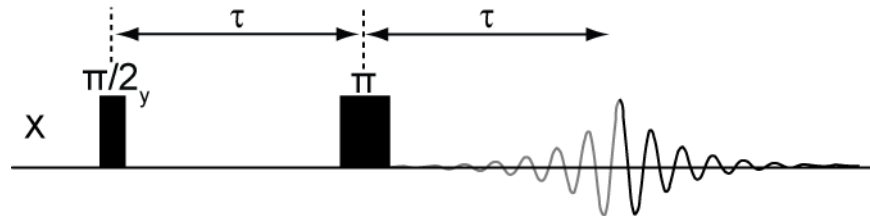


Figure 1.8. Echo pulse sequence with delay of time τ between the excitation and inversion pulse. τ is the delay time between the two pulses Grey 'FID' represents the build-up of signal which is often not acquired.

Due to the quadrupolar nature of the Spin 1 nucleus, the FID signal decays rapidly, resulting in some signal loss before acquisition is possible leading to distortions of the signal. To eliminate this effect and maximise signal, a solid echo, similar to the echo described above, is used following the pulse sequence shown in **Figure 1.9**.⁹ Due to the quadrupolar frequency being larger than the applied pulse power, it is often not possible to fully invert the magnetization for these systems, therefore only 90° pulses are used to refocus as much magnetization as has been lost from T_2 dephasing and produce a symmetrical FID. The FID can then be processed to obtain maximum signal with minimum noise.

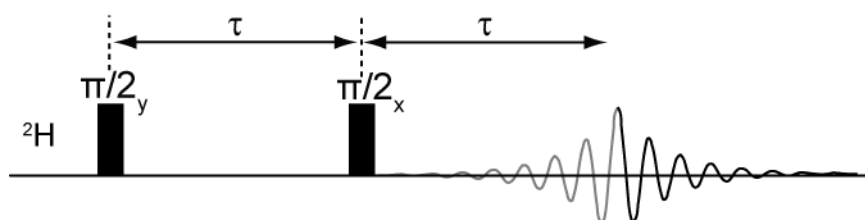


Figure 1.9. Schematic representation of a solid echo pulse sequence used for quadrupolar nuclei e.g., ^2H . τ is the delay time between the two pulses Grey 'FID' represents the build-up of signal which is often not acquired.

1.2.3.5 Heteronuclear decoupling

Heteronuclear decoupling is a valuable technique in solid state NMR. By applying heteronuclear decoupling, the heteronuclear dipolar coupling, which significantly contributes to the broadening in solid state NMR spectra, is reduced/eliminated, resulting in sharper signals which often simplify the spectrum. This technique is often used during ^{13}C acquisition and is known as the high-power decoupling (HPDec) experiment, enabling 'quantitative' ^{13}C spectra to be acquired. There are various pulse programs that apply heteronuclear decoupling, of which continuous wave is the simplest and irradiates the samples with RF of a single frequency throughout acquisition. However, many other techniques have been proposed which apply shorter pulses of RF irradiation including TPPM,¹⁰ SPINAL-64¹¹ and XiX¹². SPINAL-64 is the method of decoupling used throughout this thesis as it requires less optimisation than the TPPM techniques and is efficient at the MAS frequencies (typically 12.5 kHz) used.

1.2.3.6 ^{13}C NMR

^{13}C is the only NMR active nucleus of carbon. The sensitivity of ^{13}C NMR is hindered by its low natural abundance of 1.1%, and further by its relatively low gyromagnetic ratio (with Δ_E being dependent on γ , as shown in **Figure 1.1**), being only $\frac{1}{4}$ that of ^1H . An additional benefit is that the delay time used in these experiments relates to the ^1H relaxation time which is often considerably shorter than that of ^{13}C . This results in direct excitation spectra being time consuming to obtain in comparison to ^1H spectra.

1.2.3.6.1 Cross Polarisation

To enhance the signal obtained, we utilise the polarisation of ^1H and transfer this to ^{13}C , improving the signal theoretically by four times. The most common technique which employs this is called cross polarisation (CP).¹³ Additionally T_1 values for carbons are typically significantly longer than that of ^1H , often being in the range of tens of seconds and minutes, however, due to the direct pulse being on ^1H in the CP sequence it is the ^1H T_1 with which the recycle delay is determined. This is often much shorter and enables more scans within the same timeframe, resulting in a further enhancement of the signal-to-noise ratio. However, it should be noted that this technique is not quantitative as it depends on dipolar coupling strength and the dynamics of the system.

The pulse sequence in **Figure 1.10** shows that the initial pulse on the ^1H channel rotates the magnetization to the transverse plane, then a simultaneous pulse applies a spin lock to both the ^1H and the ^{13}C channels (following the conditions stated in the Hartmann- Hahn match - **equation 1.12**) which transfers polarisation from ^1H to the ^{13}C nuclei, transferring the ^{13}C nuclei into the transverse plane and then a FID is acquired on the ^{13}C channel, while decoupling occurs on the ^1H channel.

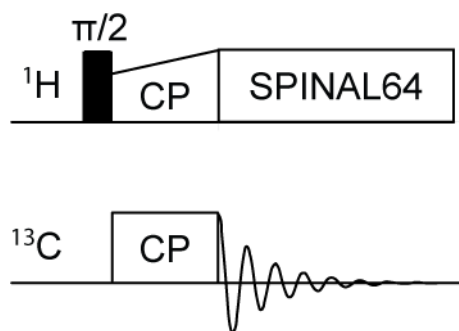


Figure 1.10. CP pulse sequence. Where the contact pulse is ramped on the ^1H channel and acquisition is obtained under SPINAL-64 decoupling.

To achieve maximum signal, the ^1H and ^{13}C signals are matched under the Hartmann-Hahn conditions stated in **equation 1.12**.^{14,15}

$$\nu(^1\text{H}) - \nu(^{13}\text{C}) = n \cdot \nu_{\text{rot}} \quad (1.12)$$

Where $\nu(^1\text{H})$ and $\nu(^{13}\text{C})$ are nutation frequencies; the frequency of the applied RF field on the respective nuclei. By matching the nutation frequencies (or matching them to a spinning sideband if $n \geq 1$) the two nuclei are put “into contact” and magnetisation can be transferred between the two nuclei *via* dipolar coupling. The efficiency of this transfer of magnetisation is proportional to the strength of the dipolar coupling and is therefore different depending on the nuclei’s surroundings.

1.2.3.6.2 Phase shifted recoupling effect a smooth transfer of order (PRESTO)

An alternative polarisation transfer technique to CP is PRESTO.¹⁶ PRESTO is often desirable when the Hartmann-Hahn match cannot be found or spin locking of the X channel proves difficult *e.g.* in quadrupolar nuclei. This technique uses symmetry-based recoupling blocks to reintroduce heteronuclear recoupling, which is averaged out under MAS, whilst implementing homonuclear decoupling on the ¹H channel. The PRESTO pulse sequence¹⁶ used within this thesis uses **R18₁**⁷ blocks to reintroduce heteronuclear dipolar coupling, enabling polarisation transfer to occur incorporating 18 pulses into two rotor periods resulting in a power of 9 x MAS rate required for optimum signal. These recoupling blocks can however require very high power, and are often adapted to “windowed” blocks if necessary, to reduce the load on the hardware. Additionally, windowed blocks can provide a larger scaling factor, which is beneficial when interactions are small.

1.2.3.6.3 ^{13}C T_1

Dynamics of nuclei are often probed by plotting the change of spin-lattice relaxation time T_1 vs. temperature enabling T_1 minima to be found and therefore correlation times to be extracted. The inherently long ^{13}C T_1 relaxation times and low sensitivity, cause traditional inversion recovery methods, which require ^{13}C to be observed directly, to be extremely long experiments for this nucleus. To maximise efficiency and reduce the time taken to measure these values, relaxation measurements are done using the CPXT $_1$ pulse program¹⁷ shown in **Figure 1.11**. The CPXT $_1$ pulse program takes advantage of the CP signal enhancement and short T_1 times of the ^1H to achieve maximum signal intensity.

The contact pulse brings the ^{13}C signal into the transverse plane, which is then pulsed in either the y or $-y$ axis resulting in z or $-z$ magnetization respectively. This magnetization relaxes over a period, τ , enabling relaxation down to the unenhanced ^{13}C Boltzmann value. This is followed by the $\frac{\pi}{2}$ read out pulse. Then the intensities obtained on the y and $-y$ axis are summed together and plotted for varying time delays an exponential curve results, giving the $5 \cdot T_1$ at its decay.

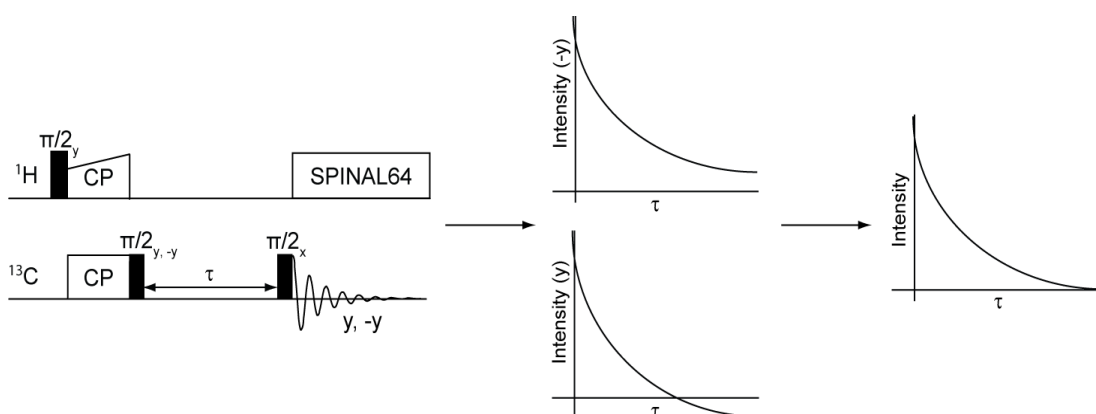


Figure 1.11. CPXT $_1$ pulse sequence, with ^1H decoupling, which provides the resulting intensity plots on the y and $-y$ axis dependent on the phase, which then sum together to obtain the final overall plot of intensity vs time to find value for T_1 .

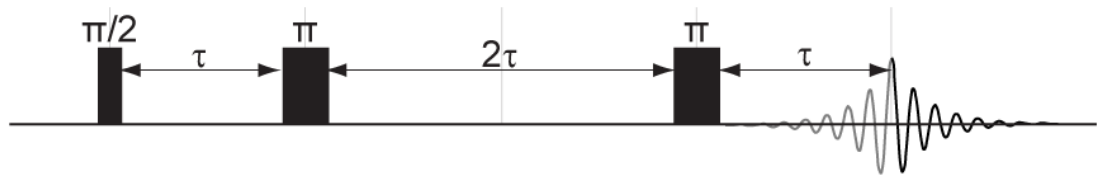
1.2.3.7 Short high powered adiabatic pulses (SHAPs)

With paramagnetic samples spanning very large chemical shift ranges, the RF pulse strength required to excite the whole spectrum requires very large powers which could cause hardware damage. Adiabatic frequency swept pulses sweep the effective magnetic field slowly as to allow for a multitude of spins with significant differing resonance frequencies to be perturbed at the same time. Hence this class of pulses have been developed further in recent years in order to overcome the problem of the large power required to excite a large range as they are able to provide large ratios between the RF power required and the achieved spectral bandwidth excitation.

These pulses work by locking magnetisation along a specific vector, quite often a hyperbolic tangent shape is used for frequency modulation, to direct it toward its required destination. It has been shown that these SHAPs with tangential frequency sweeps could be optimised to accomplish ^{13}C and ^1H broadband inversion. Further work presents a framework allowing one to define criteria for designing an adiabatic pulse that works for a specified MAS rate – a process known as ‘rotor-synchronising’ the pulse length¹⁸ and has recently been used to study paramagnetic compounds.

The double echo has the addition of a second π pulse in comparison to the spin echo described in Section 1.2.3.4 and **Figure 1.7** above. This second echo removes baseline distortion and aids in phase correction of the spectrum, ideal for large spectral widths. To further apply this to paramagnetic compounds, rotor synchronised SHAPs can be applied (**Figure 1.12(b)**) rather than the hard pulses shown in **Figure 1.12(a)**. These SHAPs replace the conventional π pulse giving more tolerance to enable the large frequency range to be refocused.

(a) Double echo (hard)



(b) Double echo (adiabatic)

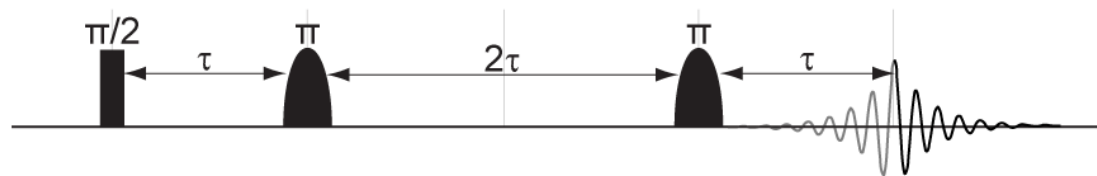


Figure 1.12. (a) Double echo pulse sequence where τ is the delay time between the first two pulses. Grey 'FID' represents the build-up of signal which is often not acquired. (b) Double echo (adiabatic) pulse sequence with SHAPs replacing the hard π pulses.

1.2.3.8 Transferred echo double rotation

The one-dimensional Transferred echo double rotation (TEDOR) experiment enables identification of the heteronuclear dipolar coupled nuclei present within the sample.¹⁹ Nuclei which are not coupled are filtered out of the spectrum making this a useful technique to identify protonated carbons.

The pulse sequence is shown in **Figure 1.13** below. Initial excitation is applied to the unobserved nuclei (^1H), followed by rotor synchronised ^{13}C -spin π pulses are introduced at $\frac{1}{4}$ and $\frac{3}{4}$ of the rotor period, reintroducing the heteronuclear dipolar coupling otherwise averaged out by MAS, whilst ^1H CSA is refocused. A simultaneous $\frac{\pi}{2}$ pulse is performed on both channels upon the completion of a rotor cycle to transfer the magnetisation from ^1H spins to dipolar coupled nearby carbon nuclei. ^1H - π pulses are then introduced at $\frac{1}{4}$ and $\frac{3}{4}$ of the rotor period and signal is acquired after a total of 2 rotor periods.

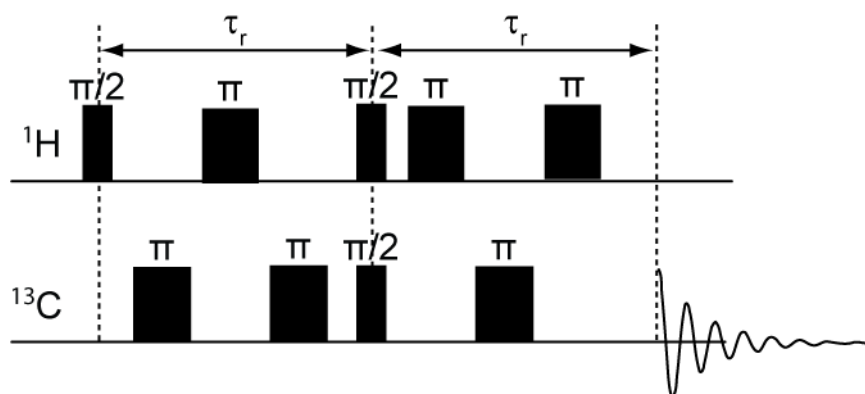


Figure 1.13. TEDOR pulse sequence. Rotor synchronised π pulses at $\frac{1}{4}$ and $\frac{3}{4}$ of the rotor period, τ_r , are applied to reintroduce heteronuclear dipolar coupling.

1.2.3.9 Two-dimensional NMR

Two-dimensional (2D) NMR techniques can be used to probe selective NMR interactions and are often very useful in unequivocal determination of the structure of a molecule. In 2D NMR signals are recorded as a function of two time variables, which can be Fourier transformed to provide two frequency axes, resulting in a correlation describing an interaction/correlation dependent on the particular experiment. A general 2D NMR scheme is laid out in **Figure 1.14** below and consists of preparation, evolution, mixing and detection periods. The value of Δ_1 during the evolution period is increased incrementally over each acquisition to build up a time domain dataset which when Fourier transformed will yield a 2D frequency domain spectrum.

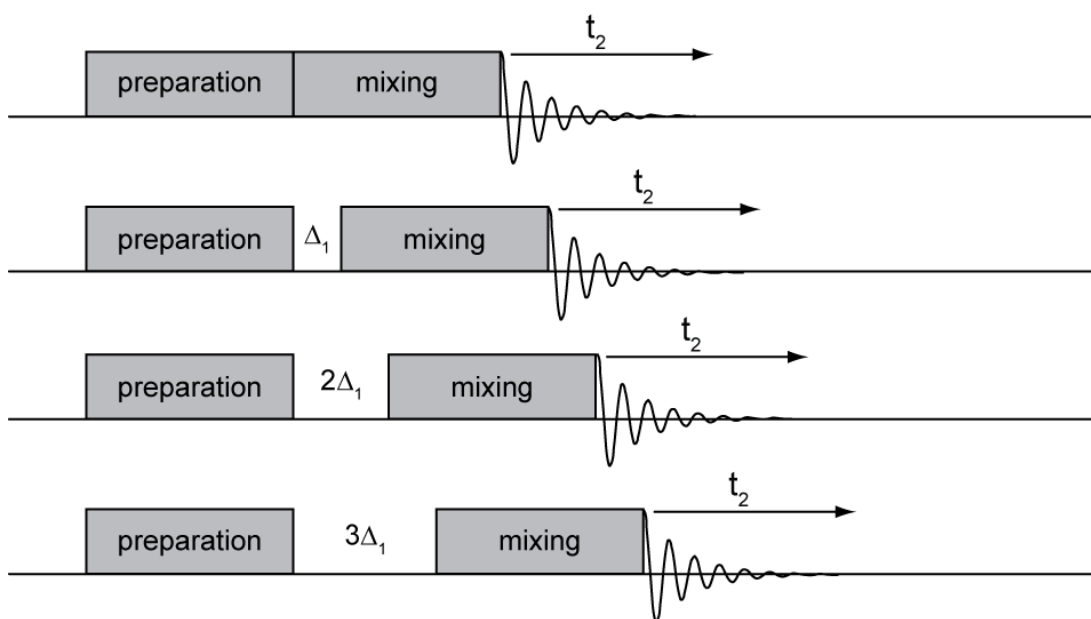


Figure 1.14. Basic 2D pulse scheme. The evolution period, Δ_1 , between the preparation and mixing time elements is increased incrementally followed by another period which allows for mixing before detection in the t_2 period.

1.2.3.9.1 INADEQUATE

Spectral assignment is key to assigning/confirming structures. Whilst this is often completed using one-dimensional techniques, more challenging structures require more information, which we can gain from more complex, two-dimensional, pulse programs. The incredible natural abundance double quantum experiment (INADEQUATE) provides through-bond connectivities of adjacent nuclei (most commonly ^{13}C), exploiting scalar couplings to do so.²⁰

The INADEQUATE pulse sequence is shown in **Figure 1.15** below. The first step requires a polarization transfer from ^1H to ^{13}C via a CP step. ^{13}C magnetization then evolves, and is refocused during the τ - π - τ period. The ^{13}C $\frac{\pi}{2}$ pulse generates double quantum coherences (a phase coherence where the state changes by a magnetic quantum number of 2, rather than single quantum coherences where the quantum number changes by the allowed value of 1) for bonded nuclei, which evolves during t_1 , and is detected in the indirect dimension. The final $\frac{\pi}{2}$ pulse enables acquisition of single quantum transitions, and a standard FID is acquired for first dimension detection (**Figure 1.15**). Although this method provides very valuable information, the low abundance of the ^{13}C nuclei result in the experiment requiring a large amount of scans, and hence a substantial amount of spectrometer time to get sufficient signal.

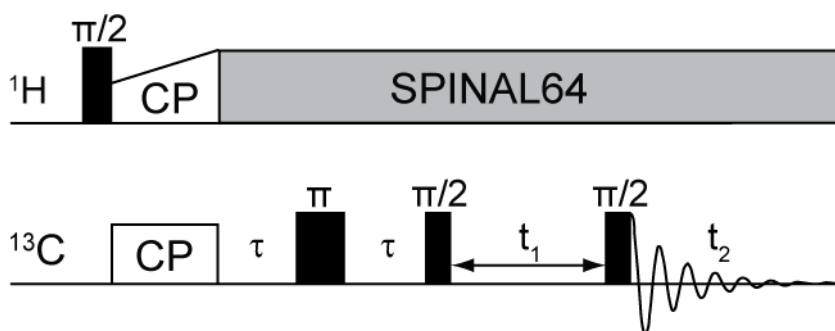


Figure 1.15. INADEQUATE pulse sequence. A cross polarisation step is used for initial polarisation transfer. SPINAL64 heteronuclear decoupling is used during ^{13}C acquisition.

1.2.3.9.2 R-PDLF (proton detected local field)

Proton detected local field (PDLF) experiments can probe dipolar coupling and hence distances in relatively small molecules.²¹ PDLF is a 2D experiment which correlates the chemical shift in the F2 dimension with the dipolar coupling in the indirect dimension allowing the dipolar coupling spectrum to be extracted at each site. It follows the pulse program in **Figure 1.16** below. During the ^1H evolution period, rotor synchronised recoupling blocks are applied to recouple the heteronuclear dipolar coupling which has been removed by MAS whilst removing homonuclear dipolar coupling. In the middle of the t_1 period a π pulse is applied to refocus the ^{13}C chemical shift. This is followed by a polarization transfer step using the PRESTO sequence which recouples the heteronuclear dipolar coupling to allow transfer, whilst decoupling ^1H and therefore eliminating any spin diffusion from occurring ready for ^{13}C detection. CP can also be used for the polarization transfer step, however it is susceptible to ^1H ^1H spin diffusion and therefore to minimise this short contact times are required, often resulting in lower signal intensity.

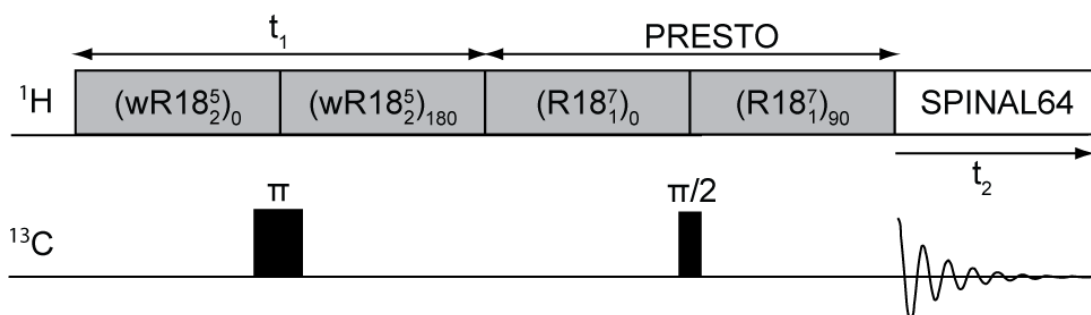


Figure 1.16. Proton Detected Local Field (PDLF) experiment using the windowed sequence (wPDLF)²⁰ that correlates the ^{13}C chemical shifts in ω_2 with the ^{13}C ^1H dipolar coupling spectra in ω_1 . **wR18₂⁵** recouples the heteronuclear dipolar interaction during the rotor synchronised evolution period t_1 to enable observation of ^{13}C ^1H dipolar spectra, whilst the **wR18₁⁷** blocks recouple the heteronuclear dipolar interaction enabling the transfer of polarization from ^{13}C to ^1H using the PRESTO sequence. SPINAL64 heteronuclear decoupling¹⁰ is used during ^{13}C acquisition.

1.3 Systems and materials used in this thesis

In this thesis the above techniques have been utilised to study advanced molecular materials.

In **chapter 3**, we explore the tubular covalent cages (TCC), a recently discovered family of porous organic cages which have been shown to have inherent porosity and are capable of applications similar to molecular organic frameworks, including molecular separation and gas storage.²² These TCCs have been chosen as they have an architecture which can permit the observation of these properties. I.e., by studying the dynamics of the “windows” in these TCCs guest capture/release can be observed.

Chapter 4 assesses the pillar[n]arene macrocycles which also have use in molecular separation.²³ The chosen pillar[n]arene; perethylated pillar[6]arene, in particular has been shown to selectively adapt and adsorb para-xylene over the other xylene isomers, which is a known challenge due to the similarity in the boiling/freezing points of these materials.²⁴ This flexibility and adaptation was an ideal property to probe in order to gain more understanding of these macrocycles.

Hybrid perovskites were explored in **chapter 5**. These three-dimensional structures are typically used as photovoltaic materials in solar cells.²⁵ Melting of these structures is often desired as the defects created in the melted structure often promote thermal and electrical conductivities. The three hybrid perovskites studied in **chapter 5** have a paramagnetic metal ion, causing challenging conditions to study these materials by NMR, however with the techniques outlined earlier in this chapter, these are overcome to confirm the structure of both the crystalline and melted materials.

1.4 Conclusion

The techniques presented here are only a small portion of those that are used within the field of NMR and there are many more schemes which can provide similar/alternative information on dynamics and structure of materials. However, these solid state NMR techniques are those selected and used routinely throughout this thesis to probe various supramolecular assemblies.

1.5 References

- (1) Apperley, D. C.; Harris, R. K.; Hodgkinson, P. *Solid-State NMR: Basic Principles and Practice*, 1st ed.; Momentum Press: New York, 2012.
- (2) O'Dell, L. A.; Ratcliffe, C. I. Quadrupolar NMR to Investigate Dynamics in Solid Materials. In *NMR of Quadrupolar Nuclei in Solid Materials*; John Wiley & Sons: Chichester, 2012; pp 213–232.
- (3) Vold, R. L.; Hoatson, G. L. Effects of Jump Dynamics on Solid State Nuclear Magnetic Resonance Line Shapes and Spin Relaxation Times. *J. Magn. Reson.* **2009**, *198*, 57–72.
- (4) The MathWorks Inc. MATLAB. Natick, MA, 2016.
- (5) Parigi, G.; Luchinat, C. Chapter 1 NMR Consequences of the Nucleus–Electron Spin Interactions. In *Paramagnetism in Experimental Biomolecular NMR*; The Royal Society of Chemistry, 2018.
- (6) Kervern, G.; Pintacuda, G.; Emsley, L. Fast Adiabatic Pulses for Solid-State NMR of Paramagnetic Systems. *Chem. Phys. Lett.* **2007**, *435*, 157–162.
- (7) Friebolin, H. *Basic One and Two Dimensional NMR Spectroscopy*, 4th ed.; WILEY-VCH: Weinheim, 2005.
- (8) Keeler, J. *Understanding NMR Spectroscopy*, 2nd ed.; John Wiley & Sons: Chichester, UK, 2010.
- (9) Antonijevic, S.; Wimperis, S. Refocussing of Chemical and Paramagnetic Shift Anisotropies in ^2H NMR Using the Quadrupolar-Echo Experiment. *J. Magn. Reson.* **2003**, *164*, 343–350.
- (10) Königsberger, E.; Sterk, H. Anisotropic Molecular Reorientation Measured by

- NMR Relaxation Including Cross Terms between Dipolar and Chemical Shift Anisotropy Interactions. *J. Chem. Phys.* **1985**, *83*, 2723–2726.
- (11) Fung, B. M.; Khitritin, A. K.; Ermolaev, K. An Improved Broadband Decoupling Sequence for Liquid Crystals and Solids. *J. Magn. Reson.* **2000**, *142*, 97–101.
- (12) Detken, A.; Hardy, E. H.; Ernst, M.; Meier, B. H. Simple and Efficient Decoupling in Magic-Angle Spinning Solid-State NMR: The XiX Scheme. *Chem. Phys. Lett.* **2002**, *356*, 298–304.
- (13) Pines, A.; Gibby, M. G.; Waugh, J. S. Proton-Enhanced NMR of Dilute Spins in Solids. *J. Chem. Phys.* **1973**, *59*, 569.
- (14) Hartmann, S. R.; Hahn, E. L. Nuclear Double Resonance in the Rotating Frame. *Phys. Rev.* **1962**, *128*, 2042–2053.
- (15) Peersen, O. B.; Wu, X. L.; Kustanovich, I.; Smith, S. O. Variable-Amplitude Cross-Polarization MAS NMR. *Journal of Magnetic Resonance, Series A*. 1993, pp 334–339.
- (16) Zhao, X.; Hoffbauer, W.; Schmedt auf der Günne, J.; Levitt, M. H. Heteronuclear Polarization Transfer by Symmetry-Based Recoupling Sequences in Solid-State NMR. *Solid State Nucl. Magn. Reson.* **2004**, *26*, 57–64.
- (17) Torchia, D. A. The Measurement of Proton-Enhanced Carbon-13 T_1 Values by a Method Which Suppresses Artifacts. *J. Magn. Reson.* **1978**, *30*, 613–616.
- (18) Hing, A. W.; Vega, S.; Schaefer, J. Transferred-Echo Double-Resonance NMR. *J. Magn. Reson.* **1992**, *96*, 205–209.
- (19) Lesage, A.; Auger, C.; Caldarelli, S.; Emsley, L. Determination of Through-Bond

Carbon-Carbon Connectivities in Solid-State NMR Using the INADEQUATE Experiment. *J. Am. Chem. Soc.* **1997**, *119*, 7867–7868.

- (20) Dvinskikh, S. V.; Zimmermann, H.; Maliniak, A.; Sandström, D. Measurements of Motionally Averaged Heteronuclear Dipolar Couplings in MAS NMR Using R-Type Recoupling. *J. Magn. Reson.* **2004**, *168*, 194–201.
- (21) Perras, F. A.; Wang, Z.; Naik, P.; Slowing, I. I.; Pruski, M. Natural Abundance ¹⁷O DNP NMR Provides Precise O–H Distances and Insights into the Brønsted Acidity of Heterogeneous Catalysts. *Angew. Chemie - Int. Ed.* **2017**, *56*, 9165–9169.
- (22) Slater, A. G.; Little, M. A.; Pulido, A.; Chong, S. Y.; Holden, D.; Chen, L.; Morgan, C.; Wu, X.; Cheng, G.; Clowes, R.; et al. Reticular Synthesis of Porous Molecular 1D Nanotubes and 3D Networks. *Nat. Chem.*, **2017**, *9*, 17–25.
- (23) Ogoshi, T.; Yamagishi, T. A.; Nakamoto, Y. Pillar-Shaped Macrocyclic Hosts Pillar[n]Arenes: New Key Players for Supramolecular Chemistry. *Chem. Rev.*, **2016**, *116* (14), 7937–8002.
- (24) Jie, K.; Liu, M.; Zhou, Y.; Little, M. A.; Pulido, A.; Chong, S. Y.; Stephenson, A.; Hughes, A. R.; Sakakibara, F.; Ogoshi, T.; et al. Near-Ideal Xylene Selectivity in Adaptive Molecular Pillar[n]Arene Crystals. *J. Am. Chem. Soc.*, 2018, *140*, 6921–6930.
- (25) Saparov, B.; Mitzi, D. Organic–Inorganic Perovskites: Structural Versatility for Functional Materials Design. *Chem. Rev.*, **2016**, *116* (7), 4558–4596.

Chapter 2: Recent Advances in Probing Host-Guest Interactions with Solid State Nuclear Magnetic Resonance

2.1 Overview

Chapter 2 is a paper entitled “Recent Advances in Probing Host-Guest Interactions with Solid State Nuclear Magnetic Resonance” by Ashlea R. Hughes, and Frédéric Blanc. Which has been submitted for publication in 2021. The author contributions are as follows: A.R.H. wrote the manuscript with consultation from F.B.

2.2 Abstract

An overview of the recent role of solid-state Nuclear Magnetic Resonance (NMR) spectroscopy in the field of supramolecular chemistry to probe host-guest interactions is provided. Over the last few years, solid state NMR methodologies have provided unique insights into the atomic level structure and dynamics of guest molecules adsorbed in solid materials that are not available by other approaches. This chapter discusses the range of NMR interactions that enable access to this information and provides a number of illustrating examples that highlight their applications in a wide range of chemical systems and porous materials covering metal organic frameworks, porous molecular solids and zeolites.

2.3. Introduction to host-guest interactions and supramolecular chemistry

Host-guest interactions are prevalent in nature and play important roles in many critical functions. These non-covalent interactions form supramolecular complexes between multiple molecules to occur by hydrogen bonding, hydrophobic forces, van der Waals forces, π - π interactions and electrostatic effects and are responsible for the three-dimensional structure of biomacromolecules, molecular recognition processes, self-assembly, and many further examples of which would not be able to perform their function without these crucial interactions.¹ These examples listed above have inspired chemists to exploit host-guest interactions for drug discovery, molecular separation and catalysis leading to the growing field of supramolecular chemistry. To the best of our knowledge, the first example of a synthetic compound capable of complexing alkali metal cations was the crown ether dibenzo-18-crown-6 (illustrated in **Figure 2.1**), discovered by Charles J. Pedersen in 1967.² The affinity of dibenzo-18-crown-6 for the potassium ion was found to be greater than that of the smaller sodium cation, enabling preferential molecular separation of these alkali metal cations. Leading on from this seminal work, Charles J. Pedersen along with Donald J. Cram and Jean-Marie Lehn were in 1987 awarded the Nobel Prize in Chemistry for their “development and use of molecules with structure-specific interactions of high selectivity”.³⁻⁵ The field of supramolecular chemistry was then again rewarded with the 2016 Nobel Prize in Chemistry to Jean-Pierre Sauvage, Sir J. Fraser Stoddart and Bernard L. Feringa for their design and production of molecular machines, where molecules are linked together *via* a mechanical bond, rather than covalent.⁶⁻⁸ The diversity of this research area causes it to be an ever growing and a rapidly developing field of chemistry.

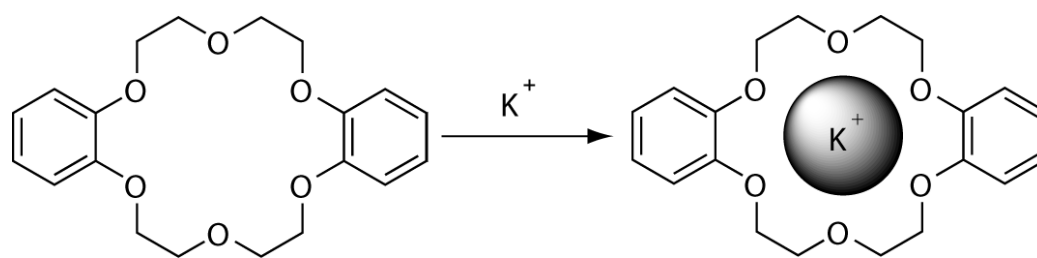


Figure 2.1. Typical host-guest chemistry example of dibenzo-18-crown-6 and K^+ ions forming supramolecular complex held together by electrostatic interactions originally discovered by Charles J. Pedersen.²

The understanding of the functionality of supramolecular materials requires the knowledge of both the structure of the materials and their configuration in relation to each other. This however, largely depends on the materials dynamics and flexibility, as these factors control the chemistry, adsorption or encapsulation. In this chapter, recent examples of host-guest interactions in supramolecular assemblies in which the understanding has been advanced by solid state NMR experiments in order to demonstrate its utility will be reviewed. This chapter will highlight the most recent advances since the last review on this topic in 2016⁹ and describe the interactions from the perspective of the solid state NMR techniques which have been used rather than either the types of interactions,^{9–11} or class of molecules.¹² Each section is illustrated by brief examples which use a particular solid state NMR technique needed to gain further insights into the structure and dynamics which are of high importance in this field.

2.4. Widely used approaches to probe host-guest interactions

A range of experimental methods has been used to investigate host-guest systems. Fluorescence spectroscopy is widely exploited within this area, due to its ability to yield key information regarding the occurrence of complexation in the form of a spectral shift¹³ whilst contributing rather limited information about the strength or location of the host-guest interaction and is therefore often combined with other methods to achieve this. Calorimetry is able to provide the strength of the host-guest interaction,¹⁴ however, the location of the guest and the type of interactions are difficult to decipher without prior knowledge of potential binding sites. Diffraction-based methods such as X-ray diffraction (XRD) probe long-range order and are critical to elucidate structural host-guest features. However, the dynamics and mobility of supramolecular assemblies are challenging to assess using these methods due to the inherent requirement to accessing short range structural information. Diffraction methods are therefore often paired with NMR to provide a more complete understanding of the interactions and dynamics at play in supramolecular assemblies.¹¹ Additionally, density functional theory (DFT) studies are becoming more and more prevalent to procure detailed structural information regarding bonding and electronic structures (*e.g.* to compute NMR parameters and support spectral assignment),¹⁵⁻¹⁷ all providing complementary information to experimental data crystallography.^{9,11,18,19} Hence, in conjunction with diffraction-based methods and computational studies, solid state NMR is playing an important role in the study of host-guest systems and has strong potential to provide information regarding both structure and dynamics of supramolecular chemistry as illustrated below.

2.5. Solid state NMR and NMR interactions as probes to study supramolecular materials

Solid state NMR is a powerful tool for understanding the short-range order and dynamics for a range of solid materials in both crystalline and amorphous states. NMR provides site-specific and local structural information, and is therefore a robust approach for probing spatial proximities. The NMR spectra of solids are affected by a number of NMR interactions which include Zeeman splitting (interaction of the nuclear spin with the external magnetic field B_0), isotropic and orientation dependent (anisotropic) chemical shifts (indirect interaction of the nuclear spin with B_0 *via* the electrons), through-space dipolar coupling (direct nuclear spin dipole-dipole coupling) and through-bond scalar J couplings (indirect nuclear spin dipole-dipole coupling *via* the electrons), and for nuclei with spin quantum number $I > 1/2$, quadrupolar interaction (interaction of the nuclear electrical quadrupolar moment with the electric field gradient (EFG)). All of these interactions affect the appearance of the NMR spectrum and provide structural and dynamics information on the local environment.

The two most common methods to explore host-guest interactions by solid state NMR methods exploit chemical shielding (directly relating to the observed chemical shift) and dipolar interactions, both of which are highly dependent on local structure and packing arrangements. The chemical shielding interaction is a sum of both the diamagnetic and paramagnetic shielding contributions. In diamagnetic materials, external magnetic fields cause movement of electrons within orbital to oppose the external magnetic field. Diamagnetic currents relate directly to the electron density surrounding a nucleus and perturbs the magnetic field which the nucleus experiences away from the external magnetic field (Zeeman interaction) causing the nucleus to resonate at a different frequency (and chemical shift) that is dependent on the local electron density. Whereas paramagnetic currents occur due to the mixing of ground and excited states that amplifies the effect of the external magnetic field causing deshielding. These paramagnetic currents are related to the average excitation energy as well as the distance between the nucleus and electrons. The dipolar interaction arises from the interaction between the nuclear magnetic moments of

two alike (homonuclear dipolar coupling) or different (heteronuclear dipolar coupling) nuclear spins and depends on both the strength of the magnetic moments and the inverse cube of the distance between both spins.

Although chemical shieldings and dipolar couplings provide a wealth of information regarding the local environment of the nucleus, the information can be challenging to extract due to the inherently low sensitivity, poor resolution, and broad resonances often dominating the experimental spectra which has led to the development of a range of methods to overcome these obstacles. The NMR sensitivity is largely dependent on the Boltzmann energy difference between the magnetic states of the nuclear spin which is determined by the strength of the external magnetic field and the value of the gyromagnetic ratio of the nucleus. High field NMR^{20–22} is therefore often used to overcome this challenge by increasing this energy gap and also often results in higher resolution by increasing chemical shift dispersion. Dynamic nuclear polarisation (DNP)^{23–25} and cross polarisation (CP)²⁶ emerged as powerful approaches to significantly increase sensitivity by polarisation transfer of the high magnetisation of electron spins to nucleus spins, and of higher polarised nucleus spins (*e.g.* ¹H) to lower polarised spins, respectively. Other hyperpolarisation methods (a branch of which DNP belongs to) that amplified the nuclear polarisation beyond that obtained by the Boltzmann distribution have also been discovered, mostly in liquid state NMR spectroscopy. Additionally, magic angle spinning (MAS)²⁷ that approximates molecular tumbling experienced in the liquid state, is routinely used in the solid state to suppress first order anisotropic interactions such as chemical shieldings and dipolar couplings increasing both sensitivity and resolution.²⁸ Many of these methods are exploited in the examples given below and their more comprehensive description being beyond the scope of this chapter, the reader is directed to explore other sources.^{11,18,29}

2.5.1. Complexation induced shift

Complexation induced shifts (CIS),³⁰ also known as chemical shift perturbation, delivers a significant advantage for structural and conformational determination in supramolecular complexes, and provides indispensable information regarding binding in supramolecular assemblies. Chemical shifts are indicative of the local

environment surrounding a nucleus as described in Section 2.5 above and complexation induced shifts probe the change in chemical shielding of the nuclei in a molecule due to electron density arising from nearby nuclei or molecules in an assembly. CISs were originally discovered in liquid state NMR due to solvent effects³⁰ and have now been used extensively in solid state NMR to observe host-guest assemblies.³¹ CH- π interactions of toluene and pyridine in *p*-tert-butylcalix[4]arene³² have been observed using CISs combining NMR crystallography and *ab initio* calculations to determine the positioning of the toluene or pyridine location inside the host structures.

Most notably, hydrogen bonding, which is one of the strongest driving forces for host-guest interactions in supramolecular assemblies, results in a very large change of ¹H chemical shifts up to approximately 20 ppm.³³ Hydrogen bonding can also be monitored *via* a heteronuclear spin (*e.g.* ¹³C) that results in reduced electron density around the bridging proton, greater amount of deshielding experienced by this nucleus and a higher chemical shift.

Hydrogen bonding interactions are often exploited in pharmaceutical sciences to obtain amorphous solid dispersions (ASD)³⁴ in which polyvinylpyrrolidone (PVP) is a common polymer used to stabilise amorphized active pharmaceutical ingredients (API) with increased oral bioavailability due to their amorphous nature increasing the exposed surface area.³⁵ ¹³C CP MAS NMR has recently been used to study the cogrinding process of the nifedipine (NIF) API with PVP and a surfactant (**Figure 2.2(a)**) and assess improved drug dissolution properties from physical cogrinding modification.³⁶ The ¹³C CP MAS NMR spectrum of the PVP NIF ASD obtained after a short period of 15 minutes of grinding (**Figure 2.2(b)**) shows two narrow well resolved signals for the two chemically inequivalent carbonyl carbons around 170 ppm³⁷ and supports a crystalline NIF phase. Upon further cogrinding to 100 minutes, these sharp carbonyl peaks significantly broaden (**Figure 2.2(b)**) and suggest complete NIF amorphization as confirmed by the absence of Bragg reflections in the XRD pattern. It was also observed that there is a small deshielded shift of the PVP carbonyl carbon during the grinding process (**Figure 2.2(b)**) which might indicate some hydrogen bonding in these systems.³⁸ This interaction between PVP and NIF potentially results

in stabilising the amorphization, making PVP an appealing polymer to increase oral bioavailability. To strengthen the argument for hydrogen bonding, a single NMR technique is rarely used and a multinuclear approach combining homonuclear/heteronuclear correlation techniques or NMR crystallography is often used to provide further insights.³⁹

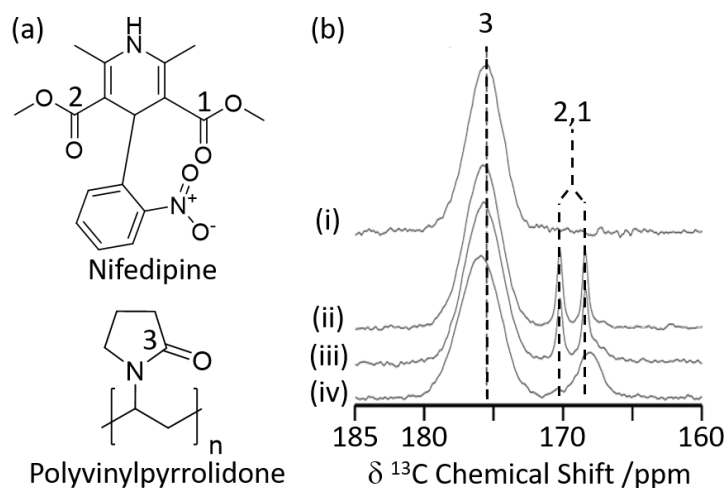


Figure 2.2. (a) Chemical structure of Nifedipine (NIF) and Polyvinylpyrrolidone (PVP). (b) ¹³C CP MAS NMR spectra of (i) PVP, a mechanically ground mixture of NIF/PVP/sodium dodecyl sulfate system ground for (ii) 15 min, (iii) 40 min, and (iv) 100 min obtained under MAS at $\nu_r = 15$ kHz. The spectral assignments are shown in the figure. Reprinted (adapted) with permission from ref 36. Copyright 2016 American Chemical Society.

2.5.2. Lineshape analysis

Deuterium ²H ($I = 1$) is a quadrupolar nucleus whose lineshape dominated by broadening arising from the quadrupolar interaction. ²H NMR is a very common tool exploited for the study of molecular dynamics as its lineshape is highly sensitive to a range of different motions and their rates on the kHz-MHz timescale.⁴⁰ The low natural abundance of this isotope (0.0115%) is both a drawback with the need for isotopic enrichment requiring additional synthetic steps and an advantage as selective labelling allows site specific information to be obtained. In the absence of motion, static ²H spin echo NMR experiments under non spinning conditions produce a Pake pattern which have outer horns that are symmetrically distributed towards the edges of the pattern (**Figure 2.3**). However, the presence of motion in the 10^3 Hz – 10^8 Hz frequency range causes changes in this lineshape to occur due to T_2

anisotropy preventing certain crystallite orientations to refocus during the spin echo sequence.^{40,41} The temperature-dependence evolution of the lineshape (**Figure 2.3**) is a function of the type of motion, geometry and reorientation rates (accessible from numerical simulations using for example the EXPRESS,⁴² MXET1⁴³ or weblab⁴⁴ packages), thereby producing a change in lineshape characterising the overall dynamics of the motion.

²H NMR has been used to explore the motion in molecular rotors in a range of systems^{45–47} and it has recently been identified that tubular covalent cages (TCC)⁴⁸ are the fastest exclusively organic molecular rotors found to date. The two TCCs that possess a central phenylene ring between either the trisubstituted aromatic (TCC2) or acetylene moieties (TCC3, **Figure 2.3(a)**)⁴⁹ have the potential to rotate in the solid state. Variable temperature ²H static NMR lineshape analysis of TCCs (that have been deuterated on the phenylene ring) show a typical Pake pattern in the slow motion regime at 105 K and a temperature dependent lineshape that is typical of a fast rotational 180° flip upon heating. Through numerical simulations, the ²H NMR lineshapes of TCC3-*R* were found to consistently have faster reorientation rates than its smaller counterpart TCC2-*R* and this is ascribed to facile rotation around the acetylene bonds due to a reduction in steric hindrance, showing structural dependency of phenylene motion.

Upon iodine loading (**Figure 2.3(b)**), the change of ²H NMR lineshape indicates significantly slower reorientation rates and demonstrates that the iodine host has hindered phenylene rotation in these TCCs molecular rotors. Upon iodine release from TCCs at 353 K, faster rotational rates are obtained, indicating that these TCCs are responsive materials not only to temperature changes, but also host-guest interactions.

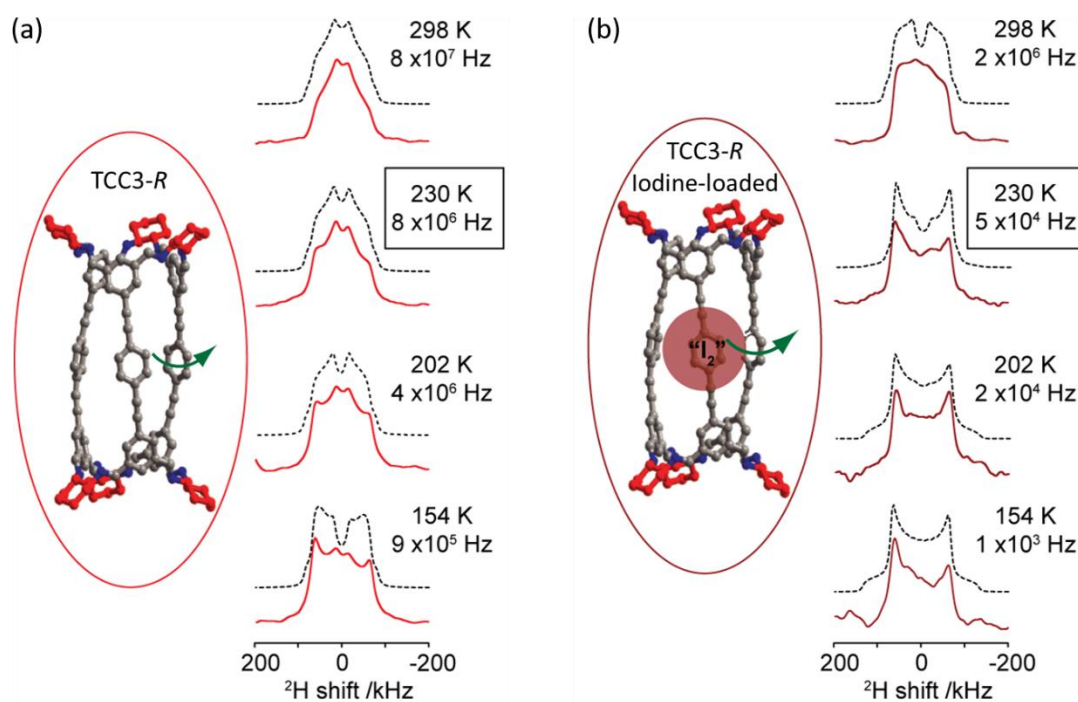


Figure 2.3. (a) TCC3-R structure (red) and variable temperature ^2H static solid echo NMR spectra of $[\text{D}_{12}]\text{TCC3-R}$. (b) iodine-loaded TCC3-R structure (burgundy) and variable temperature ^2H static solid echo NMR spectra of iodine loaded $[\text{D}_{12}]\text{TCC3-R}$. Corresponding simulated spectra (black dashed lines) and rotational rates obtained from numerical simulations of the NMR lineshape obtained at various temperatures are also given. Spectral artefacts are denoted with (#). In the crystal structures, the cyclohexane groups are represented in red; other C, grey; N, blue; H/D omitted for clarity. Ref 48 is an open access article distributed under the terms of the Creative Commons CC BY license.

^2H NMR lineshape analysis has also recently been used to study the unique dynamics of aromatic hydrocarbon tubular host, [4]CC, with corannulene (COR) guest (**Figure 2.4(a)**).⁵⁰ Theoretical DFT calculations gave insights into the presence of CH- π bonds interaction in this supramolecular assembly and revealed a bowl-in-tube host-guest structure where, despite the presence of multiple CH- π bonds binding the assembly together, guest rotation of the bowl-shaped COR guest is permissible which was further supported by experimental work deploying solid state NMR. Utilising a deuterated guest ($[\text{D}_{10}]\text{COR}$), ^2H NMR studies examined the dynamics of the bowl shaped guest in the assembly (**Figure 2.4(b)**) and show that a single resonance is observed in the ^2H Pake pattern, indicating that the COR guest molecules are all equivalent. The quadrupolar splitting measured from the horns of the Pake pattern was found to be smaller than expected value for motionless molecules, indicating some rotational motion with monotypic dynamics is occurring in the guest.

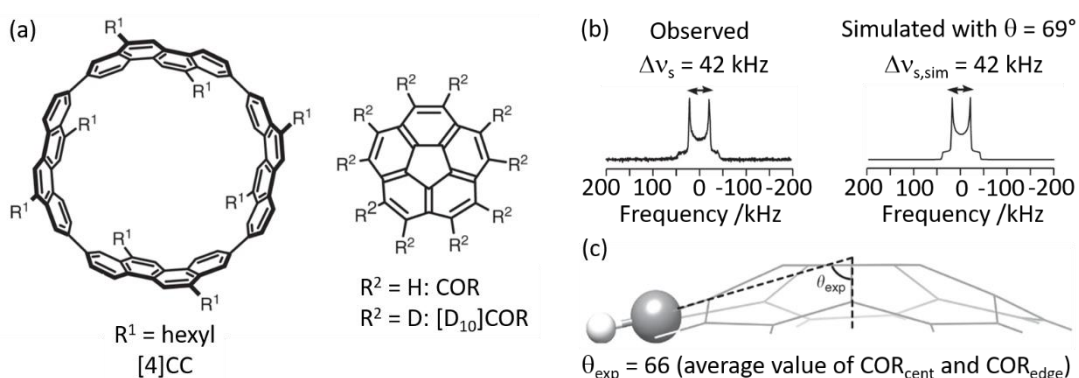


Figure 2.4. (a) Chemical structures of tubular host ([4]CC) and bowl-shaped guest (COR). (b) Observed and simulated ²H static solid echo NMR spectra of [D₁₀]COR in [4]CC obtained at 298 K. (c) Schematic of the molecular structure of COR showing a representative experimental cone angle (θ_{exp}) measured from the crystal structure. Ref 50 is an open article distributed under the terms of the Creative Commons CC BY license.

The quadrupolar splitting is dependent on the axis of rotation of the guest molecule and calculations show that the experimental splitting of 42 kHz can be obtained at either an angle of θ of 42° or 69°. X-ray crystallography and simulated ²H spectrum matching the experimental one confirmed a value of 66° (**Figure 2.4(c)**). This indicates that the guest has axial anisotropy in the host-guest complex with potential for these types of systems to be exploited for their chiro-optical properties.

¹³C is obviously a popular $I = \frac{1}{2}$ nucleus for which lineshape analysis has been extensively used to probe host and guest in supramolecular assemblies. A significant challenge is also the poor natural abundance of ¹³C (1.1%), hence isotopic enrichment or transfer of polarisation techniques such as CP are often used to improve sensitivity.

Guest capture of CO₂ is of particular interest in supramolecular chemistry^{45,51,52} and has recently been extensively investigated from the analysis of the ¹³C chemical shift anisotropy (CSA) lineshape.^{52,53} ¹³C labelled CO₂ is often used to focus on the loaded CO₂ whilst signals arising from the metal organic framework (MOF), linkers at natural abundance are highly decreased in intensity. One example compares two different metal centered (Al and Ga) MIL-53 MOFs, that contain corner sharing MO₄(OH)₂ octahedra interconnected by benzenedicarboxylate linkers, and the related amine

functionalised derivatives,⁵⁴ providing an understanding of the CO₂ dynamics within this family of MOFs. The experimental static ¹³C CSA NMR spectra could be modelled with two types of possible motion, a six- and a two-fold rotation. This analysis showed that MIL-53(Al) gave a smaller hopping angle of CO₂ rotation in comparison to MIL-53(Ga), which had more mobility, and indicates that the metal centre affects the CO₂ binding strength with Ga causing a weaker CO₂ adsorption. Adsorption of CO₂ in the NH₂ functionalised benzenedicarboxylate (Al and Ga) MIL-53 was also studied and revealed similar ¹³C CSA lineshape for both cations, although with a general greater affinity for the CO₂ in comparison to the non-functionalised MIL-53. In other work, ¹³C CSA lineshape analysis on Mg₂(dobdc) MOF-74 (dobdc⁴⁻ = 2,5-dihydroxy-1,4-benzenedicarboxylic acid)^{52,53} adsorbed with a range of CO₂ pressures showed that the CO₂ molecules have an orientation dependency on the pressure and hence the number of CO₂ molecules adsorbed.

A combination of ¹³C CSA and pulsed field gradient (PFG) experiments has recently been used to quantitatively determine the diffusion coefficients of CO₂ in Zn₂(dobpdc) (dobpdc⁴⁻ = 4,4'-dioxidobiphenyl-3,3'-dicarboxylate)⁵² which is also a MOF-74 possessing one-dimensional hexagonal channels containing unsaturated metal centres. Static ¹³C NMR spectra of ¹³CO₂ loaded Zn₂(dobdc) are shown in **Figure 2.5(a)** and do not show the expected narrow resonance expected for CO₂ in the gas phase but rather exhibit a powder pattern that corresponds to different orientations of the confined CO₂ molecules relative to B₀. This pattern is a consequence of the reduced ¹³C CSA of CO₂ confined in the pores due to preferred orientations of the crystal frame relative to B₀ (**Figure 2.5(b)**). Based on a number of considerations, including MAS NMR spectra, the sign of the ¹³C CSA, difference CO₂ dose, diffusion coefficients D values and molecular dynamics (MD) simulations, the deshielded and shielded edges of the powder pattern were assigned to crystals perpendicular (D_⊥) and parallel (D_∥) to B₀, respectively.

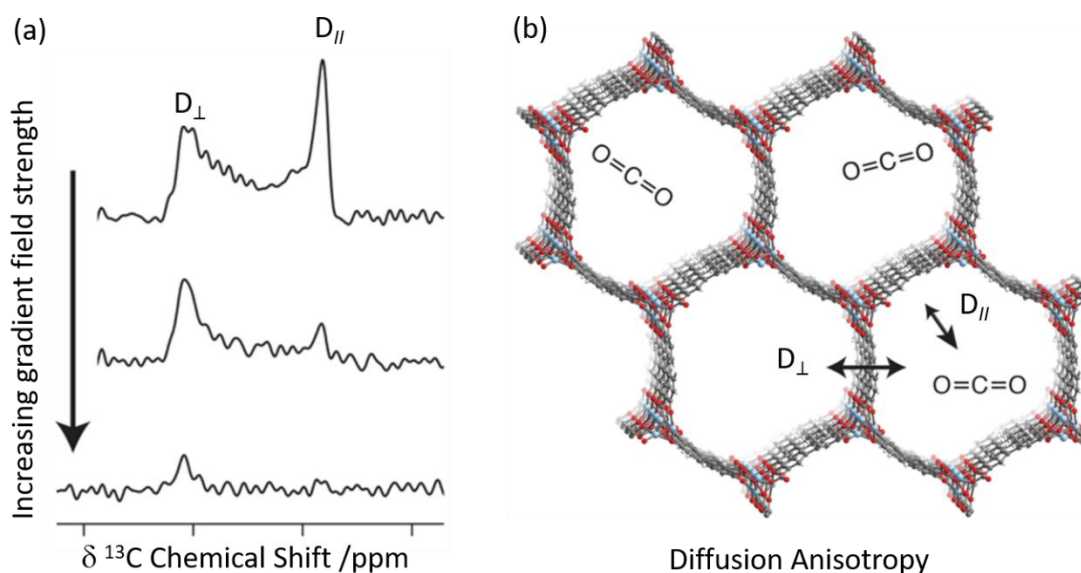


Figure 2.5. (a) ^{13}C PFG static NMR spectra for $\text{Zn}_2(\text{dobpdc})$ crystals at a pressure of 625 mbar $^{13}\text{CO}_2$ with different applied gradient strengths and at 298 K. D_{\parallel} is the signal arising from crystals parallel to the external magnetic field at a lower chemical shift, whilst those at higher chemical shift are aligned perpendicular to the field D_{\perp} . (b) Cross-section of the crystal structure of the $\text{Zn}_2(\text{dobpdc})$ framework at 298 K showing the two diffusion pathways. Light blue, red, grey, and white spheres represent Zn, O, C, and H atoms, respectively. Reprinted (adapted) with permission from ref 52. Copyright 2018 American Chemical Society.

Static ^{13}C NMR spectra of $^{13}\text{CO}_2$ loaded $\text{Zn}_2(\text{dobpdc})$ recorded as a function of increasing gradient field strengths (**Figure 2.5(a)**) have revealed faster decay of the deshielded signal than the shielded signal and enabled CO_2 self-diffusion coefficients in both the parallel (D_{\parallel}) and perpendicular (D_{\perp}) directions to the hexagonal channels to be obtained. CO_2 was observed to diffuse through the channels parallel to the crystallographic c axis (D_{\parallel}) as expected but also and, more surprisingly, between the hexagonal channels in the crystallographic ab plane (D_{\perp} , **Figure 2.5(b)**) which was attributed to defects in the MOF structure. It is worth pointing out that neither *in situ* XRD nor MD revealed this anisotropic diffusion thereby highlighting the complementarity of these methods.

2.5.3. NMR relaxometry

NMR relaxometry encompasses a wide range of experiments that access the rates of relaxation (either longitudinal relaxation times in the laboratory frame T_1 or rotating frame $T_{1\rho}$, or transverse relaxation time T_2) which measure polarisation returning to their equilibrium values in a magnetic field. Temperature dependent relaxometry measurements in particular are insightful for the study of molecular dynamics, allowing access to the correlation times of the motion and their activation energies, providing some important information about host-guest interactions.^{20,34}

The adsorption of ^{13}C labelled CO_2 in MOF-74 $\text{Zn}_2(\text{dotp})$ (where $\text{dotp}^{4-} = 2,5$ -dioxidoterephthaate, **Figure 2.6(a)**) has recently been studied using a combination of solid state NMR techniques, including ^{13}C CSA lineshape analysis, 2D exchange spectroscopy, ^{13}C MAS and NMR relaxometry.⁵⁵ The T_1 times of the CO_2 guest were found to increase with increasing numbers of CO_2 molecules (**Figure 2.6(b)**), indicating that at higher pressures the CO_2 mobility is hindered due to the CO_2 - CO_2 interactions. The correlation times obtained from T_1 data over the 305-363 K temperature range and assuming a CSA relaxation mechanism were calculated and yielded activation energies of 4.4 and 3.5 kJ mol^{-1} for two samples with different CO_2 pressure of 100 and 1000 mbar, respectively (**Figure 2.6(c)**). This slight difference supports the hypothesis that the CO_2 - CO_2 and CO_2 -pore surface interactions increase with pressure. The correlation time found was also significantly longer than that of gaseous CO_2 , also providing further evidence for the host-guest interactions occurring at the pore surface.

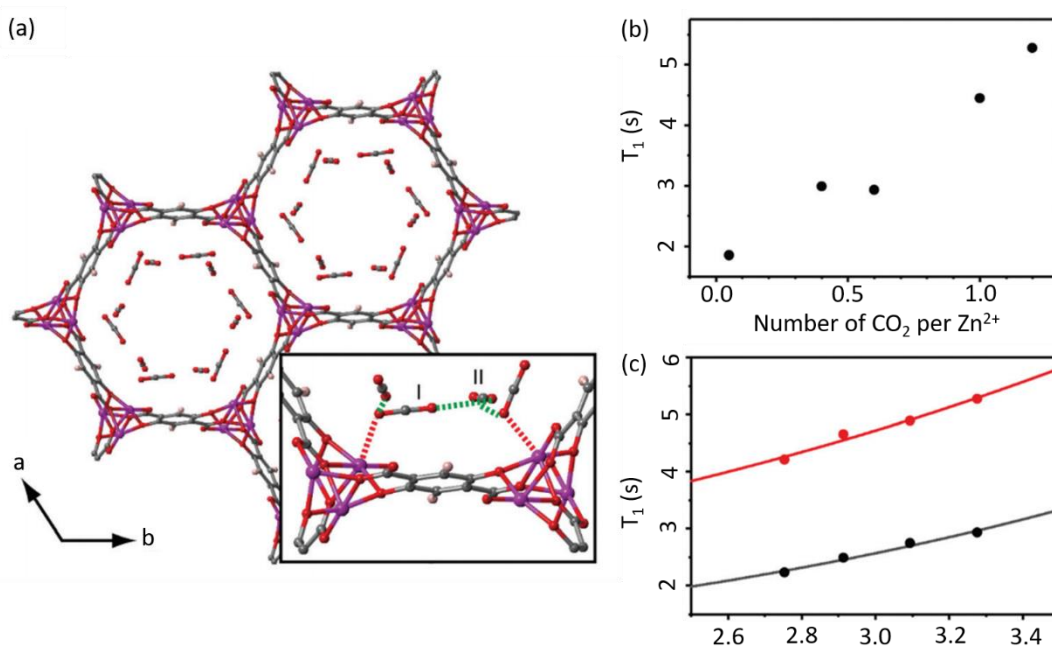


Figure 2.6. (a) MOF-74 chemical structure with adsorption sites shown. (b) Pressure and (c) temperature dependence of T_1 values for the adsorbed CO_2 in $\text{Zn}_2(\text{dotp})$ MOF-74 under MAS at $\nu_r = 6$ kHz, 305 K and at 100 mbar (black) and 1000 mbar (red), respectively. Experimental and calculated T_1 values (based on a ^{13}C CSA relaxation mechanism) are shown as data points and solid lines, respectively. Reproduced from ref. 50 with permission from the PCCP Owner Societies.

Analysis of the T_1 data in $\text{Zn}_2(\text{dotp})$ MOF-74 also revealed the occurrence of unusually slow localized wobbling and hopping motions (at a rate of 10^{-8} s) that are much smaller than for the Mg-MOF-74 (10^{-10} s) analogue and further studies are highly anticipated to provide more information on the mobility, adsorption and separation properties of these MOFs.

2.5.4. Spin Diffusion

Spin diffusion NMR experiments observe the transfer of nuclear magnetization *via* through space dipole-dipole interactions and is used to probe host-guest interactions among a range of systems.³⁹ As spin diffusion coefficients, D , are proportional to the cube root of the nuclei concentration and the square of the nuclei gyromagnetic ratio, nuclei with sufficiently high values (*e.g.* ^1H , ^7Li , etc.) are often used in these experiments and provide qualitative and quantitative information on spatial proximities.

Along with T_1 relaxometry data on $Zn_2(\text{dotp})$ MOF-74, ^{13}C two-dimensional (2D) exchange MAS NMR data was also used to investigate the diffusion of CO_2 enriched in ^{13}C thereby increasing ^{13}C spins concentration.⁵⁵ With the possibility of multiple adsorption sites, the determination of the type of sites is crucial for the understanding of the mechanism of adsorption. Surprisingly and in contrast to previous work assessing the ^{13}C CSA patterns of Mg-MOF-74,⁵⁶ two CO_2 resonances were observed in Zn-MOF-74⁵⁵ and initially assigned to a primary adsorption site and a secondary adsorption site only accessible under greater pressure. However, the corresponding 2D exchange ^{13}C MAS NMR spectra revealed that these two signals do not exchange (over 10-1000 ms mixing times) and it was therefore concluded that the second resonance is due to mobile CO_2 located in the dead space of the NMR tube rather than a secondary adsorption site.

^1H ^1H spin diffusion experiments were performed on $(\text{Zr}_6\text{O}_4(\text{OH})_4(\text{bpdc})_6)$ MOF UiO-67 (where bpdc^{2-} = biphenyl-4,4'-dicarboxylate) loaded with a range of light alkanes (methane, ethane and propane) to explore their interactions into the MOF pores (**Figure 2.7(a)**).⁵⁷ First principle calculations and neutron diffraction studies had previously been used to probe host-guest interaction in methane-loaded $\text{M}_2(\text{dhtp})$ MOFs ($\text{M} = \text{Mg}, \text{Mn}, \text{Co}, \text{Ni}, \text{Zn}$; dhtp^{2-} = 2,5-dihydroxyterephthalate),⁵⁸ however, due to the motional dynamics and disorder in these systems, significant direct experimental evidence for the interaction at room temperature has been difficult to achieve. The ^1H ^1H spin diffusion spectra of the methane loaded UiO-67 are shown in **Figure 2.7(b)** at various mixing times and reveal cross peaks correlating methane (-0.4 ppm) with aromatic protons belonging to the UiO-67 bpdc organic linker, supporting van der Waals interactions. Experiments conducted with heavier alkanes (ethane and propane) showed similar results, albeit requiring longer spin diffusion times for cross peaks to appear and suggests there is a slight preference for the smaller alkanes, and overall showing evidence that UiO-67 could be utilised for the storage of these light alkanes.

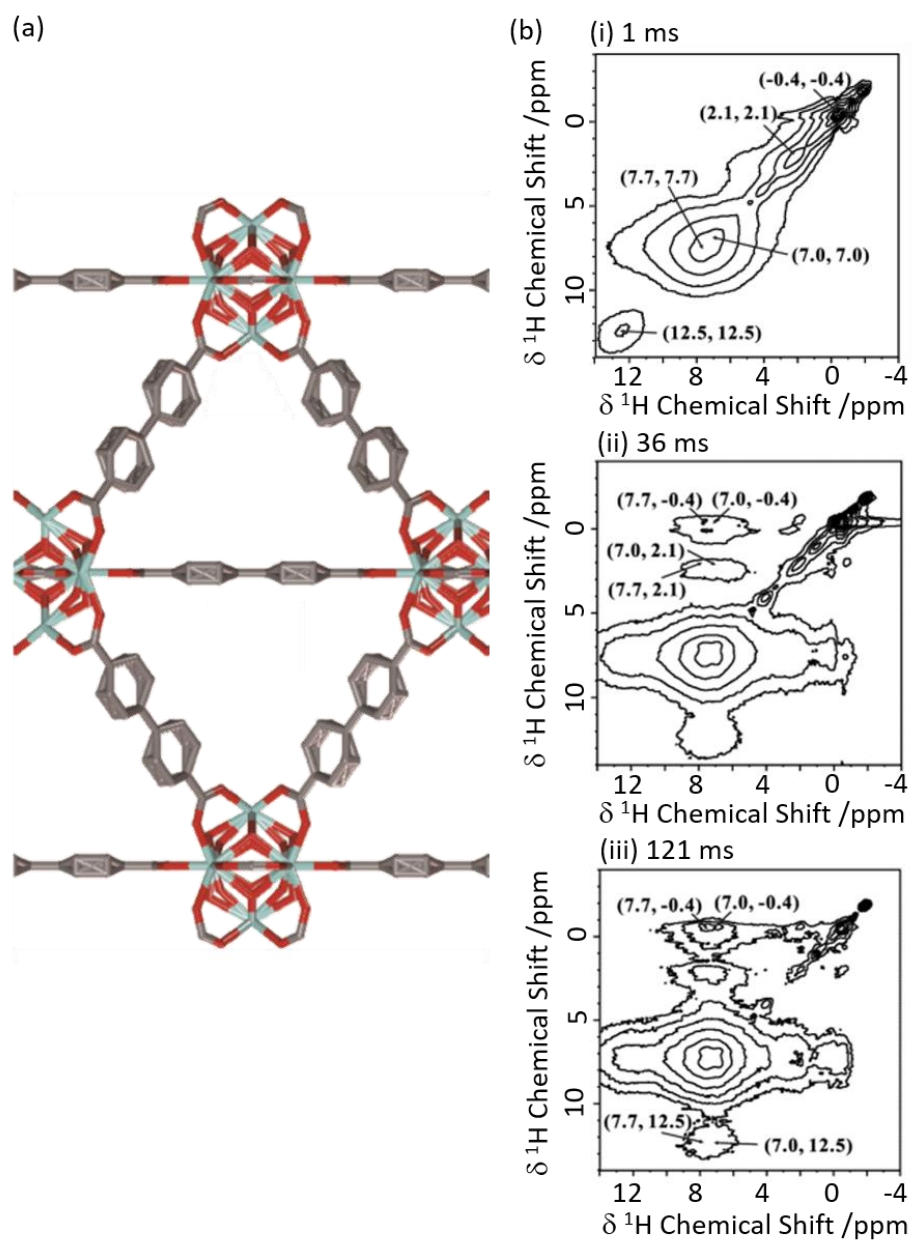


Figure 2.7. (a) Schematic structure of UiO-67. (b) 2D ^1H - ^1H spin-diffusion spectra of methane loaded UiO-67 at mixing times of (i) 1 ms, (ii) 36 ms and (iii) 121 ms obtained at a MAS rate $\nu_r = 10$ kHz. Reprinted (adapted) with permission from ref 57. Copyright 2017 American Chemical Society.

2.5.5. Xenon NMR

Xenon ^{129}Xe ($I = \frac{1}{2}$) enables detailed information about the size and shape of the cavity in porous solids⁵⁹ and is often used to probe supramolecular assemblies. This is largely due to the inert nature and large electron density of Xe which makes this nucleus particularly sensitive to the atomic scale.^{59,60} Although the high gyromagnetic ratio ($-7.441 \times 10^7 \text{ rad T}^{-1} \text{ s}^{-1}$) and natural abundance (26.4%) seem favourable for NMR detection, the reduced xenon-xenon interactions needed to promote observation of adsorption sites requires low concentration challenging detection. Hyperpolarised ^{129}Xe NMR is therefore used to perform experiments at lower xenon concentration with significant sensitivity. Importantly, changes in the chemical shifts from free gaseous xenon (at 0 ppm) indicate host-guest interactions and result from a combination of the xenon-surface interaction and the pore volume.⁵⁹

^{129}Xe has been extensively used to investigate the pore structure in solids that is largely key to the physical properties. An example of such material includes zeolites, which possess structural flexibility that is enabled by structure-directing agents leads to new catalytic applications.^{61,62} Recently, interlayer expansion of zeolites has been proposed to expand the current range of available zeolite topological structures and ^{129}Xe NMR has been shown to determine the order of the interlayer structure in a new ten-membered ring (MR) functionalised skeleton zeolite (named COE-4) prepared by expansion of the 8-MR layered silicate RUB-36 zeolite precursor.⁶³ The ^{129}Xe spectrum of the calcined RUB-36 (RUB-37) phase shows a weak signal at 89 ppm at 213 K (**Figure 2.8(a)**) and has been ascribed to accumulated Xe in the mesopores and not in the 8-MR channels (of size of $3.1 \times 4.7 \text{ \AA}$ and $2.5 \times 4.2 \text{ \AA}$ along the [010] and [001] directions, respectively) which are too small for Xe (dynamic diameter of 4.4 \AA). In COE-4, the ^{129}Xe signal appears at a larger shift of 111 ppm (**Figure 2.8(b)**) indicating the xenon is more “trapped” and these are classed as micropores. Additionally, the ^{129}Xe lineshape of the single resonance observed in COE-4 (**Figure 2.8(b)**) indicates high symmetry and a homogenous distribution of the interlayer expansion. It should also be noted that the ^{129}Xe NMR spectra of both COE-4 and ZSM-5 zeolites are very similar, indicating that the pore sizes are comparable.

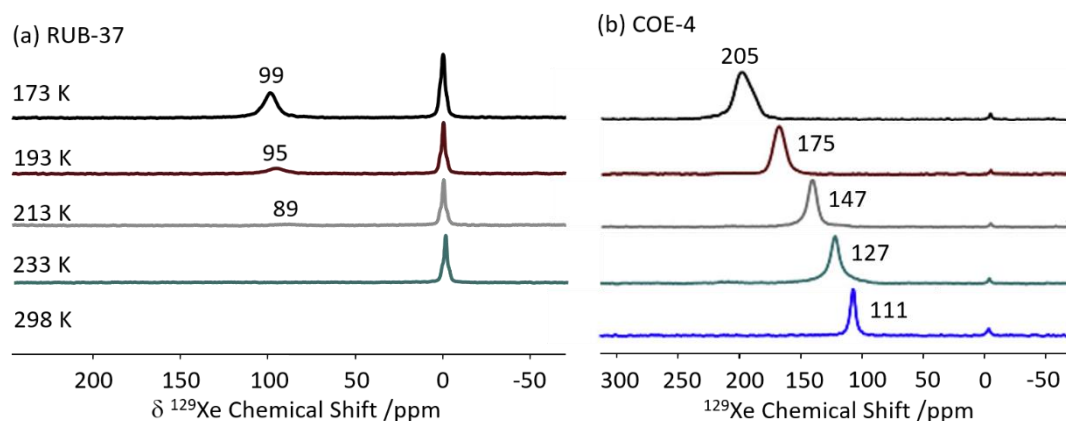


Figure 2.8. Variable temperature hyperpolarised static ^{129}Xe NMR spectra of (a) RUB-37 and (b) COE-4. Reprinted from ref 63: Structural investigation of interlayer-expanded zeolite by hyperpolarized ^{129}Xe and ^1H NMR spectroscopy, 109555, Copyright 2019, with permission from Elsevier.

Porous organic cages (POCs) are a relatively new family of supramolecular assemblies, with the above mentioned TCC3 being one of their newest members. CC3 is another POC consisting of tetrahedral cages formed by imine bonds connecting rigid aromatic rings to the more flexible cyclohexane linkers and arranges into an interconnected 3D pore structure when packed together (**Figure 2.9(a)**). Since their discovery in 2009, POCs have been shown to possess wide applications and unprecedented performance in rare gas separation.⁶⁰ The cage structure of CC3 was initially studied by ^{129}Xe NMR and it was observed that the xenon can diffuse in three dimension throughout the crystalline pore structure, moving between the window cavities *via* the cage cavities and indicating interconnectivity of the pore structure.⁶⁴ A follow up study⁶⁰ delved into the CC3 cage and its dynamics revealing only one resonance for both the cage and window sites due to fast thermal motion causing the exchange of nuclei between these sites to occur faster than the NMR timescale (**Figure 2.9(b)**). Upon Xe loading, it was observed that the ^{129}Xe chemical shift increases to 210 ppm as the more shielded window sites of the cage (as opposed to the Xe nuclei located in the less shielded cage cavities which appear at 20 ppm) become more occupied. At a lower temperature of 260 K, the chemical shift is slightly reduced due to the increase in relative occupancy of the window cavities. ^{129}Xe spin lattice relaxation rates were also explored due to their dependence on dynamics. Upon increasing Xe loading the correlation times extracted were observed to be

considerably slower in the highly loaded sample in comparison to the medium and low loadings. This indicates that the diffusion of xenon becomes restricted at high loading, giving slower T_1 rates due to all the cage and window cavities being occupied.

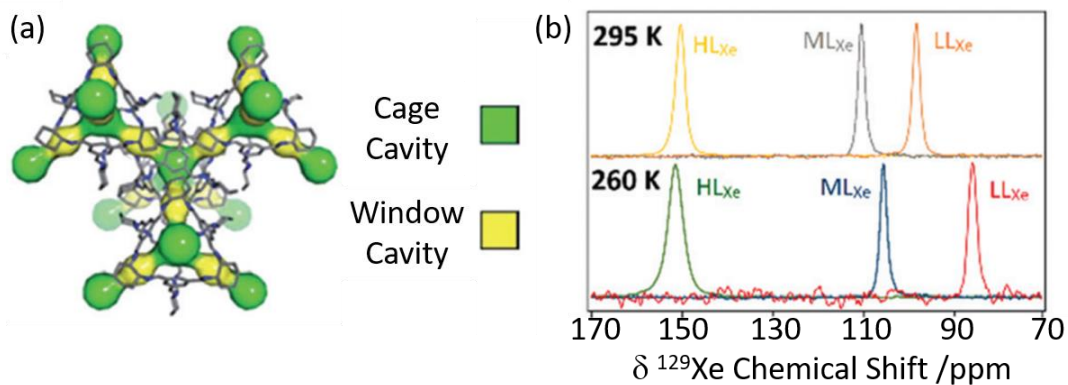


Figure 2.9. (a) Crystal structure of CC3 showing both cage cavities (yellow) and window cavities (green). (b) ^{129}Xe NMR spectra of CC3 with varying xenon loadings (HL_{Xe} – high loading, ML_{Xe} – middle loading and LL_{Xe} – low loadings) at 295 and 260 K. Ref 55 – Published by the PCCP Owner Societies.

2.5.6. Cross polarisation

CP is one of the most commonly used experiments in solid state NMR to transfer polarisation from abundant nuclei (typically ^1H) to sparse nuclei (*e.g.* ^{13}C , ^{15}N) in order to gain sensitivity. The polarisation transfer is largely dependent on the through space heteronuclear dipolar interactions, and hence can also be exploited to probe dynamics and measure distances including the observation of internuclear interactions and informing host-guest binding. MIL-53 has also been studied with CP and, recently, ^1H ^{129}Xe CP has been utilised for the first time in this class of supramolecular assemblies⁶⁵ to probe the mobility of xenon (**Figure 2.10**).

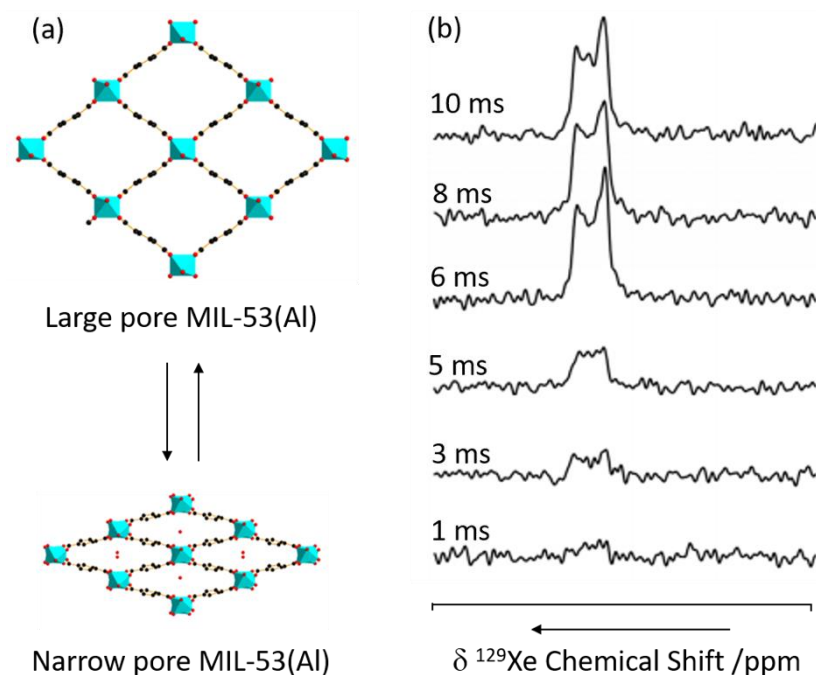


Figure 2.10. (a) 3D structure of MIL-53(Al) in exchange between the large and narrow pore form. (b) ^1H ^{129}Xe CP spectra as a function of contact time under a MAS rate $\nu_r = 8$ kHz at a temperature of 153 K and a pressure of 500 mbar. Reprinted (adapted) with permission from ref 65. Copyright 2016 American Chemical Society.

No ^{129}Xe signal is present in large-pore MIL-53 due to the high mobility completely averaging the ^1H ^{129}Xe heteronuclear dipolar interactions, and hence significantly reducing CP efficiency. The signal intensity obtained for the ^{129}Xe located in the narrow-pore MIL-53 was found to increase with CP contact time until a maximum at 10 ms which is significantly longer than in the absence of motion (2 ms), hence concluding that the xenon atoms still possess significant motions in these pores.

The zeolitic H-ZSM-5 catalysed methanol-to-hydrocarbon (MTH) process remains a highly studied industrial reaction due to its mechanistic aspects and complexity.⁶⁶ Solid state NMR has already identified a range of catalytic intermediates aiding the mechanistic understandings.⁶⁷ Recently, it has also been reported that Lewis acidity is not a spectator in this MTH reaction and that the incorporation of alkaline-earth metals into the zeolite results in a generation of Lewis acid sites changing the reactivity of the zeolite catalyst throughout the MTH process.⁶⁸ Using 1D ^1H ^{13}C CP MAS experiments performed at increasing contact times, the post reacted H-ZSM-5 and Ca-ZSM-5 zeolites have been analysed to study diffusion characteristics (**Figure 2.11**).⁶⁹ The peak at 100 ppm is assigned as an acetal (OCH_2O) and its intensity

increases with increasing contact time, indicating a more efficient CP transfer at longer contact times, suggesting that acetals are preferentially located within the zeolite framework. Direct spectral comparison of both zeolites shows large signal intensity in the 120-135 ppm region for H-ZSM-5 indicating a higher concentration of unsaturated hydrocarbon pool species (like aromatics/polyaromatics) on its surface in comparison to Ca-ZSM-5 (**Figure 2.11(a)**). Upon increasing the CP contact times to 3 ms, the aromatic peak around 133 ppm in the H-ZSM-5 spectra (**Figure 2.11(b)(i)**) disappears, implying the presence of polyaromatic products exclusively residing on the surface of the zeolite. However, this weak peak at 133 ppm is absent in the post-reacted Ca-ZSM-5 zeolite (**Figure 2.11(b)(ii)**) at short contact times, which indicates the absence of any aromatic species in the calcium modified zeolite, especially on its surface.

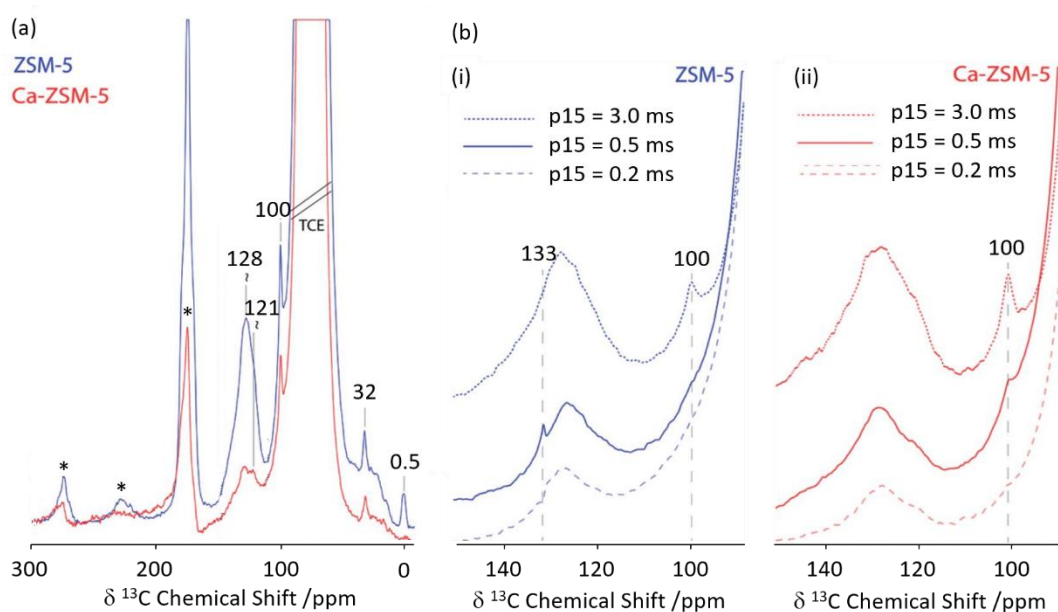


Figure 2.11. (a) $1\text{D } ^1\text{H } ^{13}\text{C}$ CP MAS DNP spectra of post-MTH reacted H-ZSM-5 (blue) and Ca-ZSM-5 (red) at a contact time of 2 ms. (b) $1\text{D } ^1\text{H } ^{13}\text{C}$ CP MAS DNP spectra at various CP contact times (p15) of (i) H-ZSM-5 (blue) and (ii) Ca-ZSM-5 (red). Samples have been formulated in a 16 mM TEKPol solution⁶⁵ in 1,1,2,2-tetrachloroethane. Data were obtained with a recycle delay of 3 s and a MAS rate $\nu_r = 8$ kHz. Ref 69 – Published by the Royal Society of Chemistry.

2.5.7. Rotational Echo Double Resonance

Driven by the need for high resolution, MAS is used extensively to average out heteronuclear dipolar interactions to zero, however, these interactions provide access to spatial proximities and hence probe host-guest interactions. Their reintroduction, whilst under MAS to still achieve the desired spectral resolution, is often achieved using recoupling pulse sequences so that the dipolar coupling is not averaged out to zero under MAS of which the Rotational Echo Double Resonance (REDOR)⁷¹ is the archetype. Spin echo experiments with (S_0) and without (S') refocusing pulses are acquired as a function of evolution time and enable access to (recoupled) heteronuclear dipolar couplings and interatomic distances. In particular, REDOR type experiments are prevalent in the study of zeolites due to their catalytic performance often being linked to host-guest interactions.

Figure 2.12 shows such ^{29}Si - ^{13}C REDOR experiments to probe the confined hydrocarbon species in the H-ZSM-5 zeolite framework.⁷² Fitted REDOR fraction (**Figure 2.12(b)**) returns a ^{29}Si - ^{13}C heteronuclear coupling of 80 Hz and an internuclear distance of 4.2 Å which highlights the strong hydrocarbon – zeolite interaction and provide insights into zeolite poisoning by blockage of the channels rather than the acid sites.

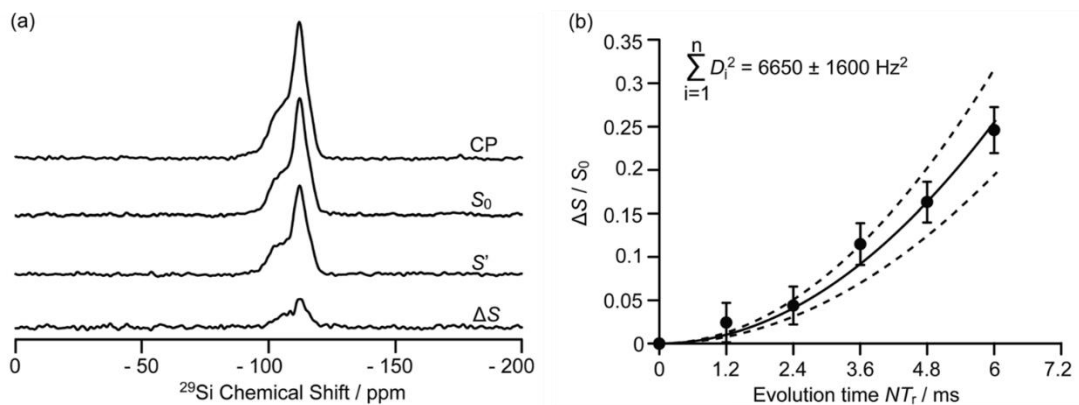


Figure 2.12. (a) ^{29}Si CP, ^{29}Si CP spin echo (S_0), and ^{29}Si $\{^{13}\text{C}\}$ REDOR signal reintroducing dipolar couplings (S') and the difference ΔS signal ($S_0 - S'$) at a MAS rate of $\nu_r = 5$ kHz for H-ZSM-5 zeolite. (b) Plot of the REDOR fraction $S_0 - S' / S_0$ as a function of evolution time N/ν_r and corresponding best-fit curve (black line) and fit boundaries (dashed lines). Ref 72 – Published by the Royal Society of Chemistry.

An adaptation of the REDOR experiment to measure dipolar interactions between spin $\frac{1}{2}$ and quadrupolar nuclei was introduced in 2010 as Symmetry-based Resonance-Echo Saturation-Pulse Double-Resonance (S-RESPDOR)⁷³ and recently used to understand spatial proximities between ^{13}C in the MTH hydrocarbon pools and ^{27}Al in zeolites having different topologies (*e.g.* H-ZSM-5, HSSZ-13 and H-MOR).⁷⁴ Comparison of both S_0 and S' RESPDOR signals (**Figure 13**) indicate the spatial proximities of methylbenzenes (17.0 and 19.3 ppm), cyclopentenyl cations (25.2, 45.8 and 48.1 ppm), surface bound methanol (58.7 ppm) and DME (60.0 and 63.4 ppm) with a preference for the latter.

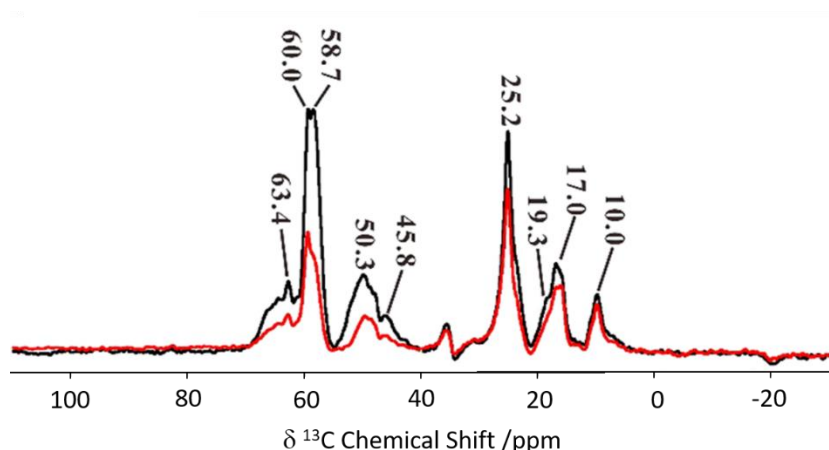


Figure 2.13. ^{13}C spectra observed with (S, black) and without (S_0 , red) $\{^{27}\text{Al}\}$ S-RESPDOR for the trapped products retained in H-ZSM-5 after reaction with methanol for 15 minutes at 573 K. NMR spectra obtained at a MAS rate of $\nu_r = 10$ kHz. Reprinted (adapted) with permission from ref 74. Copyright 2017 American Chemical Society.

Variable temperature experiments in the 300 - 400 K range showed minimal change in S_0 and S' spectra for the cyclopentenyl carbons suggesting the retention of close spatial proximity even at higher temperatures. This is in sharp contrast to the methylbenzene signals where ΔS becomes 0 at higher temperatures due to a reduction in the spatial interaction of methyl benzene enabling the guest to have more mobility within the framework. Comparison between three topologies indicates no significant difference for the cyclic carbocations, however, methylbenzenes present stronger interactions with H-SSZ-13 and H-MOR implying that these two zeolites may have a range of reactivity in the methanol to olefin reaction.

2.5.8. Separated local field NMR

Separated local field (SLF) NMR experiments correlate heteronuclear dipolar couplings with chemical shifts in two dimensional NMR spectra and provide orientation and distance dependent restraints to aid structure determination, accessing dynamics and probing host-guest interactions. These experiments were initially designed for the study of liquid crystals^{75,76} and now find widespread use including in supramolecular assemblies. A particular version of SLF is the Dipolar Chemical Shift correlation (DipShift) which uses a principle similar to REDOR that

recouple heteronuclear dipolar interactions with refocusing π pulses.¹³C - ¹H DipShift NMR was used to obtain the magnitude of the motionally averaged one-bond ¹³C ¹H dipolar couplings and values of -11.1 and -8.7 kHz were obtained for the aromatic carbons of styrene and ethyl benzene loaded on MIL-53(Al), respectively (**Figure 2.14**).⁷⁷ These values are much slower than the ones expected in the absence of motion (-23 kHz) and determined from CH distances which indicate significant dynamic processes. The lower value obtained for ethylbenzene indicates higher mobility in the MIL-53 pore than for styrene and suggests that this latter aromatic has a stronger host-guest interaction with this MOF. This work has provided direct insights into the structure-selectivity relationship in MIL-53 and has contributed to further understanding of the exceptional property of this MOF to separate both aromatics which is a challenging separation.

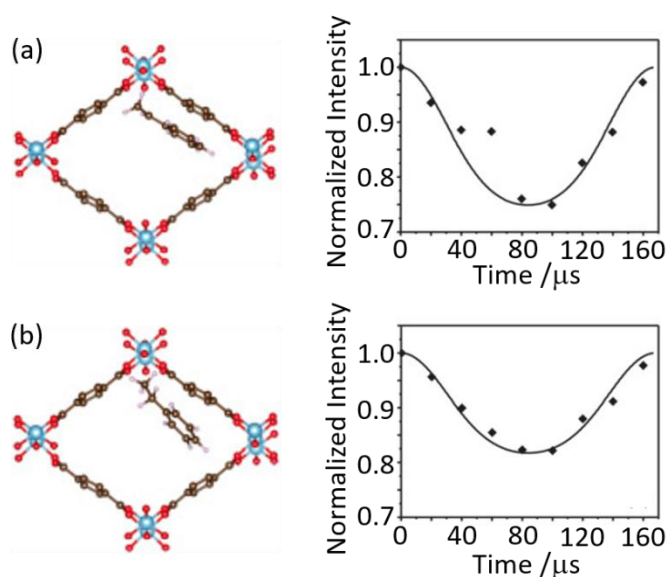


Figure 2.14. Schematic of MIL-53(Al) upon adsorption of (a) styrene and (b) ethylbenzene and their corresponding dipolar dephasing curves extracted from ¹³C-¹H DipShift MAS NMR dataset obtained at a MAS rate of $\nu_r = 6$ kHz. The CH sites at 128 and 127 ppm were chosen to capture the dynamic in styrene and ethylbenzene, respectively. Reprinted from ref 77: Host-guest interaction of styrene and ethylbenzene in MIL-53 studied by solid-state NMR, Copyright 2018, with permission from Elsevier.

2.6. Conclusion

Solid state NMR approaches that provide detailed insights into host-guest chemistry in supramolecular assemblies have been described. These studies enable understanding of the role of dynamics, binding sites and spatial interactions and often complement other approaches *e.g.* diffraction-based methods and computational investigations, to deliver comprehensive knowledge. The NMR technology plays an important role in the design and development of materials with new and improved adsorption phenomena for a wide range of applications including separation, catalysis and energy conversion and storage.

2.7. References

- 1 J. W. Steed and J. L. Atwood, *Supramolecular Chemistry*, John Wiley & Sons, Chichester, UK, 2nd edn., 2009.
- 2 C. J. Pedersen, *J. Am. Chem. Soc.*, 1967, **89**, 2495–2496.
- 3 J.-M. Lehn, *Angew. Chemie - Int. Ed.*, 1988, **27**, 89–112.
- 4 C. J. Pedersen, *Angew. Chemie - Int. Ed.*, 1988, **27**, 1021–1027.
- 5 D. J. Cram, *Angew. Chemie - Int. Ed.*, 1988, **27**, 1009–1112.
- 6 J. P. Sauvage, *Angew. Chemie - Int. Ed.*, 2017, **56**, 11080–11093.
- 7 J. F. Stoddart, *Angew. Chemie - Int. Ed.*, 2017, **56**, 11094–11125.
- 8 B. L. Feringa, *Angew. Chemie - Int. Ed.*, 2017, **56**, 11060–11078.
- 9 Y. Xu, S. A. Southern, P. M. J. Szell and D. L. Bryce, *CrystEngComm*, 2016, **18**, 5236–5252.
- 10 M. R. Chierotti and R. Gobetto, *Solid-State NMR Studies on Supramolecular Chemistry*, Wiley, Chichester, UK, 2012.
- 11 M. J. Duer, R. K. Harris and R. E. Wasylshen, *NMR Crystallography*, Wiley, Chichester, 2009.
- 12 M. J. Potrzebowski and S. Kazmierski, *Top. Curr. Chem.*, 2004, **246**, 91–140.
- 13 M. Novo, D. Granadero and J. B. W. Al-soufi, *J. Incl. Phenom. Macrocycl. Chem.*, 2011, **70**, 259–268.
- 14 F. P. Schmidtchen, in *Analytical Methods in Supramolecular Chemistry*, Wiley, Weinheim, 2nd edn., 2012, pp. 67–104.
- 15 K. Jie, M. Liu, Y. Zhou, M. A. Little, A. Pulido, S. Y. Chong, A. Stephenson, A. R. Hughes, F. Sakakibara, T. Ogoshi, F. Blanc, G. M. Day, F. Huang and A. I.

- Cooper, *J. Am. Chem. Soc.*, 2018, **140**, 6921–6930.
- 16 S. Halder, A. Barma, C. Rizzoli, P. Ghosh and P. Roy, *ACS Appl. Nano Mater.*, 2019, **2**, 5469–5474.
- 17 S. E. Ashbrook and D. M. Dawson, *Acc. Chem. Res.*, 2013, **46**, 1964–1974.
- 18 J. A. Ripmeester and R. E. Wasylshen, *CrystEngComm*, 2013, **15**, 8598.
- 19 B. Elena and L. Emsley, *J. Am. Chem. Soc.*, 2005, **127**, 9140–9146.
- 20 D. C. Apperley, R. K. Harris and P. Hodgkinson, *Solid-State NMR: Basic Principles and Practice*, Momentum Press, New York, 1st edn., 2012.
- 21 R. W. Martin, J. E. Kelly and J. I. Kelz, *J. Struct. Biol.*, 2019, **206**, 73–89.
- 22 P. Hodgkinson and S. Wimperis, *Phys. Chem. Chem. Phys.*, 2009, **11**, 6875–6875.
- 23 A. W. Overhauser, *Phys. Rev.*, 1953, **92**, 411–415.
- 24 T. R. Carver and C. P. Slichter, *Phys. Rev.*, 1956, **102**, 975–981.
- 25 A. S. L. Thankamony, J. J. Wittmann, M. Kaushik and B. Corzilius, *Prog. Nucl. Magn. Reson. Spectrosc.*, 2017, **102–103**, 120–195.
- 26 A. Pines, M. G. Gibby and J. S. Waugh, *J. Chem. Phys.*, 1973, **59**, 569.
- 27 E. R. Andrew, A. Bradbury and R. G. Eades, *Nature*, 1958, **182**, 1659.
- 28 A. Brinkmann and M. H. Levitt, *J. Chem. Phys.*, 2001, **115**, 357–384.
- 29 S. E. Ashbrook, R. G. Griffin and K. E. Johnston, *Annu. Rev. Anal. Chem.*, 2018, **11**, 485–508.
- 30 A. D. Buckingham, *Can. J. Chem.*, 1960, **38**, 300–307.
- 31 M. P. Williamson, *Prog. Nucl. Magn. Reson. Spectrosc.*, 2013, **73**, 1–16.

- 32 D. H. Brouwer, S. Alavi and J. A. Ripmeester, *Phys. Chem. Chem. Phys.*, 2008, **10**, 3857–3860.
- 33 N. Asakawa, S. Kuroki, H. Kurosu, I. Ando, A. Shoji and T. Ozaki, *J. Am. Chem. Soc.*, 1992, **114**, 3261–3265.
- 34 A. Newman, *Pharmaceutical Amorphous Solid Dispersions*, John Wiley & Sons, Hoboken, New Jersey, 1st edn., 2015.
- 35 M. Teodorescu and M. Bercea, *Polym. Plast. Technol. Eng.*, 2015, **54**, 923–943.
- 36 K. Ueda, K. Higashi and K. Moribe, *Mol. Pharm.*, 2016, **13**, 852–862.
- 37 D. C. Apperley, A. H. Forster, R. Fournier, R. K. Harris, P. Hodgkinson, R. W. Lancaster and T. Rades, *Magn. Reson. Chem.*, 2005, **43**, 881–892.
- 38 X. Yuan, D. Sperger and E. J. Munson, *Mol. Pharm.*, 2014, **11**, 329–337.
- 39 S. P. Brown, *Solid State Nucl. Magn. Reson.*, 2012, **41**, 1–27.
- 40 L. A. O'Dell and C. I. Ratcliffe, in *NMR of Quadrupolar Nuclei in Solid Materials*, John Wiley & Sons, Chichester, 1st edn., 2012, pp. 213–232.
- 41 L. S. Batchelder, in *Encyclopedia of Nuclear Magnetic Resonance*, eds. R. K. Harris and R. E. Wasylshen, John Wiley & Sons, Chichester, 1st edn., 2007.
- 42 R. L. Vold and G. L. Hoatson, *J. Magn. Reson.*, 2009, **198**, 57–72.
- 43 R. R. Vold and R. L. Vold, *Advances in Magnetic and Optical Resonance*, Academic Press, San Diego, 1991.
- 44 V. Macho, L. Brombacher and H. W. Spiess, *Appl. Magn. Reson.*, 2001, **20**, 405–432.
- 45 S. Bracco, F. Castiglioni, A. Comotti, S. Galli, M. Negroni, A. Maspero and P. Sozzani, *Chem. - A Eur. J.*, 2017, **23**, 11210–11215.

- 46 S. L. Gould, D. Tranchemontagne, O. M. Yaghi and M. A. Garcia-Garibay, *J. Am. Chem. Soc.*, 2008, **130**, 3246–3247.
- 47 S. Bracco, A. Comotti, P. Valsesia, B. F. Chmelka and P. Sozzani, *Chem. Commun.*, 2008, 4798–4800.
- 48 A. R. Hughes, N. J. Brownbill, R. C. Lalek, M. E. Briggs, A. G. Slater, A. I. Cooper and F. Blanc, *Chem. - A Eur. J.*, 2017, **23**, 17217–17221.
- 49 A. G. Slater, M. A. Little, A. Pulido, S. Y. Chong, D. Holden, L. Chen, C. Morgan, X. Wu, G. Cheng, R. Clowes, M. E. Briggs, T. Hasell, K. E. Jelfs, G. M. Day and A. I. Cooper, *Nat. Chem.*, 2017, **9**, 17–25.
- 50 T. Matsuno, M. Fujita, K. Fukunaga, S. Sato and H. Isobe, *Nat. Commun.*, 2018, **9**, 3779.
- 51 V. J. Witherspoon, J. Xu and J. A. Reimer, *Chem. Rev.*, 2018, **118**, 10033–10048.
- 52 A. C. Forse, M. I. Gonzalez, R. L. Siegelman, V. J. Witherspoon, S. Jawahery, R. Mercado, P. J. Milner, J. D. Martell, B. Smit, B. Blümich, J. R. Long and J. A. Reimer, *J. Am. Chem. Soc.*, 2018, **140**, 1663–1673.
- 53 R. M. Marti, J. D. Howe, C. R. Morelock, M. S. Conradi, K. S. Walton, D. S. Sholl and S. E. Hayes, *J. Phys. Chem. C*, 2017, **121**, 25778–25787.
- 54 Y. Zhang, B. E. G. Lucier and Y. Huang, *Phys. Chem. Chem. Phys.*, 2016, **18**, 8327–8341.
- 55 M. Inukai, T. Kurihara, Y. Noda, W. Jiang, K. Takegoshi, N. Ogiwara, H. Kitagawa and K. Nakamura, *Phys. Chem. Chem. Phys.*, 2020, **22**, 14465–14470.
- 56 L. C. Lin, J. Kim, X. Kong, E. Scott, T. M. McDonald, J. R. Long, J. A. Reimer and B. Smit, *Angew. Chemie - Int. Ed.*, 2013, **52**, 4410–4413.

- 57 J. Li, S. Li, A. Zheng, X. Liu, N. Yu and F. Deng, *J. Phys. Chem. C*, 2017, **121**, 14261–14268.
- 58 H. Wu, W. Zhou and T. Yildirim, *J. Am. Chem. Soc.*, 2009, **131**, 4995–5000.
- 59 E. Weiland, M. A. Springuel-Huet, A. Nossov and A. Gédéon, *Microporous Mesoporous Mater.*, 2016, **225**, 41–65.
- 60 P. Håkansson, M. A. Javed, S. Komulainen, L. Chen, D. Holden, T. Hasell, A. Cooper, P. Lantto and V. V. Telkki, *Phys. Chem. Chem. Phys.*, 2019, **21**, 24373–24382.
- 61 J. Li, A. Corma and J. Yu, *Chem. Soc. Rev.*, 2015, **44**, 7112–7127.
- 62 J. Xu, Q. Wang, S. Li and F. Deng, *Solid-State NMR in Zeolite Catalysis*, Springer Nature, Singapore, 1st edn., 2019.
- 63 Z. Zhao, X. Li, S. Li, S. Xu, X. Bao, Y. Bilge, P. Andrei-Nicolae, M. Ulrich and W. Zhang, *Microporous Mesoporous Mater.*, 2019, **288**, 109555.
- 64 S. Komulainen, J. Roukala, V. V. Zhivonitko, M. A. Javed, L. Chen, D. Holden, T. Hasell, A. Cooper, P. Lantto and V. V. Telkki, *Chem. Sci.*, 2017, **8**, 5721–5727.
- 65 R. Giovine, C. Volkringer, M. A. Springuel-Huet, A. Nossov, F. Blanc, J. Trébosc, T. Loiseau, J. P. Amoureux, O. Lafon and F. Pourpoint, *J. Phys. Chem. C*, 2017, **121**, 19262–19268.
- 66 P. Tian, Y. Wei, M. Ye and Z. Liu, *ACS Catal.*, 2015, **5**, 1922–1938.
- 67 I. Yarulina, A. D. Chowdhury, F. Meirer, B. M. Weckhuysen and J. Gascon, *Nat. Catal.*, 2018, **1**, 398–411.
- 68 I. Yarulina, S. Bailleul, A. Pustovarenko, J. R. Martinez, K. De Wispelaere, J. Hajek, B. M. Weckhuysen, K. Houben, M. Baldus, V. Van Speybroeck, F. Kapteijn and J. Gascon, *ChemCatChem*, 2016, **8**, 3057–3063.
- 69 A. D. Chowdhury, I. Yarulina, E. Abou-hamad, A. Gurinov and J. Gascon,

- Chem. Sci.*, 2019, **10**, 8946–8954.
- 70 A. Zagdoun, G. Casano, O. Ouari, M. Schwarzwälder, A. J. Rossini, F. Aussenac, M. Yulikov, G. Jeschke, C. Copéret, A. Lesage, P. Tordo and L. Emsley, *J. Am. Chem. Soc.*, 2013, **135**, 12790–12797.
- 71 T. Gullion and J. Schaefer, *J. Magn. Reson.*, 1989, **81**, 196–200.
- 72 D. Xiao, S. Xu, X. Han, X. Bao, Z. Liu and F. Blanc, *Chem. Sci.*, 2017, **8**, 8309–8314.
- 73 L. Chen, Q. Wang, B. Hu, O. Lafon, J. Trébosc, F. Deng and J. P. Amoureux, *Phys. Chem. Chem. Phys.*, 2010, **12**, 9395–9405.
- 74 C. Wang, J. Xu, Q. Wang, X. Zhou, G. Qi, N. Feng, X. Liu, X. Meng, F. Xiao and F. Deng, *ACS Catal.*, 2017, **7**, 6094–6103.
- 75 V. Domenici, *Liq. Cryst. Today*, 2017, **26**, 2–10.
- 76 S. V Dvinskikh, in *Thermotropic Liquid Crystals*, ed. A. Ramamoorthy, Springer Netherlands, Dordrecht, 2007, pp. 117–140.
- 77 S. Li, J. Li, J. Tang and F. Deng, *Solid State Nucl. Magn. Reson.*, 2018, **90**, 1–6.

Chapter 3: Ultra-Fast Molecular Rotors within Porous Organic Cages

3.1 Overview

Chapter 3 is adapted from a paper entitled “Ultra-Fast Molecular Rotors within Porous Organic Cages” by Ashlea R. Hughes, Nick J. Brownbill, Rachel C. Lalek, Michael E. Briggs, Anna G. Slater, Andrew I. Cooper and Frédéric Blanc which was published in *Chemistry – A European Journal* in 2017. The author contributions are as follows: F.B. devised the project. M.E.B. and A.G.S. synthesized the TCCX cages, prior to loading by A.R.H. A.R.H. conducted the NMR experiments, with support from and R.L., N.J.B. and F.B. Data analysis and interpretation was undertaken by A.R.H. A.R.H. and F.B. wrote the manuscript with consultation from all other authors.

3.2 Abstract

Using variable temperature ^2H static NMR spectra and ^{13}C spin-lattice relaxation times (T_1), we show that two different porous organic cages with tubular architectures are ultra-fast molecular rotors. The central *para*-phenylene rings, that frame the 'windows' to the cage voids, display very rapid rotational rates of the order of $1.2\text{-}8\times 10^6$ Hz at 230 K with low activation energy barriers in the $12\text{-}18$ kJ mol $^{-1}$ range. ^{13}C T_1 rates associated with the carbons on the phenylene rings were shorter in comparison with the rest of the molecule, again supporting fast motion. These cages act as hosts to iodine guest molecules, which dramatically slow down the rotational rates of the phenylene groups ($5\text{-}10\times 10^4$ Hz at 230 K), and lengthen the ^{13}C T_1 times for the carbons on the *para*-phenylene rings, demonstrating potential use in applications that require molecular capture and release. Iodine release was observed upon heating detected by thermogravimetric analysis. The release of iodine resulted in the restoration of the rapid rotational rates of the phenylene rings detected by ^2H NMR spectroscopy.

3.3 Introduction

Porous organic frameworks (POFs) are supramolecular assemblies that have ordered architectures containing an inherent void. Examples include metal organic frameworks (MOFs), covalent organic frameworks (COFs), zeolitic imidazolate frameworks (ZIFs), and porous organic cages (POCs).¹⁻⁴ POCs differ from these other framework families because they consist of discrete molecules containing both an intrinsic void within the cages in addition to voids within the overall lattice; because of these properties, POCs are also solution-processable and have been explored for a range of applications including catalysis, molecular separation and gas storage.⁵⁻¹⁰ For example, POCs have been shown to capture guest molecules such as iodine, SF₆, and hydrocarbons.¹¹ The sequestration of iodine, which is an unwanted fission product,¹²⁻¹⁴ is of strong importance for the nuclear industry.¹⁵ The selective loading and retention of guests such as iodine often relies on molecular flexibility and dynamics, and the understanding of these processes plays a central role in the design of the next generation of POFs.

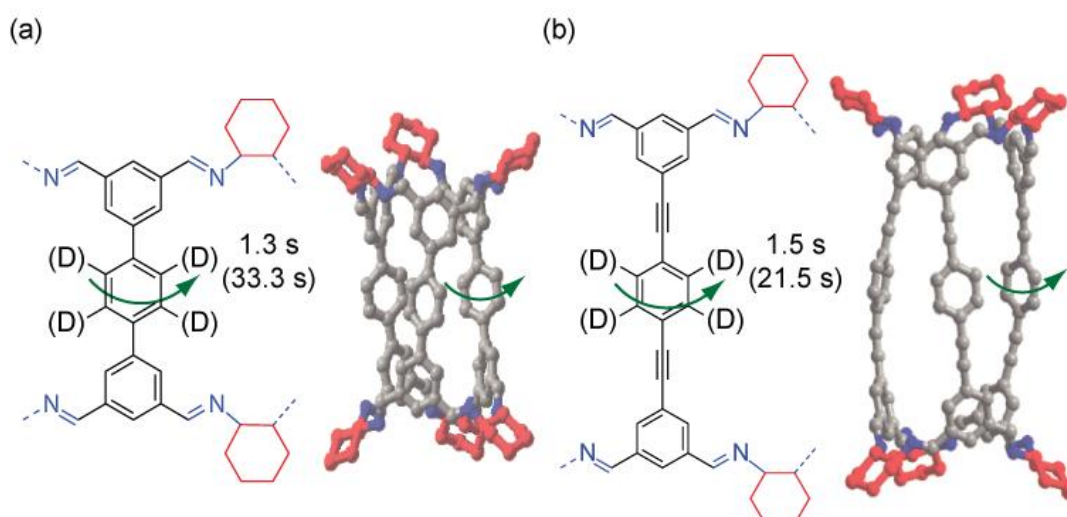


Figure 3.1. Chemical structure and side view of the X-ray crystal structure of (a) TCC2-R and (b) TCC3-R.¹⁰ The cyclohexane groups are shown in red; other C, grey; N, blue; H omitted for clarity in the crystal structure representation. The green arrows indicate fast molecular rotation of the *para*-phenylene. The ¹³C spin-lattice relaxation times (T₁) obtained for selected carbons are given in the Figure, including T₁ values after iodine loading (values in parentheses). The deuterium-labelled positions on the *para*-phenylene are also shown for [D₁₂]TCC2-R and [D₁₂]TCC3-R.

Recently, a new family of POCs with a chiral, tubular covalent cage (TCC) architecture has been discovered.¹⁰ These TCCs consist of three 'walls' bound by *trans*-imine cyclohexane linkers. Two of these structures (TCC2-*R* and TCC3-*R*) are shown in **Figure 3.1**; they differ only by the additional acetylene moieties between the phenylene rings in TCC3-*R*. The intrinsic pore within these molecules permits guest sorption into the tubular cavities.^{4, 16} The static imine cyclohexane linkers and rotating phenylene groups allow these POCs to be classified as molecular rotors.¹⁷⁻¹⁹ It is likely that the window dynamics in these molecules controls guest loading into the molecular pore, and we therefore set out to understand the response of these cages to external stimuli, such as guest inclusion.

²H solid echo NMR has become an extremely powerful tool for the understanding of dynamics in the kHz timescale,²⁰⁻²² which is enabled by the large change in the ²H NMR line shape with temperature. This approach provides a qualitative description of the motion as well as its rate and associated activation energies in both pristine fast molecular rotors and those hampered by guest loading (*e.g.*, H₂O, acetone, iodine, CH₄ and hydrocarbons);²³⁻³³ these include mesoporous *para*-phenylene silica,²³ polyaromatic frameworks (PAFs),²⁴ and MOFs.^{28, 29, 31, 33} Additionally, ¹³C T₁ values provide correlation times in the ns timescales (MHz frequency regime) and complementary details of the molecular reorientation.

Here, we performed variable temperature ²H solid echo NMR experiments and room temperature ¹³C T₁ measurements on pristine and iodine-loaded TCC2-*R* and TCC3-*R* materials to understand the rotational dynamics of the cages and their host-guest interactions.

3.4 Materials and Methods

3.4.1. General synthesis consideration for the syntheses of the chiral tubular covalent cages¹⁰

Analytical HPLC analysis was conducted using a Dionex Ultimate 3000 HPLC system. Solution NMR spectra were recorded using either a Bruker Avance 400 MHz or 500 MHz NMR spectrometer. Mass spectrometry was carried out by the EPSRC National Mass Spectrometry Facility at Swansea University using a Xevo G2-S ASAP (QTOF), GCT Premier GC/MS (GC-EI-MS), or ultrafleXtreme (MALDI) instrument, and at the Microbiorefinery (University of Liverpool) using an Agilent Technologies 6530B accurate-mass QTOF Dual ESI mass spectrometer. Thermogravimetric analysis was carried out using a Q5000IR analyser (TA Instruments). The samples were heated at a rate of 5 °C /min, being held for 10 minutes at 70 °C and 90 °C. Infrared spectra were collected on a Bruker ALPHA platinum attenuated total reflectance fourier transform infrared spectrometer (ATR-FTIR). Spectra were recorded for 24 scans in transmission mode. Laboratory powder X-ray diffraction (PXRD) data were collected in transmission mode on samples held on thin Mylar film in aluminium well plates on a Panalytical X'Pert PRO MPD equipped with a high throughput screening (HTS) XYZ stage, X-ray focusing mirror, and PIXcel detector, using Ni-filtered Cu K α radiation. Data were measured over the range 5–50° over 30 min.

The TCC2-*R* and TCC3-*R* cages were prepared according to a literature procedure.¹⁰ The deuterated cages, [D₁₂]TCC2-*R* and [D₁₂]TCC3-*R* were prepared using the syntheses outlined below. 5-Bromoisophthalaldehyde was synthesized according to literature procedures.^{41, 42} All other chemicals were purchased from Sigma Aldrich or TCI and used as received.

3.4.2 Synthesis of the aldehyde precursors

3.4.2.1 Synthesis of 2,2'-([D₄]1,4-phenylene)bis(4,4,5,5-tetramethyl-1,3,2-dioxaborolane) (1)

[1,1'-Bis(diphenylphosphino)ferrocene]dichloropalladium (II) (0.412 g, 0.563 mmol) was added to a degassed suspension of [D₄]1,4-dibromobenzene-2,3,5,6 (2.0 g, 8.3

mmol), bis(pinacolato)diboron (4.8 g, 19 mmol), and potassium acetate (5.2 g, 53 mmol) in 1,4-dioxane (40 mL) and the mixture was heated at reflux under a nitrogen atmosphere for 3 days. After cooling to ambient temperature, the reaction mixture was diluted with hexane (60 mL) and the suspension was charged to a pad of silica gel and washed with 1 % ethyl acetate/hexane until all the product had eluted. The filtrate was evaporated to dryness. The residue was redissolved in CH₂Cl₂, diluted with hexane and evaporated until ~20 mL of solvent remained. The suspension was filtered and the solid dried under vacuum to yield the desired pure compound **1** (2.0 g, 6.0 mmol, 75 %). ¹H NMR (500 MHz, CDCl₃): δ 1.35 (24 H, s, 8 x CH₃); ¹³C NMR (101 MHz, CDCl₃): δ 133.59 (t, ¹J (C,D) = 24.3 Hz), 83.97, 25.01 ppm. MS(Cl)⁺ calcd for C₁₈H₂₅D₄B₂O₄ [M+H]⁺: 335.1; found: 335.3. HRMS (TOF) calcd for C₁₈H₂₅D₄B₂O₄ [M+H]⁺: 335.2503; found: 335.2511.

3.4.2.2 Synthesis of (([D₄]1,4-phenylene)bis(ethyne-2,1-diyl))bis(trimethylsilane) (**2**)

[D₄]1,4-dibromobenzene-2,3,5,6 (2.50 g, 10.4 mmol) was added to a flame-dried, backfilled flask. Et₃N (36 mL) was added via cannula. CuI (0.048 g, 0.25 mmol) and Pd(PPh₃)₄ (0.15 g, 0.13 mmol) were added, followed by the dropwise addition of trimethylsilyl acetylene (3.7 mL, 25 mmol). The mixture was refluxed for 8 hours, cooled, and then evaporated under reduced pressure to yield a crude off-white solid. This solid was purified *via* column chromatography (Biotage Isolera4, KP-Sil cartridge, 100 % hexane) to yield the product **2** as a white solid (2.6 g, 9.5 mmol, 95 %). ¹H NMR (400 MHz, CDCl₃ + TFA): δ 0.14 (18 H, s, CH₃); ¹³C NMR (101 MHz, CDCl₃): δ 130.49 (t, ¹J (C,D) = 25.2 Hz), 103.64, 95.46, -0.96 ppm. MS(Cl)⁺ calcd for C₁₆H₁₉D₄Si₂ [M+H]⁺: 275.5; found: 275.2. HRMS (TOF) calcd for C₁₆H₁₉D₄Si₂ [M]⁺: 274.1511; found: 274.1516.

3.4.2.3 Synthesis of [D₄]1,4-diethynylbenzene-2,3,5,6 (**3**)

(([D₄]1,4-phenylene)bis(ethyne-2,1-diyl))bis(trimethylsilane) **2**, (2.5 g, 9.2 mmol) was dissolved in MeOH (50 mL) and CH₂Cl₂ (50 mL). K₂CO₃ (8.5 g, 62 mmol) was added, and the mixture stirred at room temperature for 24 hours. The colourless solution was then poured into H₂O (100 mL), extracted with Et₂O (3 x 100 mL) and washed

with brine (200 mL). The organic layer was dried over MgSO_4 , filtered, and evaporated under reduced pressure to yield the pure product **3** as a white solid (0.99 g, 7.6 mmol, 83 %). ^1H NMR (500 MHz, $\text{CDCl}_3 + \text{CF}_3\text{CO}_2\text{H}$): δ 3.17 (2 H, s, CH); ^{13}C NMR (101 MHz, CDCl_3): δ 130.76 (t, 1J (C,D) = 25.0 Hz), 121.49, 82.11, 78.24 ppm. $\text{MS}(\text{CI})^+$ calcd for $\text{C}_{10}\text{H}_3\text{D}_4$ $[\text{M}+\text{H}]^+$: 131.2; found: 131.1. HRMS (TOF) calcd for $\text{C}_{10}\text{H}_3\text{D}_4$ $[\text{M}]^+$: 130.0721; found: 130.0716.

3.4.2.4 Synthesis of [1,1':4',1''-terphenyl]-3,3''5,5''-tetracarbaldehyde (**4**)

5-Bromoisophthalaldehyde (1.9 g, 9 mmol), 2,2'-([D₄]1,4-phenylene)bis(4,4,5,5-tetramethyl-1,3,2-dioxaborolane) **1** (1.0 g, 3 mmol), and K_2CO_3 (4.1 g, 30 mmol) were suspended in $(\text{CH}_2)_4\text{O}$ (50 mL) and H_2O (15 mL) and thoroughly degassed with N_2 for 30 minutes. $\text{Pd}(\text{PPh}_3)_4$ (0.17 g, 0.15 mmol) was added and the mixture was heated at 85 °C under N_2 for 18 hours. A white precipitate was observed. The solution was then cooled to room temperature and the precipitate was collected by suction filtration. The filter cake was washed with Et_2O (100 mL), H_2O (100 mL), and a further portion of Et_2O (100 mL) and dried under suction to yield the desired pure compound **4** (0.89 g, 2.6 mmol, 87 %). ^1H NMR (400 MHz, $\text{CDCl}_3 + \text{CF}_3\text{CO}_2\text{H}$): δ 10.20 (4 H, s, CHO), 8.59 (4 H, d, 4J = 1.6 Hz, Ar-H) 8.55 (2 H, t, 4J = 1.5 Hz, Ar-H); ^{13}C NMR (101 MHz, CDCl_3): δ 194.94, 143.15, 138.38, 137.05, 134.89, 131.99, 127.95 (t, 1J (C,D) = 24.7 Hz) ppm. $\text{MS}(\text{CI})^+$ calcd for $\text{C}_{22}\text{H}_{11}\text{D}_4\text{O}_4$ $[\text{M}+\text{H}]^+$: 347.1; found: 347.1. HRMS (TOF) calcd for $\text{C}_{22}\text{H}_{11}\text{D}_4\text{O}_4$ $[\text{M}+\text{H}]^+$: 347.1221; found: 347.1220.

3.4.2.5 Synthesis of 1,4-bis(3,5-diformylphenyl)phenylethynylbenzene (**5**)

5-Bromoisophthalaldehyde (4.6 g, 22 mmol), [D₄]1,4-diethynylbenzene-2,3,5,6 (**3**) (0.99 g, 7.6 mmol), and CuI (0.05 g, 0.26 mmol) were added to a flame-dried flask which had been backfilled with N_2 three times. Et_3N (distilled, 100 mL) was added, and the mixture was degassed with N_2 for 30 minutes. $\text{Pd}(\text{PPh}_3)_4$ (0.30 g, 0.26 mmol) was then added and the mixture was heated at 60 °C for 24 hours under N_2 . The resulting suspension was diluted with water and the precipitate collected by filtration. The filter cake was washed with water and acetone, then dried under suction. The filter cake was transferred to a Soxhlet and extracted with CH_2Cl_2 for 24 hours. The CH_2Cl_2 extracts were concentrated to ~50 mL, the suspension was filtered

and the filter cake was washed with acetone and dried under suction to afford a yellow powder (1.9 g, 4.8 mmol, 63 %). ^1H NMR (500 MHz, CDCl_3): δ 10.11 (4 H, s, CHO), 8.43 (2 H, t, $^4J = 1.6$ Hz, Ar-H), 8.37 (4 H, d, $^4J = 1.6$ Hz, Ar-H). ^{13}C NMR (101 MHz, CDCl_3): δ 191.96, 137.57, 135.80, 130.75 (t, $^1J(\text{C,D}) = 24.4$ Hz), 130.01, 125.25, 121.74, 91.65, 87.47. ppm. MS(Cl) $^+$ calcd for $\text{C}_{26}\text{H}_{11}\text{D}_4\text{O}_4$ [M+H] $^+$: 395.4; found: 395.1. HRMS (TOF) calcd for $\text{C}_{26}\text{H}_{11}\text{D}_4\text{O}_4$ [M+H] $^+$: 395.1221; found: 395.1219.

3.4.3 Synthesis of the chiral tubular covalent cages

3.4.3.1 Synthesis of solvated cage compound [D₁₂]TCC2-R

To a stirred suspension of **4** (0.80 g, 2.3 mmol) and $\text{CF}_3\text{CO}_2\text{H}$ (2 drops) in CH_2Cl_2 (15 mL) was added a solution of *R,R*-cyclohexanediamine (0.53 g, 4.6 mmol) in CH_2Cl_2 (10 mL). The mixture was stirred overnight at room temperature, during which time the solution turned yellow and the tetraaldehyde compound was seen to dissolve. After five days, the reaction mixture was diluted with CH_2Cl_2 and the mixture was filtered to remove any insoluble byproducts. The filtrate was concentrated to ~20 mL, hexane (40 mL) was charged whilst undergoing stirring and the resulting white precipitate was collected via suction filtration to yield [D₁₂]TCC2-R (0.88 g, which contains 1.3 wt% hexane as calculated by integration of additional solvent peaks in the NMR at 1.26 and 0.83 ppm, adjusted yield 0.87 g, 0.58 mmol, 75 %). ^1H NMR (400 MHz, $\text{CD}_3\text{OD} + \text{CDCl}_3$): δ 8.28 (6 H, s), 8.19 (6 H, s), 7.88 (12 H, m), 7.41 (6 H, s), 3.50 (6 H, br. m.), 3.29 (6 H, m), 2.10 – 2.03 (6 H, m), 1.98 – 1.76 (30 H, m), 1.55 (12 H, m). ^{13}C NMR (101 MHz, CDCl_3): δ 162.21, 161.87, 141.21, 138.97, 136.55, 135.84, 131.99, 126.77, 125.93, 125.57, 75.20, 73.90, 32.20, 31.58, 24.26, 24.23. HRMS (TOF) calcd for $\text{C}_{102}\text{H}_{92}\text{D}_{12}\text{N}_{12}$ [M+2H] $^{2+}$: 754.4630; found: 754.4659 [M+2H] $^{2+}$ and 503.3142 [M+3H] $^{3+}$.

3.4.3.2 Synthesis of cage compound [D₁₂]TCC3-R

[D₁₂]TCC3-R was prepared using the same method as for [D₁₂]TCC2-R described above using aldehyde **5**, and required repeated recrystallisations from CH_2Cl_2 /hexane to obtain a pure product (0.40 g from 1.00 g aldehyde, no hexane observed in the ^1H NMR, 0.24 mmol, 28 %). ^1H NMR (500 MHz, $\text{MeOD}/\text{CDCl}_3$): δ 8.17 (6 H, s, N=CH), 8.16

(6 H, s, N=CH), 7.95 (6 H, m, Ar-H), 7.89 (6 H, m, Ar-H), 7.50 (6 H, m, Ar-H), 3.45 (6 H, m, NCH), 3.37 (6 H, m, NCH), 1.90–1.50 (48 H, m, CH₂) ¹³C NMR (101 MHz, CDCl₃): δ 160.37, 160.05, 136.6, 136.2, 135.9, 131.05 (t, ¹J (C,D) = 26.1 Hz), 129.64, 127.58, 123.91, 122.62, 90.27, 90.06, 75.04, 74.30, 32.71, 32.35, 24.2, 24.15. HRMS (TOF) calcd for C₁₁₄H₉₀D₁₂N₁₂ [M+2H]²⁺: 826.4630; found: 826.4674 [M+2H]²⁺ and 551.3152 [M+3H]³⁺.

3.4.3.3 Preparation of all the desolvated cages

Prior to solid state NMR, all pristine cages were dried at 333 K for 24 hours under vacuum to ensure no residual solvent or water was present.

3.4.3.4 Iodine loading into the cages¹⁶

The cages were initially desolvated under vacuum and pristine TCC2-*R*, TCC3-*R*, [D₁₂]TCC2-*R* and [D₁₂]TCC3-*R* (ca. 0.05-0.11 g, 0.03-0.07 mmol) were held in a non-porous aluminum cup in an atmosphere of I₂ in large excess (~1 g, ~4 mmol, ~60-130 equiv.) at atmospheric pressure. The uptake of iodine was monitored gravimetrically and a colour change was observed. The white [D₁₂]TCC2-*R* and pale yellow [D₁₂]TCC3-*R* cages became dark yellow within an hour and turned brown within a few hours. It was assumed that all weight increases were related only to the uptake of iodine into the cages. All NMR spectra were recorded after samples had been in an I₂ atmosphere for a minimum of 48 hours.

After 40.5 hours, [D₁₂]TCC2-*R* (0.110 g, 0.073 mmol) had absorbed 0.090 g of iodine atoms (0.709 mmol), resulting in an uptake of 10 iodine atoms per molecule. After 40.5 hours, [D₁₂]TCC3-*R* (0.049 g, 0.030 mmol) had absorbed 0.044 g of iodine atoms (0.346 mmol), resulting in an uptake of 12 iodine atoms per molecule.

Upon heating for 7 hours at 70 °C, iodine was released from the cages with the colour changing significantly from dark brown/black to light brown. Additionally, the mass decreased with a loss of 49 and 44 wt% of iodine for [D₁₂]TCC2-*R* and [D₁₂]TCC3-*R*, respectively, corresponding to almost complete release of iodine over one cycle.

3.4.3 Solid State NMR methods

All ^2H and ^{13}C solid-state NMR experiments were performed on a 9.4 T Bruker Avance III spectrometer equipped with a 4 mm HXY Magic Angle Spinning (MAS) probe in double resonance mode. The ^1H channel was tuned to $\nu_0(^1\text{H}) = 400.13$ MHz and the X channel tuned to either $\nu_0(^2\text{H}) = 61.42$ MHz, or $\nu_0(^{13}\text{C}) = 100.62$ MHz. All ^1H - ^{13}C cross polarisation (CP) spectra were recorded at $\nu_r = 12.5$ kHz with a ^{13}C RF field of 45 kHz for an optimal contact time of 2 ms, while the ^1H RF field amplitude was ramped to obtain maximum signal at approximately 60 kHz. ^1H decoupling was applied at 83 kHz with a SPINAL-64 shaped pulse.³⁴ Typically 1024-3072 scans were accumulated and were recorded with a recycle delay corresponding to the maximum signal to noise per unit time of $1.3 \times T_1$.³⁵ Variable temperature ^2H static solid echo data were obtained using a pulse delay of 30 μs at a ^2H RF field of 65 kHz. Fully relaxed spectra were acquired with a minimum of 512 scans and recycling delays ranging from 2 to 15 s depending on temperature.

NMR data were processed with TopSpin 3.2 and MATLAB R2016b.³⁶ Temperature calibration was performed prior to NMR data acquisition using the ^{207}Pb chemical shift of $\text{Pb}(\text{NO}_3)_2$ according to the procedure outlined in the literature.^{37,38} All temperatures reported are actual sample temperatures and have an estimated accuracy of ± 10 K. ^1H spectra were referenced to H_2O at 4.8 ppm, ^{13}C spectra were referenced to CH of adamantane at 29.45 ppm, corresponding to TMS at 0 ppm,³⁹ and ^2H spectra were referenced to D_2O at 0 ppm.

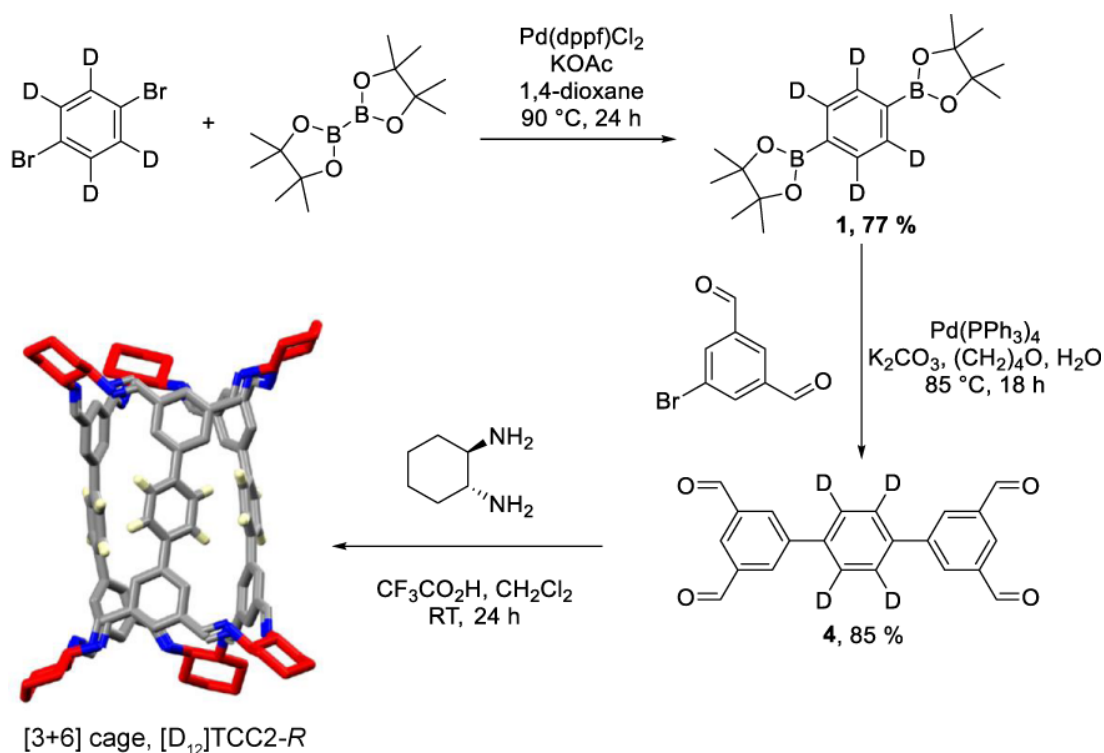
Theoretical simulation of the ^2H solid echo NMR spectra were performed using the Express 3.0 program⁴⁰ supported in MATLAB. A powder average of 1000 was used along with the ZCW tiling algorithm.⁴⁰ A two site jump model was used for the *para*-phenylene ring flip with a β angle of 60° and a γ between 0° and 180° . A probe bandwidth of 300 kHz was also applied. The resulting simulation was then left shifted to only take signal from the top of the echo and lorentzian broadening applied.

3.5 Results and Discussion

3.5.1 Synthesis of TCC(X) cages

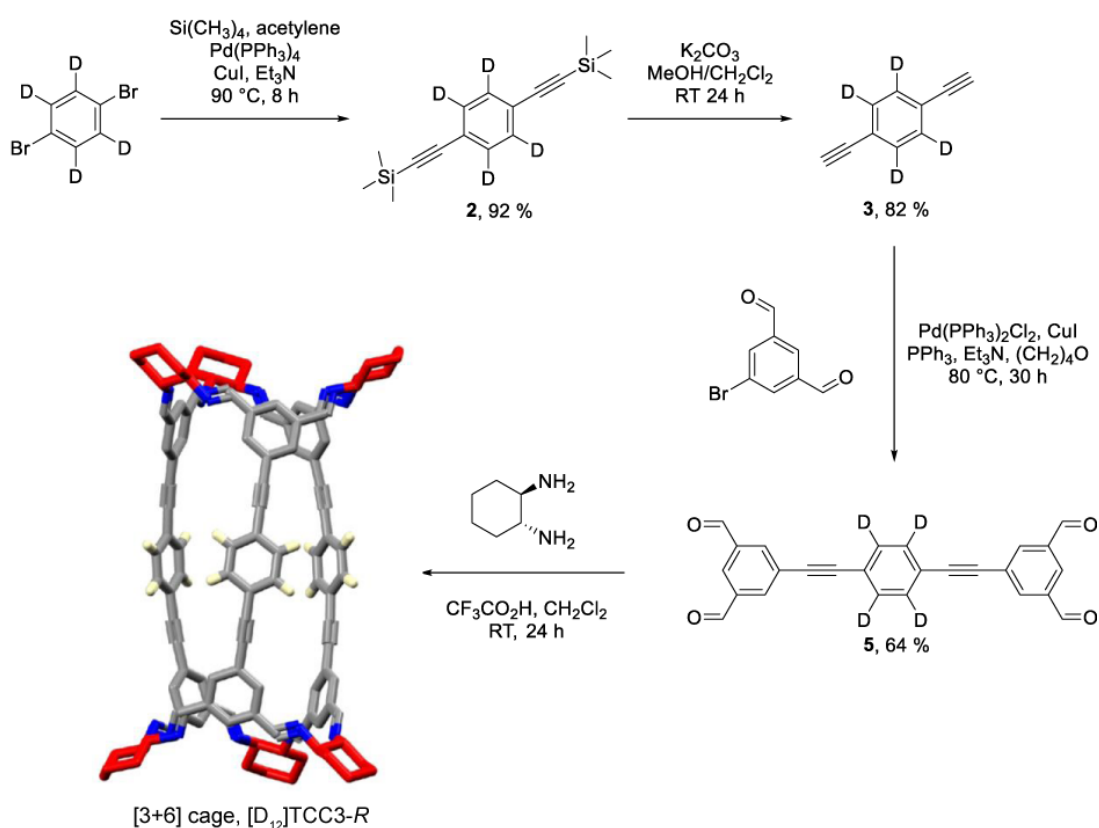
TCC2-*R* and TCC3-*R* cages were synthesized using literature procedures.¹⁰ Cages deuterated on the *para*-phenylene rings (i.e. [D₁₂]TCC2-*R* and [D₁₂]TCC3-*R*, **Figure 3.1**) were prepared via a similar approach¹⁰ described in detail in **Section 3.4** above.

The synthesis of [D₁₂]TCC2-*R* briefly consists of a palladium catalysed cross coupling reaction of [D₄]1,4-dibromobenzene-2,3,5,6 and bis(pinacolato)diboron to form 2,2'-([D₄]1,4-phenylene)bis(4,4,5,5-tetramethyl-1,3,2-dioxaborolane) followed by another palladium catalysed cross coupling reaction of the dioxaborolane with 5-Bromoisophthalaldehyde to form [1,1':4',1''-terphenyl]-3,3''5,5''-tetracarbaldehyde. This was then reacted with *R,R*-cyclohexanediamine to form the [D₁₂]TCC3-*R* structure. This synthesis is outlined in **Scheme 3.1** below.



Scheme 3.1. Synthesis of cage compound [D₁₂]TCC2-*R* from the deuterated precursor **1** and aldehyde **4** via a palladium catalysed coupling reaction. The cyclohexane groups are shown in red; other C, grey; N, blue; D, yellow; H, omitted for clarity in the crystal structure representation.

[D₁₂]TCC3-*R* was prepared in a similar manner to [D₁₂]TCC2-*R*. [D₄]1,4-dibromobenzene-2,3,5,6 was reacted with trimethylsilyl acetylene via a palladium catalysed cross coupling reaction to form (([D₄]1,4-phenylene)bis(ethyne-2,1-diyl))bis(trimethylsilane), which was then deprotected to yield [D₄]1,4-diethynylbenzene-2,3,5,6. This then underwent a further cross coupling reaction with 5-Bromoisophthalaldehyde to form 1,4-bis(3,5-diformylphenyl)phenylethynylbenzene which could then undergo imine formation resulting in the production of [D₁₂]TCC3-*R*. This is outlined in **Scheme 3.2** below.



Scheme 3.2. Synthesis of cage compound [D₁₂]TCC3-*R* from the deuterated precursor **3** and aldehyde **5** via a palladium catalysed coupling reaction. The cyclohexane groups are shown in red; other C, grey; N, blue; D, yellow; H, omitted for clarity in the crystal structure representation.

The powder XRD shown in **Figure 3.2** indicates that neither the deuterated or protonated cages show long range order. This has been observed previously that upon the removal of solvent, the homochiral cage materials (e.g. TCC2-*R*) become amorphous.¹⁰ All the cage materials used within this study were amorphous, as confirmed by powder XRD.

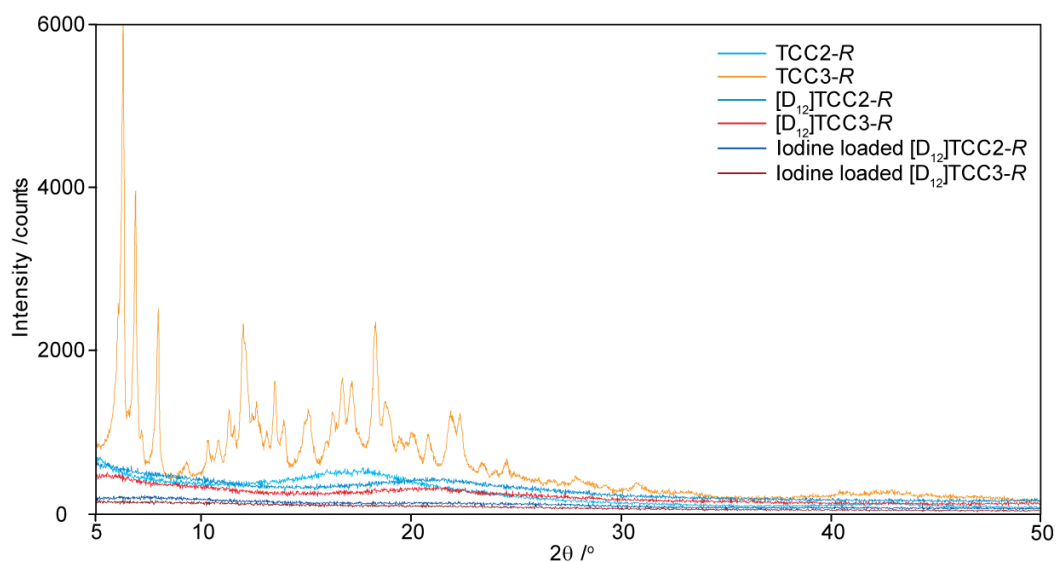


Figure 3.2. Powder XRD profiles of TCC2-*R* (light blue), TCC3-*R* (orange), [D₁₂]TCC2-*R* (blue), [D₁₂]TCC3-*R* (red), iodine-loaded [D₁₂]TCC2-*R* (dark blue) and iodine-loaded [D₁₂]TCC3-*R* (burgundy).

With the amorphous pattern obtained *via* XRD, we employed ¹³C CP MAS NMR to confirm no structural decomposition occurred during desolvation. The spectra and corresponding assignment, shown in **Figure 3.3** below, confirmed that the cage structures remained intact.

In the ²H NMR experiments conducted, we utilise the deuterated cages ([D₁₂]TCC2-*R* and [D₁₂]TCC3-*R*) due to the selective enrichment of the *para*-phenylene moieties. This allows the probing of the dynamics of only the *para*-phenylene rings within the terphenylene cage structure, as the natural abundance ²H signals (0.015%) are not detected.

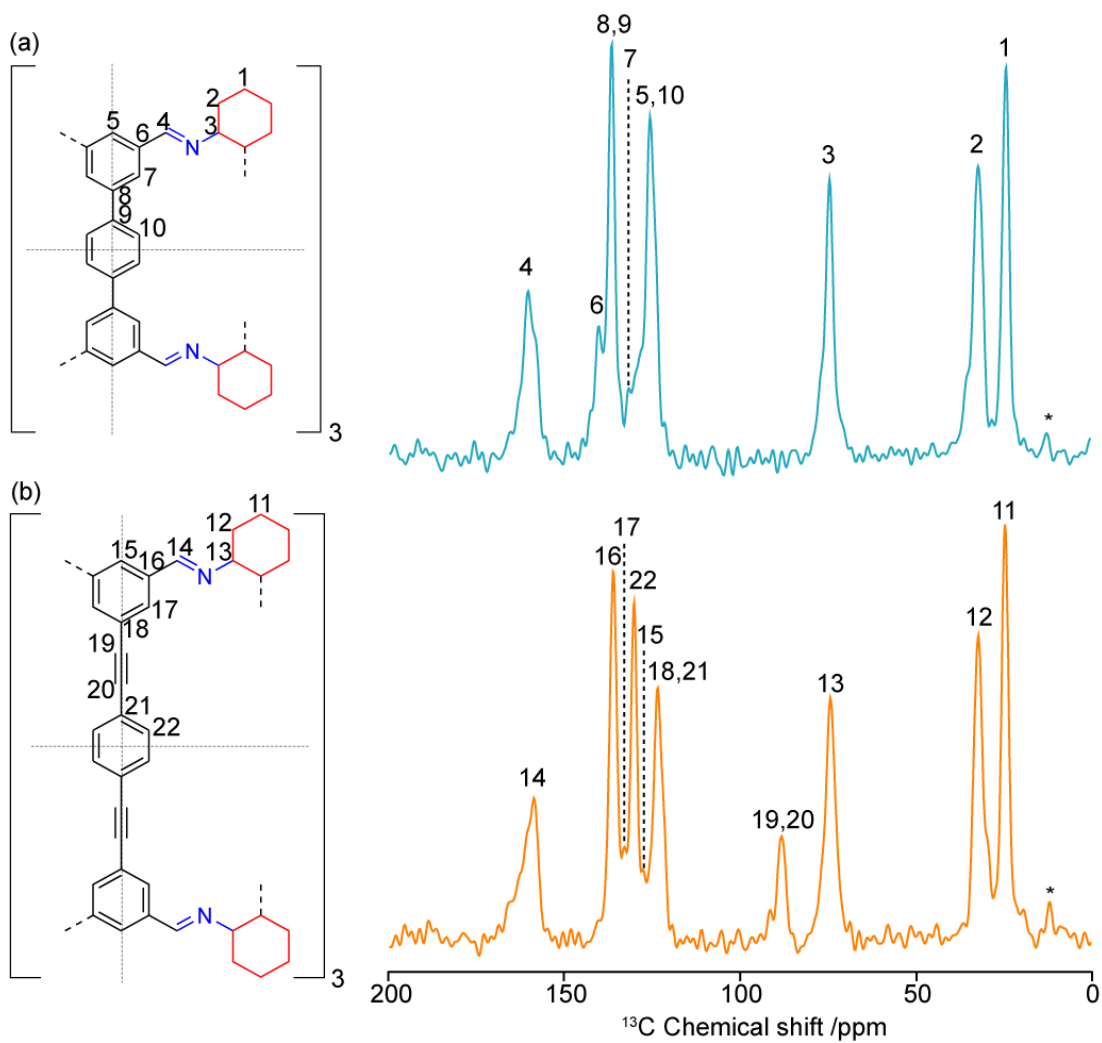


Figure 3.3. Chemical structure and corresponding ^{13}C CP MAS NMR spectra at $\nu_r = 12.5$ kHz of (a) TCC2-R (light blue) and (b) TCC3-R (orange). The spectral assignments are given in the figure, with lines of symmetry shown and spinning sidebands marked with asterisks (*).

3.5.2 ^2H NMR Studies

^2H static echo NMR spectra in the 105-298 K temperature range were recorded on desolvated and iodine-loaded $[\text{D}_{12}]\text{TCC2-R}$ and $[\text{D}_{12}]\text{TCC3-R}$ cages (**Figure 3.4**). With decreasing temperature a gradual change in the ^2H NMR line shape is observed for these materials, however, the motion induced T_2 anisotropy is dependent on the particular cage. Line shape simulations of the ^2H NMR spectra support a motion consisting of a rapid two-site 180° flip reorientation of the *para*-phenylene ring along its *para* axis, and this provides the rate of molecular reorientation (k) at each temperature on the kHz timescale.

Figure 3.4 (a) and **(c)** show the variable temperature evolution of the ^2H static echo NMR spectra of $[\text{D}_{12}]\text{TCC2-R}$ and $[\text{D}_{12}]\text{TCC3-R}$ cages. As the temperature decreases from 298 to 105 K, the appearance of the outside horns around ± 60 kHz agrees with slower rotation rates at low temperature and a static motional regime at 105 K with the anticipated Pake doublet pattern. The line shape evolution of both cages is analogous, as anticipated for materials with similar tubular covalent architectures. However, the ^2H NMR spectra of $[\text{D}_{12}]\text{TCC3-R}$ suggest a significantly larger jump rate, as evidenced by the weakening of the spectral shoulders of this cage at a lower temperature (230 K) compared to $[\text{D}_{12}]\text{TCC2-R}$ (261 K), showing slower motion for the latter.

Simulation of the ^2H solid echo NMR spectra were performed using the Express 3.0 program.⁴⁰ Rotational rates of around 1.2×10^6 and 8×10^6 Hz were extracted for $[\text{D}_{12}]\text{TCC2-R}$ and $[\text{D}_{12}]\text{TCC3-R}$ cages, respectively, at 230 K. These data suggest that the presence of an acetylene group enables easier rotation of the *para*-phenylene ring in $[\text{D}_{12}]\text{TCC3-R}$ by reducing the strong steric interactions of the *ortho*-hydrogens and opening up the void space (**Figure 3.1**). Additionally, it is also possible that small electronic factors play a role and for example include the smaller degree of conjugation between the adjacent phenylene rings in $[\text{D}_{12}]\text{TCC3-R}$ and $[\text{D}_{12}]\text{TCC2-R}$ likely also contributes to the smaller activation barrier seen for *para*-phenylene rotation in the former.

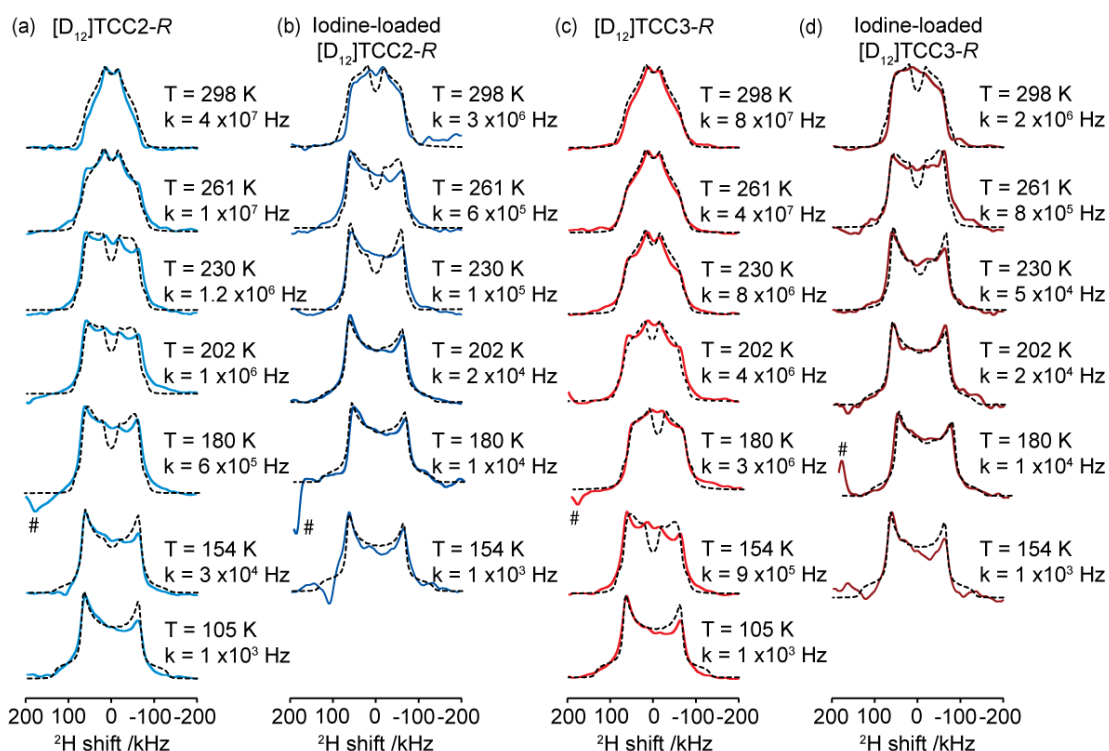
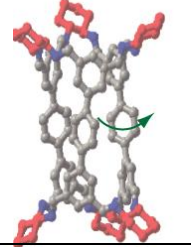
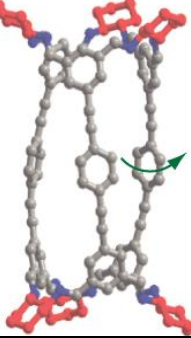
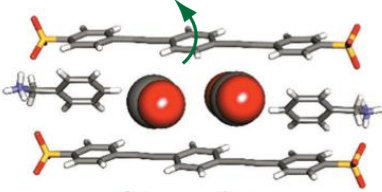
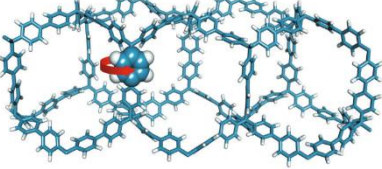
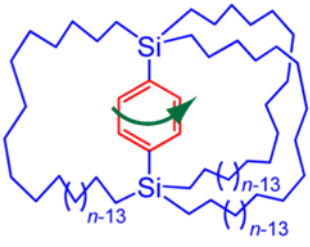
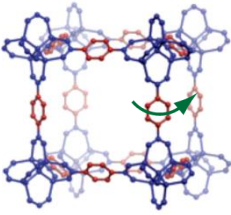


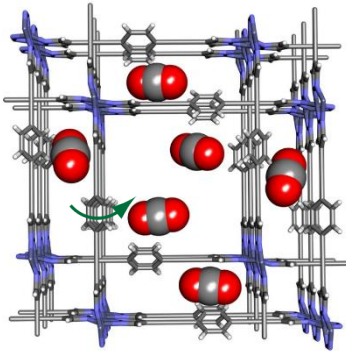
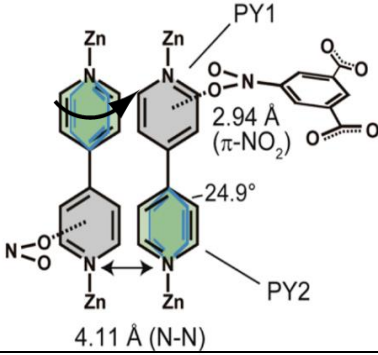
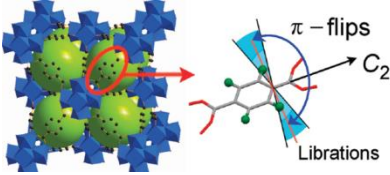
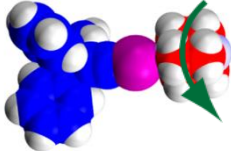
Figure 3.4. Low temperature ²H static solid echo NMR spectra of (a) [D₁₂]TCC2-R (blue), (b) iodine-loaded [D₁₂]TCC2-R (dark blue), (c) [D₁₂]TCC3-R (red), (d) iodine-loaded [D₁₂]TCC3-R (burgundy) and their corresponding simulated spectra (black dashed lines) obtained at various temperatures. The rotational rates, *k*, obtained from numerical simulations of the NMR line shapes are also given. Spectral artefacts are denoted with (#).

Moreover, while the [D₁₂]TCC2-R rate is comparable to other organic frameworks,^{27-29, 47} the very fast reorientation rate value obtained for [D₁₂]TCC3-R cage is larger than in any exclusively organic systems reported previously below ≈200 K (Table 3.1).^{18, 19, 24, 29, 32, 47-49} In particular, below this temperature, the dynamics of [D₁₂]TCC3-R are faster than those observed very recently for the *para*-phenylene reorientation in a bis(sulfophenylethynyl)-benzene frameworks based on an overall similar architecture of a phenylene molecular rotor sandwiched between two acetylene moieties (Figure 3.1 (b)), which previously showed the largest reorientation rate for porous organic materials.³²

Table 3.1. Comparison of molecular rotors in literature with rotational frequencies of 180° site reorientations exceeding 10⁵ Hz at selected temperature studied by ²H NMR.

Molecular Rotor	Temp /K	k /Hz	Ref	
Porous Organic Materials				
TCC2-R		298	4 x10 ⁷	This work
		230	1.2 x10 ⁶	
TCC3-R		298	8 x10 ⁷	This work
		230	8 x10 ⁶	
		202	4 x10 ⁶	
Bis(sulfophenylethynyl)-benzene frameworks		290	1 x 10 ⁸	32
		200	1.8 x10 ⁶	
		179	2 x10 ⁵	
PAF3 polytetraphenylsilane-d ₄ -based		300	1 x10 ⁸	24
		230 [a]	1.6 x10 ⁶	
1,4-naphthalenediyl-bridged molecular gyrotops (C ₁₈) phenylene-d ₄		290	1 x10 ⁷	19
		230 [a]	4.8 x10 ⁶	
Porous molecular crystal with 4,4'-bis(sulfophenylethynyl)benzene-d ₄ structure		230	1 x10 ⁶	27
		193	5.6 x10 ⁴	

Metal Organic Frameworks ^[b]

Zn-1,4-bis(1 <i>H</i> -pyrazol-4-ylethynyl)-benzene- <i>d</i> ₄		290	> 1 x10 ⁸	18
[Zn(5-nitroisophthalate) _x (5-methoxyisophthalate) _{1-x} (deuterated 4,4'-bipyridyl)](DMF·MeOH) _n		298	~ 5 x10 ⁷	48
Zr-UiO66- <i>d</i> ₄		296	2.3 x10 ⁶	29
Non Porous Crystalline Materials				
Co-crystal between tritylacetylene bromide TrBr and diazabicyclo[2.2.2] octane- <i>d</i> ₁₂ (dabco- <i>d</i> ₁₂)		296	> 1 x10 ⁸	49
		150	> 1 x10 ⁸	

[a] No data below 230 K are available. [b] Selection of fastest rotational frequencies of MOFs taken from within the literature.¹⁸

At temperatures higher than 298 K, the ^2H NMR line shape of the $[\text{D}_{12}]$ TCC2-*R* and $[\text{D}_{12}]$ TCC3-*R* pristine cages is characteristic of that of the fast motional regime with rates exceeding 10^8 Hz (**Figure 3.5 (a) and (c)**). No additional change in line shape occurs at higher temperature probably indicating an absence of C-D librational motion and is in sharp contrast to what is observed in PAFs.²⁴ This difference likely arises from the more flexible nature of the PAFs architecture compared to the relative rigidity of these TCC2-*R* and TCC3-*R* cage structures (**Figure 3.1**).

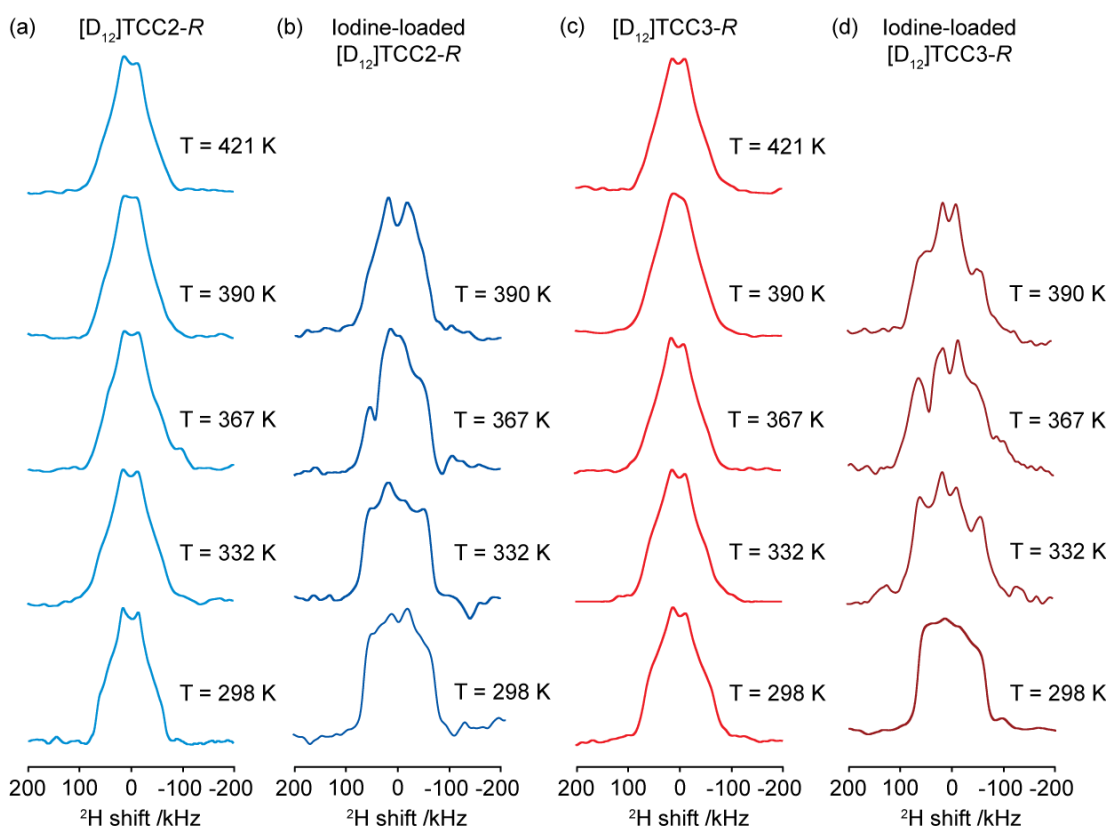


Figure 3.5. High temperature ^2H static solid echo NMR spectra of (a) $[\text{D}_{12}]$ TCC2-*R* (blue), (b) iodine-loaded $[\text{D}_{12}]$ TCC2-*R* (dark blue), (c) $[\text{D}_{12}]$ TCC3-*R* (red), (d) iodine-loaded $[\text{D}_{12}]$ TCC3-*R* (burgundy), obtained at temperatures of 298 K and above.

Using a linear regression of the Arrhenius equation of the form

$$\ln(k) = \frac{-E_a}{R} \times \frac{1}{T} + \ln(k_0) \quad (3.1)$$

a plot of $\ln(k)$ as a function of reciprocal temperature T^{-1} (**Figure 3.6**) shows a linear Arrhenius behaviour from which rotational activation energies, E_a , of 18 and 12 kJ mol⁻¹, respectively, were obtained (**Table 3.2**), along with extrapolated rotational rates at infinite temperature (attempt frequencies), k_0 , of $(9 \pm 4) \times 10^{10}$ and $(10 \pm 7) \times 10^9$ Hz for [D₁₂]TCC2-R and [D₁₂]TCC3-R, respectively. The larger E_a value obtained for [D₁₂]TCC2-R versus [D₁₂]TCC3-R is again consistent with stronger steric interactions in the terphenylene cage structure. The change in enthalpy values shown in **Table 3.1** are concordant with the activation energy data which show that the *para*-phenylene ring rotates more easily in [D₁₂]TCC3-R than in [D₁₂]TCC2-R.

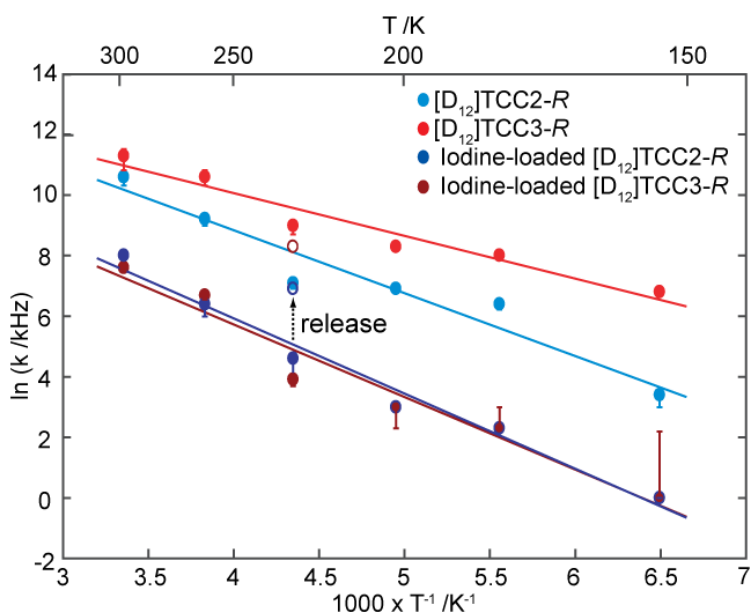


Figure 3.6. Arrhenius plot of the rotational rates, k , of the *para*-phenylene ring in desolvated and iodine-loaded [D₁₂]TCC2-R and [D₁₂]TCC3-R molecular rotor cages. The lines show the linear fit to the Arrhenius equation (3.1) with the extracted values being reported in **Table 3.2**. Error bars are estimated from comparison of the ²H NMR line shape fit at various rotational rates. The errors associated with the 154 K rates for iodine-loaded [D₁₂]TCC2-R and [D₁₂]TCC3-R are due to the indistinguishable line shape between 1 and 9 kHz. The ²H NMR rotational rates obtained at 230 K (k_{230}) from the iodine re-released [D₁₂]TCC2-R and [D₁₂]TCC3-R cages are also shown in empty circles.

The k_0 values obtained are on the low side of the $\approx 10^{12}$ Hz²² value often associated with *para*-phenylene rotation, although these values vary significantly with the systems studied and k_0 in the 10^8 - 10^{41} Hz are known.^{19, 23, 24, 27-29, 32, 46, 47, 50, 51} The associated change in entropy (ΔS) is negative for all the systems studied here and is tentatively assigned to correlated rotational motion (**Table 3.2**), leading to a relatively low attempt frequency, k_0 .^{51, 52}

Table 3.2. Comparison of the activation energy barriers (E_a) and rotational rates at 230 K (k_{230}) for all the TCC cages investigated.

Tubular covalent cages	E_a /kJ mol ⁻¹ [a]	k_{230} /K Hz ⁻¹	k_0 /Hz	ΔH /kJ mol ⁻¹	ΔS /J K ⁻¹ mol ⁻¹
[D ₁₂]TCC2-R	18 (18-20)	1.2 x10 ⁶	(9 ± 4) x10 ¹⁰	18 ± 1	-42 ± 5
Iodine-loaded [D ₁₂]TCC2-R	21 (15-21)	1 x10 ⁵	(10 ± 8) x10 ⁹	17 ± 1	-65 ± 11
[D ₁₂]TCC3-R	12 (10-13)	8 x10 ⁶	(10 ± 7) x10 ⁹	10 ± 3	-62 ± 7
Iodine-loaded [D ₁₂]TCC3-R	21 (14-21)	5 x10 ⁴	(4 ± 4) x10 ⁹	16 ± 3	-72 ± 12

[a] Range of E_a values estimated from errors in the values of k are given in brackets.

3.5.3 Iodine Loading

Iodine was loaded into $[D_{12}]TCC2-R$ and $[D_{12}]TCC3-R$ using a chemical vapour sublimation procedure, to determine if guest addition hampers motional dynamics in these systems.^{23, 24} Upon exposure to iodine at room temperature, the colour of the cages changed from yellow to black (**Figure 3.7(b)** and **(c)**), and the guest uptake was monitored gravimetrically (**Figure 3.7 (a)**). This is equivalent to a high loading of 10 and 12 iodine atoms per TCC2-*R* and TCC3-*R* cage molecule, respectively, after 40 hours of iodine exposure. The increase in weight is due to insertion of iodine into the void, however during the shallower section of the uptake (> 60 hours) for $[D_{12}]TCC2-R$, it is possible that the iodine is also interacting with the cage structure.

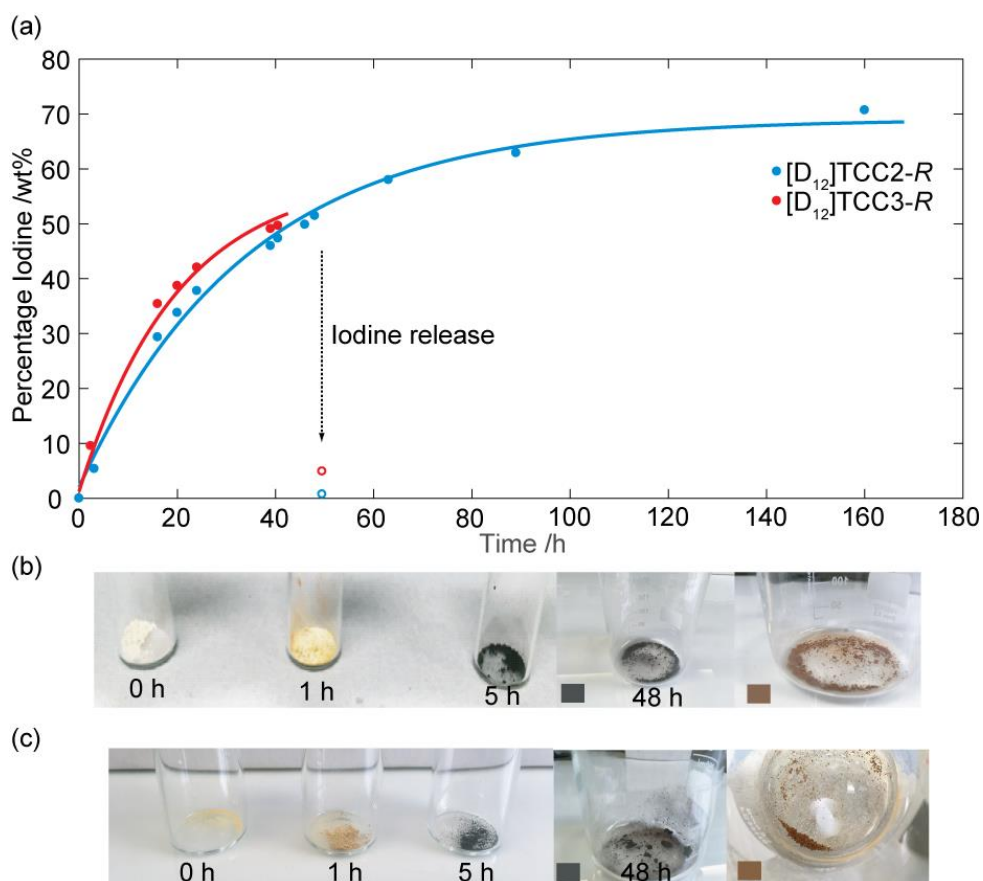


Figure 3.7. (a) Gravimetric uptake of iodine into $[D_{12}]TCC2-R$ (blue) and $[D_{12}]TCC3-R$ (red) cages as a function of time at room temperature, solid lines are a guide for the eye. Empty circles show the percentage weight of iodine left after heating the $[D_{12}]TCC2-R$ and $[D_{12}]TCC3-R$ samples for 7 hours at $70\text{ }^{\circ}\text{C}$. Photographs showing the colour change of (b) $[D_{12}]TCC2-R$ and (c) $[D_{12}]TCC3-R$ during iodine uptake after 1, 5 and 48 hours with the pictures on the right showing the iodine-released samples after 7 hours at $70\text{ }^{\circ}\text{C}$.

To confirm if the iodine is interacting with the cage structure, ^{13}C CP MAS NMR was used in conjunction with Infrared (IR) spectroscopy. **Figures 3.8, 3.9 and 3.10** do not display ^{13}C CP MAS NMR resonances or IR peaks within the aldehyde carbonyl region ($178\text{-}200\text{ ppm}$ and $1720\text{-}1740\text{ cm}^{-1}$, respectively),⁴⁴ indicating that no decomposition of the solid cages is occurring during iodine loading. The shoulder observed in the iodine-loaded $[D_{12}]TCC2-R$ IR spectrum in **Figure 3.9** at 1687 cm^{-1} is within the imine stretching region⁴³ and probably indicates that charge transfer is occurring within this cage as previously observed on the tetrahedral organic cage molecule CC3¹⁶ from IR literature data.^{43, 44}

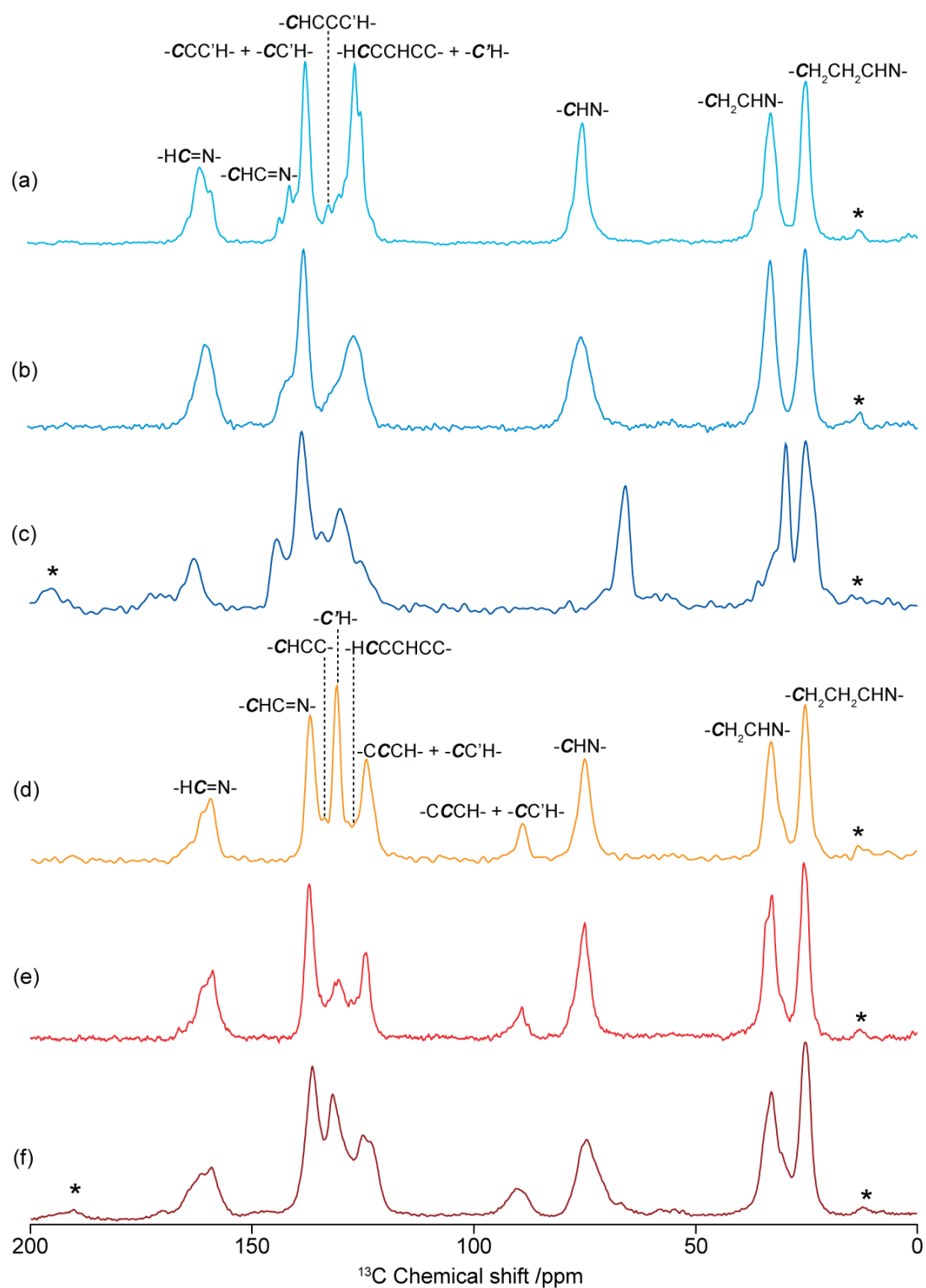


Figure 3.8. ^{13}C CP MAS NMR spectra at $\nu_r = 12.5$ kHz of (a) TCC2-*R* (light blue), (b) $[\text{D}_{12}]$ TCC2-*R* (blue), (c) iodine-loaded TCC2-*R* (dark blue), (d) TCC3-*R* (orange), (e) $[\text{D}_{12}]$ TCC3-*R* (red) and (f) iodine-loaded TCC3-*R* (burgundy). Asterisks (*) denote spinning sidebands, C' denotes the rotating carbon on the phenylene ring.

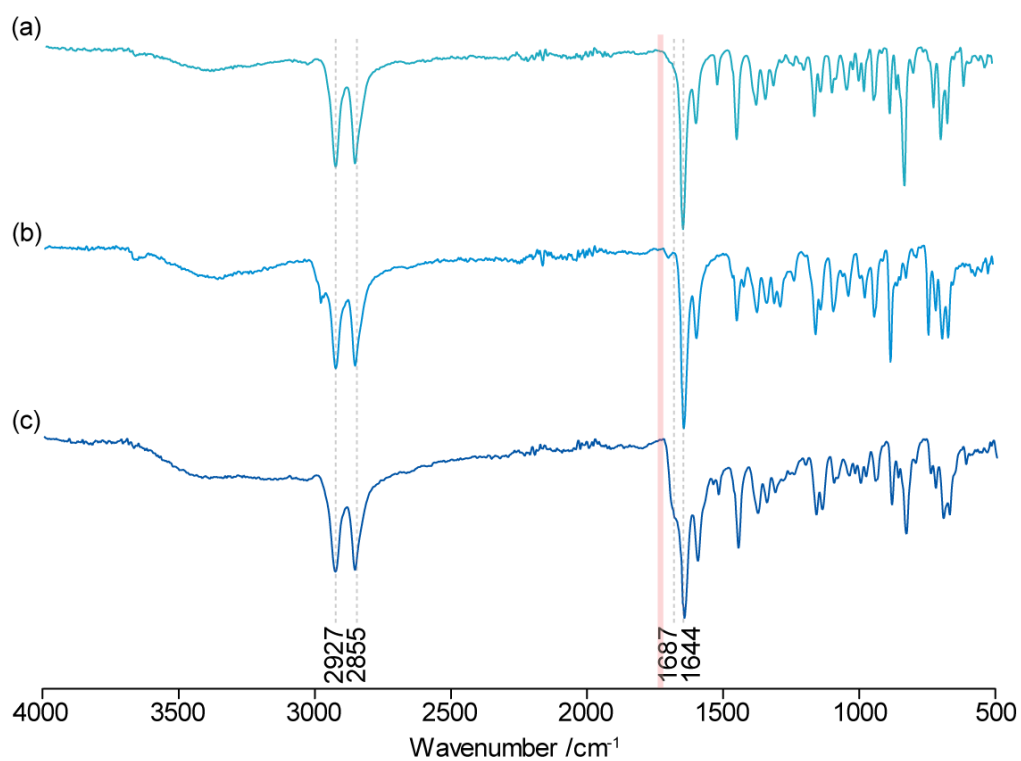


Figure 3.9. ATR-FTIR spectra of (a) TCC2-R (light blue), (b) $[\text{D}_{12}]$ TCC2-R (blue) and (c) iodine-loaded $[\text{D}_{12}]$ TCC2-R (dark blue). The red shaded region between 1720 and 1740 cm^{-1} and the dotted lines at 1687 and 1644 cm^{-1} are the anticipated area for the strong aldehyde carbonyl CO stretch⁴⁴ and the known frequencies for imine stretching mode,^{43, 44} respectively.

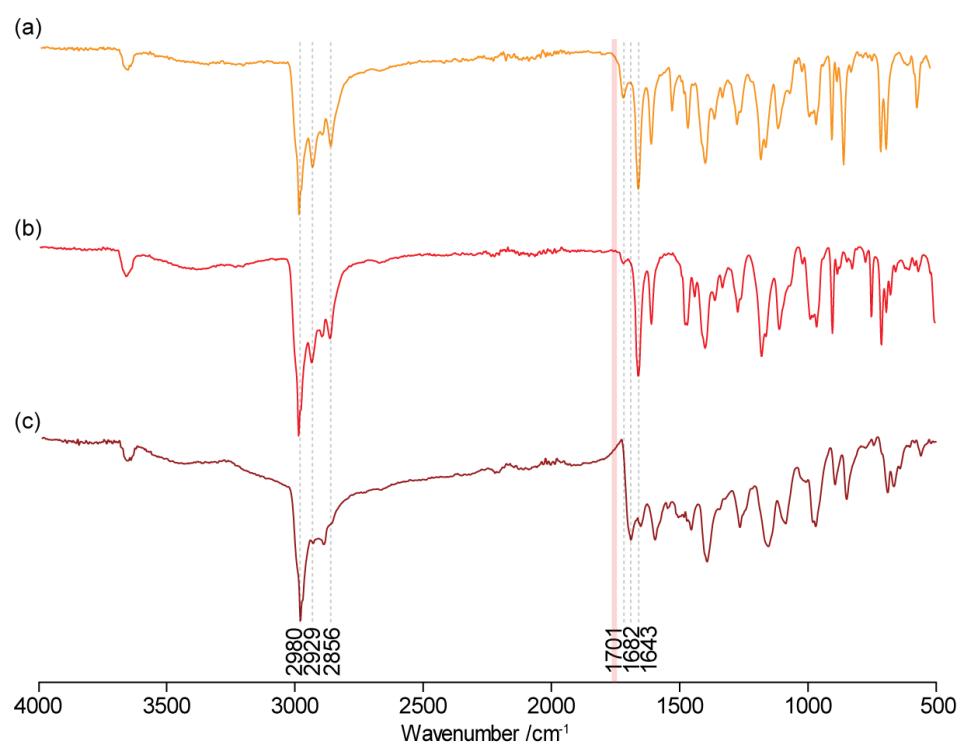


Figure 3.10. ATR-FTIR spectra of (a) TCC3-R (orange), (b) [D₁₂]TCC3-R (red) and (c) iodine-loaded [D₁₂]TCC3-R (burgundy). The red shaded region between 1720 and 1740 cm⁻¹ and the dotted lines at 1682 and 1643 cm⁻¹ are the anticipated area for the strong aldehyde carbonyl CO stretch⁴⁴ and the known frequencies for imine stretching mode,^{43,44} respectively. Flexibility within the TCC3-R structure¹⁰ allows for multiple imine modes to be visible.

The variable temperature ²H static echo NMR spectra of iodine-loaded [D₁₂]TCC2-R and [D₁₂]TCC3-R are given in **Figures 3.4 (b) and (d)** as well as **Figure 3.12 and 3.13 (a) and (b)** respectively. There is a clear difference in rotational rates of the molecular rotor between the empty and guest-loaded materials. The less rapid two-site ring flip is particularly evident at 230 K for the iodine-loaded materials, reducing the rotational rates to only 10⁵ and 5×10⁴ Hz for [D₁₂]TCC2-R and [D₁₂]TCC3-R, respectively (**Table 3.2**). This is smaller than the change seen when iodine is loaded into other porous materials,²⁴ which probably relates to the different host-guest properties of the materials. Above room temperature, the iodine-loaded cages continue to exhibit line shape narrowing at higher temperatures (**Figure 3.5**), implying faster motion, which is likely a result of iodine being released from the cages at these temperatures, as confirmed by thermogravimetric analysis (see **Figure 3.11** below).

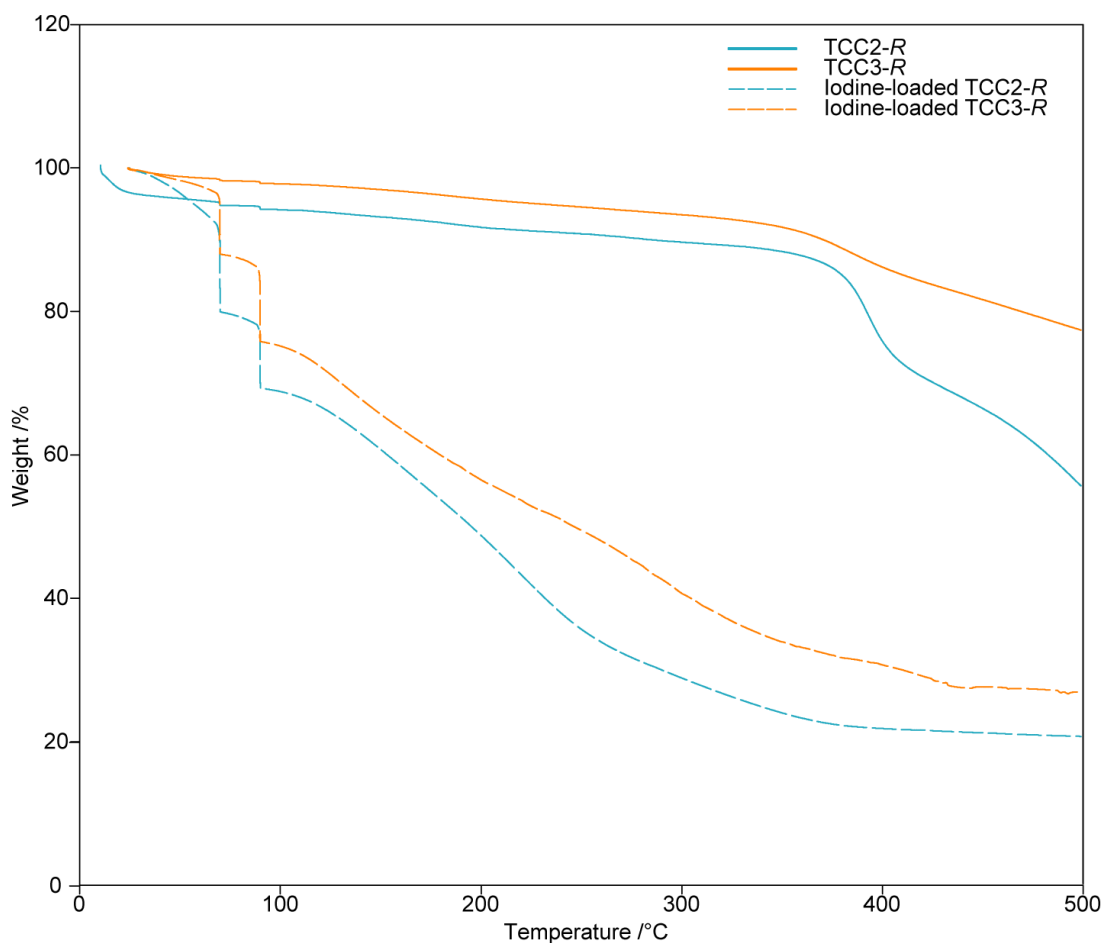


Figure 3.11. Thermogravimetric analysis of TCC2-*R* (light blue), TCC3-*R* (orange), iodine-loaded TCC2-*R* (dashed light blue) and iodine-loaded TCC3-*R* (dashed orange).

Additionally, Arrhenius plots of $\ln(k)$ as a function of T^{-1} , yield an increase of E_a with respect to the guest-free cages: from 18 to 21 kJ mol^{-1} for $[\text{D}_{12}]\text{TCC2-}R$ and from 12 to 21 kJ mol^{-1} for $[\text{D}_{12}]\text{TCC3-}R$ (**Table 3.2** and **Figure 3.6**). The value obtained for the reorientation rate at 230 K, is also reduced: from 1.2×10^6 to 1×10^5 Hz and from 8×10^6 to 5×10^4 Hz for $[\text{D}_{12}]\text{TCC2-}R$ and $[\text{D}_{12}]\text{TCC3-}R$ respectively. These data show that the presence of the iodine guest within the void of the cages, and potentially in extrinsic voids between cages, largely suppresses molecular reorientation of the *para*-phenylene rings. With iodine loading, $[\text{D}_{12}]\text{TCC3-}R$ shows a strong increase in ΔH values (**Table 3.2**), validating that rotation has become more difficult. $[\text{D}_{12}]\text{TCC2-}R$ does not show a drastic increase in enthalpy upon loading, indicating that iodine is possibly entering the voids within the lattice rather than the molecular pores.

It has been reported that when the motion of a guest molecule is restricted within a cavity, fast librational motions are expected;⁴³ this is not apparent in these TCC2-*R* and TCC3-*R* cages, since even when a guest is located inside the cages, the line shapes remain consistent with a 180° site reorientation of the *para*-phenylene rings.

After iodine-loaded [D₁₂]TCC2-*R* and [D₁₂]TCC3-*R* were heated for 7 hours at 70 °C, almost complete release of iodine over one cycle is observed as detected by thermogravimetric analysis (**Figure 3.11**) and visual inspection of the sample (**Figure 3.7 (b)** and **3.2(c)**); ²H static solid echo NMR spectra were re-ran and their simulations obtained. These are shown in **Figures 3.12** and **3.13** for [D₁₂]TCC2-*R* and [D₁₂]TCC3-*R* respectively. It can be seen that after iodine has been released from the cages, rotational rates increase to close to that of the fast motional regime shown in the pristine cages highlighting again that these materials are responsive with the rotational dynamics being modulated by the capture and release of a guest molecule.

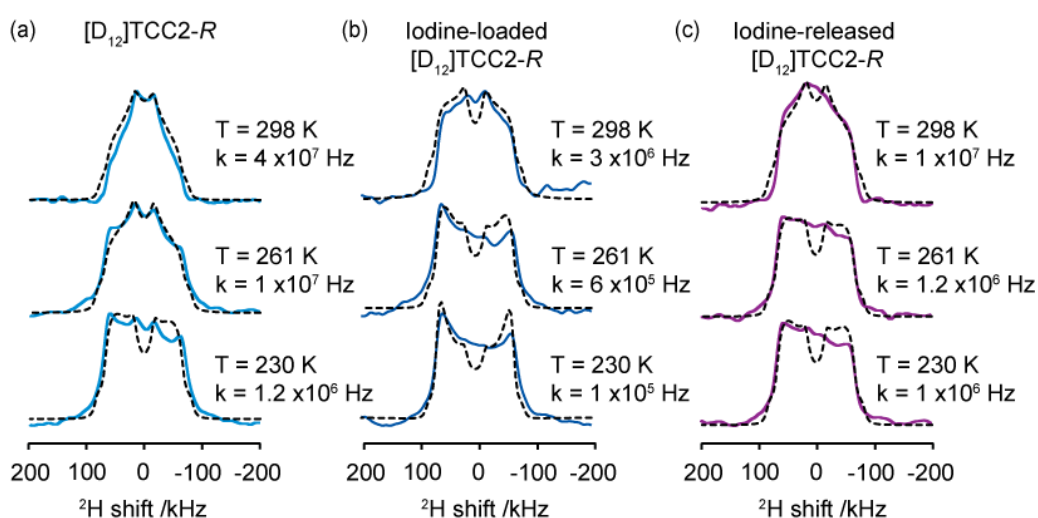


Figure 3.12. Low temperature ²H static solid echo NMR spectra of (a) [D₁₂]TCC2-*R* (blue), (b) iodine-loaded [D₁₂]TCC2-*R* (dark blue), (c) iodine-released [D₁₂]TCC2-*R* (purple), obtained at various temperatures. The rotational rates, *k*, obtained from numerical simulations of the NMR line shapes are also given.

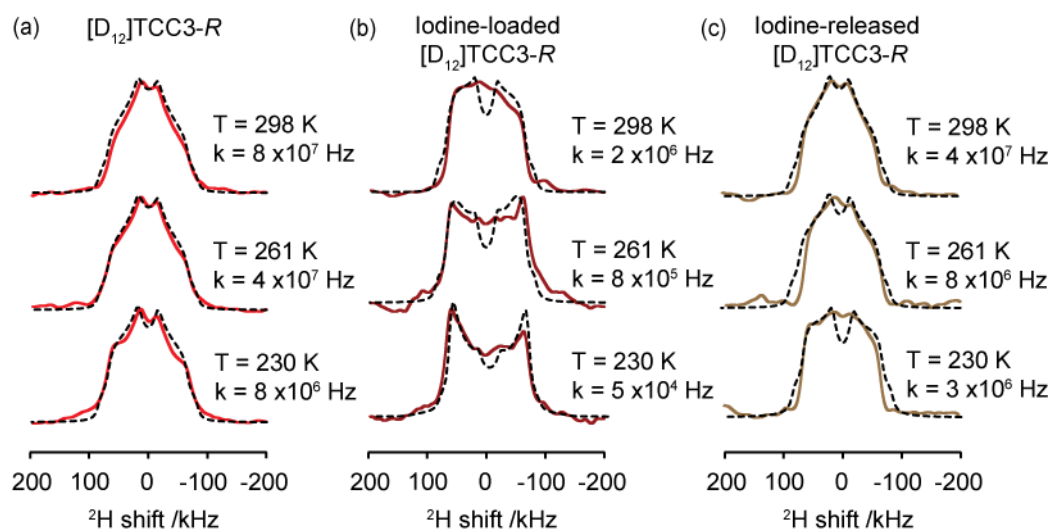


Figure 3.13. Low temperature ^2H static solid echo NMR spectra of (a) $[\text{D}_{12}]\text{TCC3-R}$ (red), (b) iodine-loaded $[\text{D}_{12}]\text{TCC3-R}$ (burgundy), (c) iodine-released $[\text{D}_{12}]\text{TCC3-R}$ (brown), obtained at various temperatures. The rotational rates, k , obtained from numerical simulations of the NMR line shapes are also given.

3.5.4 Relaxation rates

Finally, ^{13}C T_1 values were also monitored due to their strong dependence on molecular motion on the MHz timescale.⁵³ The considerably shorter room temperature ^{13}C T_1 values of 1.3-1.5 s obtained in TCC2-R and TCC3-R (see **Figure 3.1** and **Table 3.3**) for the $\text{C}'\text{H}$ carbons on the *para*-phenylene ring versus the other carbons in the cages (appearing in the range of 4-7 s) suggests an efficient relaxation mechanism and rapid molecular reorientation of the cage windows, supporting the fast molecular rotors of these cages. The ^{13}C T_1 relaxation times were found to increase significantly upon loading (**Figure 3.1, Table 3.3**), being consistent with the change in ^2H solid echo NMR line shape noted above, where guest addition into the central void slows reorientation of the phenylene rings within the cage structures.

Table 3.3. ^{13}C NMR spectra assignments, ^{13}C isotropic chemical shifts, δ , and room temperature ^{13}C spin-lattice relaxation times T_1 obtained for pristine and iodine-loaded TCC2-*R* and TCC3-*R* cages.

Assignments	^{13}C assignment numbers	δ (^{13}C) /ppm	T_1 /s	Iodine-loaded T_1 /s
TCC2- <i>R</i>				
-HC=N-	4	161	4.8 ± 1.0	32.0 ± 12.1
-CHC=N-	6	141	5.9 ± 2.3	63.7 ± 23.8
-CCC'H- + -CC'H-	8, 9	137	4.9 ± 0.5	52.2 ± 4.7
-HCCCHCC- + -C'H- + -CHCCC'H-	5, 7, 10	126	1.3 ± 0.3	33.3 ± 5.0
-CHN-	3	75	5.4 ± 1.0	20.2 ± 8.4
-CH ₂ CHN-	2	33	5.6 ± 0.8	13.9 ± 3.2
-CH ₂ CH ₂ CHN-	1	25	5.9 ± 0.9	11.5 ± 2.1
TCC3- <i>R</i>				
-HC=N-	14	161	4.2 ± 0.9	19.7 ± 5.8
-CHC=N- + -CHCC-	16, 17	137	4.9 ± 0.6	28.0 ± 4.3
-C'H-	22	132	1.5 ± 0.3	21.5 ± 2.0
-HCCCHCC- + -CCCH- + -CC'H-	15, 18, 21	125	5.8 ± 0.5	32.2 ± 4.1
-C \equiv CCC'H- + -C \equiv CCC'H-	19, 20	90	7.1 ± 2.5	38.3 ± 7.4
-CHN-	13	75	7.5 ± 0.9	31.1 ± 5.2
-CH ₂ CHN-	12	33	7.3 ± 0.5	21.6 ± 2.8
-CH ₂ CH ₂ CHN-	11	25	7.3 ± 0.5	20.3 ± 2.0

3.6 Conclusion

To conclude, we employed ^2H solid echo NMR and determined ^{13}C T_1 values to probe the rotational dynamics of the *para*-phenylene rings that define access to the central void in two porous chiral tubular covalent cages, TCC2-*R* and TCC3-*R*. Using ^2H NMR, we show that TCC2-*R* cages show reorientation rates that are comparable with the fastest molecular rotors reported for other porous frameworks; TCC3-*R* cages display even faster dynamics (below 200 K), with a very small activation energy barrier, which is ascribed to the facile rotation around the acetylene bonds, due to a reduction in the steric hindrance present. Iodine loading slows the phenylene rotation considerably, as further supported by the lengthening of the ^{13}C T_1 values, while high temperature treatment induces iodine release and reacceleration of the phenylene ring reorientation rates. These data show that the effect on cage dynamics is highly guest dependent, which might have important implications for processes such as competitive loading, molecular separation, and drug release. These findings also emphasize that models of porosity derived from static single crystal structures might be misleading, but that "time-averaged" models of the pore space could be equally inappropriate because guest inclusion can switch the rotational dynamics off. This suggests that computational models for loading in such systems need to capture the interplay of guest inclusion and rotational dynamics in the porous host.

3.7 References

- [1] O. M. Yaghi, M. O'Keeffe, N. W. Ockwig, H. K. Chae, M. Eddaoudi, J. Kim, *Nature* **2003**, *423*, 705-714.
- [2] M. Mastalerz, *Angew. Chem. Int. Ed.* **2010**, *49*, 5042-5053; *Angew. Chem. Int. Ed.* **2010**, *122*, 5164-5175.
- [3] J. Tian, P. K. Thallapally, B. P. McGrail, *CrystEngComm* **2012**, *14*, 1909-1919.
- [4] A. G. Slater, A. I. Cooper, *Science* **2015**, *348*, aaa8075.
- [5] T. Tozawa, J. T. A. Jones, S. I. Swamy, S. Jiang, D. J. Adams, S. Shakespeare, R. Clowes, D. Bradshaw, T. Hasell, S. Y. Chong, C. Tang, S. Thompson, J. Parker, A. Trewin, J. Basca, A. M. Z. Slawin, A. Stienen, A. I. Cooper, *Nat. Mater.* **2009**, *8*, 973-978.
- [6] G. Zhang, O. Presly, F. White, I. M. Oppel, M. Mastalerz, *Angew. Chem. Int. Ed.* **2014**, *53*, 1516--1520; *Angew. Chem.* **2014**, *126*, 1542-1546.
- [7] Chen, P. S. Reiss, S. Y. Chong, D. Holden, K. E. Jelfs, T. Hasell, M. A. Little, A. Kewley, M. E. Briggs, A. Stephenson, K. M. Thomas, J. A. Armstrong, J. Bell, J. Busto, R. Noel, J. Liu, D. M. Strachan, P. K. Thallapally, A. I. Cooper, *Nat. Mater.* **2014**, *13*, 954-960.
- [8] J.-H. Zhang, S.-M. Xie, B.-J. Wang, P.-G. He, L.-M. Yuan, *J. Chromatogr. A* **2015**, *1426*, 174-182.
- [9] T. Hasell, A. I. Cooper, *Nat. Rev. Mater.* **2016**, *1*, 16053.
- [10] A. G. Slater, M. A. Little, A. Pulido, S. Y. Chong, D. Holden, L. Chen, C. Morgan, X. Wu, G. Cheng, R. Clowes, M. E. Briggs, T. Hasell, K. E. Jelfs, G. M. Day, A. I. Cooper, *Nat. Chem.* **2017**, *9*, 17-25.
- [11] A. Kewley, A. Stephenson, L. Chen, M. E. Briggs, T. Hasell, A. I. Cooper, *Chem. Mater.* **2015**, *27*, 3207-3210.

- [12] B. J. Riley, J. D. Vienna, D. M. Strachan, J. S. McCloy, J. L. Jerden, *J. Nucl. Mater.* **2016**, *470*, 307--326.
- [13] C. Madic, M. Lecomte, P. Baron, B. Boullis, *Comptes Rendus Phys.* **2002**, *3*, 797-811.
- [14] K. Ioannides, K. Stamoulis, C. Papachristodoulou, *J. Radioanal. Nucl. Chem.* **2013**, *298*, 1207-1213.
- [15] D. F. Sava, M. A. Rodriguez, K. W. Chapman, P. J. Chupas, J. A. Greathouse, P. S. Crozier, T. M. Nenoff, *J. Am. Chem. Soc.* **2011**, *133*, 12398-12401.
- [16] T. Hasell, M. Schmidtman, A. I. Cooper, *J. Am. Chem. Soc.* **2011**, *133*, 14920-14923.
- [17] A. Comotti, S. Bracco, P. Sozzani, *Acc. Chem. Res.* **2016**, *49*, 1701-1710.
- [18] A. Comotti, S. Bracco, F. Castiglioni, S. Galli, M. Negroni, A. Maspero, P. Sozzani, *Chem. Eur. J.* **2017**, *23*, 11210-11215.
- [19] W. Setaka, K. Inoue, S. Higa, S. Yoshigai, H. Kono, K. Yamaguchi, *J. Org. Chem.* **2014**, *79*, 8288-8295.
- [20] K. Schmidt-Rohr, H. W. Spiess, *Multidimensional Solid-State NMR and Polymers*, Academic Press, London, **1994**.
- [21] A. Steigel, H. W. Spiess, *Dynamic NMR Spectroscopy*, Springer, Berlin Heidelberg, **1978**.
- [22] H. W. Spiess, *Colloid Polym. Sci.* **1983**, *261*, 193-209.
- [23] A. Comotti, S. Bracco, P. Valsesia, M. Beretta, P. Sozzani, *Angew. Chem. Int. Ed.* **2010**, *49*, 1760-1764; *Angew. Chem.* **2010**, *122*, 1804-1808.
- [24] A. Comotti, S. Bracco, T. Ben, S. Qiu, P. Sozzani, *Angew. Chem. Int. Ed.* **2014**, *53*, 1043-1047; *Angew. Chem.* **2014**, *126*, 1061-1065.
- [25] P. S. Sidhu, J. Bell, G. H. Penner, K. R. Jeffrey, *Can. J. Chem.* **1995**, *73*, 2196-2207.

- [26] D. F. Shantz, R. F. Lobo, *Top. Catal.* **1999**, *9*, 1-11.
- [27] S. L. Gould, D. Tranchemontagne, O. M. Yaghi, M. A. Garcia-Garibay, *J. Am. Chem. Soc.* **2008**, *130*, 3246-3247.
- [28] D. I. Kolokolov, H. Jobic, A. G. Stepanov, V. Guillerme, T. Devic, C. Serre, G. Férey, *Angew. Chem. Int. Ed.* **2010**, *49*, 4791-4794; *Angew. Chem.* **2010**, *122*, 4901-4904.
- [29] D. I. Kolokolov, A. G. Stepanov, V. Guillerme, C. Serre, B. Frick, H. Jobic, *J. Phys. Chem. C* **2012**, *116*, 12131-12136.
- [30] S. Bracco, A. Comotti, P. Valsesia, B. F. Chmelka, P. Sozzani, *Chem. Commun.* **2008**, 4798-4800.
- [31] S. Horike, R. Matsuda, D. Tanaka, S. Matsubara, M. Mizuno, K. Endo, S. Kitagawa, *Angew. Chem. Int. Ed.* **2006**, *45*, 7226-7230.
- [32] S. Bracco, T. Miyano, M. Negroni, I. Bassanetti, L. Marchio", P. Sozzani, N. Tohnai, A. Comotti, *Chem. Commun.* **2017**, *53*, 7776-7779.
- [33] D. I. Kolokolov, H. Jobic, A. G. Stepanov, J. Ollivier, S. Rives, G. Maurin, T. Devic, C. Serre, G. Férey, *J. Phys. Chem. C* **2012**, *116*, 15093-15098.
- [34] B. M. Fung, A. K. Khitrin, K. Ermolaev, *J. Magn. Reson.* **2000**, *142*, 97-101.
- [35] R. E. Ernst, G. Bodenhausen, A. Wokaun, *Principles of Nuclear Magnetic Resonance in One and Two Dimensions*, Oxford University Press, Oxford, **1987**.
- [36] The MathWorks Inc, 2016.
- [37] P. A. Beckmann, C. Dybowski, *J. Magn. Reson.* **2000**, *146*, 379-380.
- [38] A. Bielecki, D. P. Burum, *J. Magn. Reson.* **1995**, *116*, 215-220.
- [39] C. R. Morcombe, K. W. Zilm, *J. Magn. Reson.* **2003**, *162*, 479-486.
- [40] R. L. Vold, G. L. Hoatson, *J. Magn. Reson.* **2009**, *198*, 57-72.

- [41] O. A. Blackburn, B. J. Coe, M. Helliwell, J. Raftery, *Organometallics* **2012**, *31*, 5307-5320.
- [42] M. Wang, C. Wang, X.-Q. Hao, J. Liu, X. Li, C. Xu, A. Lopez, L. Sun, M.-P. Song, H.-B. Yang, X. Li, *J. Am. Chem. Soc.* **2014**, *136*, 6664–6671.
- [43] R. M. Silverstein, F. X. Webster, D. J. Kiemle, *The Spectrometric Identification of Organic Compounds*, John Wiley & Sons, New York, **2005**.
- [44] F. R. Diaz, J. Moreno, L. H. Tagle, G. A. East, D. Radic, *Synth. Met.* **1999**, *100*, 187-193.
- [45] V. Macho, L. Brombacher, H. W. Spiess, *Appl. Magn. Reson.* **2001**, *20*, 405-432.
- [46] C. S. Vogelsberg, S. Bracco, M. Beretta, A. Comotti, P. Sozzani, M. A. Garcia-Garibay, *J. Phys. Chem. B.* **2012**, *116*, 1623-1632.
- [47] A. Comotti, S. Bracco, A. Yamamoto, M. Beretta, T. Hirukawa, N. Tohnai, M. Miyata, P. Sozzani, *J. Am. Chem. Soc.* **2014**, *136*, 618-621.
- [48] M. Inukai, T. Fukushima, Y. Hijikata, N. Ogiwara, S. Horike, S. Kitagawa, *J. Am. Chem. Soc.* **2015**, *137*, 12183-12186.
- [49] L. Catalano, S. Perez-Estrada, H.-H. Wang, A. J. L. Ayitou, S. I. Khan, G. Terraneo, P. Metrangolo, S. Brown, M. A. Garcia-Garibay, *J. Am. Chem. Soc.* **2017**, *139*, 843-848.
- [50] N. B. Shustova, T. C. Ong, A. F. Cozzolino, V. K. Michaelis, R. G. Griffin, M. Dincă, *J. Am. Chem. Soc.* **2012**, *134*, 15061-15070.
- [51] B. Rodríguez-Molina, N. Farfán, M. Romero, J. M. Méndez-Stivalet, R. Santillan, M. A. Garcia-Garibay, *J. Am. Chem. Soc.* **2011**, *133*, 7280-7283.
- [52] C. Lemouchi, K. Iliopoulos, L. Zorina, S. Simonov, P. Wzietek, T. Cauchy, A. Rodríguez-Forteza, E. Canadell, J. Kaleta, J. Michl, D. Gindre, M. Chrysos, P. Batail, *J. Am. Chem. Soc.* **2013**, *135*, 9366-9376.
- [53] D. M. Jacobs, M. D. Zeidler, *J. Phys. Chem. A.* **1997**, *101*, 5241-5249.

Chapter 4: Dynamics in flexible pillar[n]arenes probed by solid-state NMR

4.1 Overview

Chapter 4 is work which has expanded from a publication¹ entitled “Near-Ideal Xylene Selectivity in Adaptive Molecular Pillar[n]arene Crystals” by Kecheng Jie, Ming Liu, Yujuan Zhou, Marc A. Little, Angeles Pulido, Samantha Y. Chong, Andrew Stephenson, Ashlea R. Hughes, Fumiyasu Sakakibara, Tomoki Ogoshi, Frédéric Blanc, Graeme M. Day, Feihe Huang, and Andrew I. Cooper in which we used solid state NMR for structural analysis, confirming the asymmetric unit cell. Following this project we studied the dynamics and flexibility of these pillar[n]arenes in a paper which has recently been sent for publication entitled “Dynamics in flexible pillar[n]arenes probed by solid-state NMR” by Ashlea R. Hughes, Ming Liu, Subhradip Paul, Andrew I. Cooper and Frédéric Blanc which is the primary focus of this chapter.

The author contributions are as follows: F.B. designed the project. A.R.H. loaded the pillar[n]arenes with M.L. A.R.H. conducted the NMR experiments, with support from F.B. S.P. assisted with NMR data acquisition at 14.1 T. Density functional theory calculations were carried out by G.M.D. NMR data analysis and interpretation was undertaken by A.R.H. A.R.H. and F.B. wrote the manuscript with consultation from all other authors.

4.2 Abstract

Pillar[n]arenes are supramolecular assemblies that can perform a range of technologically important molecular separations that are enabled by their molecular flexibility. Here, we probe dynamical behaviour by performing a range of variable temperature solid-state NMR experiments on microcrystalline perethylated pillar[n]arene ($n = 5, 6$) and the corresponding pillar[6]arene xylene adducts in the 100 – 350 K range. This was achieved either by measuring site-selective motional averaged ^{13}C ^1H heteronuclear dipolar couplings and subsequently accessing order parameters, or by determining ^1H and ^{13}C spin-lattice relaxation times and extracting correlation times based on dipolar and/or chemical shift anisotropy relaxation mechanisms. We demonstrate fast motional regimes at room temperature and highlight a significant difference in dynamics between the core of the pillar[n]arenes, the protruding flexible ethoxy groups, and the adsorbed xylene guest. Additionally, unexpected and sizeable ^{13}C ^1H heteronuclear dipolar couplings for a quaternary carbon were observed for *para*-xylene adsorbed in pillar[6]arene only, indicating a strong host-guest interaction and establishing the *para*-xylene location inside the host, confirming structural refinements.

4.3 Introduction

Host-guest chemistry is an important concept in the field of supramolecular chemistry that is driven by the interactions of molecular assemblies or ions *via* non-covalent interactions.² These interactions play a vital role in the design of advanced functional materials with improved physical properties and potential applications in processes, such as adsorption, catalysis, energy storage and molecular separations. Consequently, this area has become of increasing importance over the past few decades^{3–6} and a wide range of supramolecular assemblies with a large variety of structural motifs has been discovered. There are multiple types of macrocycles reported to date, with the most prevalent being those that are structurally tuneable, and which therefore have adaptability to host different guests depending on their purpose.⁷

Over the last decade, pillar[n]arenes (n=5-15) have emerged as a novel class of easily functionalised supramolecular macrocycles with tuneable properties such as solubility, functionality and molecular flexibility.^{8–11} Their structure consists of a generic unit of substituted phenolic moieties repeated n- times and connected by methylene linkages in the *para* position to form the macrocycle (**Figure 4.1**). For most values of n (except n = 7), the resulting architecture is a symmetrical cylindrical structure from the side view (top row in **Figure 4.1**) and a symmetrical polygon from the top views (middle row in **Figure 4.1**) that yields a single pentagonal and hexagonal cavity for n = 5 and 6, respectively, and two pentagonal and/or hexagonal cavities for n > 7. The cavity plays an important role in hosting appropriately sized guest molecules with potential applications as guest capture, molecular separation^{12–17} and controlled delivery systems.^{18,19}

Pillar[5]arenes and pillar[6]arenes have found the greatest interest, mostly due to their relatively small cavity sizes that enable them to host small molecules,¹¹ combined with substituted alkyl and branched chains that strongly affect the host-guest properties.^{20–23} Perethylated pillar[5]arene (EtP5) and perethylated pillar[6]arene (EtP6) are examples of these substituted pillar[n]arenes; these molecules contain ethoxy groups and a one-dimensional (1D) channel pore network assembled from the five or six *para*-phenylene rings (**Figure 4.1(a)** and **(b)**),

respectively. Multiple phases of EtP6 have recently been discovered recently including crystalline **EtP6- β** and the metastable **EtP6- α** .¹ Due to its large conformational flexibility, EtP6 has been found to adsorb a number of guest molecules including styrene, ethylbenzene and xylene,^{1,15} and we have recently shown that **EtP6- β** adapts during adsorption of a xylene isomer mixture to efficiently capture *para*-xylene (**pX**) over *ortho*-xylene (**oX**) and *meta*-xylene (**mX**) with a high selectivity of 90% to form **pX@EtP6** (**Figure 4.1(c)**). This is a step forward for the energy efficient separation of the xylene isomers, which are widely used as chemical feedstocks.^{1,24}

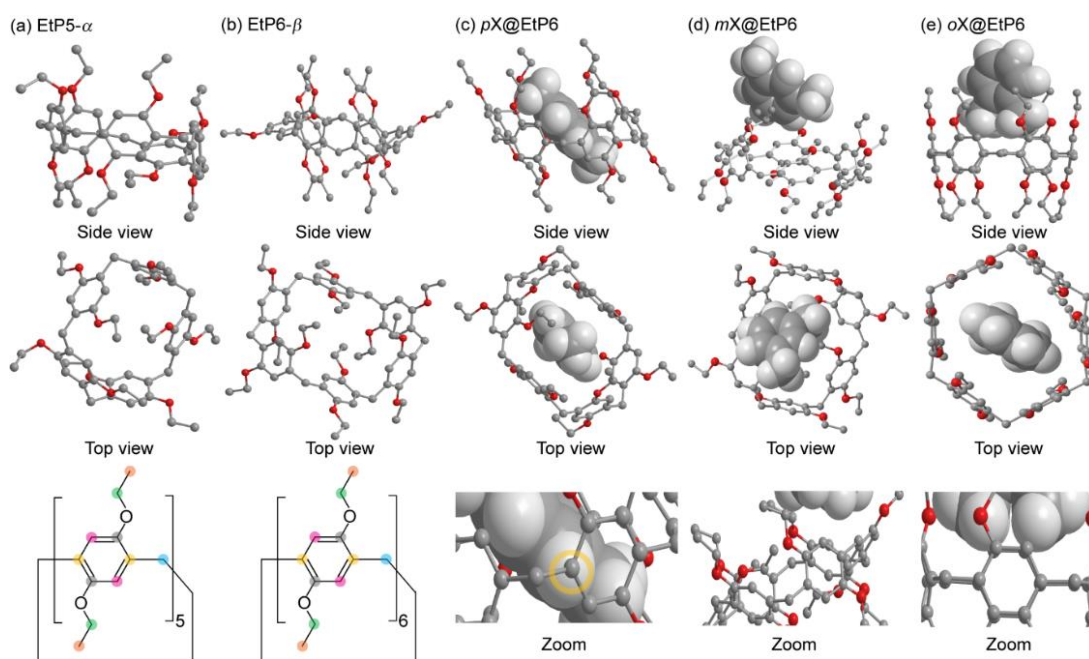


Figure 4.1. Crystal structures (a) perethylated pillar[5]arene, **EtP5- α** , (b) perethylated pillar[6]arene **EtP6- β** , (c) *para*-xylene in EtP6 (**pX@EtP6**), (d) *meta*-xylene in EtP6 (**mX@EtP6**), (e) *ortho*-xylene in EtP6 (**oX@EtP6**).¹ The side and top views are shown on the first and second rows. The pillar[n]arene host and xylene guests are denoted by ‘ball and stick’ and ‘space filling’ models, respectively, with carbons shown in grey, oxygens in red and protons omitted for clarity in the ball and stick model whilst shown in white in the space filling model. The two left panels of the third row provide the chemical structures of both **EtP5- α** and **EtP6- β** using consistent colour coding for different carbon environments (**CH**₃, orange; **CH**₂, light blue; **OCH**₂, green; **CH**, pink; **CH**₂**C**^{IV}, yellow and **OC**^{IV}, grey) throughout for NMR spectra assignments. The three right panels of the third row show a magnified view of the through space interaction between the xylene guest and EtP6 in **pX@EtP6** (yellow circle) while no interaction is observed for **mX@EtP6** and **oX@EtP6** (see text for details).

Solid-state Nuclear Magnetic Resonance (NMR), often in conjunction with computational methods such as crystal structure prediction (CSP), is playing an important role in increasing our understanding of the structure of supramolecular assemblies,^{25–30} complementing diffraction-based approaches. For example, we took advantage of the very high spectral resolution of the ¹³C NMR spectra of various guest-free pillar[n]arenes such as **EtP5- α** , **EtP6- α** and **EtP6- β** to support the conformational energy landscape exploration and identify the number of different carbons in the asymmetric unit cell.¹

One important criterion for these supramolecular structures is their adaptive behaviour and flexibility that dictates the adsorption of guest molecules in the cavity space. Understanding this flexibility and the associated dynamics are key factors to consider in the design of these pillar[n]arenes and a vital step in determining their potential applicability. Liquid state NMR has routinely been used to assess the flexibility of these materials by investigating conformational properties,^{31,32} often *via* variable temperature NMR measurements,^{33,34} to assess if rotation of the *para*-phenylene units is present, but little is known regarding the adaptive behaviour in the solid state. Thanks to a range of complementary approaches, solid-state NMR is well equipped to assess this behaviour *via* dynamics measurements performed on a very wide range of timescales from slow motion (Hz) with *e.g.* EXchange SpectroscopY (EXSY) to moderate motional rates (kHz) with residual dipolar couplings and fast motion (MHz) with relaxation measurements. By performing these measurements at various temperatures, we can access thermodynamic parameters. Recent ²H NMR work has focused on the molecular dynamics on *n*-hexane-d₁₄ in pillar[5]arene bearing different substituents that showed that the resulting varied molecular arrangement of the pillar[5]arene gave rise to a different pattern of guest uptake and release.³⁵

Here, we determine the dynamics of both guest-free **EtP5- α** and **EtP6- β** and xylene-adsorbed analogues of perethylated pillar[6]arenes over a wide time scale (kHz to MHz) by probing site selective ¹³C ¹H heteronuclear dipolar couplings from dipolar coupling spectra and accessing ¹H and ¹³C correlation times from spin lattice relaxation measurements as a function of temperature. We first utilise ¹³C isotropic

chemical shifts, spectral editing ^{13}C NMR experiments and spectral deconvolution to aid spectral assignments of the significantly different ^{13}C cross polarisation (CP) magic angle spinning (MAS) NMR spectra of the xylene-adsorbed pillar[n]arenes that arise from their various crystal structures. We find that the room temperature molecular dynamics of these systems in the kHz regime differ for each crystallographically different carbon subgroup. The flexibility of the protruding OCH_2 groups in the guest-free pillar[n]arenes is reduced when there are fewer phenolic moieties, or at temperatures below 298 K, as well as by adsorption of xylene isomers; by contrast, other carbon groups have largely similar dynamics over the temperature range studied (383 – 100 K). We identify intermolecular ^{13}C ^1H dipolar couplings at low temperatures in ***pX@EtP6***, that are absent on both ***oX@EtP6*** and ***mX@EtP6***, which provides evidence for the location of xylenes in the EtP6 architecture and highlight the host-guest interactions in ***pX@EtP6***. Finally, we exploit variable temperature spin lattice relaxation measurements to access dynamics in the MHz regime, which confirm the flexibility of the extruding ethoxy groups of these pillar[n]arenes as opposed to the carbon atoms located in the ring core.

4.4. Materials and Methods

4.4.1. Materials synthesis. Guest-free **EtP5- α** ³⁶ and **EtP6- β** ⁶ and xylene-adsorbed perethylated pillar[6]arenes¹ were synthesised using established literature procedures. Prior to adsorption, PXRD and NMR measurements, **EtP5- α** and **EtP6- β** were dried and heated under vacuum at a pressure of 10^{-3} mbar to 433 K for 2 hours to ensure no solvation and that the correct phases were obtained. **pX@EtP6** and **mX@EtP6** were synthesised using the xylene vapour adsorption method, whereas **oX@EtP6** was prepared *via* solvent evaporation.¹

4.4.2. Powder X-ray diffraction. Powder X-ray diffraction (PXRD) data were collected in transmission mode on samples held on thin Mylar film in aluminium well plates on a Panalytical X'Pert PRO MPD equipped with a high throughput screening XYZ stage, X-ray focusing mirror, and PIXcel detector, using Ni-filtered Cu K α radiation of wavelength 1.5406 Å. Data were measured over the range 5 - 50° over 30 min. All PXRD patterns (**Figure 4.2**) are consistent with those previously published in the literature.¹

4.4.3. Differential scanning calorimetry. Differential scanning calorimetry (DSC) was performed using a TA Instruments Discovery DSC with the following heat treatment: equilibrate to 298 K, then ramp to 303 K at 10 K per minute, then cooled back to 188 K and ramped again to 303 K (**Figure 4.20**).

4.4.4. NMR experiments. The ¹H and ¹³C solid-state NMR experiments at an external magnetic field $B_0 = 9.4$ T were performed on a Bruker Avance III HD NMR spectrometer equipped with a 4 mm HXY triple-resonance MAS probe in double-resonance mode tuned to Larmor frequencies of $\nu_0(^1\text{H}) = 400.13$ MHz for ¹H and $\nu_0(^{13}\text{C}) = 100.62$ MHz for $X = ^{13}\text{C}$. The $B_0 = 14.1$ T NMR experiments were performed on a 14.1 T Avance III DNP NMR spectrometer equipped with a low temperature 3.2 mm HXY triple-resonance MAS probe in double-resonance mode³⁷ tuned to $\nu_0(^1\text{H}) = 600.25$ MHz on ¹H and $\nu_0(^{13}\text{C}) = 150.93$ MHz for $X = ^{13}\text{C}$. All experiments were obtained under MAS with the sample spinning at $\nu_r = 12.5$ kHz. ¹H pulses and SPINAL-64 heteronuclear decoupling³⁸ during ¹³C acquisition performed at a radio-frequency (RF) field amplitude of 83 kHz for all samples except the room temperature CP

experiments on the guest-free samples where it was performed at 96 kHz. ^{13}C pulses were performed at a RF field of 60 and 70 kHz at 9.4 and 14.1 T, respectively. Rotor synchronised echo and z-filter delays of the INADEQUATE spectra obtained at 9.4 T were experimentally optimised for best efficiency and found to be 3.2 ms and 0.8 ms respectively. INADEQUATE spectra were obtained with 78 t_1 increments and 2048 scans. For all data obtained at 14.1 T, a presaturation block consisting of 100 ^1H pulses separated by 1 ms was used prior to the standard pulse sequences described in **Chapter 1** of the thesis. For variable temperature experiments, zirconia drive caps were used at 9.4 T and Vespel caps at 14.1 T.

In the variable temperature CP experiments the CP steps were performed with a ^{13}C RF field of 41 kHz (at 9.4 T) and 70 kHz (at 14.1 T) while the ^1H RF field amplitude was ramped to obtain maximum signal at approximately 65 kHz (at 9.4 T) and between 70 - 96 kHz (at 14.1 T), dependent on samples and temperatures. An optimised contact time of 1.5 - 3.0 ms was used. Typically, ^{13}C CP experiments were accumulated with 2048 scans (at 9.4 T) and 32 - 2048 scans (at 14.1 T) dependent on samples and temperatures, and used recycle delays of $1.3 \times ^1\text{H } T_1^{39}$ (with T_1 the spin lattice relaxation times measured as given below) that corresponds to the maximum signal to noise per unit time. Note that although ^{13}C CP MAS experiments are not quantitative, only ^{13}C integration within a chemically distinct carbon environment is given as its similar nature and mobility in these systems allows comparison of the number of carbons to be appropriately estimated.

Variable temperature ^1H and ^{13}C spin lattice relaxation times T_1 s were obtained with the saturation recovery and T_1 Torchia⁴⁰ pulse programs respectively. In the saturation recovery experiment, the magnetisation is saturated by a presaturation block consisting of 100 ^1H pulses separated by 10 ms at 9.4 T or 1 ms at 14.1 T, followed by magnetisation build-up during a variable τ delay and NMR detection. In the T_1 Torchia sequence,⁴⁰ an initial ^{13}C CP step creates ^{13}C magnetisation which then decays during a variable delay τ and ^{13}C detection is achieved using a two-step phase cycle to account for the direct (unenhanced) ^{13}C Boltzmann value rather than CP enhanced values. The data obtained *via* integrated intensities were fitted to stretch exponential functions of the form of:

$$1-\exp[-(\tau/T_1)^\alpha] \quad \text{and} \quad \exp[-((\tau/T_1)^\beta)]$$

for the ^1H and ^{13}C T_1 data, respectively, where τ is the variable delay time and α (between 0.75 and 0.96) and β (between 0.60 and 0.88) are the respective stretch exponential factors. Stretch exponentials were used due to the data showing a small amount of non-exponential magnetisation recovery. Errors associated from the T_1 values are quoted to a 95% confidence level and are smaller than the symbol sizes in all figures.

Variable temperature 2D Proton Detected Local Field (PDLF) spectra correlating ^{13}C NMR spectra in the direct frequency dimension ω_2 with ^{13}C ^1H dipolar coupling spectra in the indirect ω_1 dimension were obtained using the windowed⁴¹ sequence (wPDLF).⁴² The sequence starts with the reintroduction of the heteronuclear ^{13}C ^1H dipolar coupling under MAS during the rotor synchronised evolution period t_1 using the symmetry-based $\text{R}18_2^5$ ^1H recoupling block⁴³ which was optimised for maximum signal around the ^1H RF field amplitude of approximately $9 \times \nu_r$ (112.5 kHz). $\text{R}18_2^5$ also removes the homonuclear ^1H ^1H dipolar coupling⁴³ and the 180° phase shift in the recoupling block refocuses the (small) ^1H Chemical Shift Anisotropy (CSA) while the synchronised 180° ^{13}C pulse applied in the middle of t_1 prevents the same refocusing from occurring for the heteronuclear ^{13}C ^1H dipolar coupling and refocuses the ^{13}C chemical shift. The ^{13}C CSA is averaged out over 2 rotor periods. The ^{13}C magnetisation is therefore only modulated by the ^{13}C ^1H dipolar coupling in t_1 that yields ^{13}C ^1H dipolar coupling spectra in ω_1 . Polarisation transfer to ^{13}C is subsequently achieved using the rotor synchronised PRinciples of Echo Shifting using a Train of Observations (PRESTO)⁴⁴ pulse sequence optimised for maximum signal for the protonated resonances to a length of $\frac{16}{9} \times \tau_r$ (142 μs), where τ_r is the rotor period (80 μs), and by varying the recoupling length of the $\text{R}18_1^7$ ^1H recoupling block⁴³ (which is also optimised to a similar ^1H RF field of approximately $9 \times \nu_r$ (112.5 kHz)). PRESTO is preferred to CP for polarisation transfer as ^1H spin diffusion in the latter results in an increase of the signal intensity for the zero frequency signal.⁴² Following Fourier transformation in the F1 dimension, an effective dipolar coupling constant $\kappa_{\text{R}}d_{\text{CH}}$ (with κ_{R} the scaling factor of the wPDLF sequence and d_{CH} the dipolar coupling constant, see section 4.5.2 for the experimental determination of κ_{R}) is obtained in

the ω_1 frequency dimension.^{42,45,46} The (scaled) ^{13}C ^1H dipolar coupling spectra are then extracted at each ^{13}C isotropic resonance and the dipolar coupling values are obtained from the distance between the outer singularities to yield site-specific motional averaged dipolar coupling $\langle d_{\text{CH}} \rangle$ values. The estimated errors associated with these values are obtained from the small variations across the carbon environment (an example of which is given in **Figure 4.24** for the CH_3 resonance of **EtP6- β**).

Static dipolar coupling constants d_{CH} were calculated from **equation 4.2** and carbon proton bond lengths. These were obtained from computed CSP¹ data for the **EtP5- α** and **EtP6- β** conformers or experimental low temperature high resolution powder neutron diffraction data from *ortho*-xylenes⁴⁷ and *meta*-, *para*-xylenes⁴⁸ crystal structures for the xylene isomers.

Temperature calibrations were performed prior to NMR data acquisition using either the ^{207}Pb chemical shift thermometer of $\text{Pb}(\text{NO}_3)_2$ ^{49,50} or the ^{79}Br $T_{1\rho}$ ⁵¹ of KBr, extracted from polarisation build-up curves using the saturation recovery pulse sequence according to procedures outlined in the literature. All temperatures reported are actual sample temperatures and have an estimated accuracy of ± 10 K. NMR data were processed with TopSpin and MATLAB R2019a.⁵² ^1H and ^{13}C spectra were referenced to H_2O at 4.8 ppm and the CH of adamantane at 29.45 ppm,⁵³ respectively, both corresponding to TMS at 0 ppm. Small deviations in the observed isotropic chemical shifts (± 0.7 ppm in ^{13}C CP MAS NMR spectra) is likely attributed to small changes in shim coil temperatures during variable temperature experiments.

4.4.5. Solid state NMR calculations

The structure of **EtP6- β** was optimized at the DFT-D level with lattice vectors fixed at their experimental values and the shielding tensor was calculated at the DFT-D optimized geometry. Periodic DFT-D calculations, geometry optimizations and NMR simulations, were carried out with CASTEP program,⁵⁴ v17.21, using the functional PBE generalized gradient approximation,⁵⁵ with dispersion interactions included *via* Grimme's D2 scheme,⁵⁶ plane wave basis sets, on-the-fly generated ultra-soft pseudo-potentials and a Monkhorst-Pack grid of k-points corresponding to a

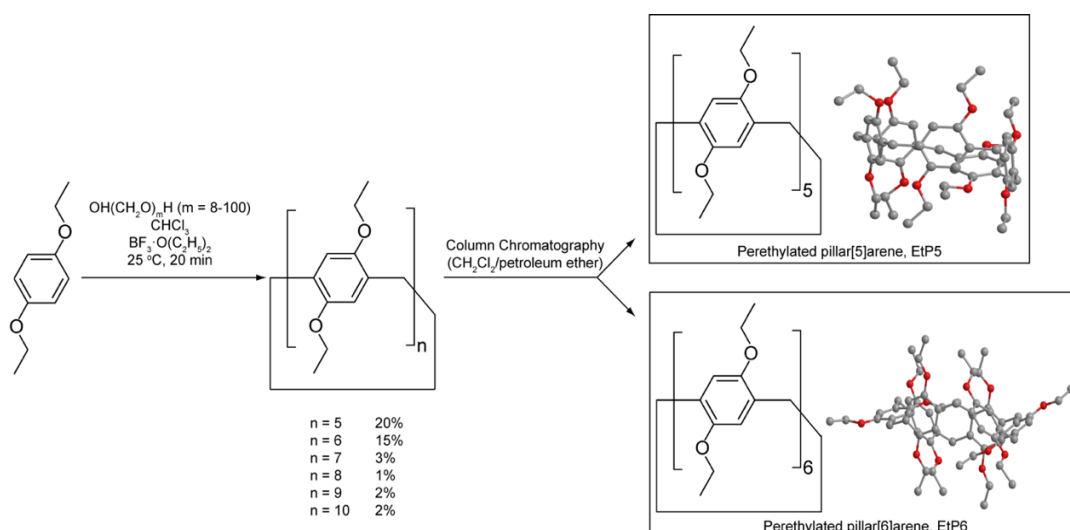
maximum spacing of 0.05 \AA^{-1} .⁵⁷ A plane-wave maximum energy cut off of 500 eV was employed during geometry optimization and was increased to 850 eV for chemical shielding calculations. The isotropic and symmetric parts of the chemical shift tensor were described by the isotropic chemical shift, δ_{iso} , span and Ω parameters. Theoretical NMR interaction tensors were derived from periodic calculations using the GIPAW method^{57–59} as implemented in CASTEP. Calculated ^{13}C isotropic chemical shifts δ were calculated from the chemical shielding values σ using the scaling parameters derived below in **equation 4.1**.⁵⁴

$$\delta = -0.9902\sigma + 169.19 \quad \text{(4.1)}$$

4.5. Results and discussion

4.5.1. NMR structural analysis

EtP5 and **EtP6** were synthesised by reaction of 1,4-diethoxybenzene with paraformaldehyde in the presence of boron trifluoride diethyl etherate followed by separation from the other pillar[n]arenes, EtP_n, by column chromatography (**Scheme 4.1**).³⁶ **EtP5- α** was obtained by recrystallisation from tetrahydrofuran followed by a drying step while **EtP6- β** was prepared by heating to 333 K for 1 hour. Subsequently, both **pX@EtP6** and **mX@EtP6** were prepared using the solid-vapour diffusion method and **oX@EtP6** *via* solvent evaporation as recently published.¹ The PXRD patterns of all materials are given in **Figure 4.2** and agree with the reported ones.¹



Scheme 4.1. Synthesis of perethylated pillar[n]arenes from 1,4-diethoxybenzene and paraformaldehyde.³⁶ The perethylated pillar[n]arenes were purified by column chromatograph to separate EtP5 and EtP6. The crystal structures of the pillar[n]arenes (5 and 6) are denoted by ‘ball and stick’ models, with carbons shown in grey, oxygens in red and protons omitted for clarity. Resulting yields obtained *via* this synthesis method are also given.³⁶

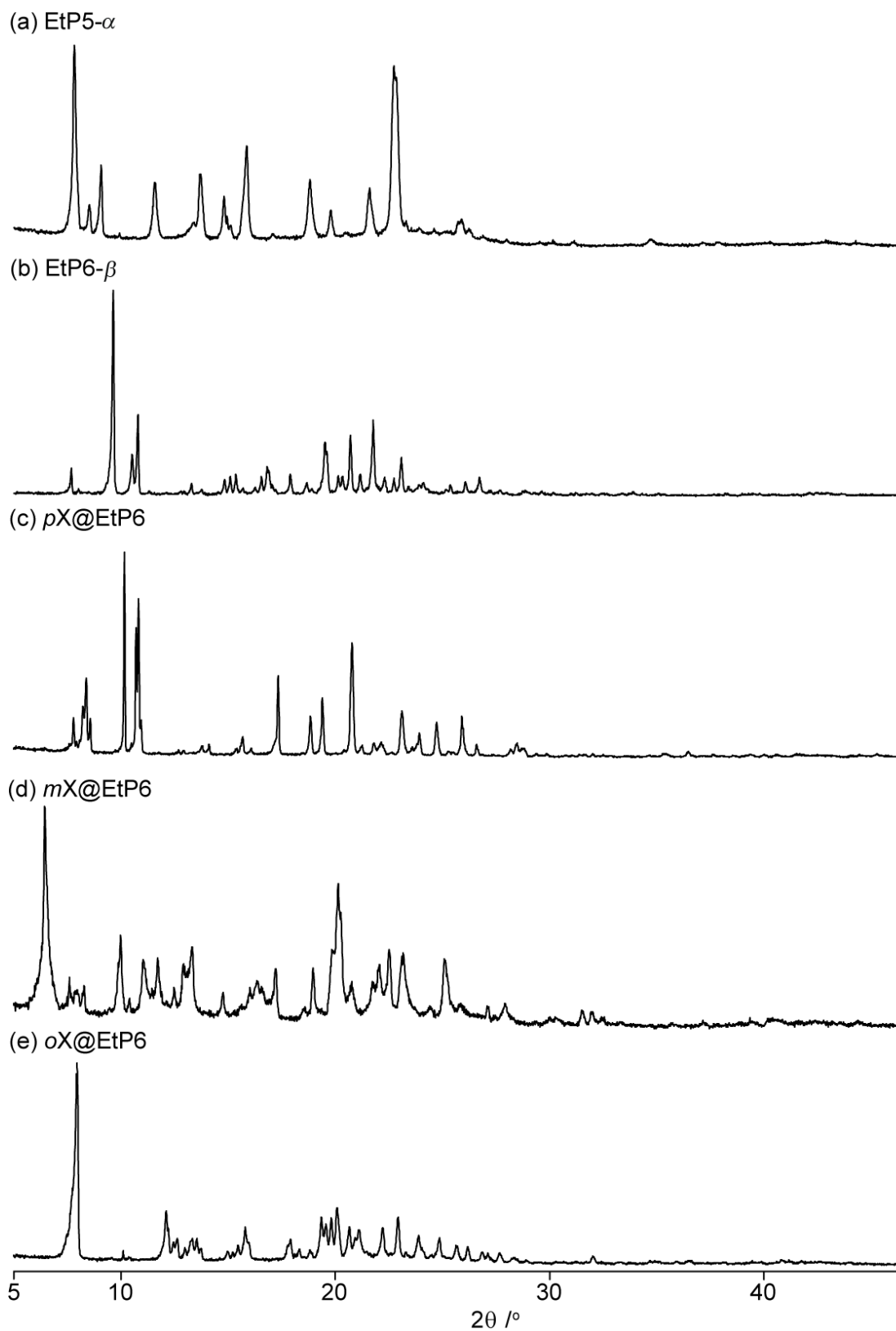


Figure 4.2. Powder XRD patterns of (a) EtP5- α , (b) EtP6- β , (c) *pX*@EtP6, (d) *mX*@EtP6 and (e) *oX*@EtP6.

The ^{13}C cross polarization (CP) magic angle spinning (MAS) NMR spectra of the three guest free pillararenes (**EtP5- α** , **EtP6- α** and **EtP6- β**) are shown in **Figure 4.3** and provide structural information regarding the asymmetric unit. **EtP6- β** shows a range of narrow and well resolved resonances that could be assembled into the six different chemical sub-groups for **EtP6**, corresponding to the chemically-distinct carbons environments; for example, the quaternary carbon atoms bonded to oxygens in OC^{IV} appear in the 149 - 155 ppm region.

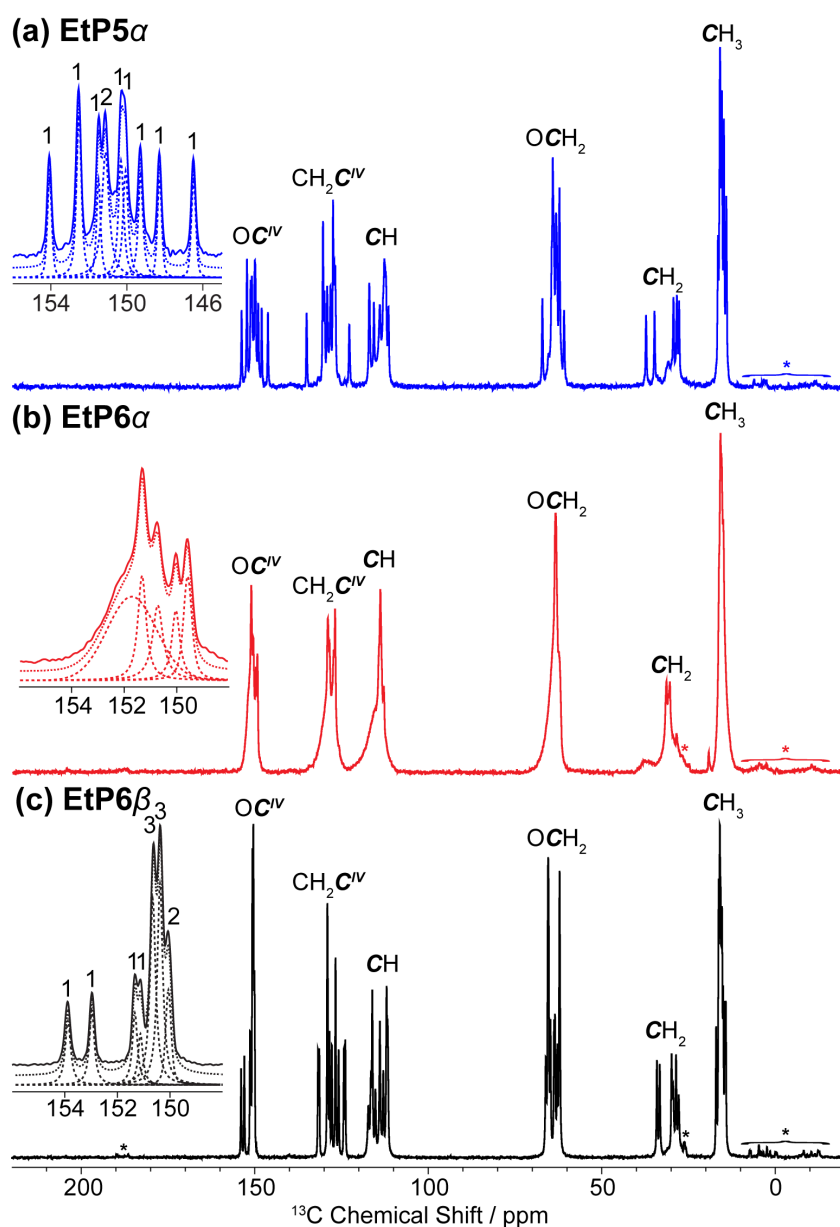


Figure 4.3 ^{13}C CP MAS NMR spectra of (a) **EtP5- α** (b) **EtP6- α** and (c) **EtP6- β** . Asterisks (*) denote spinning sidebands. The expansion shows the experimental spectrum (full line), total fit (dotted line) and spectral deconvolution (dashed lines) of the OC^{IV} carbons. Integrations obtained by deconvolution are given in respective expansion.

The assignment given is based on ^{13}C -editing NMR experiments and known ^{13}C chemical shift values from the literature.⁶⁰ With remarkable sharp lines acquired at natural abundance, the carbon connectivities obtained from the two-dimensional ^{13}C through-bond INADEQUATE⁶¹ correlation spectrum (**Figure 4.4(a)**) further confirmed the assignment.

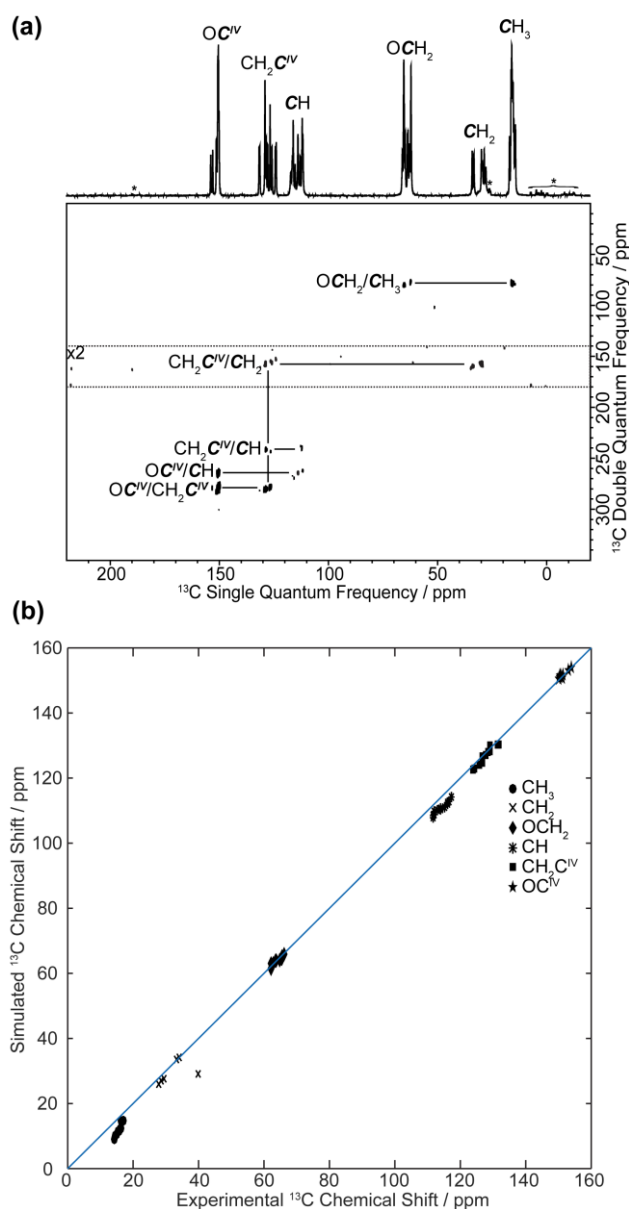


Figure 4.4. (a) 2D z-filter refocused INADEQUATE⁶¹ spectrum of natural abundance **EtP6-β**, showing a limited number of linkages between the carbon signals. Top is the 1D ^{13}C CP MAS NMR spectrum. Spectral assignments are based on known ^{13}C chemical shifts⁶⁰ and calculations. The asterisks (*) denote spinning sidebands. (b) Plot of simulated and experimental ^{13}C NMR chemical shifts for **EtP6-β**. Each chemically distinct carbon environments are given with a different marker as indicated in the figure itself. The root-mean-square error for all of the ^{13}C shifts was found to be 1.9 ppm.

The insert in **Figure 4.3(c)** (and the full spectral deconvolution in **Figure 4.5**) shows that each environment consists of multiple ^{13}C peaks whose integrations match well with the expected number of non-equivalent carbon atoms in the asymmetric units, as determined by X-ray diffraction (**Figure 4.2**). For example, seven OC^{IV} resonances are resolved integrating 1:1:1:1:3:3:2 (from high to low frequency) and matching the expected twelve OC^{IV} carbons in of **EtP6- β** . Calculations of the ^{13}C chemical shifts of **EtP6- β** was also carried out, which was used to compare with the experimental chemical shifts (as shown in **Figure 4.4(b)**). The comparison shows to be in excellent agreement with the experimental chemical shifts (**Table 4.1**), further validating the spectral assignments. It also provides proof of the good match between the experimentally obtained crystal structures and the calculated conformers.¹

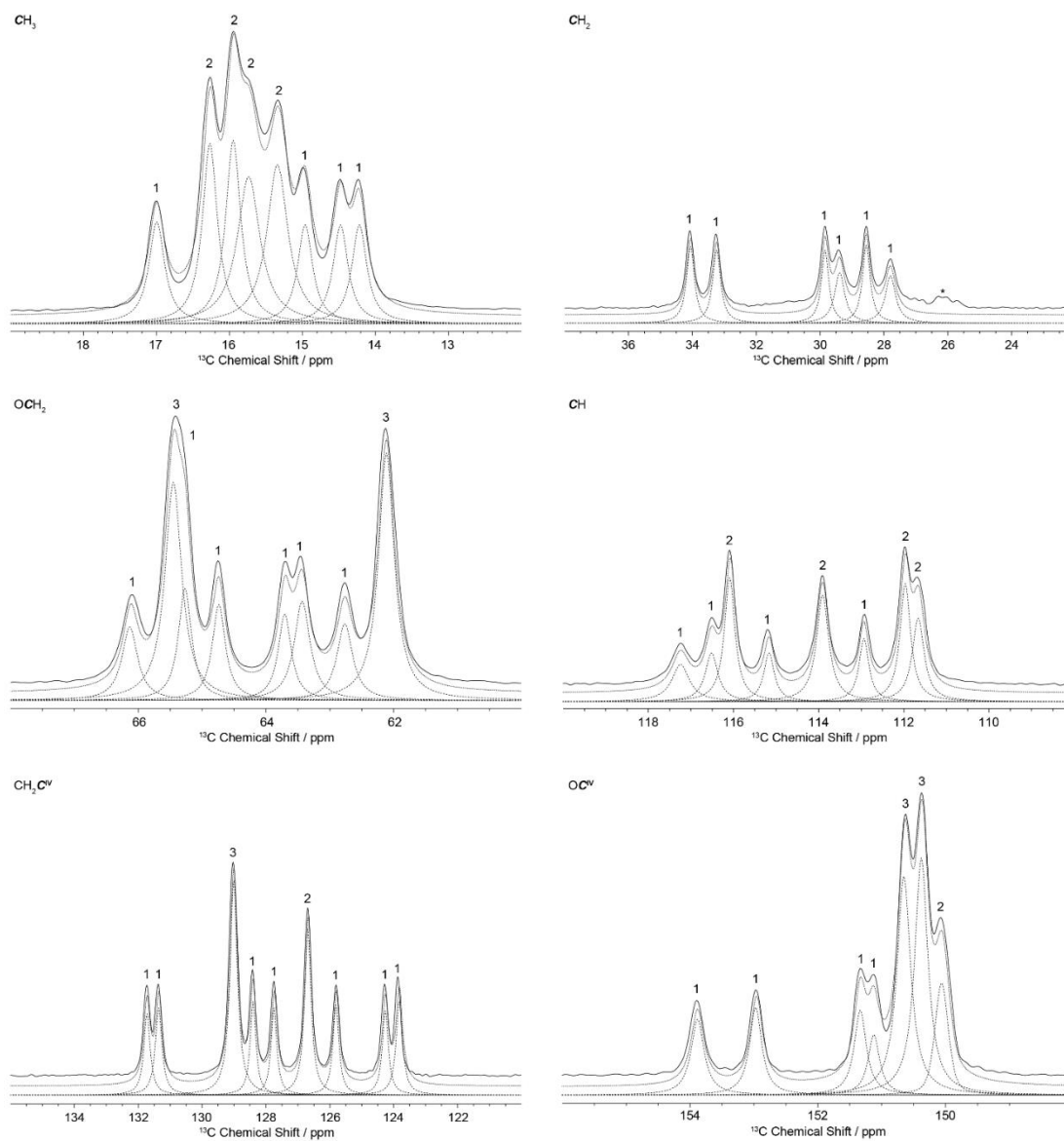


Figure 4.5. Experimental ^{13}C CP MAS NMR spectrum of EtP6- β (full line) with the total fit and spectrum deconvolutions shown with dotted and dashed lines, respectively. Each panel shows chemically distinct carbon environments. Whilst the ^{13}C CP spectrum is not quantitative, the similar nature of each carbon environments allows for the peaks ratio (given above each signal with error around ± 0.3) to be estimated. Asterisks (*) denote spinning sidebands.

Table 4.1. ^{13}C NMR assignments for **EtP6- β** (**Figure 4.3(c)**) with isotropic chemical shifts δ_{iso} from deconvoluted data previously published,¹ spin lattice relaxation times T_1 obtained *via* area integration, motional averaged dipolar coupling constants $\langle d_{\text{CH}} \rangle$ and order parameters $\langle S_{\text{CH}} \rangle$. Data obtained at room temperature and 9.4 T.

Assignment	^{13}C δ_{iso} /ppm	T_1 /s	$\langle d_{\text{CH}} \rangle$ /kHz	$\langle S_{\text{CH}} \rangle$
CH₃	14.25	2.4 ± 0.1	-7.2 ± 0.5	0.31 ± 0.03
	14.52			
	15.00			
	15.36			
	15.75			
	15.99			
	16.30			
	17.03			
CH₂	27.83	181.9 ± 33.5	-22.4 ± 0.8	0.97 ± 0.03
	28.58			
	29.43			
	29.88			
	33.27			
	34.09			
OCH₂	62.15	24.8 ± 2.2	-18.1 ± 0.7	0.78 ± 0.03
	62.80			
	63.47			
	63.75			
	64.78			
	65.30			
	65.48			
	66.15			
CH	111.68	261.6 ± 27.1	-23.9 ± 0.8	1.03 ± 0.03
	112.01			
	112.98			
	113.95			
	115.20			
	116.11			
	116.55			
	117.28			
CH₂C^{IV}	123.86	236.4 ± 26.4	N/A ^a	N/A
	124.30			
	125.83			
	126.72			
	127.77			
	128.45			
	129.05			
	131.38			
	131.76			
OC^{IV}	150.08	227.4 ± 13.9	N/A	N/A
	151.13			
	150.40			
	150.67			
	151.38			
	153.00			
	153.92			

^a Not Applicable.

Similarly, the highly resolved ^{13}C CP MAS NMR spectrum of **EtP5- α** allows each carbon environment to be observed and quantified; there is a good agreement between the deconvoluted spectra and the expected number of non-equivalent carbon atoms in **EtP5- α** . (e.g. ten OC^{IV} carbons, **Figure 4.3(a)** and **4.6**).

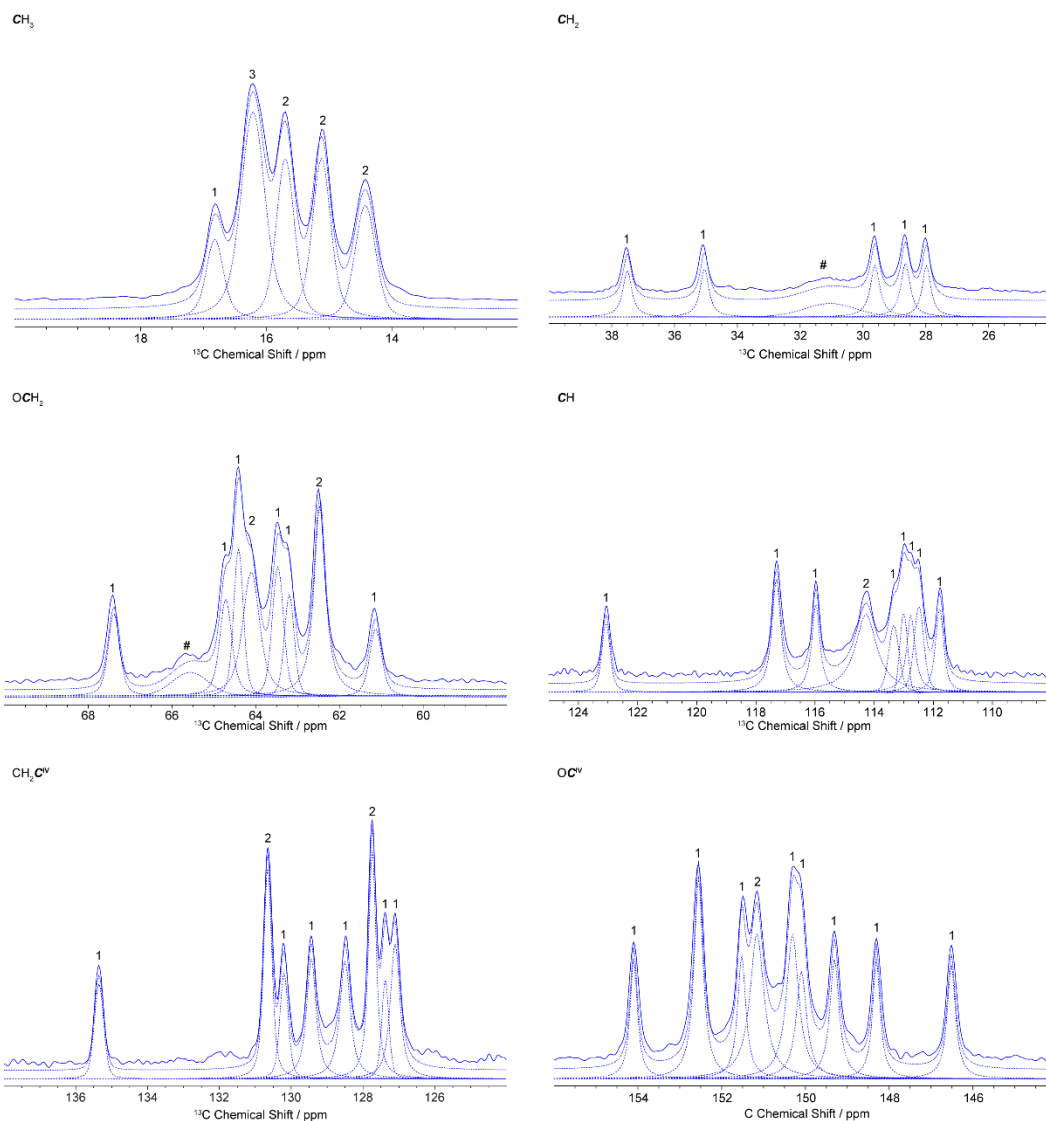


Figure 4.6. Experimental ^{13}C CP MAS NMR spectrum of **EtP5- α** (full line) with the total fit and spectrum deconvolutions shown with dotted and dashed lines, respectively. Each panel shows chemically distinct carbon environments. Whilst the ^{13}C CP spectrum is not quantitative, the similar nature of each carbon environments allows for the peak ratio (given above each signal with error around ± 0.3) to be estimated. ^{13}C CP NMR measured at short contact times enabled the identification of protonated carbons. Asterisks (*) denote spinning sidebands and hashes (#) denote impurities.

Table 4.2. ^{13}C NMR assignments for **EtP5- α** (Figure 4.3(a)) with isotropic chemical shifts δ_{iso} from deconvoluted data previously published,¹ spin lattice relaxation times T_1 obtained, motional averaged dipolar coupling constants $\langle d_{\text{CH}} \rangle$ and order parameters $\langle S_{\text{CH}} \rangle$. Data obtained at room temperature and 9.4 T.

Assignment	^{13}C δ_{iso} /ppm	T_1 /s	$\langle d_{\text{CH}} \rangle$ /kHz	$\langle S_{\text{CH}} \rangle$
CH₃	14.42	1.7 ± 0.1	-7.2 ± 0.5	0.31 ± 0.03
	15.13			
	15.71			
	16.22			
	16.83			
CH₂	28.01	165.8 ± 48.4	-23.3 ± 0.8	1.01 ± 0.03
	28.67			
	29.63			
	35.07			
	37.53			
OCH₂	61.16	44.5 ± 5.0	-18.4 ± 0.7	0.79 ± 0.03
	62.50			
	63.22			
	64.15			
	64.45			
	64.73			
CH	67.42	246.2 ± 27.0	-23.8 ± 0.8	1.03 ± 0.03
	111.78			
	112.49			
	112.76			
	113.00			
	113.35			
	114.29			
	115.97			
	117.32			
123.06				
CH₂C^{IV}	127.12	262.0 ± 56.0	N/A ^a	N/A
	127.39			
	127.75			
	128.49			
	129.44			
	130.22			
	130.65			
	135.36			
OC^{IV}	146.51	217.2 ± 32.8	N/A	N/A
	148.30			
	149.33			
	150.12			
	150.31			
	151.16			
	151.53			
	152.56			
	154.12			

^a Not Applicable.

However, by comparison, the resolution of the **EtP6- α** spectrum is much poorer with broader peaks observed (**Figure 4.3(b)** and **4.7**). This indicates that unlike **EtP6- β** and **EtP5- α** , **EtP6- α** is not phase pure which we attribute to the existence of multiple **EtP6** conformers in the metastable **EtP6- α** activated material and highlights the importance of correlating X-ray diffraction studies with solid state NMR measurements. Due to the less stable nature of this phase, it will not be studied further here.

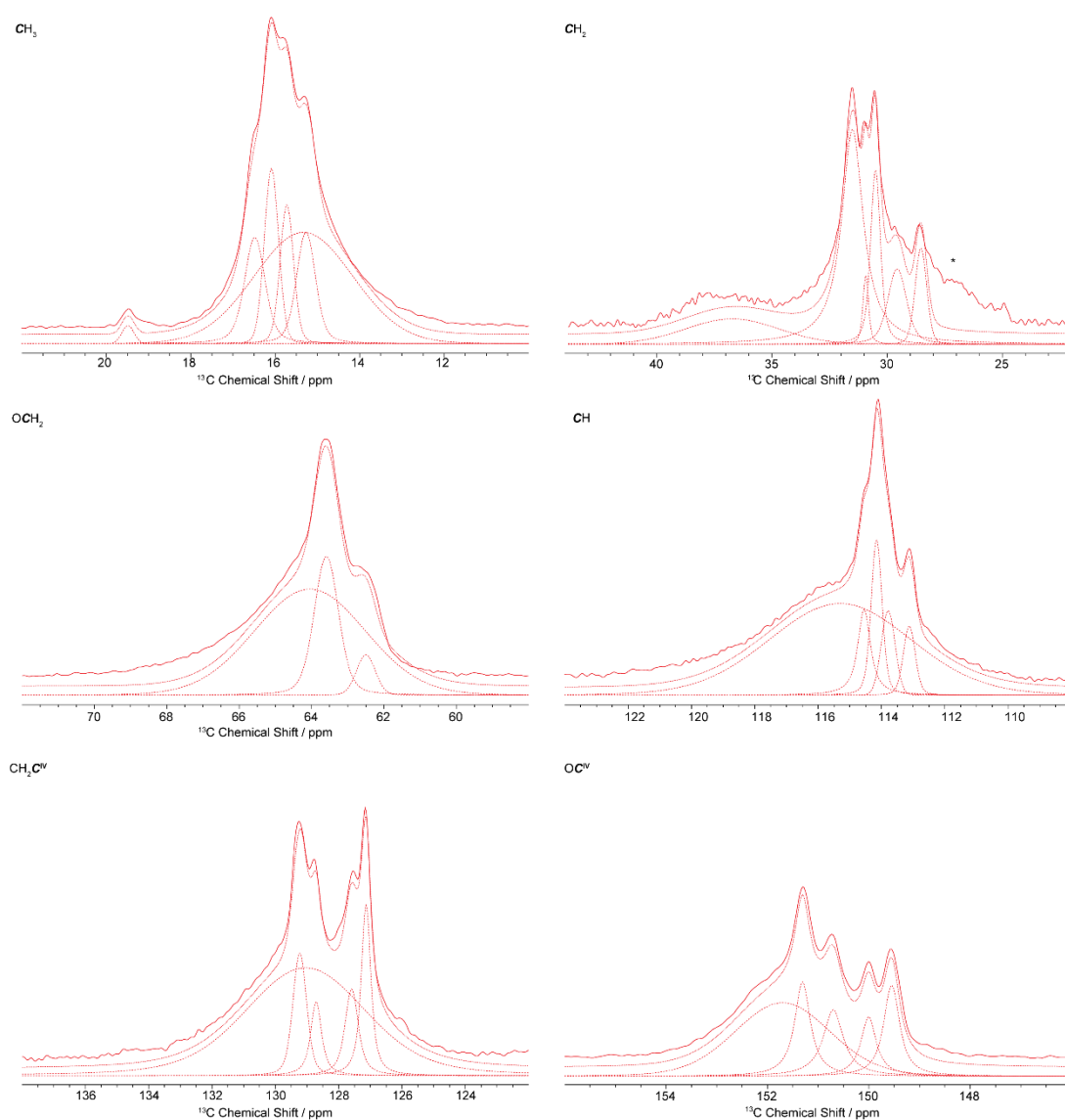


Figure 4.7. Experimental ^{13}C CP MAS NMR spectrum of **EtP6- α** (full line) with the total fit and spectrum deconvolutions shown with dotted and dashed lines, respectively. Each panel shows chemically distinct carbons environments. Asterisks (*) denote spinning sidebands.

The ^{13}C CP MAS NMR spectra of guest-free **EtP5- α** and **EtP6- β** collected under MAS at 12.5 kHz and at a magnetic field of 9.4 T are shown in **Figure 4.3(b)** and **(c)** as well as **Figure 4.8(a)** and **(b)**¹ and are extremely well resolved with full width at half maximum lines typically around 30 Hz (or 0.3 ppm at 9.4 T), in agreement with the excellent crystallinity of these samples. Each different chemical subgroup is assigned straightforwardly and the remarkable resolution obtained enables the observation of all non-equivalent magnetically distinct carbon atoms in the asymmetric unit cells, as previously discussed.¹ The ^{13}C CP MAS NMR spectra of all xylene-adsorbed EtP6 molecules are given in **Figures 4.8(c-e)** and are all different from **EtP6- β** and from each other, as previously identified by CSP of the molecular conformational space. Therefore, the spectral identification of the corresponding resonances of the xylenes (red daggers in **Figures 4.8(c-e)**) is not straightforward and is obtained based on comparisons with well-established chemical shift values,⁶²⁻⁶⁴ ^{13}C -edited NMR experiments (**Figures 4.9, 4.11** and **4.13**) employing CP steps of various contact times, the existence of CH dipolar coupling (see PDLF data below, **Figure 4.29**) and spectral deconvolution (**Figures 4.10, 4.12** and **4.14**).

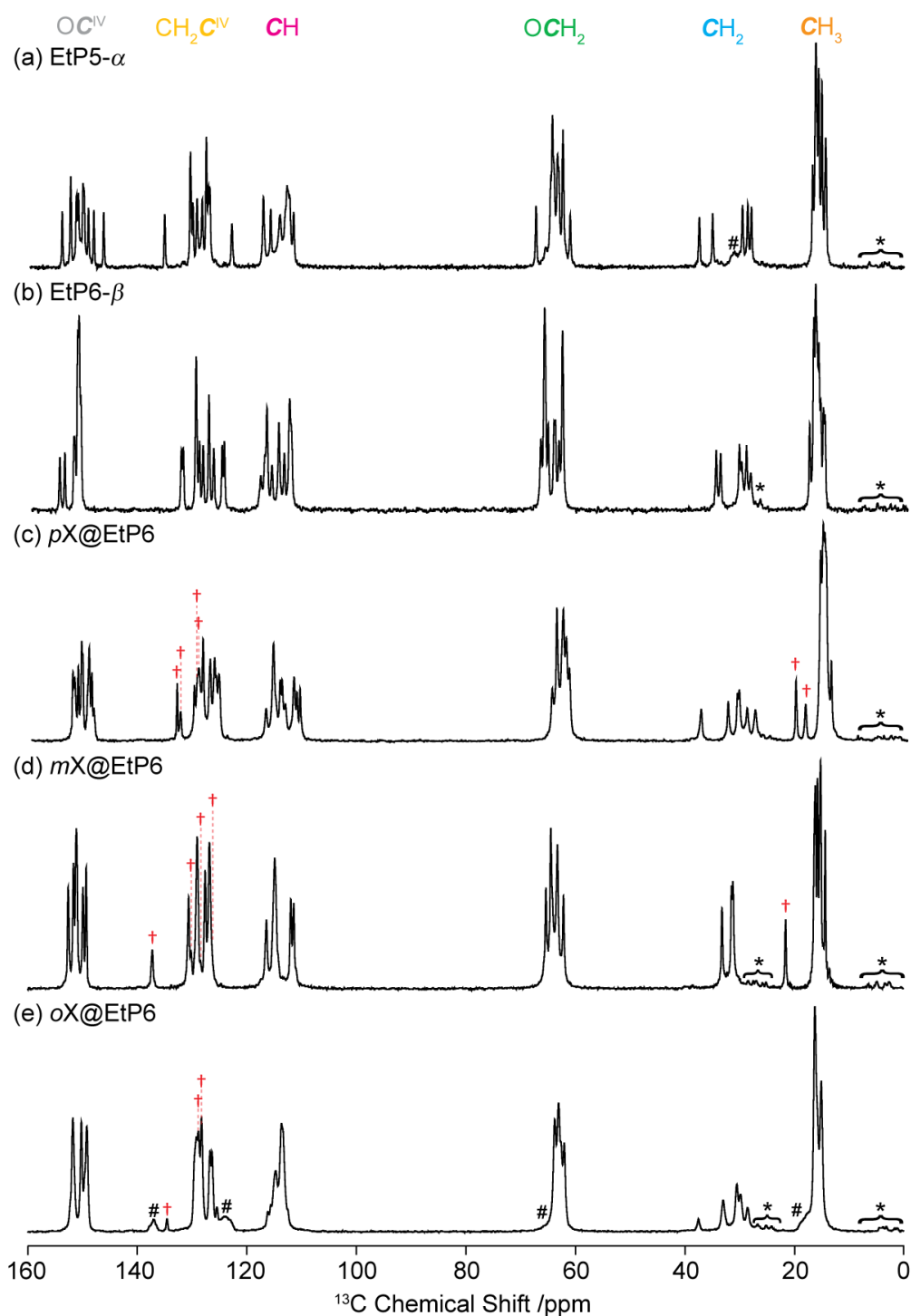


Figure 4.8. ¹³C CP MAS NMR spectra of (a) EtP5- α , (b) EtP6- β , (c) *pX*@EtP6, (d) *mX*@EtP6 and (e) *oX*@EtP6 obtained at a magnetic field of 9.4 T. The spectra for EtP5- α and EtP6- β are identical to those previously published.¹ Spectral assignments are given in the figure (see Figure 4.1) and are obtained from known isotropic chemical shifts,¹³C-edited CP experiments (Figures 4.9, 4.11 and 4.13), spectral deconvolution (Figures 4.10, 4.12 and 4.14) and 2D PDLF data (see below). The red daggers (†) denote signals arising from the xylene guests. The CH₃ originating from the *ortho*-xylene guest in (e) is unidentifiable due to spectral broadening and overlapping resonances with the CH₃ signals of the EtP6 host. Asterisks (*) and hashes (#) denote spinning sidebands and amorphous impurities, respectively.

More specifically, in ***pX@EtP6***, each group of resonances that are attributed to the different carbon subgroups in the EtP6 host (e.g., **CH₂** at 27 - 38 ppm or **OC^{IV}** at 148 - 154 ppm) consist of multiple peaks which number and integration (when the peaks are partially resolved) are in agreement with the expected number of carbons in asymmetric unit cell (e.g., 6 for **CH₂**, 12 for **OC^{IV}** etc.),¹ while the *para*-xylene resonances can be mostly assigned based on their isotropic chemical shifts. There are spectral overlaps in the 124 - 136 ppm region between the quaternary **CH₂C^{IV}** resonances of EtP6 host and the protonated **CHs** of *para*-xylene and the spectral assignment was performed by comparing the ¹³C-edited CP MAS spectra obtained with a very short contact time of 50 μs that predominantly enhance protonated carbons vs. longer contact times that enhance all ¹³C signals (**Figure 4.9**). Two distinguishable **CH₃s**, **CHs** and quaternary carbons resonances are therefore observed for *para*-xylene in ***pX@EtP6*** which is in agreement with the asymmetric unit cell of this phase that contains two xylene molecules, enabling a full spectral assignment of ***pX@EtP6*** (**Figure 4.8(c)** and **Table 4.3**).

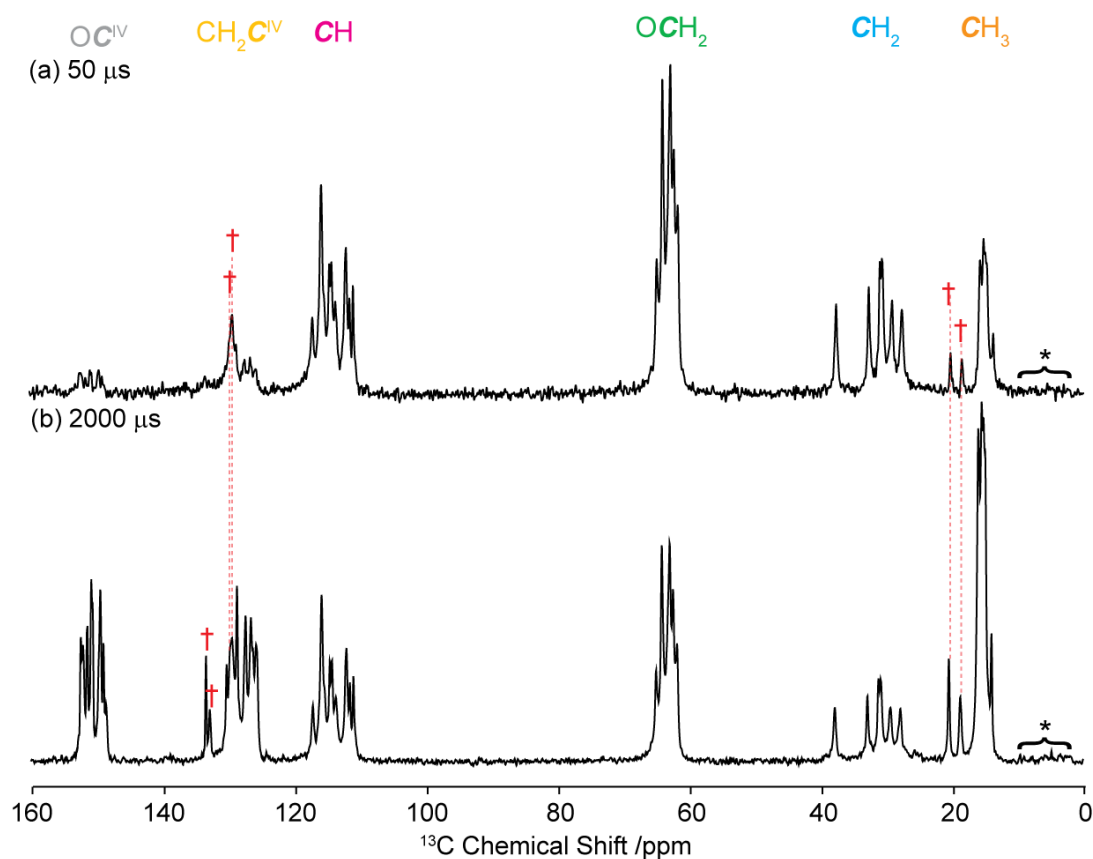


Figure 4.9. ^{13}C edited experiments of $p\text{X@EtP6}$ obtained by comparing the ^{13}C CP MAS NMR spectra acquired with contact times of (a) $50\ \mu\text{s}$ and (b) $2000\ \mu\text{s}$. Data were obtained at a magnetic field of 9.4 T. Spectral assignments are given in the figure (see **Figure 4.1**). The red daggers (†) (also shown in red in the spectral deconvolution in **Figure 4.10**) denote signals arising from the *para*-xylene guest. The CH resonances of *para*-xylene are apparent in the spectrum obtained at a short contact time of $50\ \mu\text{s}$ where the signal intensities of the quaternary carbons are largely reduced. Spinning sidebands are marked with asterisks (*).

Table 4.3. ^{13}C NMR assignments for *pX@EtP6* (Figure 4.8(c)) with isotropic chemical shifts δ_{iso} from spectral deconvolution in Figure 4.10, spin lattice relaxation times T_1 obtained *via* area integration, motional averaged dipolar coupling constants $\langle d_{\text{CH}} \rangle$ and order parameters $\langle S_{\text{CH}} \rangle$. Data obtained at room temperature and 9.4 T. Red daggers (†) denote signals arising from *para*-xylene guest.

Assignment	^{13}C δ_{iso} /ppm	T_1 /s	$\langle d_{\text{CH}} \rangle$ /kHz	$\langle S_{\text{CH}} \rangle$
CH_3	14.0	15.9 ± 0.1	-6.9 ± 0.5	0.30 ± 0.03
	14.4			
	14.9			
	15.2			
	15.5			
	16.0			
	18.7 (†)			
	20.5 (†)			
CH_2	27.9	85.6 ± 31.7	-21.6 ± 0.8	0.94 ± 0.03
	29.4			
	30.8			
	31.2			
	32.8			
	37.8			
OCH_2	61.8	39.2 ± 2.8	-18.4 ± 0.7	0.81 ± 0.03
	62.4			
	62.9			
	63.3			
	63.9			
	64.1			
	64.8			
65.0				
CH	111.0	139.6 ± 9.9	-22.4 ± 0.8	0.94 ± 0.03
	111.5			
	112.1			
	113.6			
	114.2			
	114.6			
	115.4			
	115.8			
117.2				
$\text{CH}_2\text{C}^{\text{IV}}$	125.8	139.9 ± 15.2	N/A ^a	N/A
	126.3			
	126.6			
	127.4			
	127.6			
	128.7			
	129.4 (†)			
	129.8 (†)			
	130.3			
	132.8 (†)			
133.4 (†)				
OC^{IV}	148.6	127.3 ± 11.1	N/A	N/A
	149.0			
	149.5			
	149.7			
	150.6			
	150.9			
	151.5			
	152.1			
152.5				

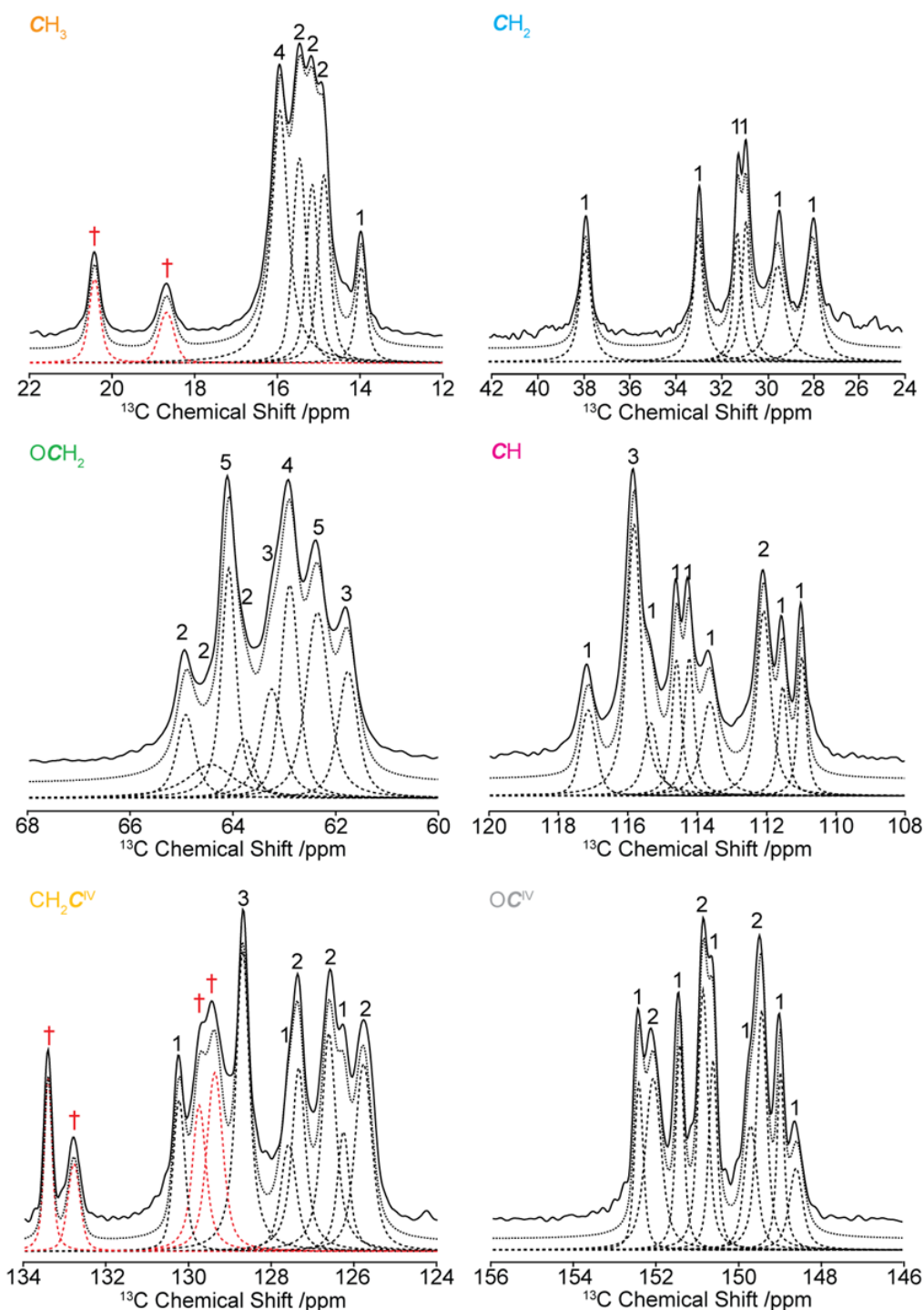


Figure 4.10. Experimental ^{13}C CP MAS NMR spectrum of $p\text{X}@EtP6$ (full line) with the total fit and spectrum deconvolutions shown with dotted and dashed lines, respectively. Integration values for each carbon subgroup are given. Data obtained at 298 K and 9.4 T. Each panel shows chemically distinct carbons environments of the EtP6 host. Spectral assignments are given in the figure (see **Figure 4.1**) and are obtained from known isotropic chemical shifts, ^{13}C -edited experiments and 2D PDLF data (see manuscript). Note that the low resolution of some of the resonances results in uncertainty in the estimated integration. Red daggers (†) denote signals arising from the *para*-xylene guest.

Likewise, all ^{13}C NMR resonances in ***mX@EtP6*** are assigned (**Table 4.4**) using ^{13}C -edited experiments (**Figure 4.11**) and spectral deconvolution (**Figure 4.12**) which reveal one *meta*-xylene molecule per host in the asymmetric unit cell. We point out that the ^{13}C resonances for *meta*-xylene in ***mX@EtP6*** and free *meta*-xylene (in solution)⁶² are very close (less than 1.6 ppm), which strongly supports a limited effect on the chemical shielding of *meta*-xylene from EtP6 resulting from its structural deformation and *meta*-xylene - EtP6 size exclusion (**Figure 4.1(d)**).

Table 4.4. ^{13}C NMR assignments for ***mX@EtP6*** (**Figure 4.8(d)**) with isotropic chemical shifts δ_{iso} from spectral deconvolution in **Figure 4.12**, spin lattice relaxation times T_1 obtained *via* area integration, motional averaged dipolar coupling constants $\langle d_{\text{CH}} \rangle$ and order parameters $\langle S_{\text{CH}} \rangle$. Data obtained at room temperature and 9.4 T. Red daggers (†) denote signals arising from *meta*-xylene guest.

Assignment	^{13}C δ_{iso} /ppm	T_1 /s	$\langle d_{\text{CH}} \rangle$ /kHz	$\langle S_{\text{CH}} \rangle$
CH₃	14.4	2.8 ± 0.1	-6.9 ± 0.5	0.30 ± 0.03
	15.2			
	15.3			
	15.8			
	16.2			
	16.4			
	21.6 (†)			
CH₂	31.2	168.2 ± 17.4	-22.2 ± 0.8	0.97 ± 0.03
	31.5			
	33.2			
OCH₂	62.2	44.9 ± 2.8	-19.2 ± 0.7	0.84 ± 0.03
	63.3			
	64.2			
	64.5			
	65.4			
CH	111.4	158.4 ± 10.9	-23.5 ± 0.8	0.99 ± 0.03
	111.9			
	114.9			
	116.4			
CH₂C^{IV}	126.6 (†)	136.4 ± 9.2	N/A ^a	N/A
	126.8			
	127.6			
	128.4 (†)			
	129.0			
	130.1 (†)			
	130.6			
137.2 (†)				
OC^{IV}	149.3	189.5 ± 11.3	N/A	N/A
	149.9			
	151.1			
	151.6			
	152.5			

^a Not Applicable.

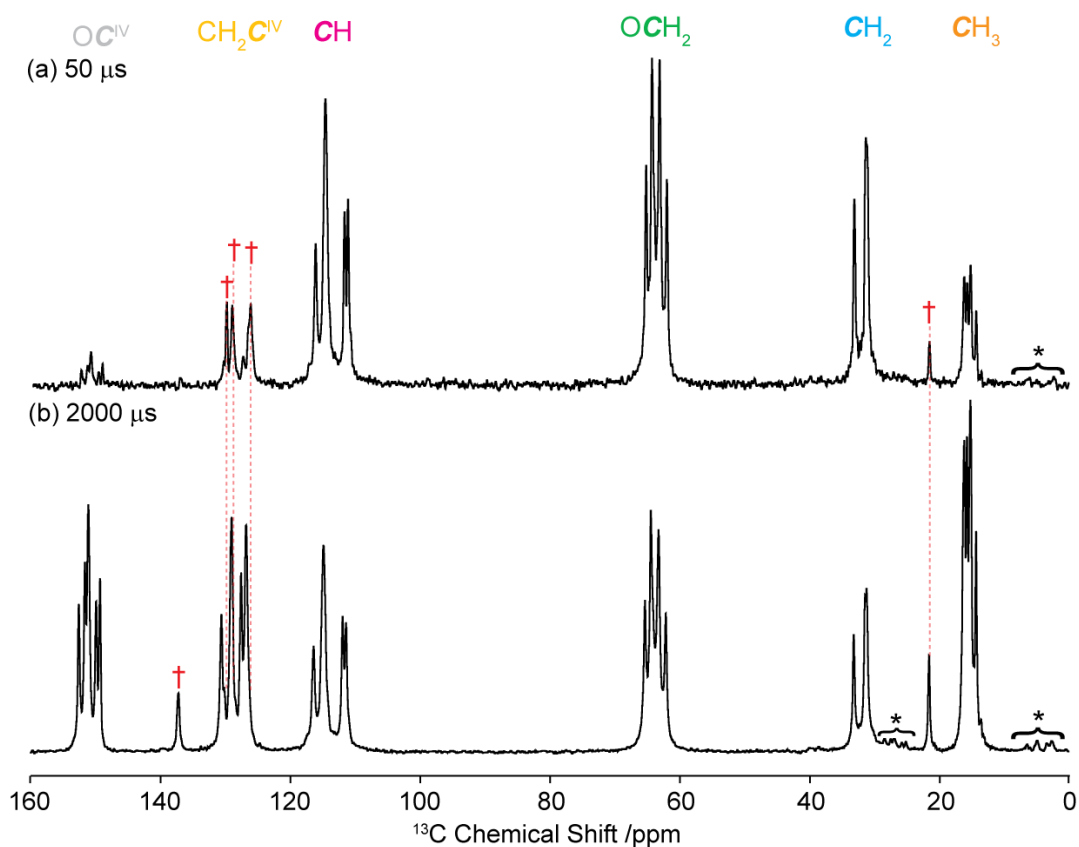


Figure 4.11. ^{13}C edited experiments of *mX@EtP6* obtained by comparing the ^{13}C CP MAS NMR spectra acquired with contact times of (a) $50\ \mu\text{s}$ and (b) $2000\ \mu\text{s}$. Data were obtained at a magnetic field of 9.4 T. Spectral assignments are given in the figure (see **Figure 4.1**). The red daggers (\dagger) (also shown in red in the spectral deconvolution in **Figure 4.12**) denote signals arising from the *para*-xylene guest. The CH resonances of *para*-xylene are apparent in the spectrum obtained at a short contact time of $50\ \mu\text{s}$ where the signal intensities of the quaternary carbons are largely reduced. Spinning sidebands are marked with asterisks (*).

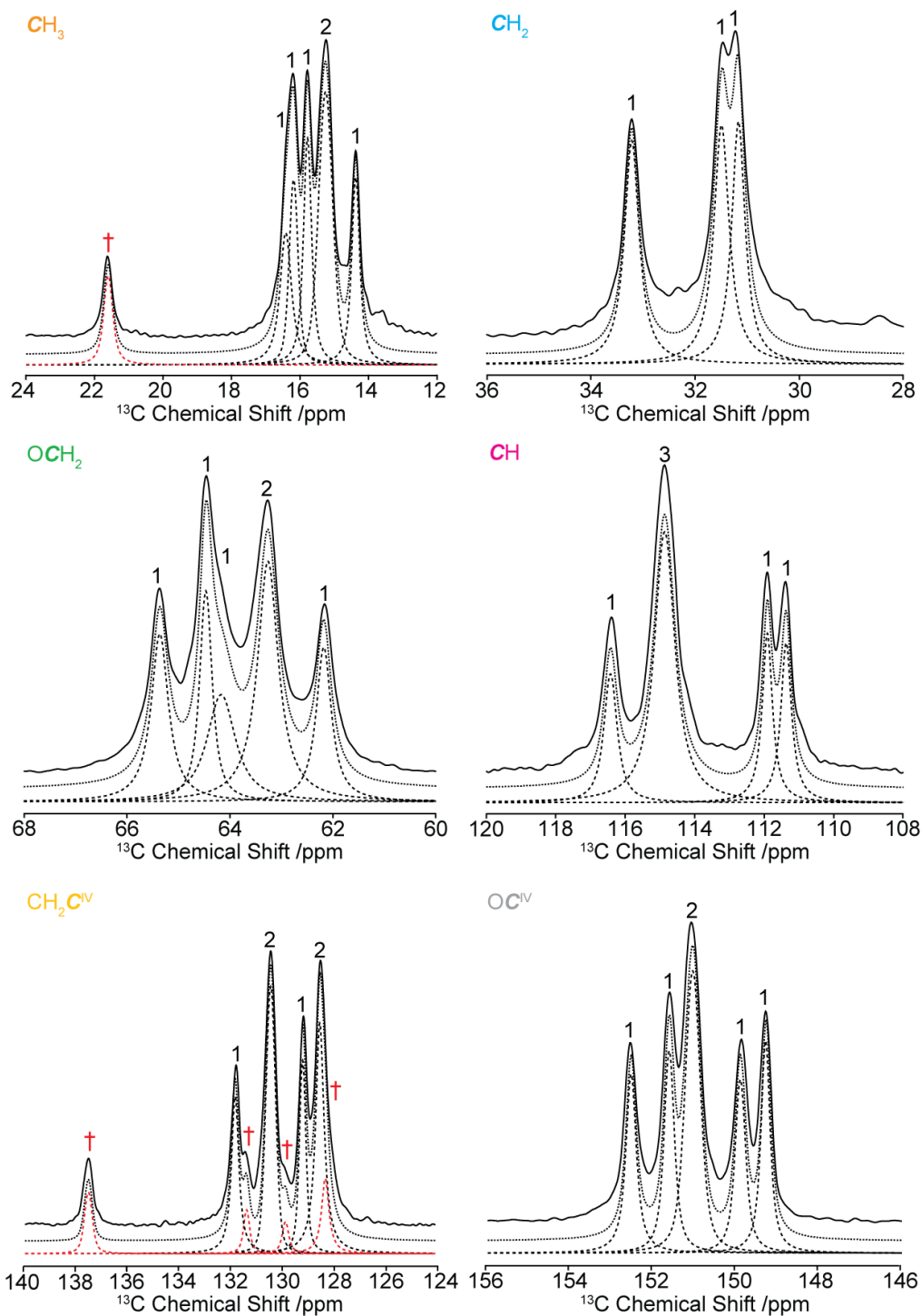


Figure 4.12. Experimental ^{13}C CP MAS NMR spectrum of *mX@EtP6* (full line) with the total fit and spectrum deconvolutions shown with dotted and dashed lines, respectively. Integration values for each carbon subgroup are given. Data obtained at 298 K and 9.4 T. Each panel shows chemically distinct carbons environments of the EtP6 host. Spectral assignments are given in the figure (see **Figure 4.1**) and are obtained from known isotropic chemical shifts, ^{13}C -edited experiments and 2D PDLF data (see manuscript). Red daggers (\dagger) denote signals arising from the *meta*-xylene guest.

The ^{13}C NMR spectrum of **oX@EtP6** is given in **Figure 4.8(e)** and allows the observation of all different types of carbon in EtP6. However, the spectrum is more poorly resolved than those of **pX@EtP6** and **mX@EtP6**, likely due to the lower crystallinity of this material as seen by the broad lines in both PXRD data (**Figure 4.2**) and solid-state NMR (**Figure 4.8(e)**), and for which we only provide a tentative assignment for overlapping resonances between *ortho*-xylene and the EtP6 host (**Table 4.5**). Notably, the short contact time ^{13}C CP spectrum (**Figure 4.13**) only enables clear identification of the CHs originating from the *ortho*-xylene while its CH_3 resonance is not directly attributable. This resonance is likely shifted to a lower frequency than in **mX@EtP6** and **pX@EtP6** due to the increased shielding effect of the *ortho*-xylene methyl groups located in the centre of the cavity (**Figure 4.1(e)**) and is therefore expected to overlap with the CH_3 resonances of the ethyl group around 16 ppm.

Table 4.5. ^{13}C NMR assignments for **oX@EtP6 (Figure 4.8(e))** with isotropic chemical shifts δ_{iso} from spectral deconvolution shown in **Figure 4.14**, spin lattice relaxation times T_1 obtained *via* area integration, motional averaged dipolar coupling constants $\langle d_{\text{CH}} \rangle$ and order parameters $\langle S_{\text{CH}} \rangle$. Data obtained at room temperature and 9.4 T. Red daggers (†) denote signals arising from *ortho*-xylene guest and (#) denote amorphous signals. Overlapping resonances between the guest and the host in the in the 15-17 ppm and 123-137 ppm region of the ^{13}C CP MAS NMR spectrum prevents spectral assignment of the CH_3 and only allow tentative assignment of the $\text{CH}_2\text{C}^{\text{IV}}$ carbons.

Assignment	^{13}C δ_{iso} /ppm	T_1 /s	$\langle d_{\text{CH}} \rangle$ /kHz	$\langle S_{\text{CH}} \rangle$
CH_3	15.1	2.0 ± 0.1	-7.1 ± 0.5	0.31 ± 0.03
	15.9			
	16.3			
CH_2	28.6	65.2 ± 6.7	-23.8 ± 0.8	1.03 ± 0.03
	29.8			
	30.6			
	33.0			
	37.6			
OCH_2	62.1	25.8 ± 1.5	-18.3 ± 0.7	0.81 ± 0.03
	62.7			
	63.1			
	63.8			
	65.4 (#)			
CH	111.4	89.3 ± 4.1	-23.8 ± 0.8	1.00 ± 0.03
	111.9			
	114.9			
	116.4			
$\text{CH}_2\text{C}^{\text{IV}}$	124.0 (#)	52.2 ± 4.8	N/A ^a	N/A
	125.4			
	126.3			
	126.7			
	128.2 (†)			
	128.8 (†)			
	129.2			
	129.5			
	134.6 (†)			
137.0 (#)				
OC^{IV}	149.2	88.0 ± 3.9	N/A	N/A
	149.6			
	150.2			
	151.8			
	151.5			
	152.1			

^a Not Applicable.

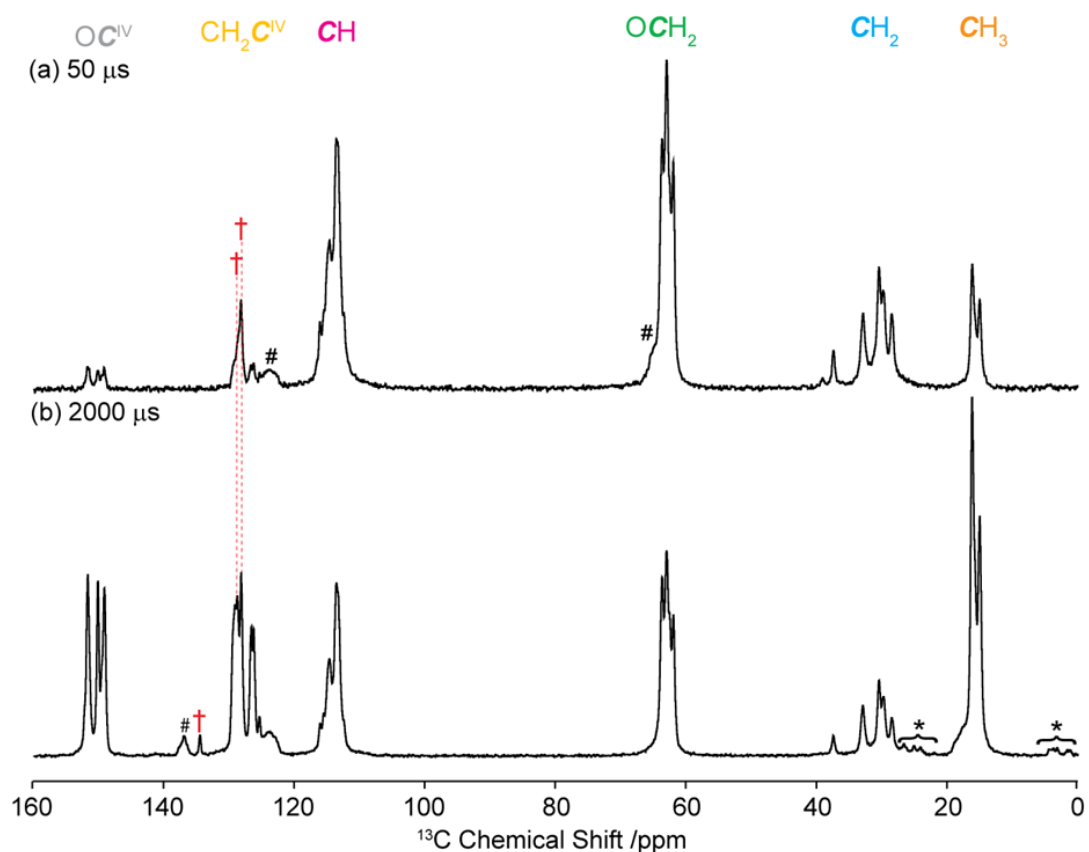


Figure 4.13. ^{13}C edited experiments of ***oX@EtP6*** obtained by comparing the ^{13}C CP MAS NMR spectra acquired with contact times of (a) $50\ \mu\text{s}$ and (b) $2000\ \mu\text{s}$. Data were obtained at a magnetic field of 9.4 T. Spectral assignments are given in the figure (see **Figure 4.1**). The red daggers (\dagger) (also shown in red in the spectral deconvolution (**Figure 4.14**)) denote signals arising from the *ortho*-xylene guest. The CH resonances of *ortho*-xylene are apparent in the spectrum obtained at a short contact time of $50\ \mu\text{s}$ where the signal intensities of the quaternary carbons are largely reduced. Spinning sidebands and signals arising from unknown minor phase(s) are marked with asterisks (*) and dashes (#), respectively.

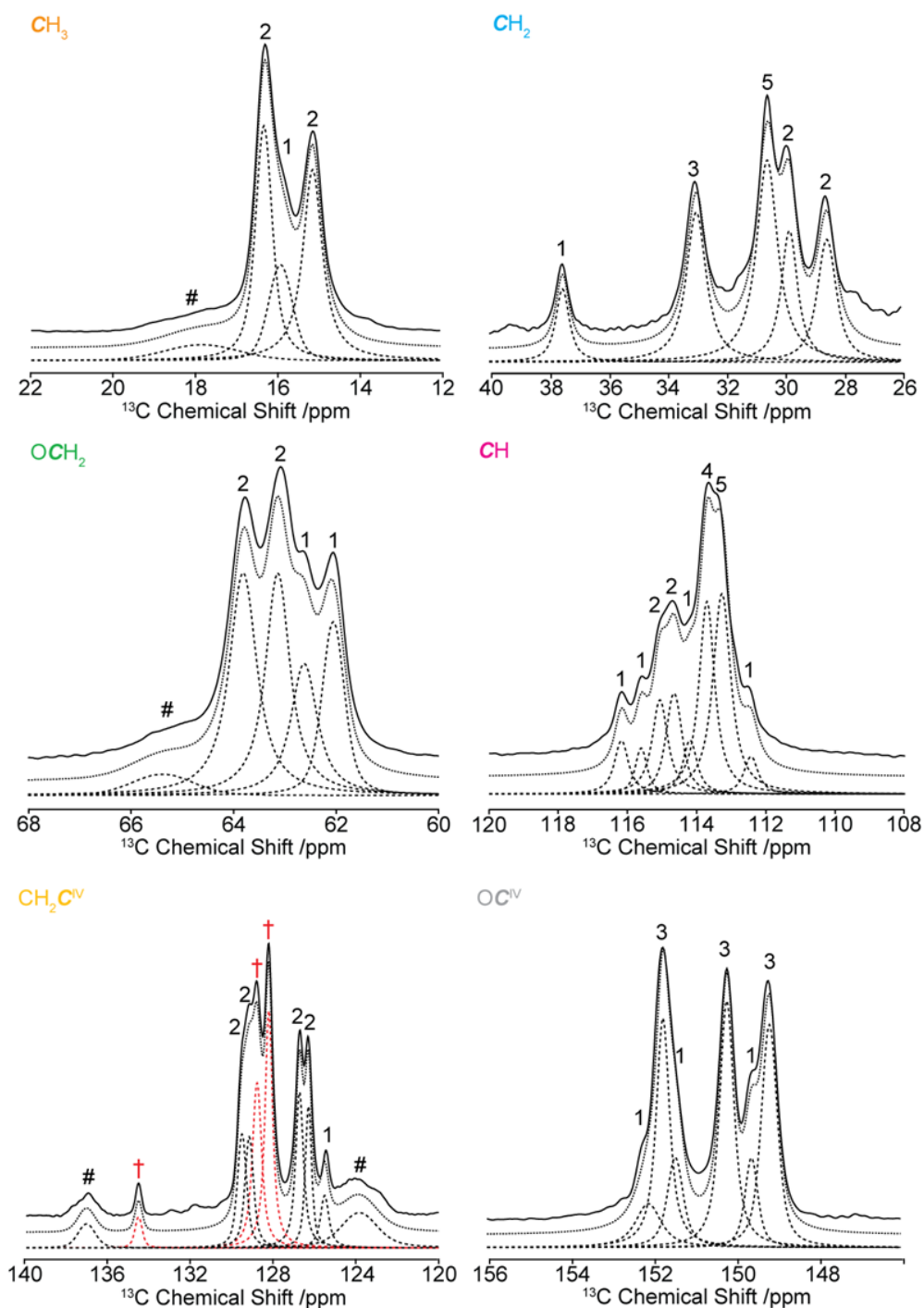


Figure 4.14. Experimental ^{13}C CP MAS NMR spectrum of oX@EtP6 (full line) with the total fit and spectrum deconvolutions shown with dotted and dashed lines, respectively. Integration values for each carbon subgroup are given. Data obtained at 298 K and 9.4 T. Each panel shows chemically distinct carbons environments of the EtP6 host. Spectral assignments are given in the figure (see **Figure 4.1**) and are obtained from known isotropic chemical shifts, ^{13}C -edited experiments and 2D PDLF data (see manuscript). Note that the low resolution of some of the resonances results in uncertainty in the estimated integration. The overlapping peaks in the CH_3 region do not allow for the CH_3 of the *ortho*-xylene guest to be accurately identified. Broad signals tentatively assigned to some unknown amorphous phase(s) are marked with dashes (#). Red daggers (+) denote signals arising from the *ortho*-xylene guest.

Variable temperatures ^{13}C CP MAS NMR spectra (**Figures 4.15-4.19**) of all five materials were performed in the 383 - 100 K temperature range (down to only 243 K for EtP5). Upon cooling, significantly broader ^{13}C NMR resonances are observed at low temperature (e.g., from 30 Hz at 298 K to 60 Hz at 100 K for the CH resonance of EtP6- \square at 14.1 T) as anticipated from the macrocycles being trapped in a variety of conformations and leading to inhomogeneous broadening. There is minimal change in the intensity of the spinning sidebands which likely indicates that the ^{13}C CSA is largely unchanged in the temperature range studied here while also suggesting that accessing ^{13}C CSAs is likely not a suitable method to obtain dynamics information in the kHz regime for the majority of carbon environments for these materials as discussed in Section 4.5.5. There is also no evidence of signal coalescence due to chemical exchange.

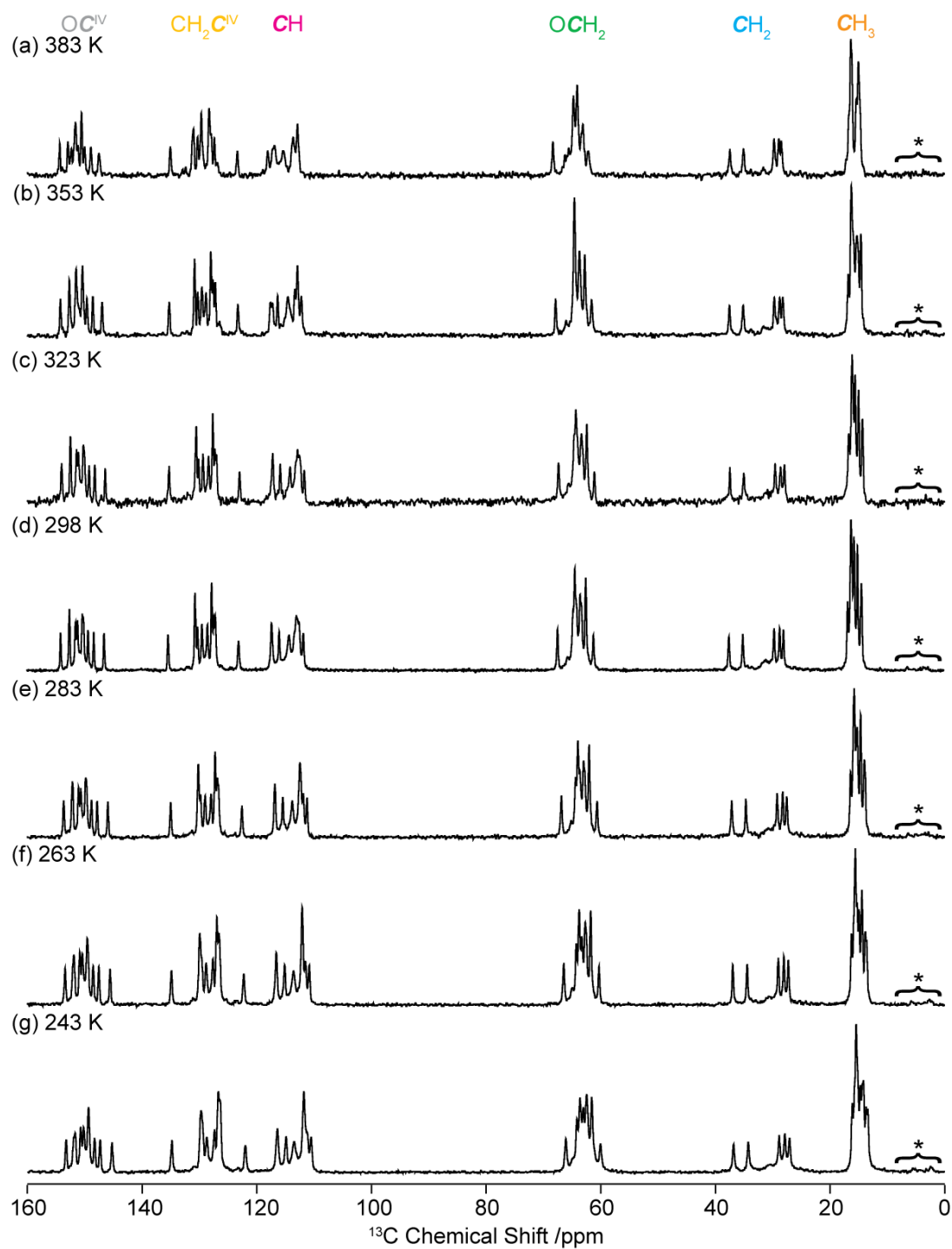


Figure 4.15. Variable temperature ¹³C CP NMR spectra of guest-free EtP5- α collected at the temperatures given in the figure. Data was obtained at 9.4 T. Spectral assignments are given in the figure (see **Figure 4.1**) and correspond to those previously published.¹ Asterisks (*) denote spinning sidebands.

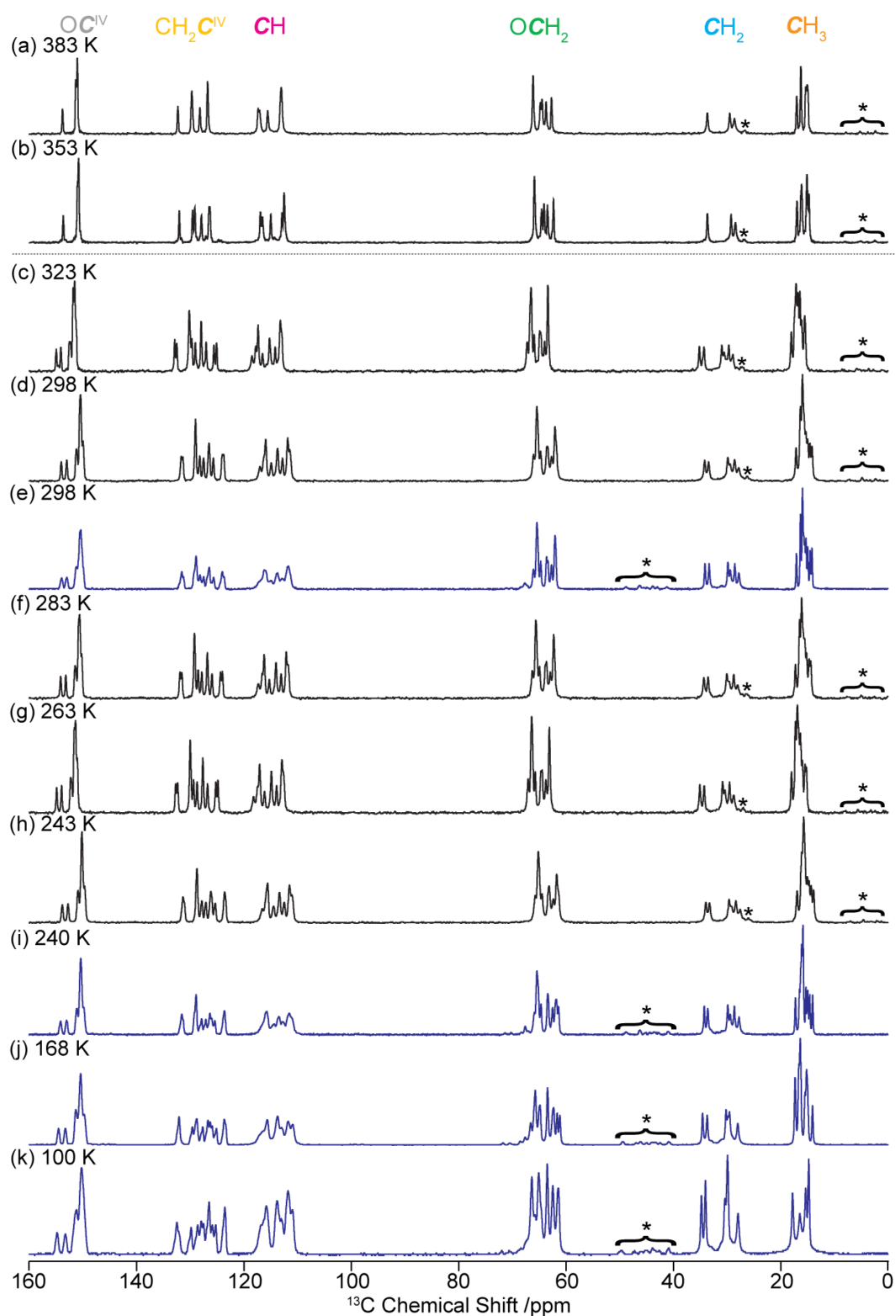


Figure 4.16. Variable temperature ^{13}C CP NMR spectra of guest-free **EtP6- β** collected at the temperatures given in the figure. Data shown in black and blue were obtained at 9.4 and 14.1 T, respectively. Spectral assignments are given in the figure (see **Figure 4.1**) and correspond to those previously published.¹ The dotted line indicates a polymorphic transition in **EtP6- β** (see DSC data in **Figure 4.20**). Asterisks (*) denote spinning sidebands.

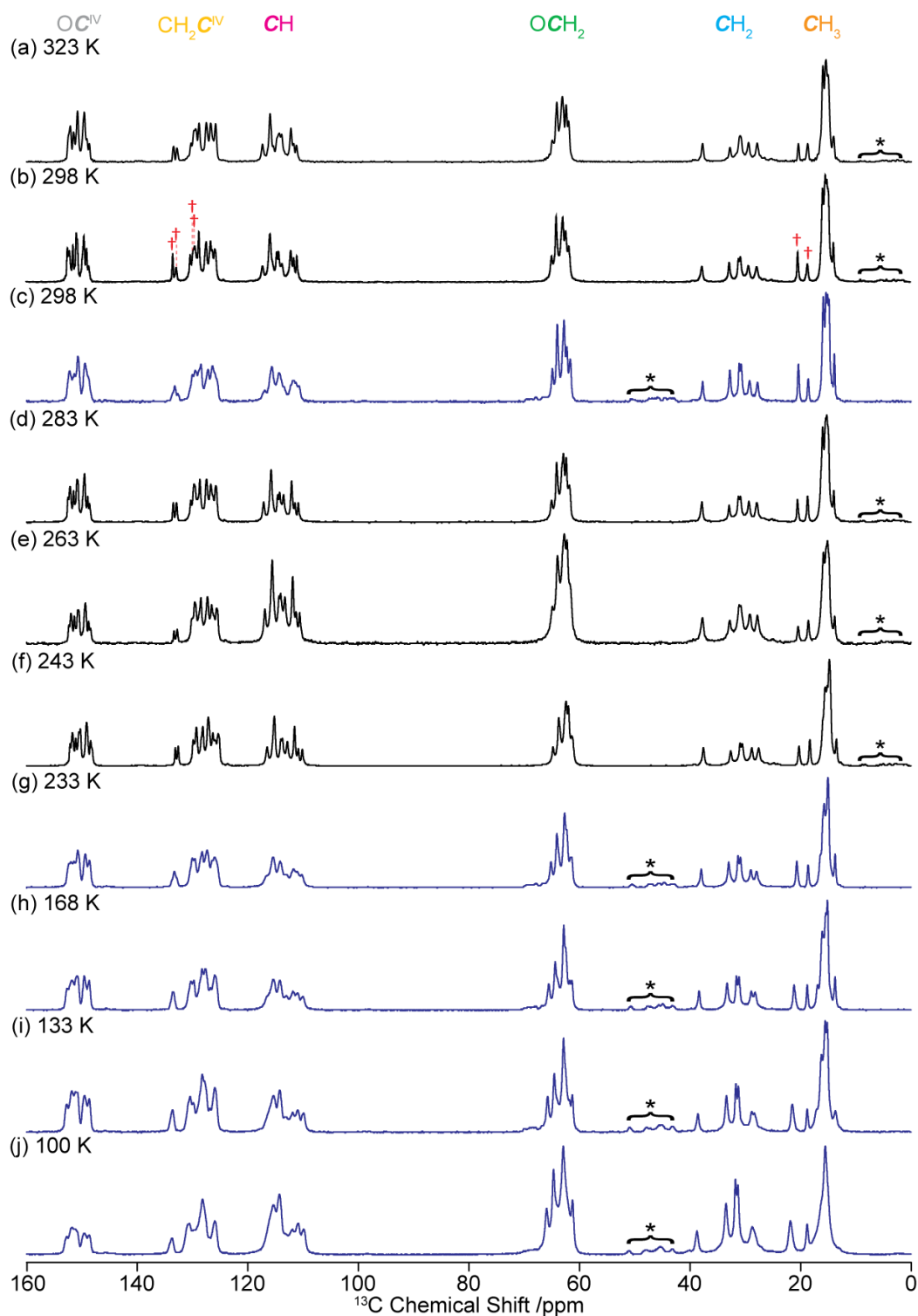


Figure 4.17. Variable temperature ^{13}C CP NMR spectra of *pX@EtP6* collected at the temperatures given in the figure. Data shown in black and blue were obtained at 9.4 T and 14.1 T, respectively. Spectral assignments are given in the figure (see **Figure 4.1**) and are derived from known isotropic chemical shifts,⁶² ^{13}C -edited experiments (**Figure 4.9**) and PDLF data. Red daggers (†) and asterisks (*) denote signals arising from the *para*-xylene guest and spinning sidebands, respectively

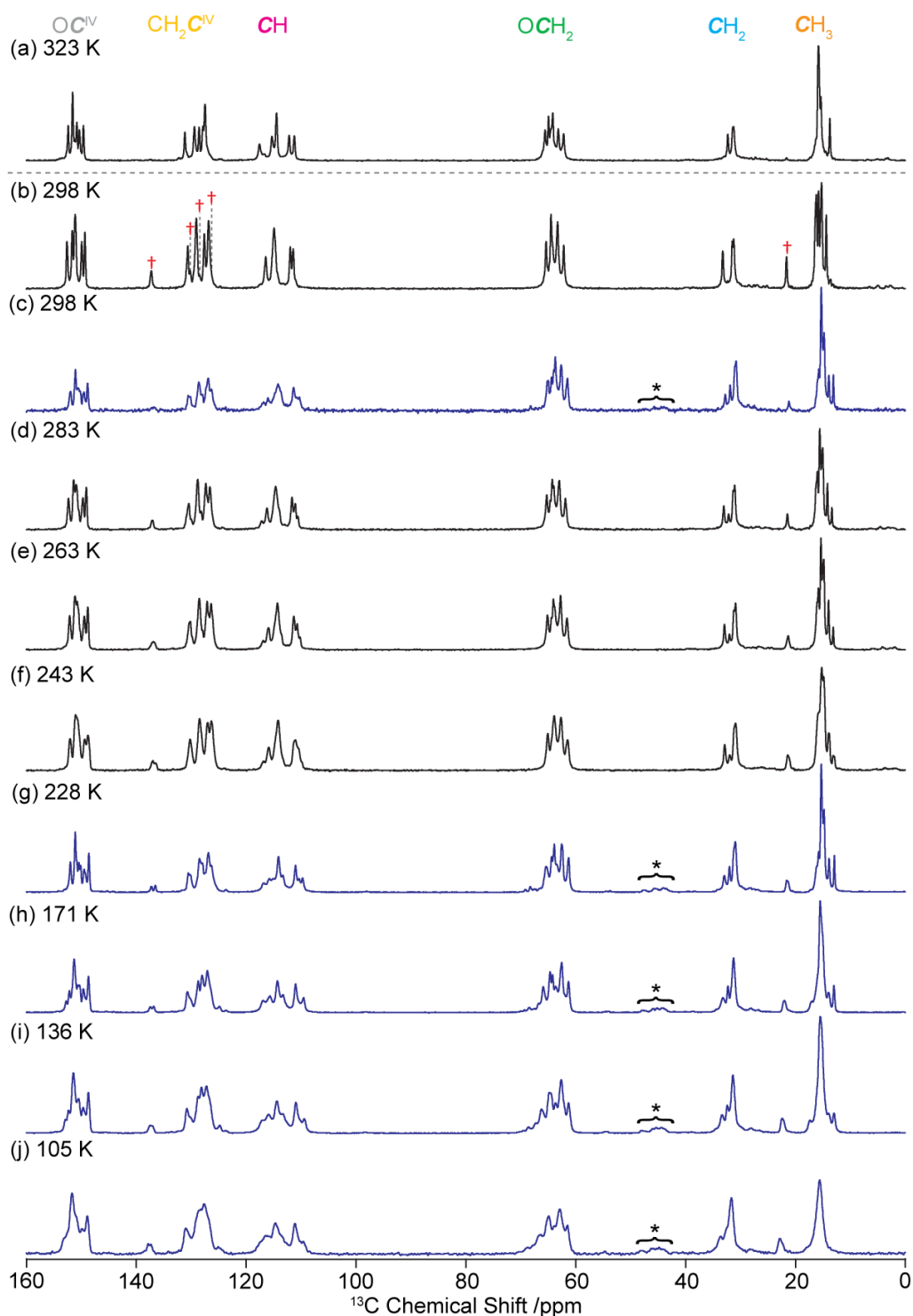


Figure 4.18. Variable temperature ^{13}C CP NMR spectra of *mX@EtP6* collected at the temperatures given in the figure. Data shown in black and blue were obtained at 9.4 T and 14.1 T, respectively. Spectral assignments are given in the figure (see **Figure 4.1**) and are derived from the known isotropic chemical shifts, 62 ^{13}C -edited experiments (**Figure 4.11**) and PDLF data. The dashed line indicates that *meta*-xylene is lost between room temperature and 323 K. Red daggers (†) and asterisks (*) denote signals arising from the *meta*-xylene guest and spinning sidebands, respectively.

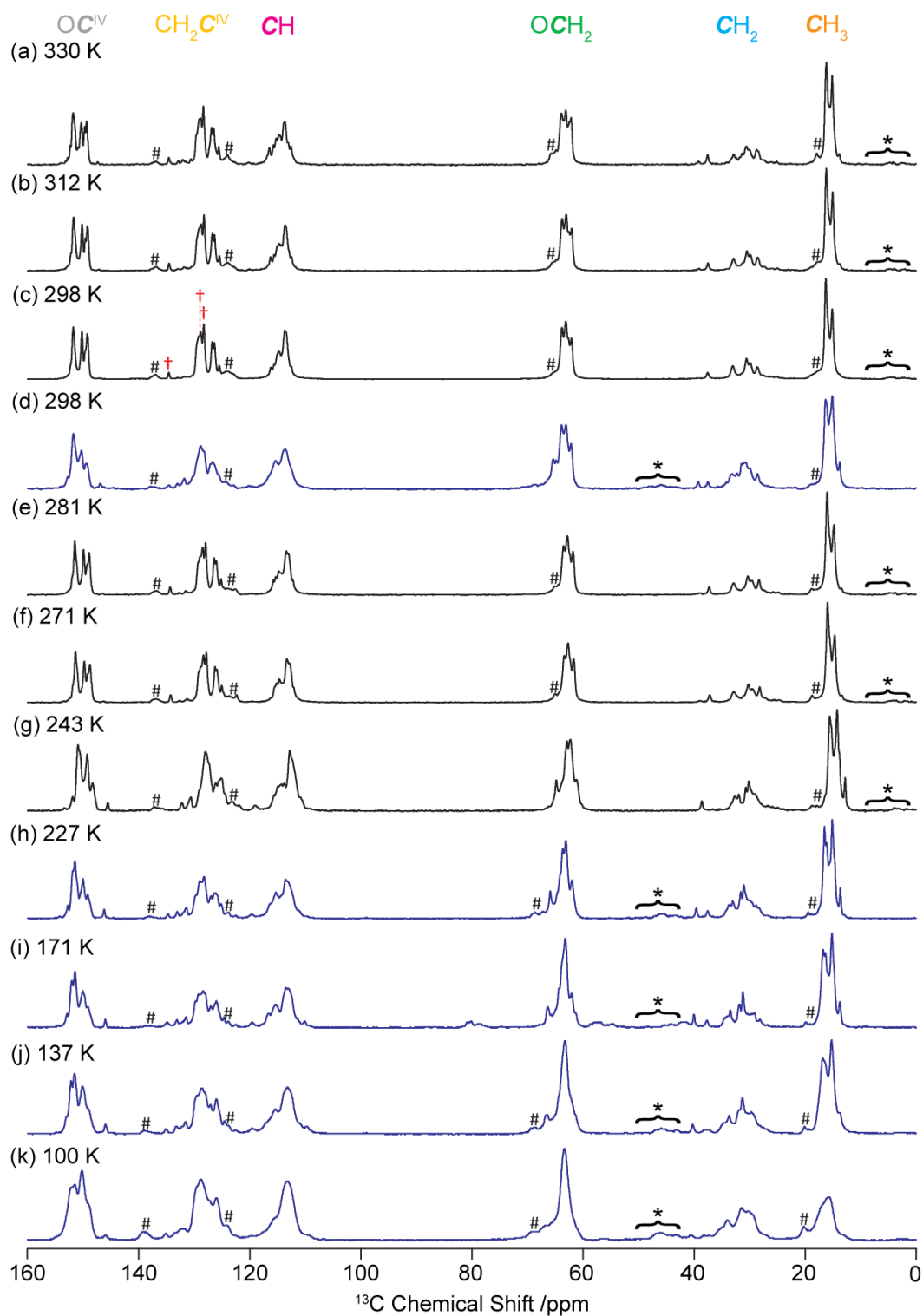


Figure 4.19. Variable temperature ^{13}C CP NMR spectra of **oX@EtP6** collected at the temperatures given in the figure. Data shown in black and blue were obtained at 9.4 T and 14.1 T respectively. Spectral assignments are given in the figure (see **Figure 4.1**) and are derived from known isotropic chemical shifts,⁶² ^{13}C -edited experiments (**Figure 4.13**) and PDLF data. Broad signals tentatively assigned to some unknown amorphous phase(s) are marked with dashes (#). Red daggers (†) and asterisks (*) denote signals arising from the *ortho*-xylene guest and spinning sidebands, respectively.

Upon heating above 323 K, the ^{13}C CP MAS NMR spectrum of **EtP6- β** remains very well resolved and the number of resonances halves (vs. 298 K), indicating a crystal structure of higher symmetry. The change of symmetry and a polymorphic phase transition are in agreement with both the DSC data (**Figure 4.20**), that shows an endothermic peak at 339 K, and with refined XRD data at 433 K that indicated a transition from triclinic $P\bar{1}$ **EtP6- β** at room temperature to a different metastable triclinic $P\bar{1}$ state at 339 K with data that could be fitted with a unit cell with halved volume of the room temperature data.¹ Spectral deconvolution of a corresponding ^{13}C CP MAS NMR spectrum at 383 K (**Figure 4.21**) also provides signal integrations reflecting this observation. In contrast, the ^{13}C CP MAS NMR spectrum of **EtP5- α** up to 383 K remains unchanged upon heating (**Figure 4.15**) and no polymorphic transition is therefore observed.

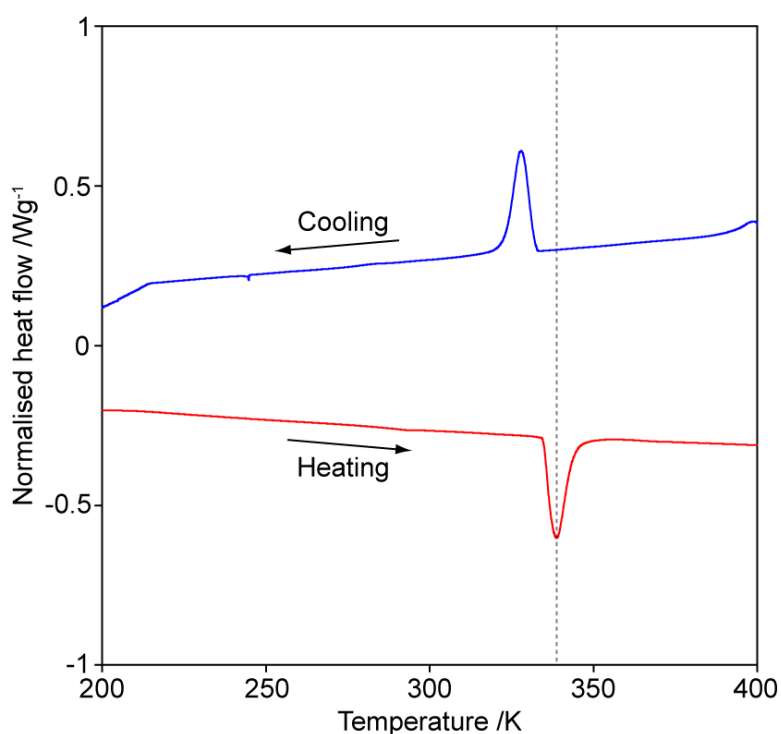


Figure 4.20. Differential scanning calorimetry thermogram of **EtP6- β** showing a phase transition from triclinic $P\bar{1}$ to a metastable, triclinic $P\bar{1}$ state with higher symmetry at 339 K (dashed line).¹

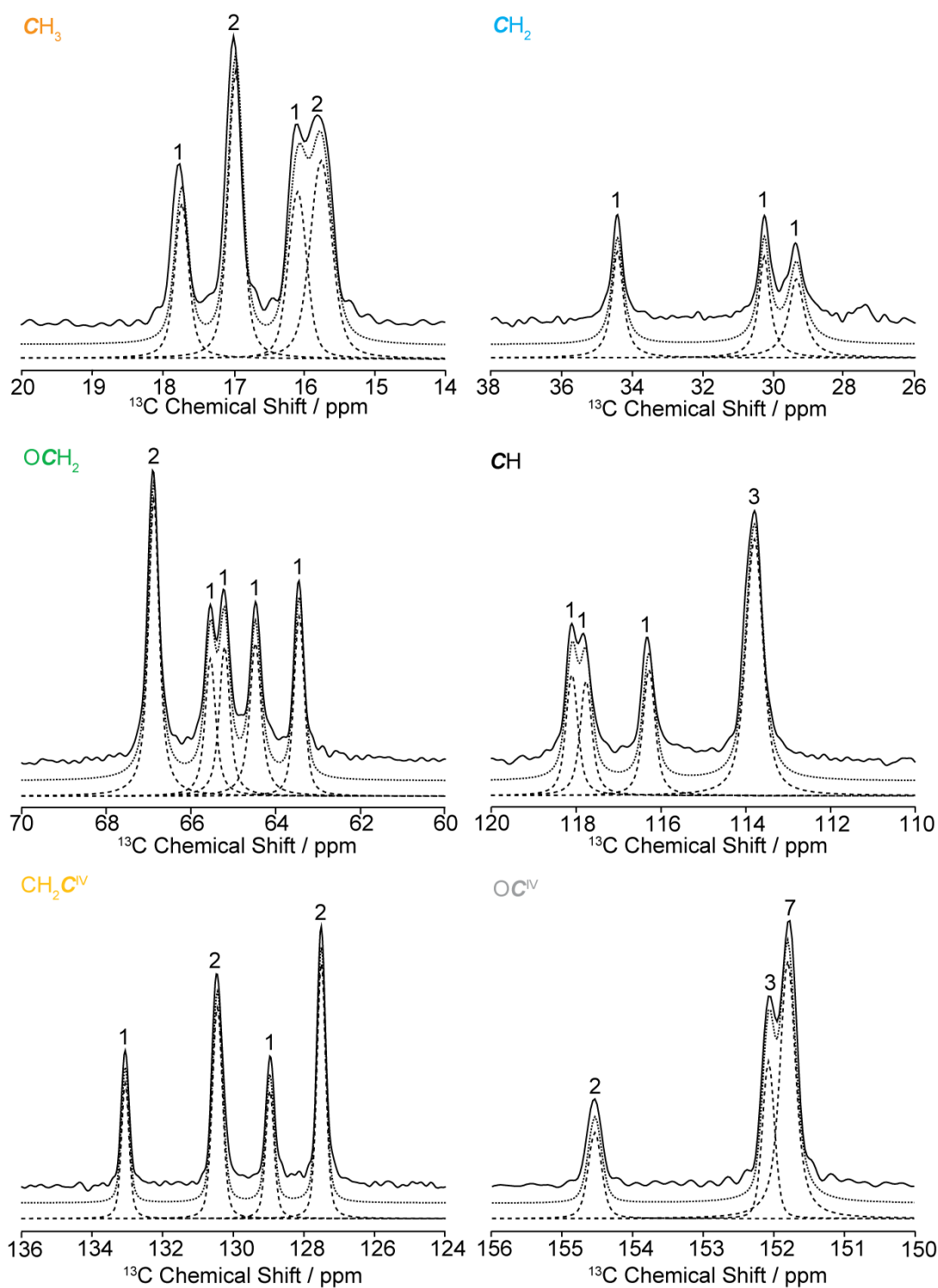


Figure 4.21. Experimental ^{13}C CP MAS NMR spectrum of **EtP6** (full line) obtained at 383 K and 9.4 T with the total fit and spectrum deconvolutions shown with dotted and dashed lines, respectively. Integration values for each carbon subgroup are given. Each panel shows chemically distinct carbon environments of **EtP6**. Spectral assignments are given in the figure (see **Figure 4.1**). Integrations match with half the number of non-equivalent carbon atoms in the asymmetric unit cell of **EtP6- β** .

No changes in the ^{13}C CP MAS NMR spectra upon the heating of ***pX@EtP6*** or ***oX@EtP6*** to 323 - 330 K occurred (**Figures 4.17** and **4.19**). This is consistent with previous DSC and thermogravimetric analysis (TGA) work that show that the adsorbed xylenes are only lost from the pores at temperatures exceeding 415 K for ***pX@EtP6*** and 433 K for ***oX@EtP6***¹ (these temperatures have not been accessed in this NMR work). The ^{13}C CP MAS NMR spectrum of ***mX@EtP6*** at 323 K (**Figure 4.18**), however, shows the disappearance of the peaks assigned to the adsorbed xylene and accounts for the loss of the *meta*-xylene from the pores. It is likely that the *meta*-xylene remains in the MAS rotor as a liquid phase that would not be detectable under the CP conditions used. Upon cooling this sample back to room temperature, the ^{13}C CP MAS NMR spectrum (data not shown) indicates that the material has not returned back to ***EtP6- β*** as this process only occurs at temperatures higher than 433 K.¹ We ascribe this difference of behaviours between ***mX@EtP6***, and ***pX@EtP6*** and ***oX@EtP6*** to the smaller cavity of the former preventing the *meta*-xylene guest (**Figure 4.1**) to be fully accommodated in the pores and facilitating this removal upon heating.

4.5.2. Temperature dependent motional averaged site-selectivity in guest-free pillar[n]arenes

Heteronuclear dipolar couplings are dependent on distance and motion, and the magnitude of this dipole-dipole coupling is given by the following expression:

$$d_{ij} = -\frac{\mu_0}{4\pi} \frac{\hbar\gamma_i\gamma_j}{r_{ij}^3} \quad (4.2)$$

where d_{ij} is the dipolar coupling constant for the nuclei i and j in rad s^{-1} , μ_0 is the vacuum permittivity, \hbar is the reduced Planck constant, γ_i and γ_j are the respective gyromagnetic ratios for nuclei i and j and r_{ij} is the distance between the i and j nuclei. Dipolar couplings are often highly temperature dependent, enabling the conformational dynamics and flexibility to be assessed over a wide temperature range. Hence, dipolar couplings are a useful tool to probe host-guest interactions and dynamics.⁶⁵

Motional averaged dipolar couplings $\langle d_{CH} \rangle$ can be obtained by two-dimensional (2D) Proton Detected Local Field (PDLF)^{41,42,66} experiments that correlate the ^{13}C isotropic chemical shifts with their corresponding ^{13}C ^1H dipolar spectra, providing site-selective heteronuclear dipolar coupling constants. These experiments employ R-type recoupling blocks⁶⁷ to reintroduce the heteronuclear dipolar couplings averaged out by MAS whilst also suppressing the ^1H ^1H homonuclear dipolar couplings and ^{13}C CSA (see Materials and Methods section 4.4 for further details). We have employed this approach to observe the temperature dependent dynamics of guest-free and xylene-adsorbed pillar[n]arenes.

Recoupling sequences to reintroduce heteronuclear dipolar coupling d_{CH} such as the R symmetry class^{43,46,67,68} used in this work results in an effective dipolar coupling constant d_{CH}^m according to:

$$d_{CH}^m = \kappa_R d_{CH} \quad (4.3)$$

where κ_R is the scaling factor of the recoupling sequences. Whilst this can often be determined numerically,⁶⁷ this is beyond the scope of this work for the $wR18_2^5$ block used and we have instead used a robust experimental method to determine κ_R from a $wR18_2^5$ PDLF experiment on model D-alanine as a reference. The corresponding ^{13}C CP NMR, 2D PDLF and site specific ^{13}C ^1H dipolar spectra are shown in **Figure 4.22** from which d_{CH}^{K} could be determined from the outer singularities (see Materials and Methods section) of the C_α carbon ($d_{\text{CH}}^{\text{K}} = -7.55$ kHz, **Table 4.6**). Comparison with the rigid d_{CH} value (-23.14 kHz) obtained from **equation 4.3** and the α -carbon proton bond length (1.093 Å) determined from neutron diffraction⁶⁹ affords:

$$\kappa_R = \frac{d_{\text{CH}}^{\text{K}}}{d_{\text{CH}}} = \frac{-7550}{-23140} = 0.326 \quad (4.4)$$

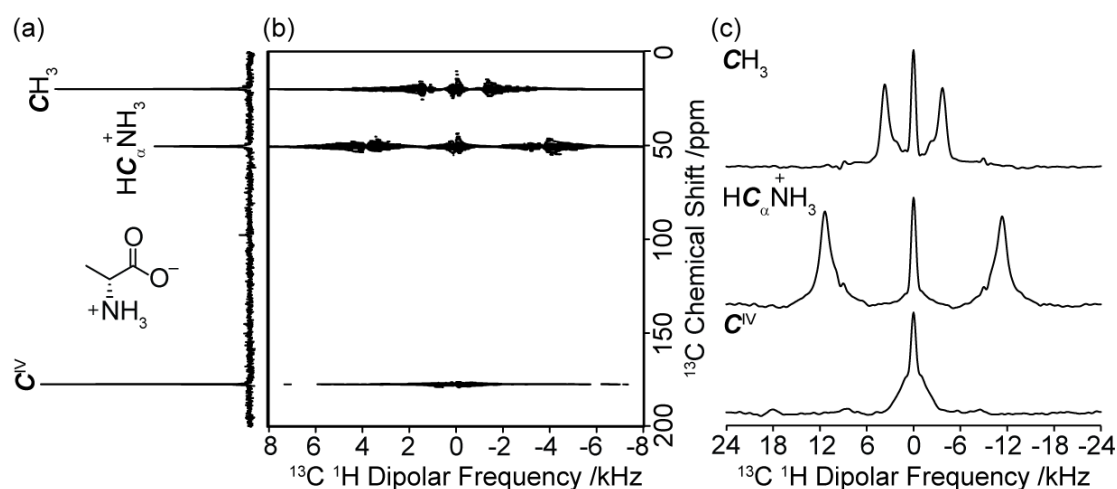


Figure 4.22. (a) ^{13}C CP MAS spectrum and chemical structure, (b) PDLF spectrum and (c) site-specific ^{13}C ^1H dipolar spectra of D-alanine. Spectral assignments are given in the figure. Data obtained at 298 K and 9.4 T. d_{CH}^{K} is measured using the outer singularities of the dipolar coupling spectra. Vertical light grey lines in the dipolar coupling spectra indicate the static limit dipolar coupling constants d_{CH} .

Table 4.6. ^{13}C NMR spectrum assignments, ^{13}C isotropic chemical shifts and the motional averaged dipolar coupling obtained from the 2D PDLF spectrum of D-alanine shown in **Figure 4.22** above.

Assignment	^{13}C δ_{iso} /ppm	d_{CH}^{K} /kHz	d_{CH} /kHz
CH_3	20.7	-2.45	-7.50
$\text{HC}_{\alpha}\text{NH}_3$	51.2	-7.55	-23.10
C^{V}	178.1	-0.65	-1.99

Figure 4.23 presents the room temperature 2D PDLF spectrum of **EtP6- β** that, as expected, shows dipolar coupling for all protonated carbons. The corresponding ^{13}C ^1H dipolar spectra can be extracted at each ^{13}C shifts (**Figure 4.23(c)**) and the motional averaged dipolar coupling $\langle d_{\text{CH}} \rangle$ measured from their outer singularities revealing significant differences in $\langle d_{\text{CH}} \rangle$ between each carbon subgroup. For example, smaller dipolar coupling constants $\langle d_{\text{CH}} \rangle$ of -7.2 ± 0.5 and -18.1 ± 0.7 kHz are obtained for the CH_3 and OCH_2 carbons of the ethoxy group, respectively, while larger values of -22.4 ± 0.8 and -23.9 ± 0.8 kHz are extracted for the CH_2 and CH carbons of the pillar[6]arene backbone ring (**Tables 4.7** and **4.1**). Note that the variation of $\langle d_{\text{CH}} \rangle$ values obtained from each carbon resonance for a particular carbon subgroup (**Figure 4.24**) is within the estimated error so we have chosen to give an averaged value for $\langle d_{\text{CH}} \rangle$. Whilst no dipolar coupling splitting is apparent for the quaternary OC^{IV} carbons, partially resolved small couplings of -2.9 ± 0.3 kHz are obtained for the $\text{CH}_2\text{C}^{\text{IV}}$ carbons. This is likely due long range through space coupling of these carbons to the nearby methylene CH_2 group of the ring that is absent for OC^{IV} which is more isolated from any protons. Similar long range dipolar couplings can also be observed around dipolar frequencies of -4.0 ± 0.3 and -6.1 ± 0.5 kHz in the dipolar coupling spectra of the CH_3 and CH_2 environments, respectively, which arise from spatial proximity with protons on the nearby carbons.

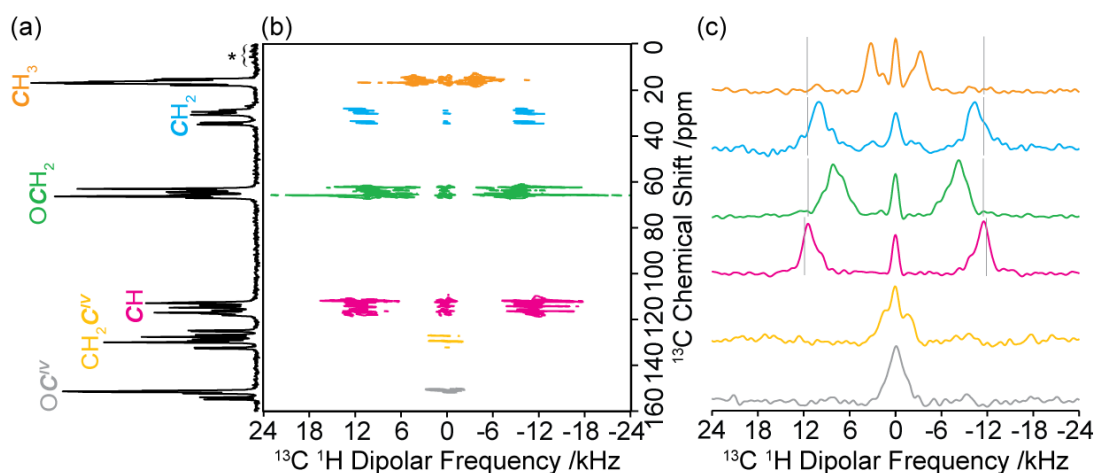


Figure 4.23. (a) ^{13}C CP MAS spectrum, (b) PDLF spectrum and (c) selected site-specific ^{13}C ^1H dipolar spectra for guest-free **EtP6- β** . Spectral assignments are given in the figure and correspond to those previously published.¹ The data presented above was obtained at 298 K and 9.4 T. $\langle d_{\text{CH}} \rangle$ is measured using the outer singularities of the dipolar coupling spectra as highlighted in the experimental section. Vertical light grey lines indicate the static limit dipolar coupling constants d_{CH} calculated from **equation 4.2** and the computed CH distances obtained at the DFT level on the various conformers identified by CSP.¹ OCH_2 distances are shorter than CH yielding larger d_{CH} . Asterisks (*) denote spinning sidebands.

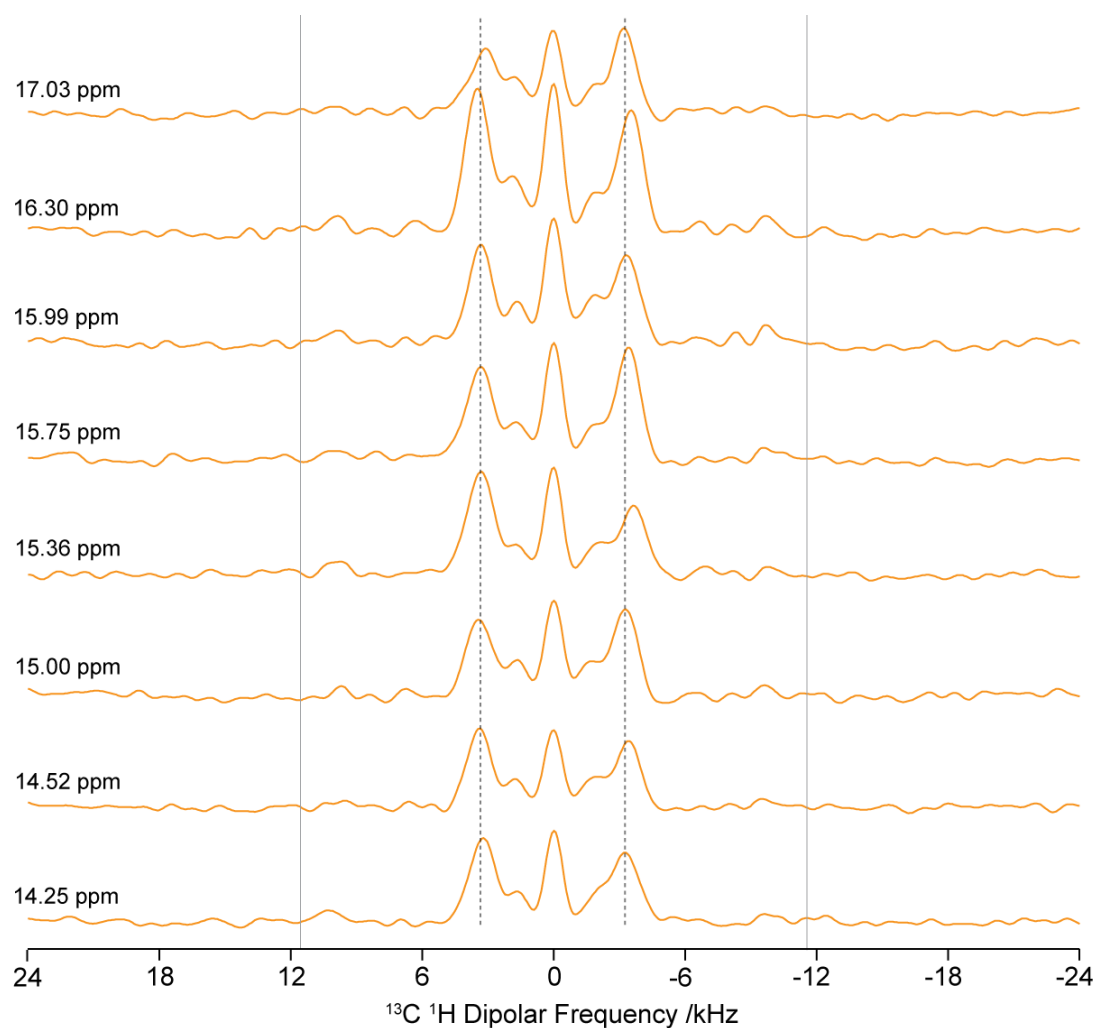


Figure 4.24. Comparison of the ^{13}C ^1H dipolar spectra for each resolved CH_3 resonance in **EtP6- β .1** Data were obtained at 298 K and a magnetic field of 9.4 T. The corresponding ^{13}C isotropic chemical shift is given next to each dipolar spectrum. Dashed lines indicate the average $\langle d_{\text{CH}} \rangle = -7.2$ kHz obtained from this data which also illustrate very small change between each dipolar spectrum ($\Delta\langle d_{\text{CH}} \rangle = 1.0$ kHz); hence, in this dataset $\langle d_{\text{CH}} \rangle = -7.1 \pm 0.5$ kHz. Vertical light grey lines in the spectra indicate the static limit dipolar coupling constants d_{CH} .

Table 4.7. ^{13}C NMR assignments, ^{13}C isotropic chemical shifts δ_{iso} from spectral deconvolution, calculated static dipolar coupling constants d_{CH} , experimentally found motional averaged dipolar coupling constants $\langle d_{\text{CH}} \rangle$ and order parameters $\langle S_{\text{CH}} \rangle$ for protonated carbons in **EtP5- α** , **EtP6- β** , **pX@EtP6**, **mX@EtP6** and **oX@EtP6** at 298 and 243 K. Red daggers (\dagger) denote signals from xylenes.

Assignment	^{13}C δ_{iso} /ppm ^a	d_{CH} /kHz ^b	298 K, 9.4 T		243 K, 14.1 T	
			$\langle d_{\text{CH}} \rangle$ /kHz ^c	$\langle S_{\text{CH}} \rangle$ ^d	$\langle d_{\text{CH}} \rangle$ /kHz ^c	$\langle S_{\text{CH}} \rangle$ ^d
EtP5-α						
CH₃	14-17	-23.1	-7.2 ± 0.5	0.31 ± 0.02	-7.5 ± 0.5	0.32 ± 0.02
CH₂	28-38	-23.0	-23.3 ± 0.8	1.01 ± 0.04	-22.8 ± 0.8	0.98 ± 0.04
OCH₂	61-68	-22.8	-18.4 ± 0.7	0.81 ± 0.03	-19.8 ± 0.7	0.87 ± 0.03
CH	111-124	-23.8	-23.8 ± 0.8	1.00 ± 0.03	-23.4 ± 0.8	0.98 ± 0.04
EtP6-β						
CH₃	14-18	-23.1	-7.2 ± 0.5	0.31 ± 0.02	-7.2 ± 0.5	0.31 ± 0.02
CH₂	27-35	-23.0	-22.4 ± 0.8	0.97 ± 0.04	-21.7 ± 0.8	0.94 ± 0.04
OCH₂	62-67	-22.8	-18.1 ± 0.7	0.79 ± 0.03	-18.3 ± 0.7	0.80 ± 0.03
CH	111-118	-23.8	-23.9 ± 0.8	1.00 ± 0.04	-23.4 ± 0.8	0.98 ± 0.03
pX@EtP6						
CH₃	13-16	-23.1	-6.9 ± 0.5	0.30 ± 0.02	-7.3 ± 0.5	0.32 ± 0.03
CH₃(\dagger)	18-21	-23.7	-7.0 ± 0.5	0.30 ± 0.03	-7.1 ± 0.5	0.30 ± 0.02
CH₂	27-38	-23.1	-21.6 ± 0.8	0.94 ± 0.04	-21.3 ± 0.8	0.92 ± 0.04
OCH₂	61-65	-22.9	-18.4 ± 0.7	0.80 ± 0.03	-19.2 ± 0.7	0.84 ± 0.03
CH	110-118	-23.8	-22.4 ± 0.8	0.94 ± 0.03	-22.5 ± 0.8	0.95 ± 0.04
CH(\dagger)	129-130	-23.7	-21.6 ± 0.8	0.91 ± 0.04	-22.6 ± 0.8	0.95 ± 0.04
mX@EtP6						
CH₃	14-17	-23.1	-6.9 ± 0.5	0.30 ± 0.02	-7.0 ± 0.5	0.30 ± 0.02
CH₃(\dagger)	21-22	-24.4	-6.2 ± 0.5	0.25 ± 0.02	-6.7 ± 0.5	0.27 ± 0.03
CH₂	31-34	-23.1	-22.2 ± 0.8	0.96 ± 0.04	-21.2 ± 0.8	0.92 ± 0.04
OCH₂	62-66	-22.8	-19.2 ± 0.7	0.84 ± 0.03	-20.0 ± 0.7	0.88 ± 0.03
CH	111-117	-23.7	-23.5 ± 0.8	0.99 ± 0.03	-23.2 ± 0.8	0.98 ± 0.03
CH(\dagger)	126-131	-24.0	-22.5 ± 0.8	0.94 ± 0.04	-22.3 ± 0.8	0.93 ± 0.03
oX@EtP6						
CH₃	14-17	-23.1	-7.1 ± 0.5	0.31 ± 0.02	-7.0 ± 0.5	0.30 ± 0.02
CH₃(\dagger)^e		-23.7				
CH₂	28-38	-23.2	-23.8 ± 0.8	1.03 ± 0.04	-22.2 ± 0.8	0.96 ± 0.04
OCH₂	62-66	-22.7	-18.3 ± 0.7	0.81 ± 0.03	-18.8 ± 0.7	0.83 ± 0.03
CH	111-116	-23.9	-23.8 ± 0.8	1.00 ± 0.04	-22.8 ± 0.8	0.96 ± 0.04
CH(\dagger)^e	128-129	-23.6	-17.0 ± 0.7	0.72 ± 0.03	-18.8 ± 0.7	0.80 ± 0.03

^a Range of ^{13}C isotropic chemical shifts obtained at room temperature are given for each carbon subgroup. Exact isotropic chemical shifts for all individual carbons are provided in **Tables 4.1-4.5**. ^b Static dipolar coupling constants were calculated as described in the Materials and Methods section. ^c Only the short range $\langle d_{\text{CH}} \rangle$ constants are given (see text for details). Errors are estimated from the uncertainty in the determination of the position of the outer singularities of the ^{13}C ^1H dipolar coupling spectra. ^d Estimated errors are calculated from the errors in $\langle d_{\text{CH}} \rangle$. ^e Overlapping resonances between the guest and the host in the ^{13}C CP MAS NMR spectrum of **oX@EtP6** prevents spectral assignment of the **CH₃** and only allow tentative assignment of the **CH₂C^V** carbons.

Motion can be quantified by a site-specific order parameter $\langle S_{\text{CH}} \rangle$ (**Table 4.7** and **Figure 4.25**) that compares the motional averaged dipolar coupling constants $\langle d_{\text{CH}} \rangle$ with the static limit dipolar coupling constants d_{CH} in the absence of motion (determined as indicated in the Materials and Methods section 4.4, **Table 4.7**) and ranges from 0 for isotropic motion to 1 for a rigid system:

$$\langle S_{\text{CH}} \rangle = \frac{\langle d_{\text{CH}} \rangle}{d_{\text{CH}}} \quad (4.5)$$

The order parameters $\langle S_{\text{CH}} \rangle$ obtained for each carbon subgroup in **EtP6- β** are found to be 0.31 ± 0.02 for **CH₃**, 0.97 ± 0.04 for **CH₂**, 0.79 ± 0.03 for **OCH₂** and 1.00 ± 0.04 for **CH** (**Table 4.7**) at room temperature. There is therefore no (or limited) motion for the **CH₂** and **CH** carbons of pillar[6]arene and is to be expected for these carbons which are situated in the arene core of the pillar[n]arene ring. However, both **CH₃** and **OCH₂** carbons in the ethoxy group show motional averaging caused by dynamics which is ascribed to rotational and librational motions of these carbons. While this effect is fairly small for the **OCH₂** carbon ($\langle S_{\text{CH}} \rangle = 0.79$), motion is particularly pronounced for the **CH₃** group which $\langle d_{\text{CH}} \rangle$ is approximately one third of the d_{CH} yielding $\langle S_{\text{CH}} \rangle = 0.31$, as rapid rotation of the methyl group is permitted further away from the arene core

To access the temperature dependency of $\langle S_{CH} \rangle$, site selective $\langle d_{CH} \rangle$ were measured for **EtP6- β** over an extended temperature range from 383 K down to 100 K and $\langle S_{CH} \rangle$ reported as function of these temperatures (**Figure 4.25(b)**). The $\langle S_{CH} \rangle$ values for **CH₃** group remain largely constant at 0.31 ± 0.02 over this temperature range indicating that this group still possesses significant motion even at 100 K. This is consistent with literature report indicating that temperatures lower than 100 K are required to “freeze” the rapid 3-site hopping motion of **CH₃** in various biomolecules.^{70,71} This is in contrast to the $\langle S_{CH} \rangle$ values of the **OCH₂** which increase significantly upon cooling from 0.79 ± 0.03 at 298 K to 0.95 ± 0.03 at 100 K, supporting reduction in motion and lower flexibility by the pillar[n]arene at lower temperatures.

Similarly, variable temperature 2D PDLF NMR experiments were recorded on guest-free **EtP5- α** and averaged dipolar coupling $\langle d_{CH} \rangle$ were extracted and order parameters $\langle S_{CH} \rangle$ obtained (**Table 4.7** and **Figure 4.25(a)**). While the room temperature $\langle S_{CH} \rangle$ values for the **CH₃**, **CH₂** and **CH** carbon subgroups are virtually identical to those determined for **EtP6- β** (**Table 4.7**), a difference was observed for the **OCH₂** group upon cooling with $\langle d_{CH} \rangle$ increasing from -18.3 ± 0.7 kHz in **EtP6- β** to -19.8 ± 0.7 kHz in **EtP5- α** as evidenced by larger splitting of the outer singularities in the ¹³C ¹H dipolar spectra at 243 K (**Figures 4.25(b)**) and resulting larger $\langle S_{CH} \rangle$ values for this **OCH₂** site in **EtP5- α** (0.87 ± 0.03) than in **EtP6- β** (0.80 ± 0.03). Similarly, at higher temperature (383 K), the ¹³C ¹H dipolar coupling spectra of the **OCH₂** group yield larger $\langle d_{CH} \rangle$ values (-16.6 ± 0.7 and -14.5 ± 0.6 kHz) and smaller $\langle S_{CH} \rangle$ values (0.73 ± 0.03 vs. 0.64 ± 0.03) in **EtP5- α** than in **EtP6- β** , respectively. This indicates more restricted motion and increased hindrance which is likely due to the reduced void space of the smaller **EtP5- α** assembly versus **EtP6- β** .

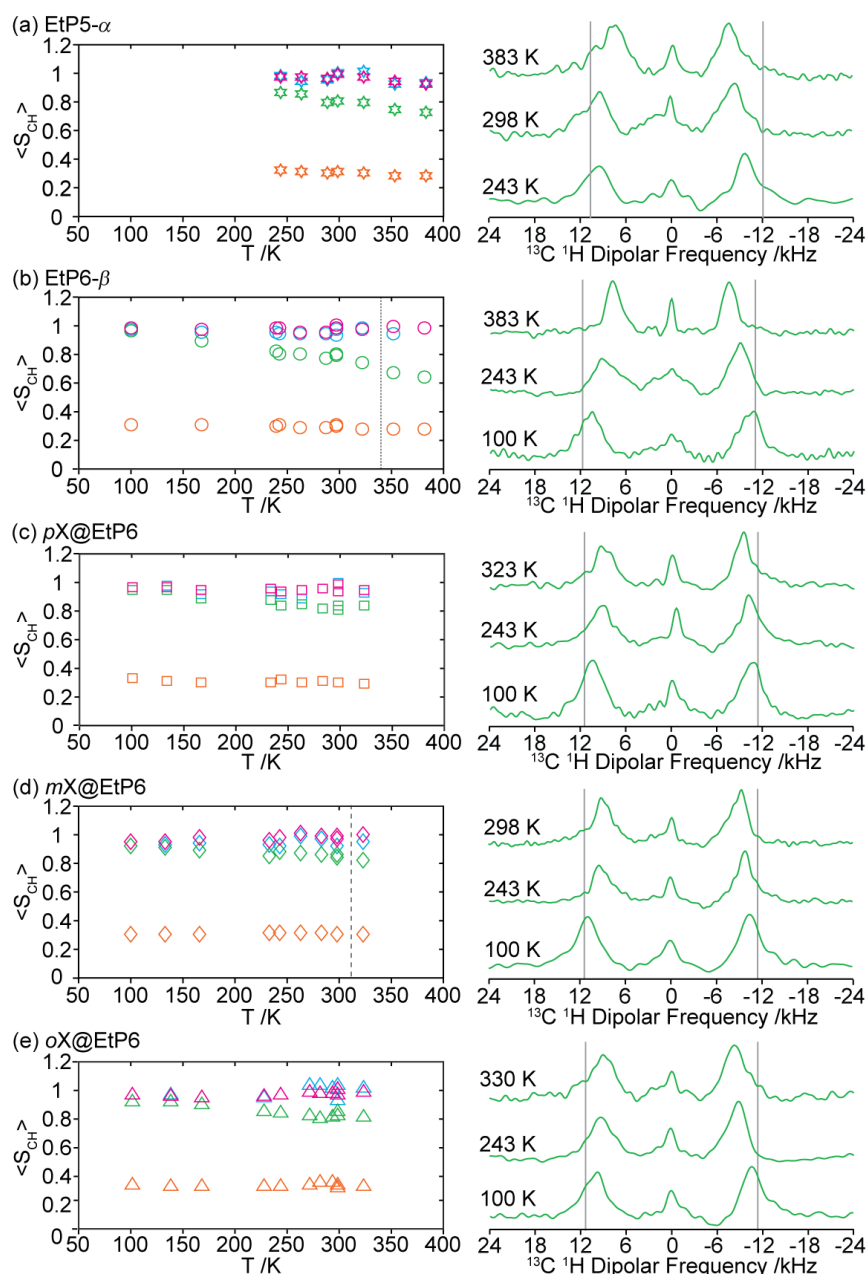


Figure 4.25. (Left) Temperature dependency of the motional averaged CH dipolar coupling order parameters $\langle S_{CH} \rangle$ and (right) selected ^{13}C ^1H dipolar coupling spectra of the OCH_2 signals at various temperatures for (a) guest-free **EtP5- α** (stars), (b) guest-free **EtP6- β** (circles) (c) **pX@EtP6** (squares) (d) **mX@EtP6** (diamonds) and (e) **oX@EtP6** (triangles). The different carbon subgroups can be identified with the following colour coding for CH_3 (orange), CH_2 (light blue), OCH_2 (green) and CH (pink) (**Figure 4.1**). Data recorded at room temperature have been collected at both 9.4 and 14.1 T. Error bars in $\langle S_{CH} \rangle$ (ΔS_{CH}) are consistently smaller than 0.04 and are obtained from estimated errors in the determination of $\langle d_{CH} \rangle$ and small variations in the dipolar coupling values across one carbon subgroup (**Figure 4.24**); these errors are less than the symbol size. Data below 243 K were not recorded for **EtP5- α** . The dotted line in (b) indicates a polymorphic transition in **EtP6- β** at 339 K (**Figure 4.20**). Dashed line in (d) represents the temperature at which *meta*-xylene is lost from **mX@EtP6** as identified by the changing NMR spectrum (**Figure 4.18**). *Para*- and *ortho*-xylenes are lost from **pX@EtP6** and **oX@EtP6** at 415 and 433 K,¹ respectively, outside the temperature range used here. Vertical light grey lines in the dipolar coupling spectra indicate the static limit dipolar coupling constants d_{CH} .

4.5.3. Temperature dependent motional averaged site-selectivity in xylene-loaded pillar[6]arenes

Variable temperature 2D PDLF experiments were also acquired for the three guest-adsorbed xylene adducts in EtP6 (**Figure 4.25(c-e)**) and the trends are largely similar to data obtained for **EtP6- β** with temperature independent $\langle S_{CH} \rangle$ around 1 for the **CH₂** and **CH** carbons in the pillar[n]arene core, around 0.3 for the **CH₃** and increasing towards 1 for the **OCH₂** group as temperatures are lowered into the static regime. Although the $\langle d_{CH} \rangle$ and hence the $\langle S_{CH} \rangle$ room temperature values for the **CH₃**, **CH₂** and **CH** carbon subgroups are within error of each other for **EtP6- β** and the xylene-adsorbed adducts, there is a significant difference observed in the $\langle S_{CH} \rangle$ values obtained for the **OCH₂** group in ***mX@EtP6*** vs. **EtP6- β /*oX@EtP6*/*pX@EtP6***. More specifically, in this **OCH₂** group, at room temperature, there is a slight increase of the site-specific order parameters $\langle S_{CH} \rangle$ from 0.79 ± 0.03 , 0.81 ± 0.03 and 0.80 ± 0.03 in **EtP6- β** , ***oX@EtP6*** and ***pX@EtP6***, respectively, to 0.84 ± 0.03 in ***mX@EtP6*** (**Table 4.7**). This small difference is enhanced upon cooling to 243 K from 0.80 ± 0.03 , 0.83 ± 0.03 and 0.84 ± 0.03 in **EtP6- β** , ***oX@EtP6*** and ***pX@EtP6***, respectively, to 0.88 ± 0.03 in ***mX@EtP6***. The data therefore seems to suggest marginally slower dynamics of the **OCH₂** group in ***mX@EtP6*** than in **EtP6- β** , ***oX@EtP6*** and ***pX@EtP6***. In contrast to ***oX@EtP6*** and ***pX@EtP6***, the xylene in ***mX@EtP6*** lies on top of the EtP6 host rather than within the void space, as illustrated in **Figure 4.1** from experimental XRD data and computational CSP methods, therefore the interaction of the *meta*-xylene with the protruding ethoxy groups is likely to cause their slower dynamics, at least for the **OCH₂** subgroup. These experiments therefore highlight small change in structure flexibility between guest-free and guest-adsorbed EtP6 assemblies.

All **CH₃**s in xylenes and ethoxy groups in all samples and at all temperatures studied here have $\langle S_{CH} \rangle$ around 0.3 as is commonly observed for methyl groups above around 100 K due to rapid **CH₃** motion as discussed above,⁷² this highlights that the adsorption into the EtP6 host does not induce any other motion in these groups. The room temperature PDLF data on the three xylene adducts revealed observable dipolar coupling for the methyl groups and **CH**s of the xylenes as expected (**Figures 4.26 – 4.28**), which combined with ¹³C-edited CP MAS spectra (**Figures 4.9, 4.11** and

4.13), were used to aid spectral assignments, in particular by differentiating these CHs from the $\text{CH}_2\text{C}^{\text{IV}}$ resonances of EtP6 that appear in the same spectral region (Figures 4.8 and 4.26 – 4.28). At room temperature, whilst the corresponding $\langle d_{\text{CH}} \rangle$ for these CHs in *pX@EtP6* and *mX@EtP6* indicate limited motion with $\langle S_{\text{CH}} \rangle$ values found in the $0.91 - 0.94 \pm 0.04$ range (Table 4.7), the CHs in *oX@EtP6* show considerably more motion with smaller $\langle S_{\text{CH}} \rangle$ values of 0.72 ± 0.04 at 298 K. This indicates that the *ortho*-xylene has a significant amount of spatial freedom to allow for mobility and that the CH and CH_3 motion of the xylene is not completely limited upon loading into the EtP6 cavity at room temperature.

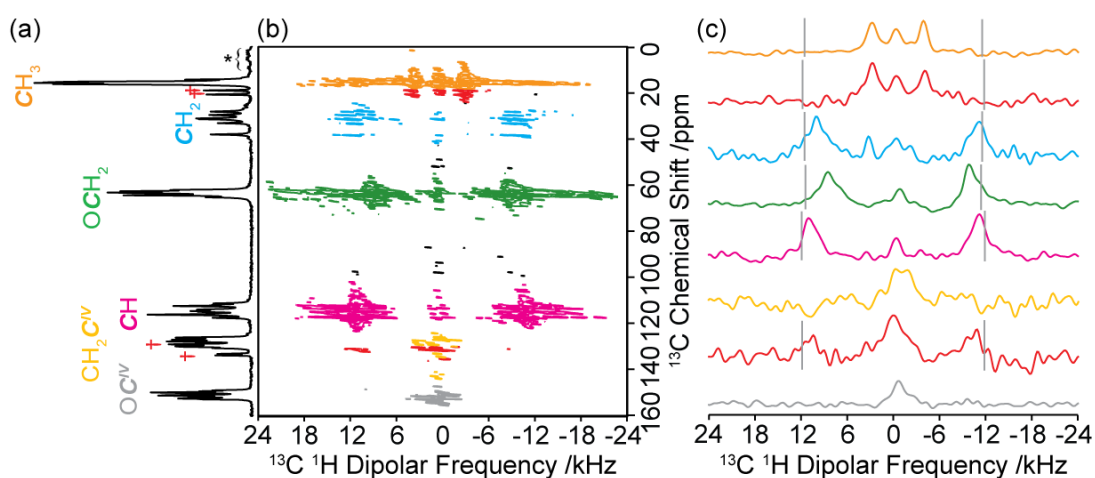


Figure 4.26. (a) ^{13}C CP MAS spectrum, (b) PDLF spectrum and (c) selected site-specific ^{13}C ^1H dipolar spectra for *pX@EtP6*. Spectral assignments are given in the figure and correspond to those previously published.¹ The data presented above was obtained at 298 K and 9.4 T. $\langle d_{\text{CH}} \rangle$ is measured using the outer singularities of the dipolar coupling spectra as highlighted in the experimental section. Vertical light grey lines indicate the static limit dipolar coupling constants d_{CH} calculated from equation 4.2 and the computed CH distances obtained at the DFT level on the various conformers identified by CSP. Red daggers (†) and asterisks (*) denote signals arising from the *para*-xylene guest and spinning sidebands, respectively.

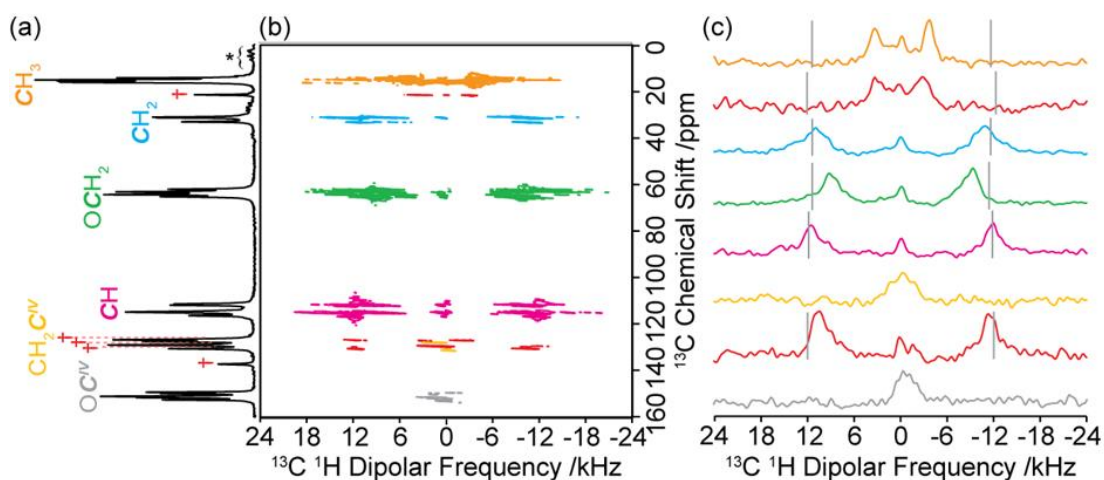


Figure 4.27. (a) ^{13}C CP MAS spectrum, (b) PDLF spectrum and (c) selected site-specific ^{13}C ^1H dipolar spectra for *mX@EtP6*. Spectral assignments are given in the figure and correspond to those previously published.¹ The data presented above was obtained at 298 K and 9.4 T. $\langle d_{\text{CH}} \rangle$ is measured using the outer singularities of the dipolar coupling spectra as highlighted in the experimental section. Vertical light grey lines indicate the static limit dipolar coupling constants d_{CH} calculated from **equation 4.2** and the computed CH distances obtained at the DFT level on the various conformers identified by CSP. Red daggers (†) and asterisks (*) denote signals arising from the *meta*-xylene guest and spinning sidebands, respectively.

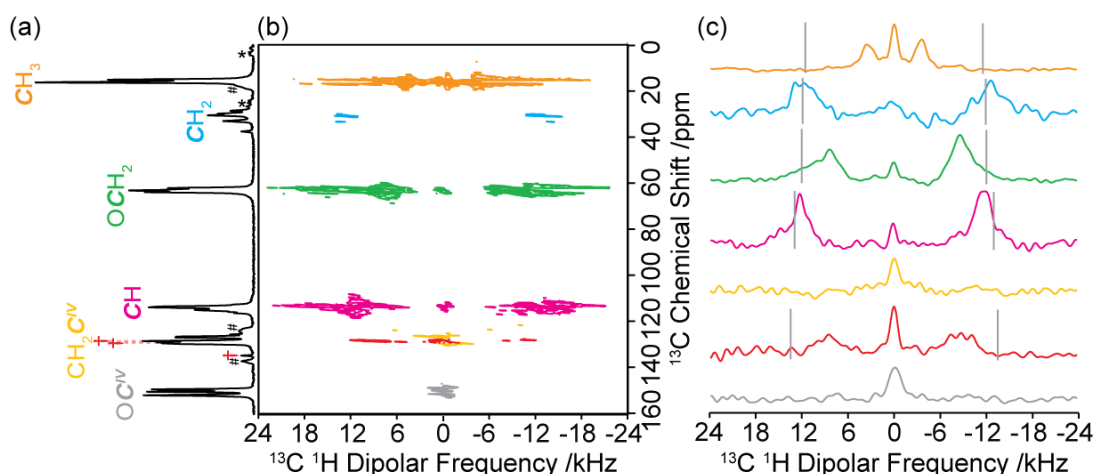


Figure 4.28. (a) ^{13}C CP MAS spectrum, (b) PDLF spectrum and (c) selected site-specific ^{13}C ^1H dipolar spectra for **oX@EtP6**. Spectral assignments are given in the figure and correspond to those previously published.¹ The data presented above was obtained at 298 K and 9.4 T. $\langle d_{\text{CH}} \rangle$ is measured using the outer singularities of the dipolar coupling spectra as highlighted in the experimental section. Vertical light grey lines indicate the static limit dipolar coupling constants d_{CH} calculated from **equation 4.2** and the computed CH distances obtained at the DFT level on the various conformers identified by CSP. Broad signals tentatively assigned to some unknown amorphous phase(s) are marked with dashes (#). Red daggers (†) and asterisks (*) denote signals arising from the *ortho*-xylene guest and spinning sidebands, respectively.

4.5.4. Host-guest interaction probed by dipolar coupling in xylene-loaded pillar[6]arenes

No large dipolar coupling is observed at room temperature for the quaternary carbons of either the xylenes or the pillar[6]arene host in *pX@EtP6*, *mX@EtP6* and *oX@EtP6* (Figures 4.23 and 4.26-4.28) as expected, however, surprisingly, upon cooling *pX@EtP6* to 100 K, strong dipolar couplings of -23.4 ± 0.8 kHz were observed for the $\text{CH}_2\text{C}^{\text{IV}}$ carbon (Figures 4.29 and 4.30(c)). These couplings in *pX@EtP6* do not originate from either of the CHs in the xylene which appear at 129.4 and 129.8 ppm and appear in the $\text{CH}_2\text{C}^{\text{IV}}$ chemical shift region of 125-131 ppm or a long range interaction in the EtP6 architecture as no coupling is observed in the $\text{CH}_2\text{C}^{\text{IV}}$ of guest-free EtP6- β (Figure 4.23 at room temperature and Figure 4.31 at 100 K). Therefore, this coupling was ascribed to intermolecular heteronuclear dipolar coupling between the quaternary $\text{CH}_2\text{C}^{\text{IV}}$ carbon of the EtP6 host and the protons of *para*-xylene identifying EtP6-*para*-xylene spatial interaction and strong host-guest interaction. These results are in sharp contrast to the 100 K PDLF data for *mX@EtP6* and *oX@EtP6* adducts (Figures 4.32 and 4.33 respectively) for which no coupling is observed for $\text{CH}_2\text{C}^{\text{IV}}$ s suggesting an absence of host-guest interaction (or that the corresponding intermolecular coupling is likely still averaged out at 100 K).

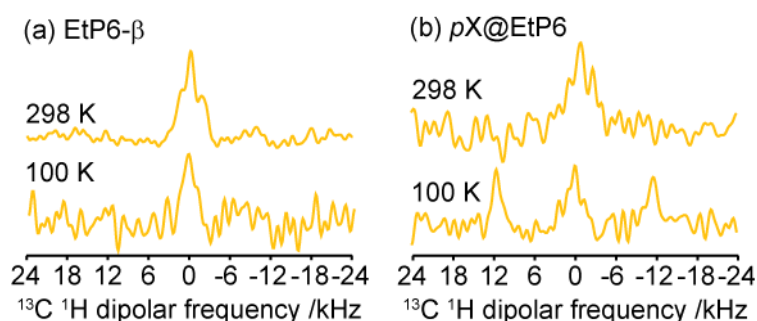


Figure 4.29. Comparison of selected $\text{CH}_2\text{C}^{\text{IV}}$ ^{13}C ^1H dipolar spectra for (a) EtP6- β and (b) *pX@EtP6* obtained at 298 K and 9.4 T, and at 100 K and 14.1 T. The polarisation transfer to ^{13}C during the PRESTO block of 2D PDLF sequence was optimised for maximum signal on the protonated resonances (see Materials and Methods section 4.4) which accounts for the signal to noise of these quaternary carbon resonances.

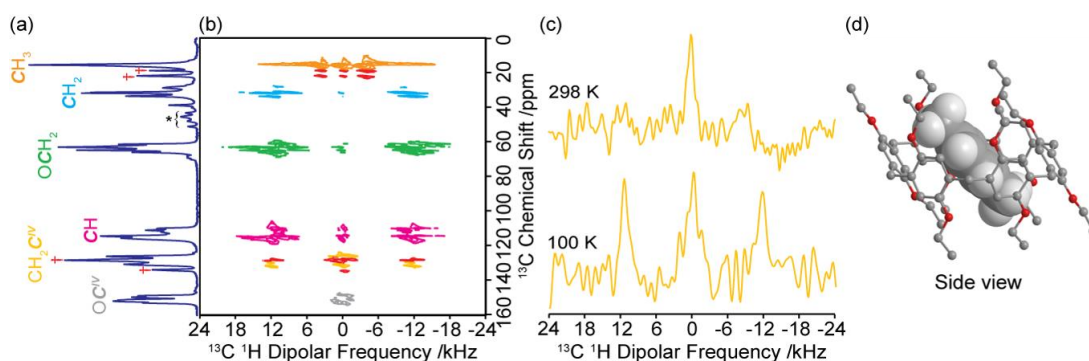


Figure 4.30. (a) ^{13}C CP MAS spectrum at 100 K, (b) PDLF spectrum at 100 K and (c) comparison of selected site-specific ^{13}C ^1H dipolar spectra for the host $\text{CH}_2\text{C}^{\text{IV}}$ quaternary carbon in $p\text{X}@EtP6$ obtained at 298 K and 100 K. Data presented above were obtained at 14.1 T, (d) side view of $p\text{X}@EtP6$. Spectral assignments are given in the figure. Signals arising from the adsorbed *para*-xylene guest are assigned with red daggers (\dagger). Vertical light grey lines in the spectra indicate the static limit dipolar coupling constants d_{CH} . Asterisks (*) denote spinning sidebands.

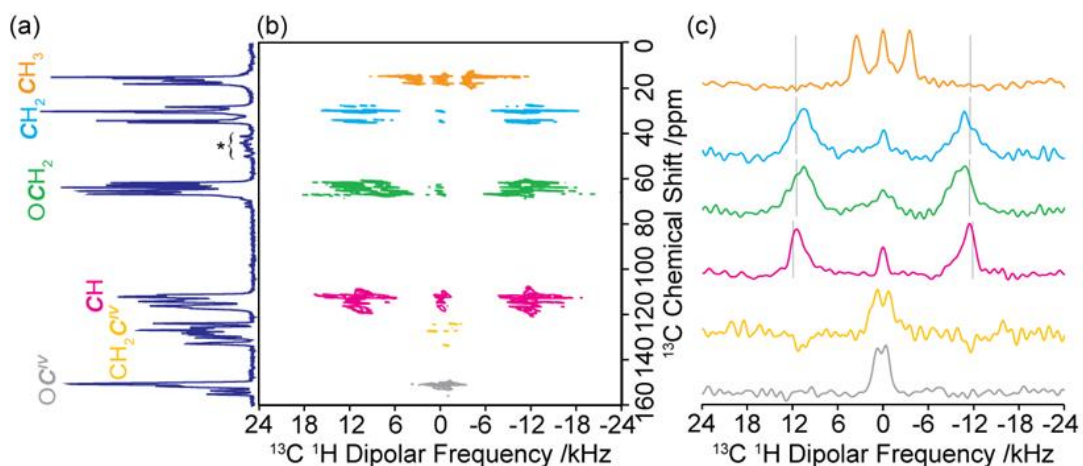


Figure 4.31. (a) ^{13}C CP MAS spectrum, (b) PDLF spectrum and (c) selected site-specific ^{13}C ^1H dipolar spectra for guest-free $\text{EtP6-}\beta$. Spectral assignments are given in the figure and correspond to those previously published.¹ The data presented above was obtained at 100 K and 9.4 T. $\langle d_{\text{CH}} \rangle$ is measured using the outer singularities of the dipolar coupling spectra as highlighted in the experimental section. Vertical light grey lines indicate the static limit dipolar coupling constants d_{CH} calculated from **equation 4.2** and the computed CH distances obtained at the DFT level on the various conformers identified by CSP. Asterisks (*) denote spinning sidebands.

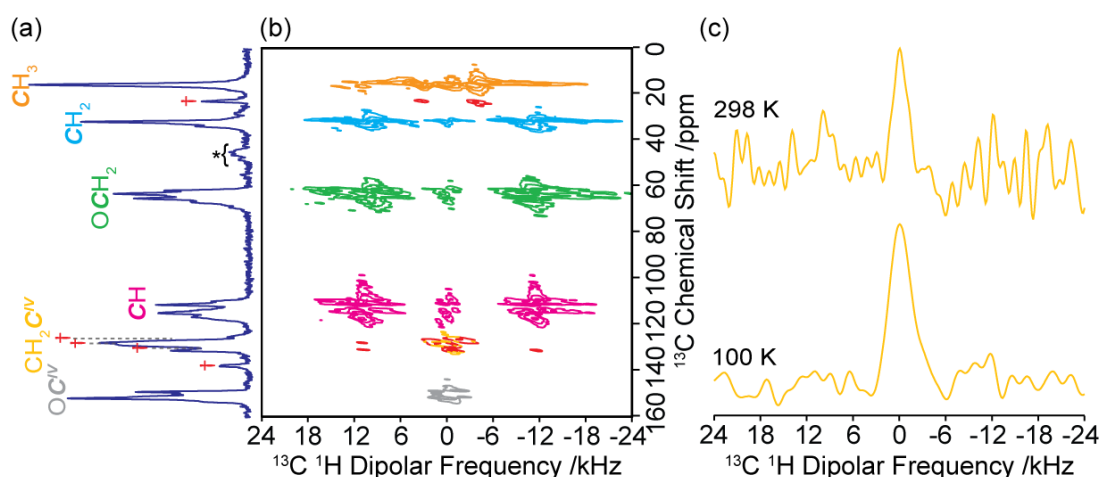


Figure 4.32. (a) ^{13}C CP MAS spectrum at 100 K, (b) PDLF spectrum at 100 K and (c) comparison of selected site-specific ^{13}C ^1H dipolar spectra for the host $\text{CH}_2\text{C}^{\text{IV}}$ quaternary carbon in *mX@EtP6* obtained at 298 and 100 K. Data presented above were obtained at 14.1 T. Spectral assignments are given in the figure. Signals arising from the adsorbed *meta*-xylene guest are assigned with red daggers (\dagger). No 2D PDLF signal is observed for the quaternary carbon of the *meta*-xylene due to poor signal to noise. Vertical light grey lines in the spectra indicate the static limit dipolar coupling constants d_{CH} . Asterisks (*) denote spinning sidebands.

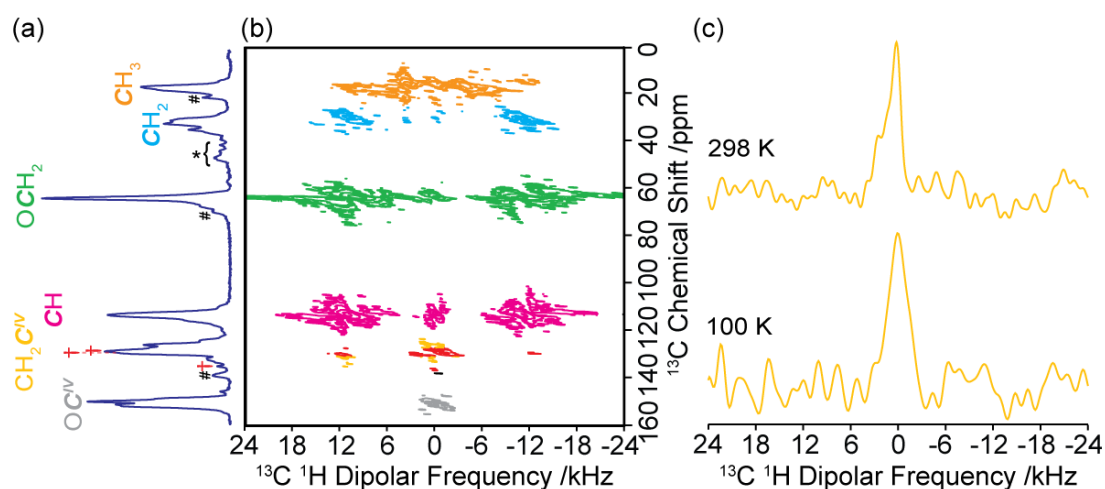


Figure 4.33. (a) ^{13}C CP MAS spectrum at 100 K, (b) PDLF spectrum at 100 K and (c) comparison of selected site-specific ^{13}C ^1H dipolar spectra for the host $\text{CH}_2\text{C}^{\text{IV}}$ s quaternary carbon in *oX@EtP6*. Data presented above were obtained at 14.1 T. Spectral assignments are given in the figure. Signals arising from the adsorbed *ortho*-xylene guest are assigned with red daggers (\dagger), except the corresponding methyl resonance which is not directly attributable (see text). Broad signals tentatively assigned to some unknown amorphous phase(s) are marked with dashes (#). Vertical light grey lines in the spectra indicate the static limit dipolar coupling constants d_{CH} . Asterisks (*) denote spinning sidebands.

These results strongly support the structures obtained from single crystal X-ray studies¹ illustrated in **Figure 4.1**. In particular, in ***pX@EtP6***, *para*-xylene is located in the centre of the EtP6 cavity which is stabilised by strong π - π stacking with two aromatic rings from EtP6 (**Figure 4.1(c)**), yielding strong heteronuclear dipolar coupling $\langle d_{\text{CH}} \rangle$ between the $\text{CH}_2\text{C}^{\text{V}}$ carbons of the pillar[6]arene backbone with the *para*-xylene protons. It is also likely that this coupling arises preferentially from the aromatic protons of *para*-xylene rather than the methyl protons as their $\langle d_{\text{CH}} \rangle$ are small and averaged out to one third by methyl group rotation around the carbon-carbon single bond. In ***oX@EtP6***, similar rotational dynamics prevent coupling of the methyl protons of *ortho*-xylene located inside the cavity to the EtP6 backbone while the aromatic protons are positioned outside the cavity (**Figure 4.1(e)**) from which a small static dipolar coupling would only be expected (0.44 kHz based on the smallest 4.1 Å distance with the EtP6 $\text{CH}_2\text{C}^{\text{V}}$ carbon). The small EtP6 cavity in ***mX@EtP6*** is too small to host *meta*-xylene (**Figure 4.1(d)**) resulting in *m*-xylene to be excluded from the host and the absence of dipolar coupling interaction with EtP6.

4.5.5. Temperature dependent relaxation studies of guest-free and loaded pillar[n]arenes

T_1 relaxation is a measure of the time for the spin population to recover to equilibrium after a perturbation and is mediated by fluctuations of the local magnetic fields, as quantified by the correlation times of the motion τ_c with corresponding frequencies τ_c^{-1} on the order of the Larmor frequency, *i.e.*, MHz. The ^1H and ^{13}C spin lattice relaxation rates T_1^{-1} s have been obtained versus temperatures (**Figures 4.34 - 4.38**) in the 383 - 243 K and 298 - 100 K temperature range at 9.4 T ($\nu_0(^1\text{H}) = 400$ MHz, $\nu_0(^{13}\text{C}) = 100$ MHz) and 14.1 T ($\nu_0(^1\text{H}) = 600$ MHz, $\nu_0(^{13}\text{C}) = 150$ MHz), respectively, for **EtP6- β** , all xylene-adsorbed EtP6 adducts and **EtP5- α** (data only available at 9.4 T for this phase).

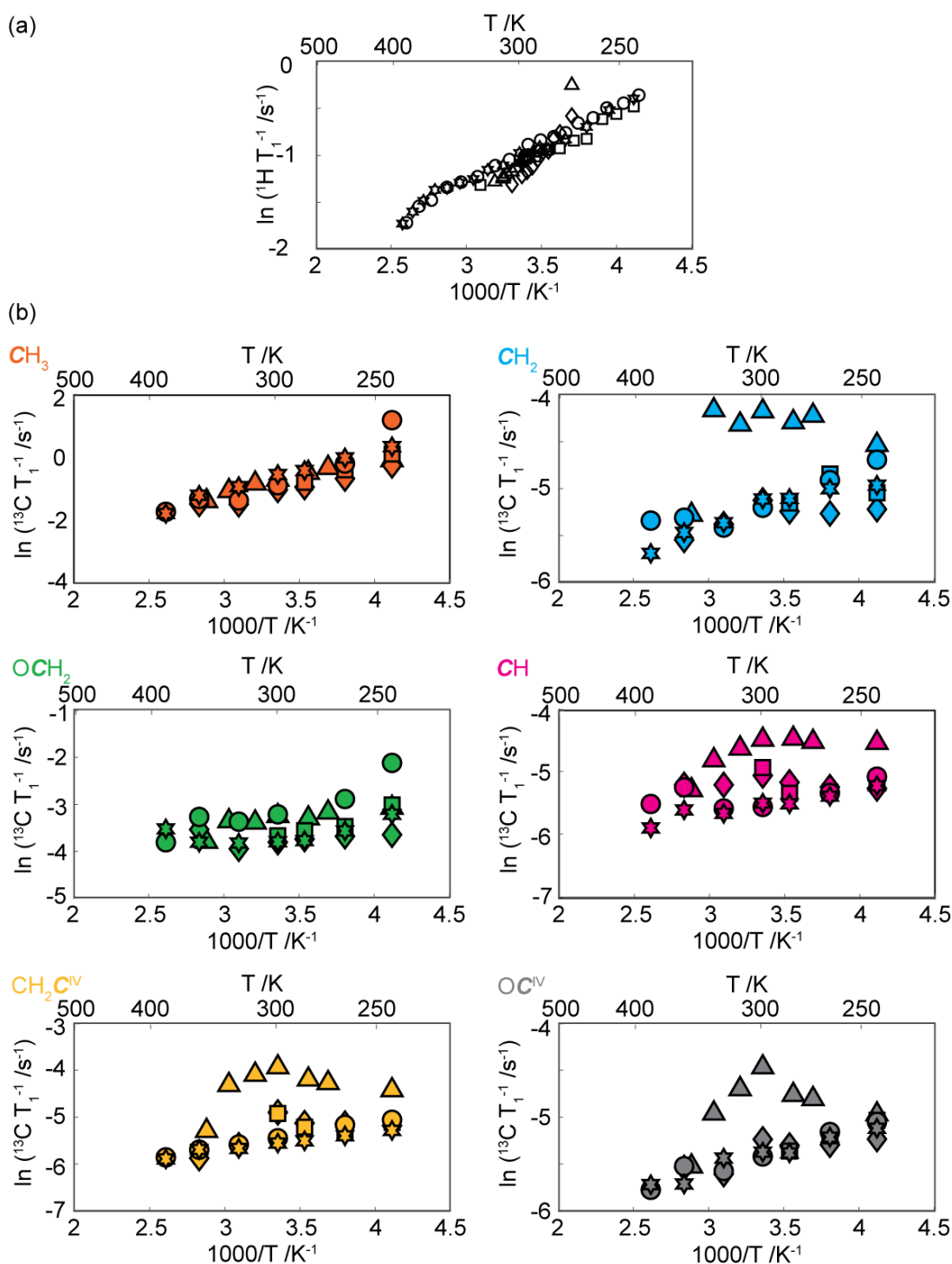


Figure 4.34. (a) ^1H and (b) ^{13}C spin-lattice relaxation rates (T_1^{-1}) Arrhenius plots. Data were obtained at 9.4 T for guest-free **EtP5- α** (stars), guest-free **EtP6- β** (circles), **pX@EtP6** (squares), **mX@EtP6** (diamonds) and **oX@EtP6** (triangles). The data were fitted to a stretch exponential function in the form of $1 - \exp[-(\tau/T_1)^\alpha]$ and the errors associated are given to a 95% confidence level and are smaller than the symbol sizes.

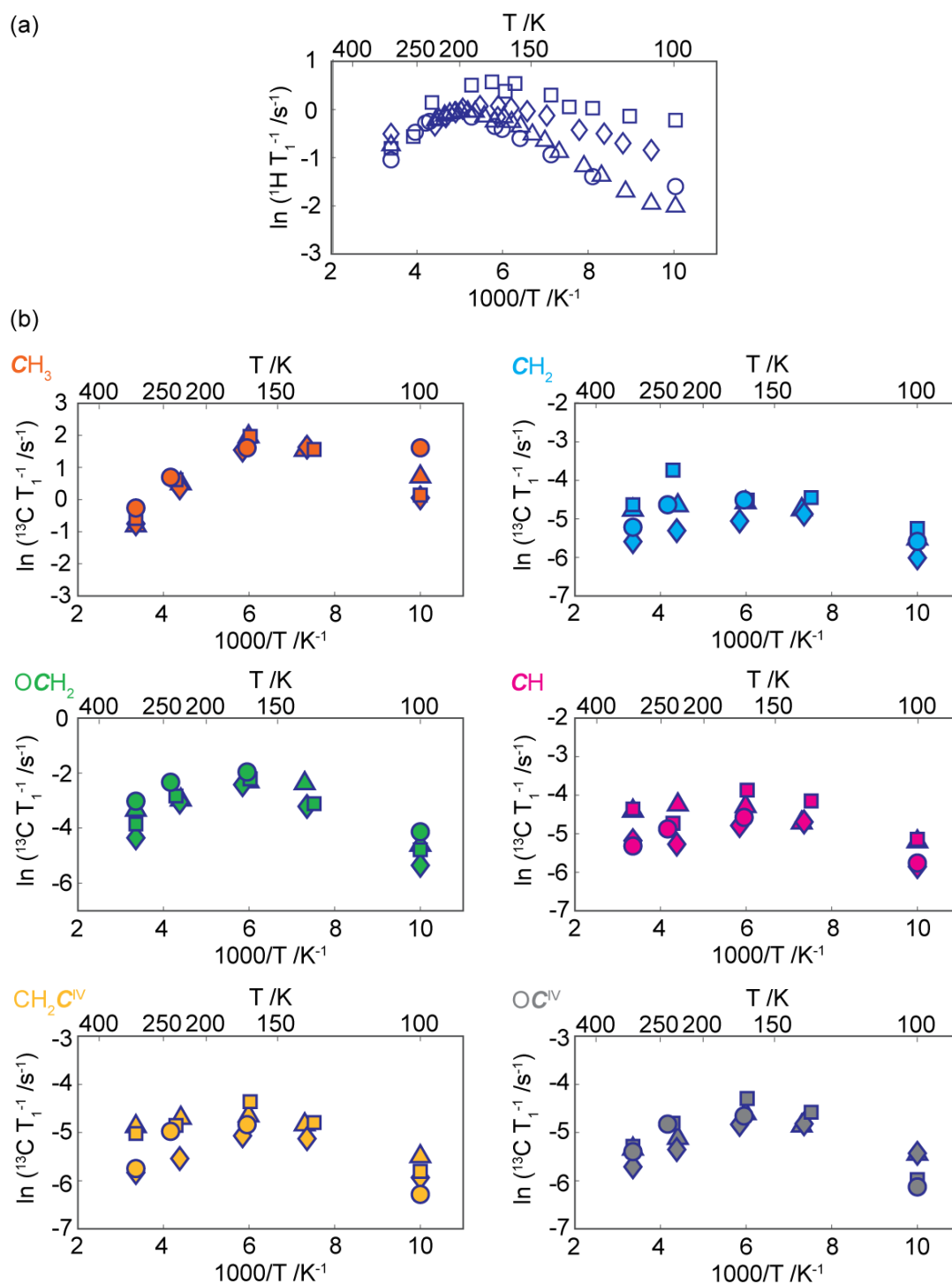


Figure 4.35. (a) ^1H and (b) ^{13}C spin-lattice relaxation rates (T_1^{-1}) Arrhenius plots. Data were obtained at 14.1 T for **EtP6- β** (circles), **pX@EtP6** (squares), **mX@EtP6** (diamonds) and **oX@EtP6** (triangles). The data were fitted to a stretch exponential function in the form of $1 - \exp[-(\tau/T_1)^\alpha]$ and the errors associated are given to a 95% confidence level and are smaller than the symbol sizes.

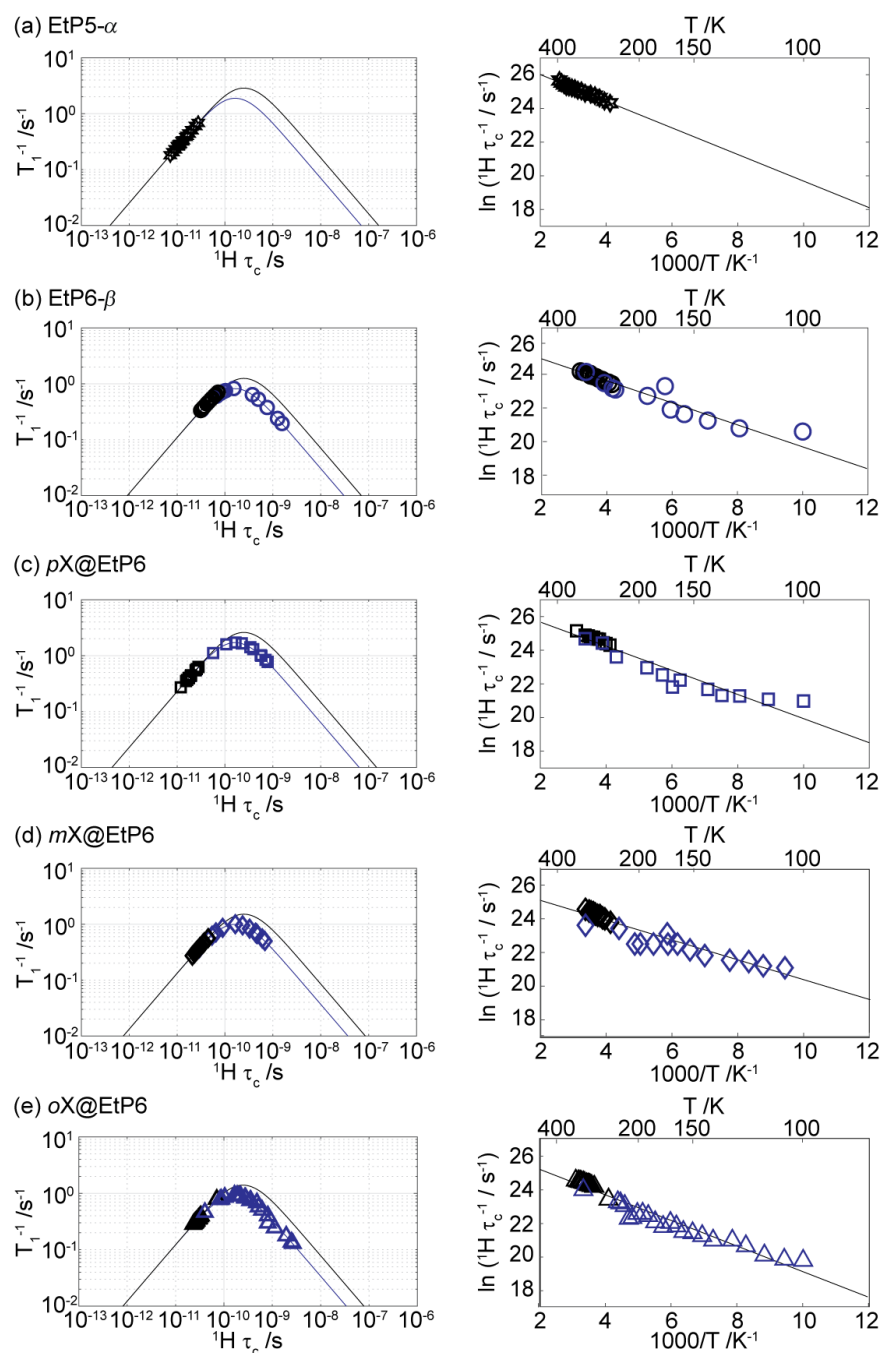


Figure 4.36. (Left) ^1H spin–lattice relaxation rates T_1^{-1} against correlation times τ_c and (right) corresponding ^1H correlation frequencies τ_c^{-1} Arrhenius plots. Data shown in black and blue were obtained at 9.4 T and 14.1 T, respectively, for (a) guest-free **EtP5- α** (stars), (b) guest-free **EtP6- β** (circles), (c) **pX@EtP6** (squares), (d) **mX@EtP6** (diamonds) and (e) **oX@EtP6** (triangles). The associated errors are smaller than the symbol sizes. The solid (-) lines in the left panels are those obtained from a dipolar coupling relaxation mechanism (equation 4.7) at both fields using experimentally determined local field fluctuations terms of 2×10^9 , 5×10^9 , 3×10^9 and $2 \times 10^9 \text{ s}^{-2}$ for **EtP6- β** , **pX@EtP6**, **mX@EtP6** and **oX@EtP6**, respectively (A calculated value of $5 \times 10^9 \text{ s}^{-2}$ from the ^1H - ^1H distances computed by CSP was used for **EtP5- α** as no T_1 minimum was found in the temperature range studied) and in the right panels are fit to the Arrhenius equation.

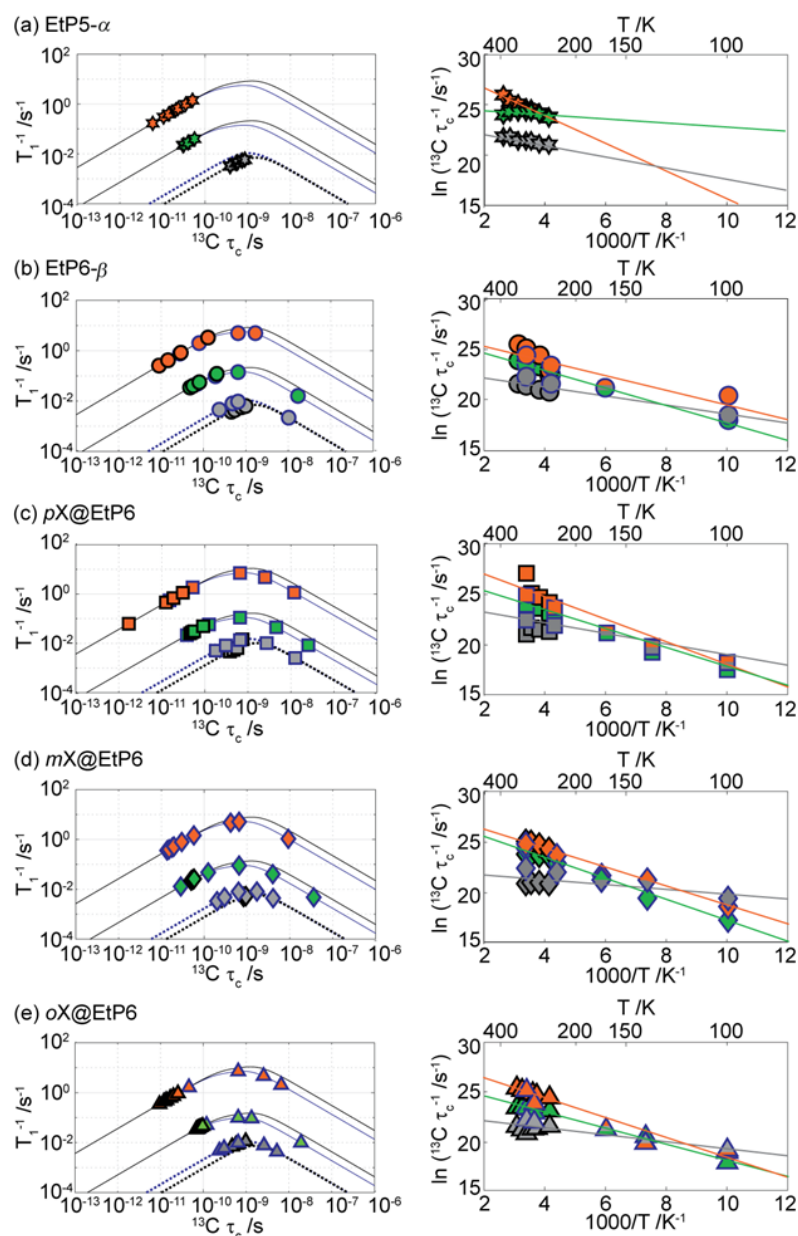


Figure 4.37. (Left) ^{13}C spin-lattice relaxation rates T_1^{-1} against correlation times τ_c and (right) corresponding ^{13}C correlation frequencies τ_c^{-1} Arrhenius plots. Data shown in black and blue outlines were obtained at 9.4 T and 14.1 T, respectively, for (a) guest-free **EtP5- α** (stars), (b) guest-free **EtP6- β** (circles), (c) **pX@EtP6** (squares), (d) **mX@EtP6** (diamonds) and (e) **oX@EtP6** (triangles). Selected carbon subgroups have been plotted here with the following colour coding for CH $_3$ (orange), OCH $_2$ (green) and OC $^{\text{IV}}$ (grey) (**Figure 4.1**) whilst plot giving the three other carbons are given in **Figure 4.38**. The associated errors are smaller than the symbol sizes. In the left panels, the solid (-) lines are those obtained from a dipolar coupling relaxation mechanism (**equation 4.10**) for CH $_3$ (orange) and OCH $_2$ (green) and the dotted (· ·) lines from a CSA relaxation mechanism (**equation 4.11**) for OC $^{\text{IV}}$ (grey) at both fields, using the experimentally determined local magnetic fields terms (values from **EtP6- β** were used for **EtP5- α** as no T_1 minimum was found in the temperature range studied). A T_1 minima was found for OC $^{\text{IV}}$ in **oX@EtP6** in the temperature range studied at 9.4 T, therefore this data was used to extract correlation times and is plotted for this series. In the right panels, the lines are fit to the experimental data using the Arrhenius equation.

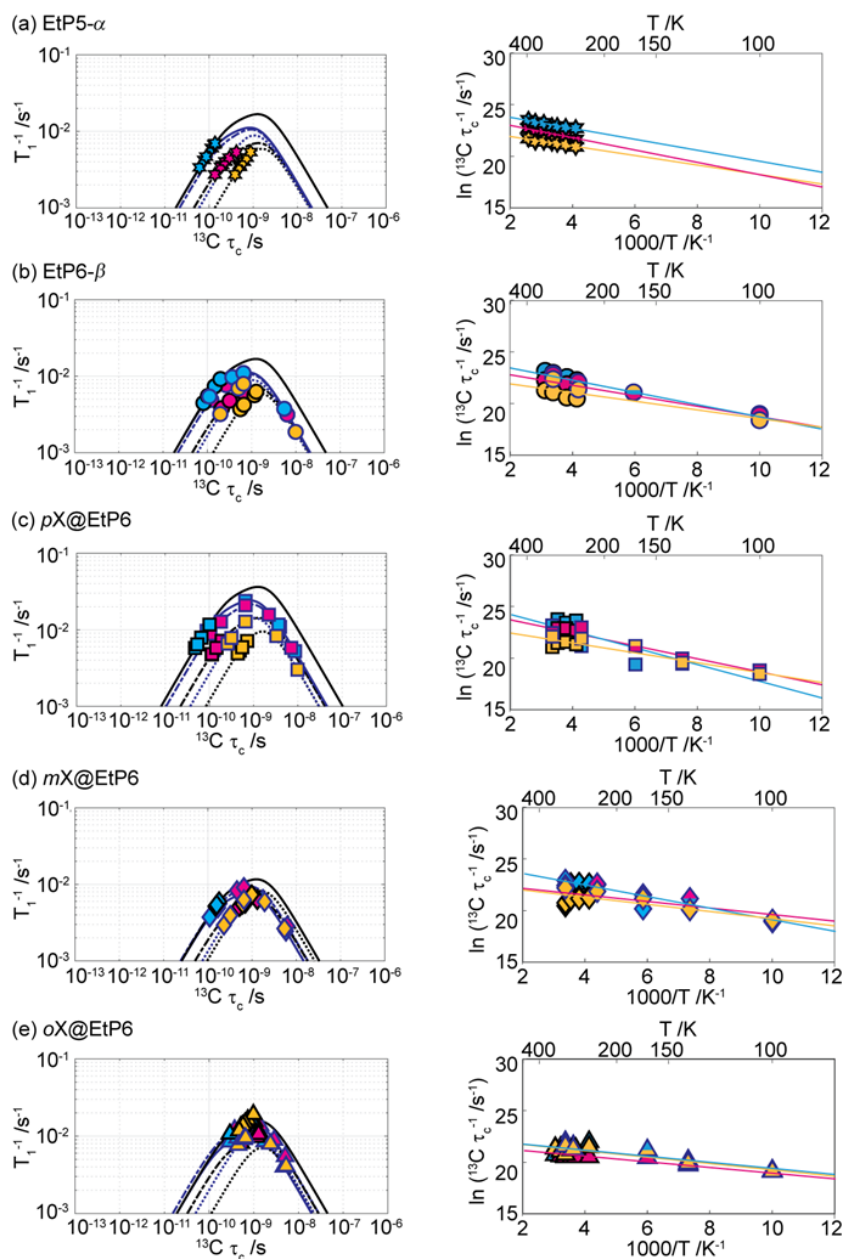


Figure 4.38. (Left) ^{13}C spin–lattice relaxation rates T_1^{-1} against correlation times τ_c and (right) corresponding ^{13}C correlation frequencies τ_c^{-1} Arrhenius plots. Data shown in black and blue outlines were obtained at 9.4 T and 14.1 T, respectively, for (a) guest-free **EtP5- α** (stars), (b) guest-free **EtP6- β** (circles), (c) **pX@EtP6** (squares), (d) **mX@EtP6** (diamonds) and (e) **oX@EtP6** (triangles). Selected carbon subgroups have been plotted here with the following colour coding for CH_2 (light blue), CH (pink) and $\text{CH}_2\text{C}^{\text{IV}}$ (yellow) (**Figure 4.1**) whilst plot giving the three other carbons are given in **Figure 4.37**. The associated errors are smaller than the symbol sizes. In the left panels, the dashed (–) lines are those obtained from dipolar coupling and CSA relaxation mechanisms (**equation 4.9**) for CH (pink), the solid lines (–) from a dipolar coupling relaxation mechanism (**equation 4.10**) for CH_2 (light blue) and the dotted (·) lines from a CSA relaxation mechanism (**equation 4.11**) for $\text{CH}_2\text{C}^{\text{IV}}$ (yellow) at both fields, using the experimentally determined local magnetic fields terms (values from **EtP6- β** were used for **EtP5- α** as no T_1 minimum was found in the temperature range studied). A T_1 minima was found for OC^{V} in **oX@EtP6** in the temperature range studied at 9.4 T, this data was used to extract correlation times and is plotted for this series. In the right panels, the lines are fit to the experimental data using the Arrhenius equation.

The corresponding ^1H one pulse spectra were obtained at 9.4 T for **EtP5- α** , **EtP6- β** , **pX@EtP6**, **mX@EtP6** and **oX@EtP6** as shown in panel (a) in **Figures 4.39-4.43** respectively. Limited resolution allows for identification of very chemically distinct sites. Upon increasing the field to 20 T and increasing the MAS rate to 60 kHz, resolution of the ^1H one pulse spectra increases, to allow further sites to be identified (panel (c) in **Figures 4.39-4.43**) however, due to the significant broadening due to ^1H ^1H dipolar coupling within ^1H spectra within the solid state, only limited information can be obtained. The ^1H one pulse spectra obtained upon variable temperature at 14.1 T are shown in panel (b) of **Figures 4.39-4.43**. The T_1 values extracted from the corresponding variable temperature saturation recovery experiments obtained *via* spectral integration of the entire spectra are shown in **Figure 4.35(a)** and used to extract corresponding correlation times τ_c discussed throughout this manuscript.

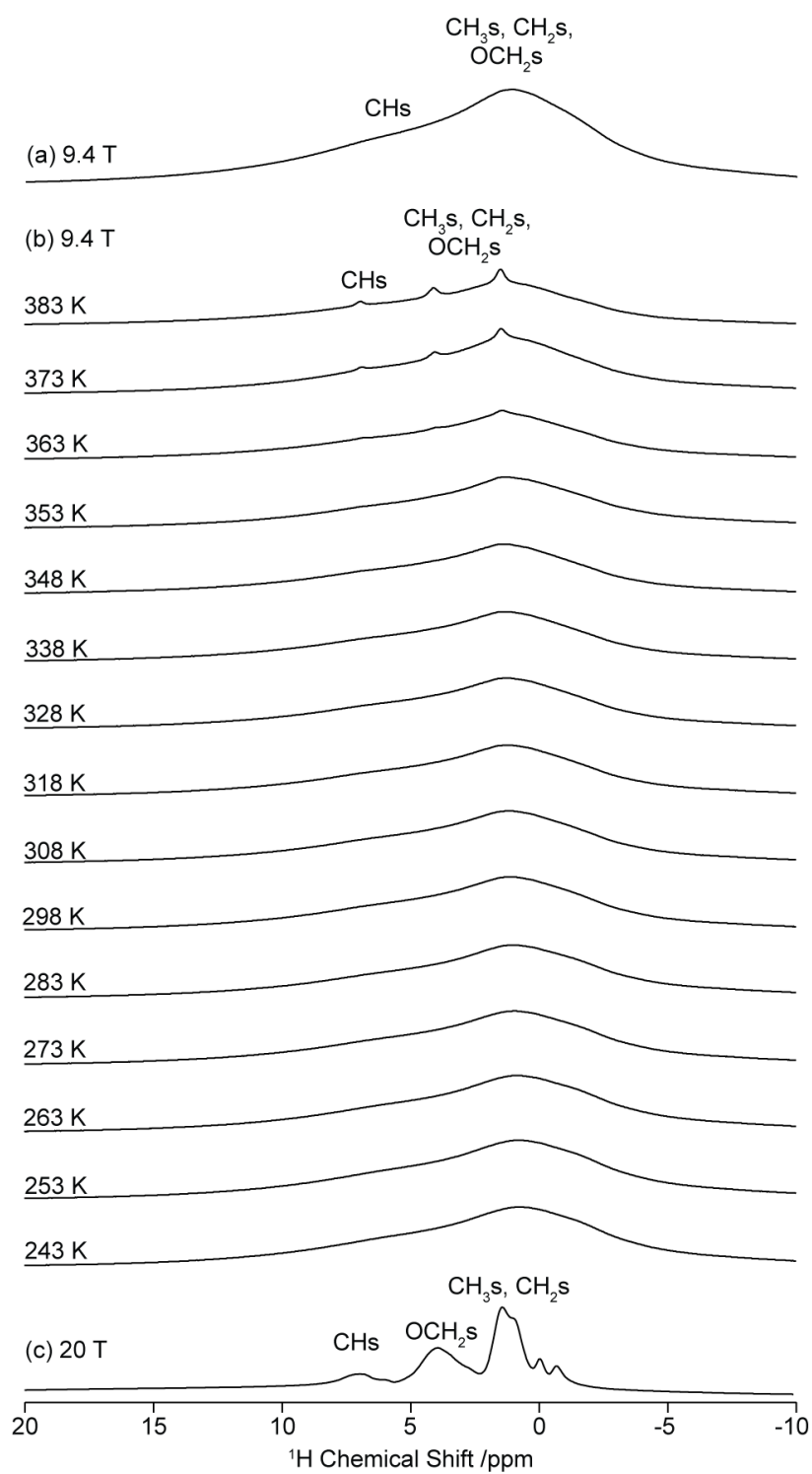


Figure 4.39. ^1H one pulse MAS NMR spectra of EtP5- α obtained (a) under MAS at $\nu_r = 12.5$ kHz and 9.4 T, (b) under variable temperature conditions at $\nu_r = 12.5$ kHz and 9.4 T and (c) at $\nu_r = 60$ kHz at 20 T. Spectral assignments are given in the figure.

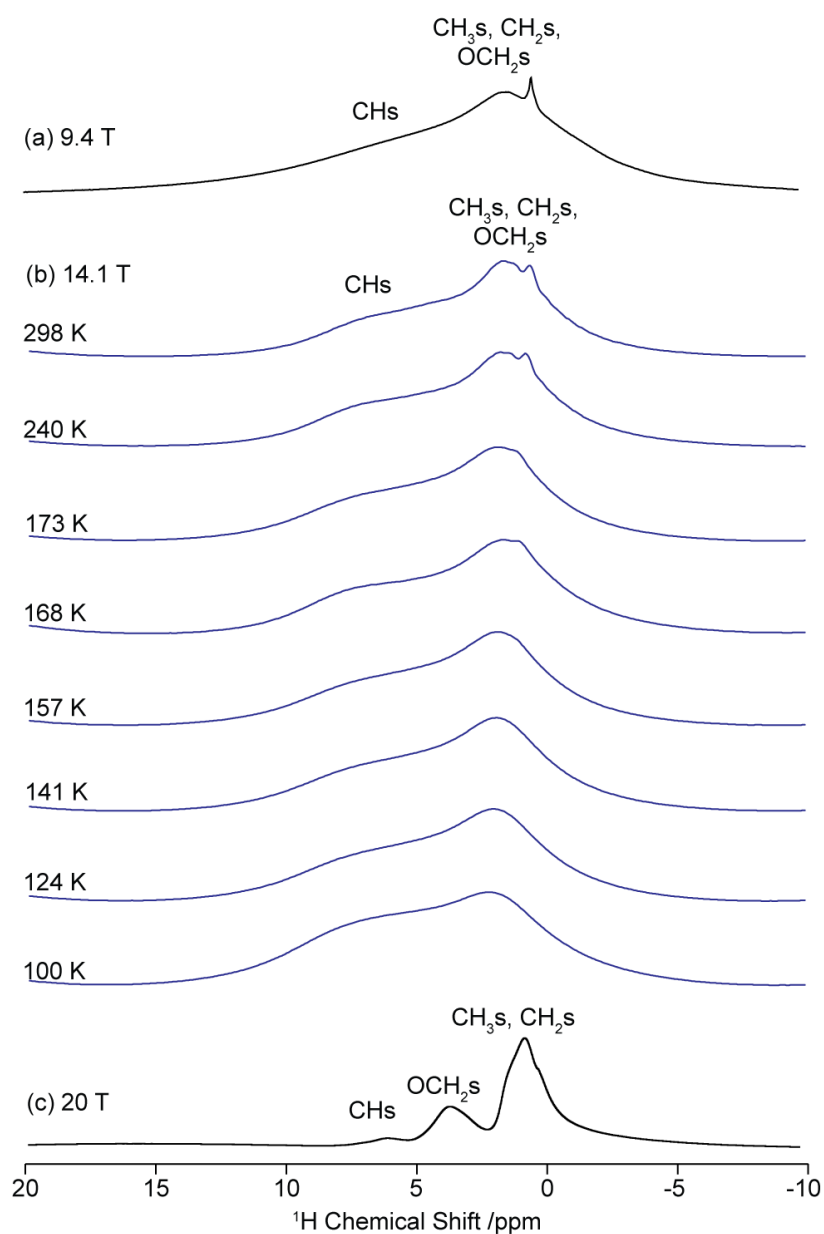


Figure 4.40. ^1H one pulse NMR spectra of **EtP6- β** (a) obtained at $\nu_r = 12.5$ kHz and 9.4 T (b) obtained under variable temperature conditions at $\nu_r = 12.5$ kHz and 9.4 T and (c) obtained at $\nu_r = 60$ kHz at 20 T. Spectral assignments are given in the figure.

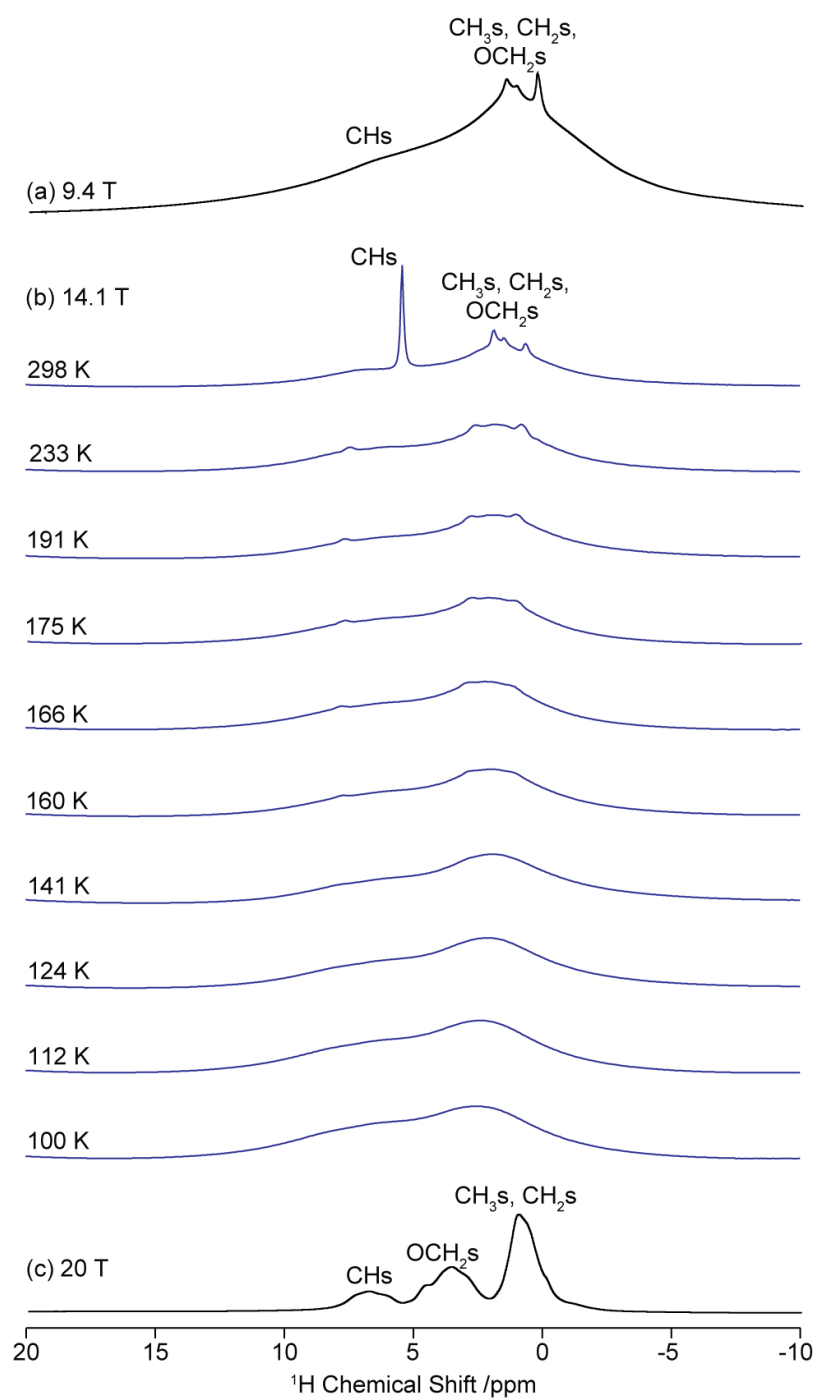


Figure 4.41. ^1H one pulse NMR spectra of $p\text{X}@EtP6$ (a) obtained at $\nu_r = 12.5$ kHz and 9.4 T (b) obtained under variable temperature conditions at $\nu_r = 12.5$ kHz and 9.4 T and (c) obtained at $\nu_r = 60$ kHz at 20 T. Spectral assignments are given in the figure.

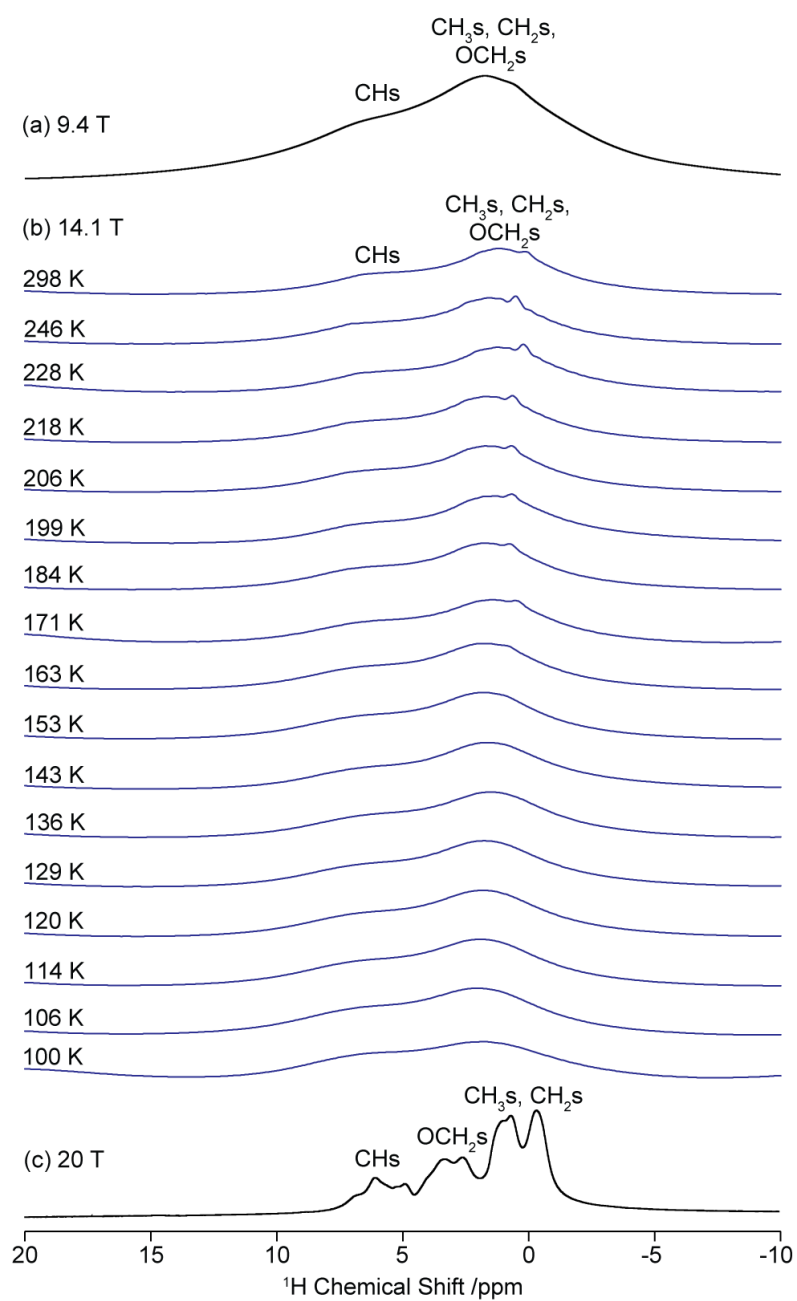


Figure 4.42. ^1H one pulse NMR spectra of $m\text{X@EtP6}$ (a) obtained at $\nu_r = 12.5$ kHz and 9.4 T (b) obtained under variable temperature conditions at $\nu_r = 12.5$ kHz and 9.4 T and (c) obtained at $\nu_r = 60$ kHz at 20 T. Spectral assignments are given in the figure.

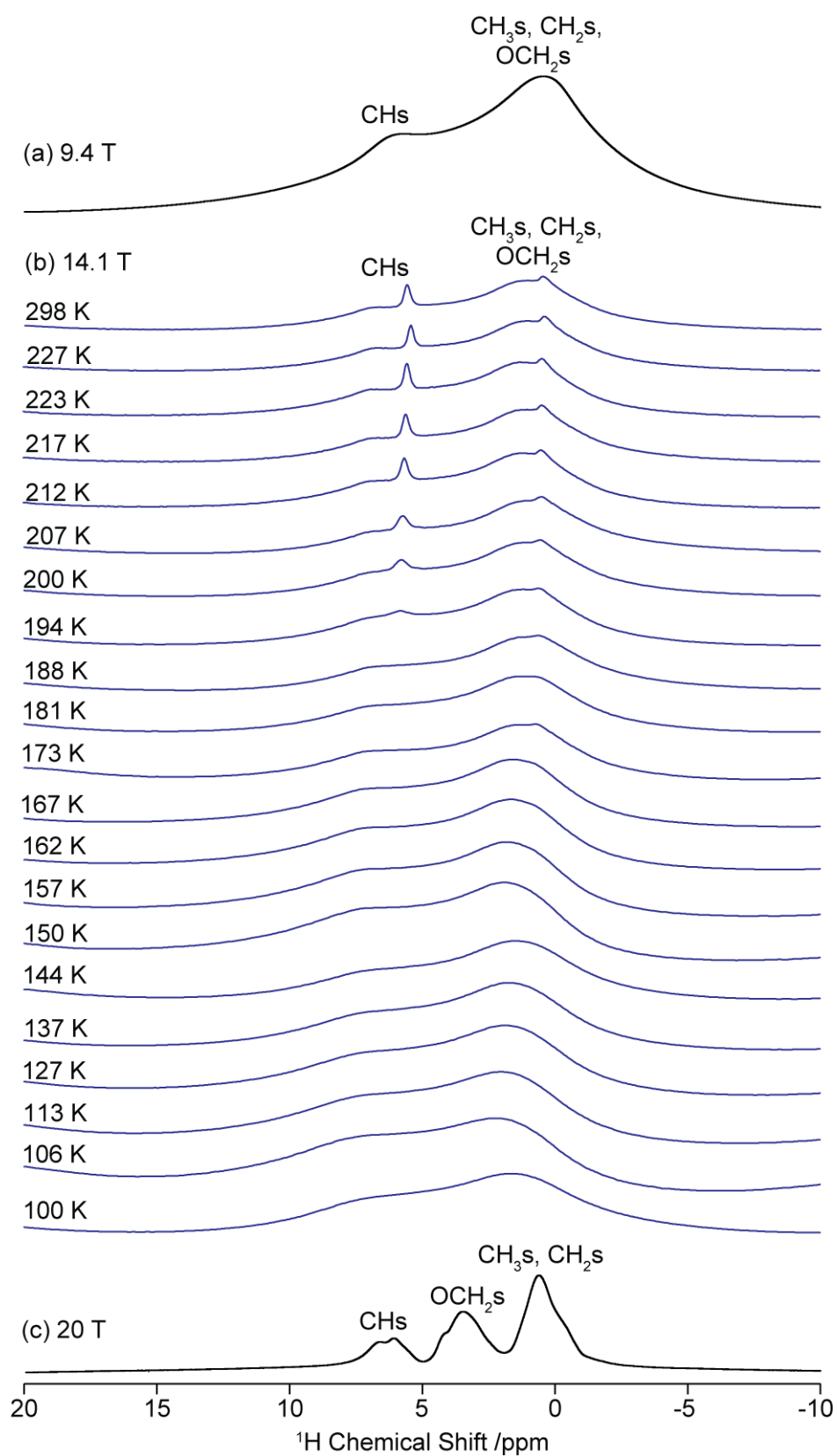


Figure 4.43. ^1H one pulse NMR spectra of oX@EtP6 (a) obtained at $\nu_r = 12.5$ kHz and 9.4 T (b) obtained under variable temperature conditions at $\nu_r = 12.5$ kHz and 9.4 T and (c) obtained at $\nu_r = 60$ kHz at 20 T. Spectral assignments are given in the figure.

Additionally, the ^1H T_1 's are fairly long (3 s for **EtP6- β** at 298 K and 9.4 T) and ^1H ^1H spin diffusion results in an equilibration of the T_1 values for all resonances so that it is likely that the ^1H T_1 s detect the same motional processes. At 14.1 T and for all materials, the ^1H T_1^{-1} values increase with increasing temperatures, reaching a maximum around 160 K for **pX@EtP6**, 170 K for **mX@EtP6** and 190 K for both **EtP6- β** and **oX@EtP6**, and then decreasing above these temperatures (**Figure 4.35(b)**). At these T_1^{-1} maxima, the motion is near the ^1H Larmor frequency $\omega_{0,\text{H}}$ (in $\text{rad}\cdot\text{s}^{-1}$) with the following expression being satisfied:⁷³

$$\omega_{0,\text{H}}\tau_c \approx 0.62 \quad (4.6)$$

from which a τ_c value of 2.5×10^{-10} s at the aforementioned temperatures for the named materials could be obtained for ^1H at 14.1 T. The ^1H T_1^{-1} s maxima are not observed in the 383 - 243 K temperature range accessible on the MAS probe at 9.4 T which is in agreement with the largely magnetic field independence of dipolar coupling driven T_1 s values as illustrated in **Figure 4.34 - 4.36**, and **equation 4.7** (see below).

Importantly, there is a marked dependency of the T_1^{-1} maxima temperature with the materials under consideration which decrease from ~ 190 K for **EtP6- β** and **oX@EtP6** to ~ 170 K for **mX@EtP6** and ~ 160 K for **pX@EtP6**. It is well known that the position of the T_1^{-1} maximum depends on τ_c with lower temperatures required to satisfy **equation 4.6** for larger molecular size resulting in slower tumbling.⁷³ The temperature dependency of the T_1^{-1} maximum therefore indicates decreasing tumbling rates for **EtP6- β** and **oX@EtP6** to **mX@EtP6** and to **pX@EtP6** that are associated with larger molecular assemblies. These suggest that *ortho*-xylene has little effect on the relaxation rates of the host due to its larger spatial freedom as observed above from xylene CH dipolar coupling experiments, whereas both *meta*-xylene and *para*-xylene shift this maximum towards lower temperatures (170 K and 160 K, respectively) suggesting that the filling of the pillar[6]arene void upon loading of *meta*-xylene and the adaptive adsorption of *para*-xylene results in an overall smaller conformation.

It is assumed that the ^1H relaxation is driven by ^1H - ^1H homonuclear dipole-dipole coupling and the longitudinal relaxation rates T_1^{-1} can be related to τ_c with the following equation (in the approximation of isotropic motion):^{73,74}

$$\frac{1}{T_1} = \frac{3}{10} \left(\frac{\mu_0}{4\pi} \right)^2 \gamma_{\text{H}}^4 \hbar^2 \left(\sum_i \frac{1}{r_i^6} \right) \left[\frac{\tau_c}{1 + \omega_{0,\text{H}}^2 \tau_c^2} + \frac{4\tau_c}{1 + 4\omega_{0,\text{H}}^2 \tau_c^2} \right] \quad (4.7)$$

by summing over all the effective ^1H - ^1H internuclear distances r_i . The local magnetic field fluctuation term of this expression, displayed prior to the square brackets, is proportional to the square of the dipole-dipole coupling constant (**equation 1.9**) while the terms in squared bracket are the spectral density functions. All other possible relaxation mechanisms for a spin 1/2 nucleus such as those driven by CSA, spin-rotation or scalar coupling are likely quite small for ^1H to satisfy the frequencies for relaxation and have therefore been neglected.

Combining **equation 4.6** and **4.7** above at the temperatures of the ^1H T_1 minimum allows the determination of the local dipolar magnetic field fluctuation term to be determined. Experimental values of $2 \times 10^9 \text{ s}^{-2}$ for **EtP6- β** and **oX@EtP6**, $3 \times 10^9 \text{ s}^{-2}$ for **mX@EtP6** and $5 \times 10^9 \text{ s}^{-2}$ for **pX@EtP6** were obtained which compares extremely well with the value of $5 \times 10^9 \text{ s}^{-2}$ calculated for all materials from the explicit expression of the local fields and using the shortest ^1H - ^1H distances in the known CSP data of these phases.¹ No T_1 minimum is observed for **EtP5- α** in the temperature range studied preventing the local field term to be determined so this later calculated value was used.

Figure 4.36 displays the corresponding ^1H T_1^{-1} versus τ_c logarithmic plots for all samples at 9.4 T (black data) and 14.1 T (blue data). The T_1^{-1} and τ_c values extracted from this approach show no field dependence in the fast motion limit where τ_c are much shorter than the Larmor frequency *i.e.* $\omega_{0,\text{H}}\tau_c \ll 1$ (left hand side of the T_1^{-1} maxima) as expected from **equation 4.7**. The τ_c 's extracted from this approach do not vary significantly between the materials and suggest the same similar motional process. The temperature dependence of the correlation frequencies τ_c^{-1} was subsequently modelled with the Arrhenius equation of the form:

$$\tau_c^{-1} = \tau_{c,0}^{-1} \exp\left(-\frac{E_a}{RT}\right) \quad (4.8)$$

with $\tau_{c,0}^{-1}$, E_a and R the attempt frequency and activation energy of the thermally activated motional process, and the universal gas constant, respectively. Assuming a single activation energy, fit to τ_c^{-1} versus reciprocal temperatures (**Figure 4.36**) is satisfactory and the extracted E_{as} (**Table 4.8**) are small, suggesting similar facile motion of the pillar[n]arene assemblies. Upon adsorption of *para*-xylene and *ortho*-xylene into **EtP6- β** , the activation barriers very slightly increase by *ca.* 0.5-0.8 kJ mol⁻¹ while it decreases by 0.6 kJ mol⁻¹ in the case of **mX@EtP6** material. The assumed isotropic motion and associated errors with these values imply that the activation energies obtained should simply be taken as an indication of possible motional effects of xylenes into **EtP6- β** . In the case of **pX@EtP6** and **oX@EtP6**, it is postulated that their larger E_{as} vs. the one for **EtP6- β** capture increase in the steric hindrance of the assemblies upon adsorption of *para*-xylene and *ortho*-xylene (**Figures 4.1(c)** and **4.1(e)**), resulting in overall larger conformation of these materials and therefore slower overall dynamics when xylenes occupy (**pX@EtP6**) or partially occupy (**oX@EtP6**) the pillar[6]arene void. In contrast, the smaller E_a obtained for **mX@EtP6** could be potentially due to folding of the pillar[6]arene void upon *meta*-xylene adsorption (**Figure 4.1(d)**) and associated with the position of the *meta*-xylene on top of the pillar[6]arene core.

Table 4.8. Comparison of the attempt frequencies $\tau_{c,0}^{-1}$ and activation energy barriers E_a of guest-free **EtP5- α** , guest-free **EtP6- β** , **pX@EtP6**, **mX@EtP6** and **oX@EtP6** obtained from the Arrhenius plots of the ^1H correlation frequencies.

Pillar[n]arenes	$\tau_{c,0}^{-1} / \text{s}^{-1}$	$E_a / \text{kJ mol}^{-1}$ ^a
EtP5-α ^b	9×10^{11}	7
EtP6-β	2×10^{11}	6
pX@EtP6	6×10^{11}	6
mX@EtP6	2×10^{11}	5
oX@EtP6	4×10^{11}	6

^a Errors are in the order of 1 kJ mol⁻¹. ^b Data in the 383 - 243 K temperature range only available.

Site specific ^{13}C T_1 values for all carbons at 9.4 T between 383 and 243 K and at 14.1 T between 298 K and 100 K were measured experimentally using the T_1 Torchia approach (**Figure 4.35(b)**).⁴⁰ Illustration of the data obtained at room temperature and 9.4 T are given in **Tables 4.1-4.5** for **EtP5- α** , **EtP6- β** , **pX@EtP6**, **mX@EtP6** and **oX@EtP6**, respectively, and we have chosen to give a single T_1 value (with associated errors) for each carbon subgroup as these are within errors of each other. The following general trend is observed in all of the guest-free and xylene-adsorbed pillar[n]arenes: the **CH₃** group has the shortest relaxation times (approx. 2 s at room temperature) of all the carbon environments as it is well known that methyl groups are relaxation sinks due to their facile 3-site hopping motions in the temperature range studied here and efficient ^{13}C ^1H heteronuclear dipole-dipole coupling relaxation; the ^{13}C T_1 times of the **OCH₂** moieties are also relatively short (approx. 20 - 40 s) and likely due to rotation around the O-C bond; these T_1 s are in contrast with

the ones of the CH_2 (and CH) groups that are in the 10^2 s range and suggest a lack of the relaxation pathways which arise from limited motional freedom and rigidity of these groups which are located in the pillar[6]arene core; the OC^{IV} and $\text{CH}_2\text{C}^{\text{IV}}$ carbons yield the longest relaxation times as the dominant relaxation mechanism of CSA (see below) is less efficient than dipolar coupling to ^1H for these non-protonated carbons. Note that upon loading of *para* and *meta*-xylene, the OCH_2 group shows an increase in $T_{1\text{s}}$ at room temperature (**Figure 4.35(b)**), suggesting that guest addition lowers the flexibility of the pillar[n]arenes. ***oX@EtP6*** shows a reduction in nearly all $T_{1\text{s}}$ in comparison to ***EtP6- β*** , however this is likely attributed to the more amorphous nature of this material.

The ^{13}C T_1^{-1} rates for each carbon subgroup in ***EtP6- β*** and its xylene-adsorbed adducts typically increase with increasing temperatures. Maxima are reached at 165 - 168 K (at 14.1 T) for the majority of resonances (excluding the CH_2 in ***pX@EtP6***, CH in ***oX@EtP6*** and the CH_3 , CH_2 , CH and OC^{IV} in ***mX@EtP6***) followed by a decrease in ^{13}C T_1^{-1} rates at higher temperatures (**Figure 4.35(b)**). These maxima are not observed at 9.4 T due to limitation on the lowest temperatures accessible (243 K) for the majority of resonances (**Figure 4.34(b)**). At these T_1^{-1} maxima at 14.1 T, and using **equation 4.6** for the ^{13}C Larmor frequency $\omega_{0,\text{C}}$ (in $\text{rad}\cdot\text{s}^{-1}$), a τ_c value of 6.5×10^{-10} s for these materials at the temperatures of the T_1^{-1} maxima are obtained.

Assuming negligible contribution from spin-rotation and scalar coupling relaxation mechanisms, the ^{13}C longitudinal relaxation rates T_1^{-1} can generally be expressed as the sum of both ^{13}C ^1H heteronuclear dipolar coupling and ^{13}C CSA relaxation mechanisms and be written as:^{73,74}

$$\frac{1}{T_1} = \left(\frac{1}{T_1}\right)_{\text{dd}} + \left(\frac{1}{T_1}\right)_{\text{CSA}} \quad (4.9)$$

with the dipolar coupling term given by:

$$\left(\frac{1}{T_1}\right)_{dd} = \frac{n}{10} \left(\frac{\mu_0}{4\pi}\right)^2 \frac{\gamma_H^2 \gamma_C^2 \hbar^2}{r_{CH}^6} \left[\frac{\tau_c}{1 + (\omega_{0,C} - \omega_{0,H})^2 \tau_c^2} + \frac{3\tau_c}{1 + \omega_{0,C}^2 \tau_c^2} + \frac{6\tau_c}{1 + (\omega_{0,C} + \omega_{0,H})^2 \tau_c^2} \right] \quad (4.10)$$

and the CSA term by:

$$\left(\frac{1}{T_1}\right)_{CSA} = \frac{2}{15} \omega_{0,C}^2 (\Delta\delta_C)^2 \left(1 + \frac{\eta_C^2}{3}\right) \left[\frac{\tau_c}{1 + \omega_{0,C}^2 \tau_c^2} \right] \quad (4.11)$$

with n the number of protons attached to ^{13}C , r_{CH} the effective ^{13}C - ^1H distance, $\Delta\delta_C$ the (reduced) anisotropy (sensitivity of the chemical shift interaction to the orientation) and η_C the asymmetry parameter (deviation from axial symmetry) of the second rank ^{13}C chemical shift tensor with principal components δ_{11} , δ_{22} and δ_{33} . Using the Haeberlen convention,⁷⁵ these are defined as:

$$\Delta\delta_C = \delta_{33} - \frac{\delta_{11} + \delta_{22}}{2} \quad (4.12)$$

and

$$\eta_C = \frac{\delta_{22} - \delta_{11}}{\delta_{33} - \delta_{iso}} \quad (4.13)$$

with δ_{iso} the isotropic chemical shift (trace of the tensor):

$$\delta_{iso} = \frac{\delta_{11} + \delta_{22} + \delta_{33}}{3} \quad (4.14)$$

The local magnetic fields fluctuation term of the CSA expression is magnetic field dependent and proportional to the square of the Larmor frequency and anisotropy.

^{13}C relaxation arises from ^{13}C - ^1H heteronuclear dipole-dipole coupling for protonated carbons with small CSA, *i.e.* CH_3 , OCH_2 and CH_2 , and from ^{13}C CSA for quaternary aromatic carbons, *i.e.* OC^{IV} and $\text{CH}_2\text{C}^{\text{IV}}$ as generally assumed in the literature and specifically revealed by comparing the local dipolar and CSA magnetic field terms in **equations 4.10** and **4.11**. For example, in ***mX@EtP6*** (similar observations were made on the other materials), the calculated local dipolar magnetic field term for CH_3 ($6 \times 10^9 \text{ s}^{-2}$ determined using the known carbon-proton CSP distances in this phase) is two orders of magnitude larger than the calculated CSA term ($8 \times 10^7 \text{ s}^{-2}$ at 14.1 T assuming a typical ^{13}C $\Delta\delta_{\text{C}}$ for this carbon of 25 ppm),⁷⁶ while for OC^{IV} , the CSA term largely dominates even at the lower magnetic field of 9.4 T ($1 \times 10^9 \text{ s}^{-2}$ at 14.1 T for a similar carbon environment with a ^{13}C $\Delta\delta_{\text{C}}$ of -142 ppm vs. $4 \times 10^7 \text{ s}^{-2}$ using the shortest distance from CSP). However, for the remaining aromatic CH sites, ^{13}C relaxation derives from cross terms between dipolar and CSA interactions⁷⁷ as both local magnetic field contributions are comparable ($2 \times 10^9 \text{ s}^{-2}$ for dipolar vs. $3 \times 10^9 \text{ s}^{-2}$ at 14.1 T and $1 \times 10^9 \text{ s}^{-2}$ at 9.4 T for CSA using an aromatic CH with a ^{13}C $\Delta\delta_{\text{C}}$ of -147 ppm)⁷⁸ and is further suggested by the slight magnetic field dependency of the $T_{1\text{s}}$ (*e.g.* in ***mX@EtP6*** and at room temperature, $T_1 = 160$ and 180 s at 9.4 and 14.1 T, respectively).

Observation of the temperatures of the ^{13}C T_1 minimum, and assuming a predominant relaxation mechanism(s) as explained above, allows experimental access to the local magnetic field term by combining **equation 4.6** (for ^{13}C) and either **4.10** (for heteronuclear dipolar coupling relaxation), **4.11** (for CSA relaxation), or **4.8** (for both mechanisms). For example, in keeping with ***mX@EtP6***, the experimentally determined local dipolar magnetic field term for CH_3 ($3 \times 10^9 \text{ s}^{-2}$) compares well with the calculated value ($6 \times 10^9 \text{ s}^{-2}$). The experimentally determined terms were then used to obtain τ_{c} at all temperatures and **Figures 4.37** and **4.38(b)** show the corresponding ^{13}C T_1^{-1} versus τ_{c} logarithmic plots for all materials for CH_3 , OCH_2 and OC^{IV} (**Figure 4.37**) and CH_2 , CH and $\text{CH}_2\text{C}^{\text{IV}}$ (**Figure 4.38(b)**).

Room temperature correlation times τ_{c} extracted from this approach for all materials are the shortest for the CH_3 and OCH_2 groups supporting that indeed these sites are significantly mobile while τ_{c} values for groups in the arene ring core of the

pillar[n]arene. The activation energies E_a of the motion were obtained from Arrhenius plots of the corresponding τ_c^{-1} frequencies versus reciprocal temperatures (**Figures 4.37** and **4.38**) and are summarised in **Table 4.9**. The activation energy for CH_3 in **EtP6- β** (6 kJ mol^{-1}) is significantly smaller than in **EtP5- α** (11 kJ mol^{-1}) and is likely due to the smaller ring size of the latter hindering molecular rotation. Upon addition of any guest of **EtP6- β** , the E_a for CH_3 increases to $8\text{-}10 \text{ kJ mol}^{-1}$ which suggests enhanced restricted motion caused by their spatial proximities. No significant differences between the different guest-adsorbed materials were however observed. A similar trend is largely also noted for the OCH_2 groups. Much smaller changes in the T_1 times and hence τ_c values are detected and would therefore indicate that, within the temperature range probed, all materials experience the same motional processes.

Correlation times τ_c were also extracted for the methyl groups of the xylene guests in both ***pX@EtP6*** and ***mX@EtP6*** as shown in **Figure 4.44** (overlaps of these resonances with the host CH_3 region in ***oX@EtP6***, **Figure 4.19**, prevent these T_1 s to be measured) and the temperature dependency of their correlation frequencies was used to extract E_a values (**Figure 4.44**). In both materials, activation energies for the xylene CH_3 groups are small ($1\text{ - }3 \text{ kJ mol}^{-1}$, **Table 4.9**) and significantly less than the activation energies determined for the CH_3 groups of the host (10 kJ mol^{-1} in ***pX@EtP6***; 8 kJ mol^{-1} in ***mX@EtP6***), indicating that the xylene CH_3 groups still have significantly higher degree of motion than those groups in the backbone of the pillar[6]arene. Additionally, further comparison between the xylene CH_3 in ***pX@EtP6*** and ***mX@EtP6*** reveals higher E_a in the former and supports the xylene location inside the arene core.

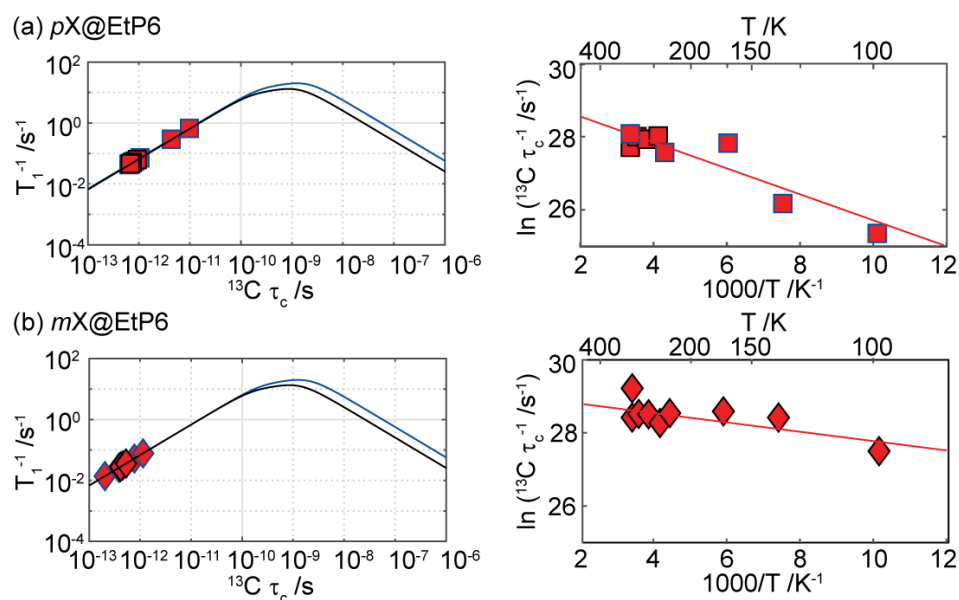


Figure 4.44. (Left) ^{13}C spin–lattice relaxation rates T_1^{-1} against correlation times τ_c and (right) corresponding ^{13}C correlation frequencies τ_c^{-1} Arrhenius plots. Data shown in black and blue outlines were obtained at 9.4 T and 14.1 T, respectively, for the xylene methyl groups in (a) *pX@EtP6* (squares) and (b) *mX@EtP6* (diamonds). The associated errors are smaller than the symbol sizes. In the left panels, the solid (–) lines are those obtained from a dipolar coupling relaxation mechanism (equation 4.10) for CH_3 at both fields, using the calculated local magnetic fields term and distances available in literature from diffraction data.⁴⁸ In the right panels, the lines are fit to the experimental data using the Arrhenius equation.

Table 4.9. Comparison of the attempt frequencies $\tau_{c,0}^{-1}$ and activation energy barriers E_a of guest-free **EtP5- α** , guest-free **EtP6- β** , **pX@EtP6**, **mX@EtP6** and **oX@EtP6** obtained from the Arrhenius plots of the ^{13}C correlation frequencies. Red daggers (\dagger) denote signals from xylenes.

Carbon subgroup	$\tau_{c,0}^{-1} / \text{s}^{-1}$	$E_a / \text{kJ mol}^{-1 \text{a}}$
EtP5-α^b		
CH ₃	5×10^{12}	11
CH ₂	6×10^{10}	5
OCH ₂	6×10^{10}	2
CH	4×10^{10}	5
CH ₂ C ^{IV}	5×10^{12}	4
OC ^{IV}	4×10^{10}	5
EtP6-β		
CH ₃	4×10^{11}	6
CH ₂	6×10^{10}	5
OCH ₂	2×10^{11}	7
CH	3×10^{10}	4
CH ₂ C ^{IV}	8×10^9	3
OC ^{IV}	1×10^{10}	4
pX@EtP6		
CH ₃	5×10^{12}	10
CH ₃ (\dagger)	5×10^{12}	3
CH ₂	2×10^{11}	7
OCH ₂	7×10^{11}	8
CH	7×10^{10}	5
CH ₂ C ^{IV}	1×10^{10}	4
CH(\dagger) ^{c,d}		
OC ^{IV}	2×10^{10}	4
mX@EtP6		
CH ₃	2×10^{12}	8
CH ₃ (\dagger)	4×10^{12}	1
CH ₂	5×10^{10}	5
OCH ₂	1×10^{12}	9
CH	8×10^9	3
CH ₂ C ^{IV}	7×10^9	3
CH(\dagger) ^{c,d}		
OC ^{IV}	5×10^9	2
oX@EtP6		
CH ₃	2×10^{12}	8
CH ₃ (\dagger) ^c		
CH ₂	5×10^9	2
OCH ₂	2×10^{11}	7
CH	3×10^9	2
CH ₂ C ^{IV}	5×10^9	3
CH(\dagger) ^{c,d}		
OC ^{IV}	7×10^9	3

^a Errors are in the order of 1 kJ mol^{-1} . ^b Data in the 383 - 243 K temperature range only available. ^c Overlapping resonances between guest and host in the ^{13}C CP MAS NMR spectra prevents measurements of T_1 times. ^d Signal to noise of some of the signals are also too weak for accurate determination of T_1 times.

4.6. Conclusions

We employed a range of multinuclear solid-state NMR experiments to provide a detailed understanding of the structure and dynamics in guest-free perethylated pillar[5]arene and pillar[6]arene, and as well as pillar[6]arene with adsorbed xylene guests. The resulting ^{13}C CP MAS NMR spectra of the guest-adsorbed pillar[6]arenes are very well resolved owing to the high crystallinity of these materials and ^{13}C isotropic chemical shifts values combined with ^{13}C edited experiments and spectral deconvolution identified most expected carbon resonances. Using 2D PDLF experiments, variable temperature site-selective ^{13}C ^1H dipolar spectra in the 100 - 330 K range were obtained and allowed for the determination of motional averaged heteronuclear ^{13}C ^1H dipolar couplings and quantification of order parameters that reveal differential dynamics properties. Protruding carbons were found to have faster dynamics than those within the pillar[n]arene core while the larger void size of the **EtP6- β** hexagonal cavity than the **EtP5- α** pentagonal cavity results in a less restricted OCH_2 motion of the perethylated group which slows down with lower temperatures.

Upon adsorption of the various xylenes into EtP6, low temperature ^{13}C ^1H dipolar spectra identified dipolar coupling, and hence spatial proximity, between the $\text{CH}_2\text{C}^{\text{IV}}$ quaternary carbon of the EtP6 host and *para*-xylene in ***pX@EtP6*** while this dipolar coupling was not detected (or still had significant motional averaging at 100 K) for the other two xylenes adducts ***oX@EtP6*** and ***mX@EtP5***. This demonstrates a significantly strong π - π stacking host guest interaction in this ***pX@EtP6*** system where *para*-xylene is situated in the centre of the void while *ortho*- and *meta*-xylenes are mainly located at the entrance of the cavity, supporting the crystal structure of these phases and the adaptive behaviour of EtP6.

Variable temperature ^1H and ^{13}C relaxation times T_1 obtained at multiple external magnetic fields were experimentally determined and allowed access to temperature-dependent correlation frequencies of the motion from T_1 minimum and a range of dipolar and/or CSA relaxation mechanisms. The resulting ^1H data would tentatively suggest that ***oX@EtP6*** has the largest size conformation, while ***mX@EtP6*** and ***pX@EtP6*** have the smallest, thus supporting the guest locations and folding of the EtP6 pillar[6]arene in the *meta*-xylene adduct previously determined. Site-specific ^{13}C

NMR correlation times indicate largely restricted motion for pillar[n]arene carbons core and extensive motional dynamics of the perethylated and xylene methyl carbons, further reinforcing the dynamical behaviours captured from ^{13}C ^1H dipolar coupling order parameters.

This work demonstrates that NMR spectroscopy enables the capture of structural transformations resulting from host-guest interactions and motional effects in adaptive pillar[n]arene materials, which could have implications for processes such as competitive loading, molecular separation, and drug release. This adds to our understanding of motion in flexible molecular solid state systems and opens up new perspectives in the rational design of materials with enhanced physical properties.

4.7 References

- (1) Jie, K.; Liu, M.; Zhou, Y.; Little, M. A.; Pulido, A.; Chong, S. Y.; Stephenson, A.; Hughes, A. R.; Sakakibara, F.; Ogoshi, T.; Blanc, F.; Day, G. M.; Huang, F.; Cooper, A. I. Near-Ideal Xylene Selectivity in Adaptive Molecular Pillar[n]Arene Crystals. *J. Am. Chem. Soc.* **2018**, *140*, 6921–6930.
- (2) Cram, D. J. The Design of Molecular Hosts, Guests and Their Complexes. *Angew. Chemie - Int. Ed.* **1988**, *27*, 1009–1020.
- (3) Steed, J. W.; Gale, P. A. *Supramolecular Chemistry: From Molecules to Nanomaterials*, 2nd ed.; Wiley: Chichester, 2012.
- (4) Ma, X.; Zhao, Y. Biomedical Applications of Supramolecular Systems Based on Host-Guest Interactions. *Chem. Rev.* **2015**, *115*, 7794–7839.
- (5) Ariga, K. .; Kunitake, T. *Supramolecular Chemistry — Fundamentals and Applications*; Springer: Heidelberg, 2006.
- (6) Slater, A. G.; Cooper, A. I. Function-Led Design of New Porous Materials. *Science* **2015**, *348*, aaa8075-1-aaa807510.
- (7) *Macrocyclic and Supramolecular Chemistry*; Izatt, R. M., Ed.; John Wiley & Sons: Chichester, UK, 2016.
- (8) Ogoshi, T.; Kanai, S.; Fujinami, S.; Yamagishi, T. Para-Bridged Symmetrical Pillar[5]Arenes: Their Lewis Acid Catalyzed Synthesis and Host–Guest Property. *J. Am. Chem. Soc.* **2008**, *130*, 5022–5023.
- (9) Xue, M.; Yang, Y.; Chi, X.; Zhang, Z.; Huang, F. Pillararenes, A New Class of Macrocycles for Supramolecular Chemistry. *Acc. Chem. Res.* **2012**, *45*, 1294–1308.
- (10) Yang, K.; Pei, Y.; Wen, J.; Pei, Z. Recent Advances in Pillar[n]Arenes: Synthesis and Applications Based on Host–Guest Interactions. *Chem. Commun.* **2016**, *52*, 9316–9326.

- (11) Ogoshi, T.; Yamagishi, T. A.; Nakamoto, Y. Pillar-Shaped Macrocyclic Hosts Pillar[n]Arenes: New Key Players for Supramolecular Chemistry. *Chem. Rev.* **2016**, *116*, 7937–8002.
- (12) Wang, M.; Zhou, J.; Li, E.; Zhou, Y.; Li, Q.; Huang, F. Separation of Monochlorotoluene Isomers by Nonporous Adaptive Crystals of Perethylated Pillar[5]Arene and Pillar[6]Arene. *J. Am. Chem. Soc.* **2019**, *141*, 17102–17106.
- (13) Xiao, C.; Wu, W.; Liang, W.; Zhou, D.; Kanagaraj, K.; Cheng, G.; Su, D.; Zhong, Z.; Chruma, J. J.; Yang, C. Redox-Triggered Chirality Switching and Guest-Capture/Release with a Pillar[6]Arene-Based Molecular Universal Joint. *Angew. Chemie - Int. Ed.* **2020**, *59*, 8094–8098.
- (14) Wang, Y.; Ping, G.; Li, C. Efficient Complexation between Pillar[5]Arenes and Neutral Guests : From Host – Guest Chemistry to Functional Materials. *Chem. Commun.* **2016**, *52*, 9858–9872.
- (15) Jie, K.; Liu, M.; Zhou, Y.; Little, M. A.; Bonakala, S.; Chong, S. Y.; Stephenson, A.; Chen, L.; Huang, F.; Cooper, A. I. Styrene Purification by Guest-Induced Restructuring of Pillar[6]Arene. *J. Am. Chem. Soc.* **2017**, *139*, 2908–2911.
- (16) Jie, K.; Zhou, Y.; Li, E.; Zhao, R.; Huang, F. Aromatics/Cyclic Aliphatics Separation by Nonporous Adaptive Pillararene Crystals. *Angew. Chemie - Int. Ed.* **2018**, *57*, 12845–12849.
- (17) Hongqi, T. A. O.; Derong, C. A. O.; Luzhi, L. I. U.; Yuhui, K. O. U.; Lingyun, W.; Herbert, M. Synthesis and Host-Guest Properties of Pillar[6]Arenes. *Sci. China Chem.* **2012**, *55*, 223–228.
- (18) Sun, Y. L.; Yang, Y. W.; Chen, D. X.; Wang, G.; Zhou, Y.; Wang, C. Y.; Stoddart, J. F. Mechanized Silica Nanoparticles Based on Pillar[5]Arenes for on-Command Cargo Release. *Small* **2013**, *9*, 3224–3229.
- (19) Song, N.; Yang, Y. W. Applications of Pillarenes, an Emerging Class of Synthetic Macrocycles. *Sci. China Chem.* **2014**, *57*, 1185–1198.

- (20) Ogoshi, T.; Kitajima, K.; Aoki, T.; Fujinami, S.; Yamagishi, T.; Nakamoto, Y. Synthesis and Conformational Characteristics of Alkyl-Substituted Pillar[5]Arenes. *J. Org. Chem.* **2010**, *75*, 3268–3273.
- (21) Ogoshi, T.; Yamagishi, T. Pillar[5]- and Pillar[6]Arene-Based Supramolecular Assemblies Built by Using Their Cavity-Size-Dependent Host–Guest Interactions. *Chem. Commun.* **2014**, *50*, 4776–4787.
- (22) Athare, S. V; Gejji, S. P. Perethylated Pillar[n]Arenes versus Pillar[n]Arenes: Theoretical Perspectives. *J. Mol. Model.* **2020**, *26*, 1–11.
- (23) Santra, S.; Kopchuk, D. S.; Kovalev, I. S.; Zyryanov, G. V; Majee, A.; Charushin, V. N.; Chupakhin, O. N. Solvent-Free Synthesis of Pillar[6]Arenes. *Green Chem.* **2016**, *18*, 423–426.
- (24) Ren, T.; Patel, M.; Blok, K. Olefins from Conventional and Heavy Feedstocks: Energy Use in Steam Cracking and Alternative Processes. *Energy* **2006**, *31*, 425–451.
- (25) Jayachandrababu, K. C.; Verploegh, R. J.; Leisen, J.; Nieuwendaal, R. C.; Sholl, D. S.; Nair, S. Structure Elucidation of Mixed-Linker Zeolitic Imidazolate Frameworks by Solid-State ¹H CRAMPS NMR Spectroscopy and Computational Modeling. *J. Am. Chem. Soc.* **2016**, *138*, 7325–7336.
- (26) Rapp, A.; Schnell, I.; Sebastiani, D.; Brown, S. P.; Percec, V.; Spiess, H. W.; Planck, M.; Pennsylv, V. Supramolecular Assembly of Dendritic Polymers Elucidated by ¹H and ¹³C Solid-State MAS NMR Spectroscopy. *J. Am. Chem. Soc.* **2003**, *125*, 13284–13297.
- (27) Weingarth, M.; Baldus, M. Solid-State NMR-Based Approaches for Supramolecular Structure Elucidation. *Acc. Chem. Res.* **2013**, *46*, 2037–2046.
- (28) Duer, M. J.; Harris, R. K.; Wasylshen, R. E. *NMR Crystallography*; Robin K. Harris, R. E. W., Ed.; Wiley: Chichester, 2009.
- (29) Fricke, P.; Chevelkov, V.; Shi, C.; Lange, A. Strategies for Solid-State NMR

Investigations of Supramolecular Assemblies with Large Subunit Sizes. *J. Magn. Reson.* **2015**, *253*, 2–9.

- (30) Wong, Y. T. A.; Martins, V.; Lucier, B. E. G.; Huang, Y. Solid-State NMR Spectroscopy: A Powerful Technique to Directly Study Small Gas Molecules Adsorbed in Metal–Organic Frameworks. *Chem. - A Eur. J.* **2019**, *25*, 1848–1853.
- (31) Ogoshi, T.; Shiga, R.; Yamagishi, T. A.; Nakamoto, Y. Planar-Chiral Pillar[5]Arene: Chiral Switches Induced by Multiexternal Stimulus of Temperature, Solvents, and Addition of Achiral Guest Molecule. *J. Org. Chem.* **2011**, *76*, 618–622.
- (32) Liu, Y.; Zhou, F.; Yang, F.; Ma, D. Carboxylated Pillar[n]Arene (n = 5–7) Host Molecules: High Affinity and Selective Binding in Water. *Org. Biomol. Chem.* **2019**, *17*, 5106–5111.
- (33) Ogoshi, T.; Shiga, R.; Hashizume, M.; Yamagishi, T. A. “Clickable” Pillar[5]Arenes. *Chem. Commun.* **2011**, *47*, 6927–6929.
- (34) Al-Azemi, T. F.; Vinodh, M.; Alipour, F. H.; Mohamod, A. A. Synthesis, Functionalization, and Isolation of Planar-Chiral Pillar[5]Arenes with Bulky Substituents Using a Chiral Derivatization Agent. *RSC Adv.* **2019**, *9*, 23295–23301.
- (35) Ogoshi, T.; Hamada, Y.; Sueto, R.; Sakata, Y.; Akine, S.; Moeljadi, A. M. P.; Hirao, H.; Kakuta, T.; Yamagishi, T. aki; Mizuno, M. Host–Guest Complexation Using Pillar[5]Arene Crystals: Crystal-Structure Dependent Uptake, Release, and Molecular Dynamics of an Alkane Guest. *Chem. - A Eur. J.* **2019**, *25*, 2497–2502.
- (36) Hu, X.-B.; Chen, Z.; Chen, L.; Zhang, L.; Hou, J.-L.; Li, Z.-T. Pillar[n]Arenes (n = 8–10) with Two Cavities: Synthesis, Structures and Complexing Properties. *Chem. Commun.* **2012**, *48*, 10999–11001.
- (37) Rosay, M.; Tometich, L.; Pawsey, S.; Bader, R.; Schauwecker, R.; Blank, M.; Borchard, P. M.; Cauffman, S. R.; Felch, K. L.; Weber, R. T.; Temkin, R. J.; Griffin,

- R. G.; Mass, W. E. Solid-State Dynamic Nuclear Polarization at 263 GHz: Spectrometer Design and Experimental Results. *Phys. Chem. Chem. Phys.* **2010**, *12*, 5850–5860.
- (38) Fung, B. M.; Khitrin, A. K.; Ermolaev, K. An Improved Broadband Decoupling Sequence for Liquid Crystals and Solids. *J. Magn. Reson.* **2000**, *142*, 97–101.
- (39) Ernst, R. E.; Bodenhausen, G.; Wokaun, A. *Principles of Nuclear Magnetic Resonance in One and Two Dimensions*; Oxford University Press: Oxford, 1987.
- (40) Torchia, D. A. The Measurement of Proton-Enhanced Carbon-13 T_1 Values by a Method Which Suppresses Artifacts. *J. Magn. Reson.* **1978**, *30*, 613–616.
- (41) Perras, F. A.; Wang, Z.; Naik, P.; Slowing, I. I.; Pruski, M. Natural Abundance ^{17}O DNP NMR Provides Precise O–H Distances and Insights into the Brønsted Acidity of Heterogeneous Catalysts. *Angew. Chemie - Int. Ed.* **2017**, *56*, 9165–9169.
- (42) Dvinskikh, S. V.; Zimmermann, H.; Maliniak, A.; Sandström, D. Measurements of Motionally Averaged Heteronuclear Dipolar Couplings in MAS NMR Using R-Type Recoupling. *J. Magn. Reson.* **2004**, *168*, 194–201.
- (43) Zhao, X.; Edén, M.; Levitt, M. H. Recoupling of Heteronuclear Dipolar Interactions in Solid-State NMR Using Symmetry-Based Pulse Sequences. *Chem. Phys. Lett.* **2001**, *342*, 353–361.
- (44) Zhao, X.; Hoffbauer, W.; Schmedt auf der Günne, J.; Levitt, M. H. Heteronuclear Polarization Transfer by Symmetry-Based Recoupling Sequences in Solid-State NMR. *Solid State Nucl. Magn. Reson.* **2004**, *26*, 57–64.
- (45) Wu, C. H.; Das, B. B.; Opella, S. J. ^1H – ^{13}C Hetero-Nuclear Dipole–Dipole Couplings of Methyl Groups in Stationary and Magic Angle Spinning Solid-State NMR Experiments of Peptides and Proteins. *J. Magn. Reson.* **2010**, *202*, 127–134.
- (46) Edén, M. Enhanced Symmetry-Based Dipolar Recoupling in Solid-State NMR.

Chem. Phys. Lett. **2003**, *378*, 55–64.

- (47) Ibberson, R. M.; Morrison, C.; Prager, M. Neutron Powder and Ab Initio Structure of Ortho-Xylene: The Influence of Crystal Packing on Phenyl Ring Geometry at 2 K. *Chem. Commun.* **2000**, 539–540.
- (48) Ibberson, R. M.; David, W. I. F.; Parsons, S.; Prager, M.; Shankland, K. The Crystal Structure of m-Xylene and p-Xylene, C₈D₁₀, at 4.5 K. *J. Mol. Struct.* **2000**, *524*, 121–128.
- (49) Beckmann, P. A.; Dybowski, C. A Thermometer for Nonspinning Solid-State NMR Spectroscopy. *J. Magn. Reson.* **2000**, *146*, 379–380.
- (50) Bielecki, A.; Burum, D. P. Temperature Dependence of ²⁰⁷Pb MAS Spectra of Solid Lead Nitrate . An Accurate , Sensitive Thermometer for Variable-Temperature MAS. *J. Magn. Reson.* **1995**, *116*, 215–220.
- (51) Thurber, K. R.; Tycko, R. Measurement of Sample Temperatures under Magic-Angle Spinning from the Chemical Shift and Spin-Lattice Relaxation Rate of ⁷⁹Br in KBr Powder. *J. Magn. Reson.* **2009**, *196*, 84–87.
- (52) The MathWorks Inc. MATLAB. Natick, MA, 2016.
- (53) Morcombe, C. R.; Zilm, K. W. Chemical Shift Referencing in MAS Solid State NMR. *J. Magn. Reson.* **2003**, *162*, 479–486.
- (54) Clark, S. J.; Segall, M. D.; Pickard, C. J.; Hasnip, P. J.; Probert, M. I. J.; Refson, K.; Payne, M. C. First Principles Methods Using CASTEP. *Zeitschrift fur Krist.* **2005**, *220*, 567–570.
- (55) Perdew, J. P.; Burke, K.; Ernzerhof, M. Generalized Gradient Approximation Made Simple. *Phys. Rev. Lett.* **1996**, *77*, 3865–3868.
- (56) Monkhorst, H. J.; Pack, J. D. Special Points for Brillouin-Zone Integrations. *Phys. Rev. B* **1976**, *13*, 5188.
- (57) Pickard, C. J.; Mauri, F. All-Electron Magnetic Response with Pseudopotentials:

- NMR Chemical Shifts. *Phys. Rev. B - Condens. Matter Mater. Phys.* **2001**, *63*, 2451011–2451013.
- (58) Profeta, M.; Mauri, F.; Pickard, C. J. Accurate First Principles Prediction of 17O NMR Parameters in SiO₂: Assignment of the Zeolite Ferrierite Spectrum. *J. Am. Chem. Soc.* **2003**, *125*, 541–548.
- (59) Yates, J. R.; Pickard, C. J.; Mauri, F. Calculation of NMR Chemical Shifts for Extended Systems Using Ultrasoft Pseudopotentials. *Phys. Rev. B* **2007**, *76*, 024401.
- (60) Silverstein, R. M.; Webster, F. X.; Kiemle, D. J. *The Spectrometric Identification of Organic Compounds*, 7th ed.; John Wiley & Sons: New York, 2005.
- (61) Lesage, A.; Auger, C.; Caldarelli, S.; Emsley, L. Determination of Through-Bond Carbon-Carbon Connectivities in Solid-State NMR Using the INADEQUATE Experiment. *J. Am. Chem. Soc.* **1997**, *119*, 7867–7868.
- (62) Krüger, T.; Vorndran, K.; Linker, T. Regioselective Arene Functionalization: Simple Substitution of Carboxylate by Alkyl Groups. *Chem. - A Eur. J.* **2009**, *15*, 12082–12091.
- (63) Shapiro, M. J. Pi-Inductive Effect in Benzyl Compounds. *J. Org. Chem.* **1977**, *42*, 762–763.
- (64) Adcock, W.; Gupta, B. D.; Khor, T. C.; Doddrell, D.; Kitching, W. Carbon-13 Nuclear Magnetic Resonance Studies of Benzocycloalkenes. *J. Org. Chem.* **1976**, *41*, 751–759.
- (65) Reichert, D.; Saalwächter, K. Dipolar Coupling: Molecular-Level Mobility. *eMagRes*. October 15, 2008.
- (66) Magnuson, M. L.; Tanner, L. F.; Fung, B. M. Determination of Order Parameters from Carbon–Fluorine Dipolar Coupling. *Liq. Cryst.* **1994**, *16*, 857–867.
- (67) Brinkmann, A.; Levitt, M. H. Symmetry Principles in the Nuclear Magnetic

- Resonance of Spinning Solids: Heteronuclear Recoupling by Generalized Hartmann-Hahn Sequences. *J. Chem. Phys.* **2001**, *115*, 357–384.
- (68) Carravetta, M.; Edén, M.; Zhao, X.; Brinkmann, A.; Levitt, M. H. Symmetry Principles for the Design of Radiofrequency Pulse Sequences in the Nuclear Magnetic Resonance of Rotating Solids. *Chem. Phys. Lett.* **2000**, *321*, 205–215.
- (69) Lehmann, M. S.; Koetzle, T. F.; Hamilton, W. C. Precision Neutron Diffraction Structure Determination of Protein and Nucleic Acid Components. I. The Crystal and Molecular Structure of the Amino Acid L-Alanine. *J. Am. Chem. Soc.* **1972**, *94*, 2657–2660.
- (70) Barnes, A. B.; Corzilius, B.; Mak-Jurkauskas, M. L.; Andreas, L. B.; Bajaj, V. S.; Matsuki, Y.; Belenky, M. L.; Lugtenburg, J.; Sirigiri, J. R.; Temkin, R. J.; Herzfeld, J.; Griffin, R. G. Resolution and Polarization Distribution in Cryogenic DNP/ MAS Experiments. *Phys. Chem. Chem. Phys.* **2010**, *12*, 5861–5867.
- (71) Ni, Q. Z.; Markhasin, E.; Can, T. V.; Corzilius, B.; Tan, K. O.; Barnes, A. B.; Daviso, E.; Su, Y.; Herzfeld, J.; Gri, R. G. Peptide and Protein Dynamics and Low-Temperature/DNP Magic Angle Spinning NMR. *J. Phys. Chem. B* **2017**, *121*, 4497–5006.
- (72) de Alba, E.; Tjandra, N. Orientational Restraints. In *BioNMR in Drug Research*; Zerbe, O., Ed.; Methods and Principles in Medicinal Chemistry; Wiley VCH: Weinheim, 2002; pp 179–205.
- (73) Abragam, A. *Principles of Nuclear Magnetism*; Oxford University Press: New York, 1963.
- (74) Steigel, A.; Spiess, H. W. Rotation of Molecules and Nuclear Spin Relaxation. In *Dynamic NMR Spectroscopy*; Diehl, P., Fluck, E., Kosfeld, R., Ed.; Springer-Verlag Belin Heidelberg: New York, 1978; pp 55–214.
- (75) Haeberlen, U. *High Resolution NMR in Solids. Selective Averaging*; Academic Press: New York, 1968.

- (76) Wei, Y.; Le, D. K.; Ramamoorthy, A. Solid-State ^{13}C NMR Chemical Shift Anisotropy Tensors of Polypeptides. *J. Am. Chem. Soc.* **2001**, *123*, 6118–6126.
- (77) Königsberger, E.; Sterk, H. Anisotropic Molecular Reorientation Measured by NMR Relaxation Including Cross Terms between Dipolar and Chemical Shift Anisotropy Interactions. *J. Chem. Phys.* **1985**, *83*, 2723–2726.
- (78) Lobo, N. P.; Prakash, M.; Narasimhaswamy, T.; Ramanathan, K. V. Determination of ^{13}C Chemical Shift Anisotropy Tensors and Molecular Order of 4-Hydroxybenzoic Acid. *J. Phys. Chem. A* **2012**, *116*, 7508–7515.

Chapter 5: Melting of Hybrid Organic-Inorganic Perovskites

5.1 Overview

Chapter 5 is adapted from a paper entitled “Melting of Hybrid Organic-Inorganic Perovskites” by Bikash Kumar Shaw, Ashlea R. Hughes, Maxime Ducamp, Stephen Moss, Anup Debnath, Adam F. Sapnik, Michael F. Thorne, Lauren McHugh, Andrea Pugliese, Dean Keeble, Philip Chater, Juan M. Bermudez-Garcia, Xavier Moya, Shyamal K. Saha, David A. Keen, Francois-Xavier Coudert, Frédéric Blanc and Thomas D. Bennett which has been submitted to the ChemRxiv archive: (2020): Hybrid Inorganic-Organic Perovskite Glasses. ChemRxiv. Preprint. <https://doi.org/10.26434/chemrxiv.11956599.v1>. This manuscript has since been submitted to a peer reviewed journal and is currently under review. As this is a large collaborative project, the manuscript has been edited for use in the thesis to focus on the solid state NMR data acquisition and analysis which was undertaken by A.R.H. and supported by F.B. B.K.S and T.D.B. prepared the samples prior to NMR analysis. B.K.S ran both the DSC and the IR data shown in this chapter.

5.2 Abstract

Hybrid perovskites occupy a prominent position within solid-state materials chemistry due to their (*e.g.*) ionic transport, photoconductivity ferroelectricity and multiferroicity. Here we show that a series of dicyanamide based hybrid organic-inorganic perovskites melt below 300 °C. Solid state NMR along with other approaches demonstrates that they also form glasses upon melt quenching. These largely retain the inorganic-organic bonding of the three-dimensional crystalline phase. Work from other co-authors which explores the very low thermal conductivities of these glasses ($\sim 0.2 \text{ W m}^{-1} \text{ K}^{-1}$), combined with moderate electrical conductivities ($10^{-2} - 10^{-4} \text{ S m}^{-1}$) and thermo-mechanical properties reminiscent of polymeric materials identifying them as a new family of functional glass-formers will not be explored within this thesis.

5.3 Introduction

ABX_3 hybrid organic-inorganic perovskites (HOIPs) are an emerging family of materials, where A = organic cation, B = metal ion and X = bridging ligand. The family occupies a prominent position within solid state chemistry and materials science due to interest in their utility in *e.g.* ionic transport, ferroelectric, luminescent and multiferroic applications.¹⁻³

Hybrid lead halide perovskites in particular have been extensively studied for their performance and efficiency in photovoltaic devices.^{4,5} The replacement of the halide ion by flexible bidentate bridging ligands, such as formate [HCOO^-],⁶ hypophosphite [H_2POO^-]⁷ and dicyanamide [dca , $\text{N}(\text{CN})_2^-$]⁸ gives rise to an even wider array of functional properties, while preserving their three-dimensional (3D) coordination polymer structures.⁹

Crystalline materials dominate the field of HOIP research, and show rich structural behaviour such as octahedral tilting, columnar shifts and molecular disordering associated with phase transitions.¹⁰ Non-crystalline materials receive comparatively little attention, though the reversible pressure-induced amorphization of 3D methylammonium lead halide perovskites has been studied.^{11,12} Melting of the two dimensional layered HOIP series $[(\text{C}_4\text{H}_9\text{NH}_3)_2\text{Ml}_4]$ ($\text{M} = \text{Ge}, \text{Sn}, \text{Pb}$) has also been observed and ascribed to the weakening of inter-layer non-covalent interactions, or 'chain-melting'.¹³

Solid-liquid transitions have however started to be reported in 3D metal-organic frameworks (MOFs).⁹ For example, the melt-quenching of several $\text{Zn}(\text{Im})_2$ structures results in the formation of a new category of glasses, which are structurally similar to silica glass, yet contain linked inorganic and organic components.¹⁰ Accordingly, the mechanical and optical properties of 'hybrid' glasses, or those which contain both inorganic and organic components, are of great interest and routes to expand this family are sought after.

Density has been observed to play a key role in the stabilization of the liquid state of zeolitic imidazolate frameworks (ZIFs),¹⁴ though the requirement for dense starting structures means that the number of 3D structures which exhibit melting is limited.

Chemical variance within the lower dimensionality coordination polymers reported to melt is equally constrained. The HOIP family on the other hand displays great chemical variance whilst retaining similar, dense 3D structures.

Solid state nuclear magnetic resonance (NMR) spectroscopy has had major advances in recent years with regards to very fast magic angle spinning (MAS) and broadband inversion pulses which can aid in the study of paramagnetic materials,^{15,16} resulting in an increase of its use to study such structures throughout literature.^{16–18} The typical challenges of solid state NMR are augmented with paramagnetic materials due to their large chemical shift anisotropy (CSA) causing numerous spinning sidebands subsequently resulting in a poor signal to noise ratio. This challenge combined with short transverse relaxation rates which can add to a loss of signal and poor resolution. Short high powered adiabatic pulses (SHAPs) have been developed,¹⁹ which when combined with echo sequences can overcome some of these challenges.

Motivated by the above, in this report we extend the phenomenon of melting to the ABX_3 perovskite family. Three $[TPrA][M(dca)_3]$ ($TPrA$ = tetrapropylammonium, $(CH_3CH_2CH_2)_4N^+$, $M = Mn^{2+}, Fe^{2+}, Co^{2+}$) materials were selected for study due to the multiple possible coordination modes possible for the dca ligands, which bridge transition metal cations through the N atom in $\mu_{1,5}$ end-to-end connectivity. The TPrA cations are situated in the pseudo-cubic cavities, resulting in 3D perovskite architectures (**Figure 5.1**). At room temperature, both $[TPrA][Co(dca)_3]$ and $[TPrA][Fe(dca)_3]$ crystallise in an orthorhombic space group ($Pnna$), as opposed to the tetragonal Mn analogue, which crystallizes in $P-42_1c$.

In this work, we show that these materials melt at temperatures lower than existing MOFs, and that the liquids can be quenched into hybrid glasses. The amorphous nature of the melted glasses can be confirmed using solid state NMR techniques which also are able to establish that the amorphous glasses have not decoordinated during the melt/quench process. The 3D nature of the parent perovskites means that the recrystallisation observed in lower dimensional zinc phosphate coordination polymer glasses is avoided,²⁰ whilst the presence of organic cations distinguishes them from the three dimensional MOFs found to melt thus far.

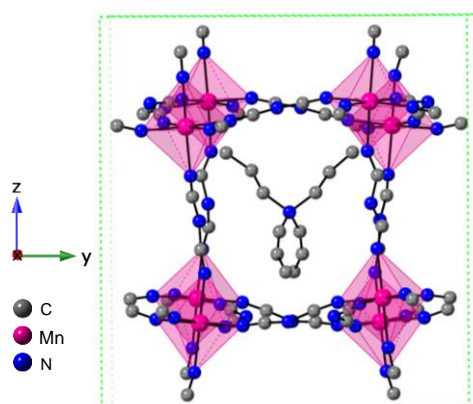


Figure 5.1. Hybrid perovskites structure. Simplified representation of perovskite structure [TPrA][Mn(dca)₃] at room temperature.⁴ Mn, C and N atoms are shown as pink, grey and blue spheres, respectively. All H atoms have been omitted for clarity, as have all TPrA ions except the TPrA ion located on the body-centre. Furthermore, only one of the possible orientations of the TPrA and dca ions within the average crystal structure are shown.²¹

5.4 Materials and Methods

5.4.1 Synthesis of Hybrid Organic-Inorganic Perovskites

The synthesis reported in the literature was followed.^{21–23} Specifically, 10 ml of an aqueous solution of metal salt (2 mmol M: Mn²⁺, Fe²⁺, Co²⁺) was placed at the bottom of a thin crystallization tube and layered with a mixture of a solution of Na(dca) (6 mmol in 10 ml of water) and (TPrA)Br (2 mmol in 10 ml of ethanol). Block-shaped single crystals were obtained from the mother liquor after one week of slow evaporation in an open atmosphere.

The amorphous glasses were heated to temperatures beyond their previously reported solid-solid polymorphic phase transitions,^{21,23} until a visual change was seen corresponding to the melting of these structures and amorphous glasses being formed upon cooling as observed by differential scanning calorimetry (DSC) (**Figure 5.2**). The glasses, in keeping with the existing nomenclature on hybrid glasses, are termed a_g[TPrA][M(dca)₃] (a_g : melt quenched glass).

5.4.2 Solid State NMR

Solid state NMR experiments were performed on a 9.4 T Bruker Avance III HD spectrometer equipped with a 1.3 mm HXY magic angle spinning (MAS) probe in double resonance mode. The ¹H channel was tuned to $\nu_0(^1\text{H}) = 400.13$ MHz and the X channel was tuned to $\nu_0(^{13}\text{C}) = 100.61$ MHz. Spectra were recorded under an optimised approach for paramagnetic systems combining very fast MAS¹⁸ with double adiabatic echo detection and shaped pulses.¹⁹ All NMR spectra were recorded at a spinning rate of 60 kHz, which heats the sample to a temperature of *ca.* 45 °C (as measured from the ⁷⁹Br NMR chemical shift change of KBr²⁴), and pulses were applied at a radiofrequency field of 200 kHz at an offset of 0 ppm for [TPrA][Mn(dca)₃], and 2985 ppm for both [TPrA][Fe(dca)₃] and [TPrA][Co(dca)₃]. The double adiabatic echo pulse sequence¹⁹ (**Figure 5.3(a)**) was employed to record the MAS NMR spectra and used square $\pi/2$ excitation pulses of duration 1.25 μs and rotor synchronised short (50 μs) high powered adiabatic tanh/tan (SHAPs)¹⁹ inversion pulses sweeping through 10 MHz to refocus the chemical shift evolution¹⁹; this sequence shows an approximate two-fold increase in signal intensity versus the double echo pulse

sequence employing square $\pi/2$ and π pulses, largely in agreement with the literature.¹⁹ TEDOR experiments^{19,25} (**Figure 5.3(b)**) were performed with an optimised recoupling time equal to 3 rotor periods (50 μs) and adiabatic SHAPs inversion pulses applied to the ^1H channel to improve polarization transfer.¹⁹ TEDOR experiments were performed with a recycle delay of $1.3 \times ^1\text{H } T_1$ to ensure maximum signal to noise per unit time. No ^1H decoupling was used during any ^{13}C acquisition. The ^{13}C MAS NMR spectra were typically accumulated with 2 million scans with recycle delays of 0.01 s which were found to be long enough to avoid saturation. Note that the ^{13}C signal intensities do not directly relate to the number of carbons present as the optimised data acquisition strategy is not quantitative due to the likely large differences in the $^{13}\text{C } T_2'$ values. ^1H spectra were referenced to H_2O at 4.8 ppm and ^{13}C spectra were reference to the CH peak of adamantane at 29.45 ppm corresponding to TMS at 0 ppm.²⁶ All samples for solid-state NMR were finely ground.

5.5 Results and Discussion

5.5.1 Synthesis of amorphous glasses

Crystalline $[\text{TPrA}][\text{Mn}(\text{dca})_3]$, $[\text{TPrA}][\text{Fe}(\text{dca})_3]$ and $[\text{TPrA}][\text{Co}(\text{dca})_3]$ were synthesized using literature procedures as detailed in section 5.4.1 above.^{21–23}

DSC was carried out on each sample, and upon initial heating sharp endotherms were identified at temperatures far in excess of the reported solid-solid polymorphic phase transitions.^{21,23} The temperatures of these features, indicative of a previously unreported phase transition, correspond to melting (T_m) at 271 °C, 263 °C and 230 °C for the Mn, Fe and Co analogues (**Figure 5.2**) forming amorphous glasses. The increase in melting temperature from Co to Mn follows the trend in the ionic radii $r_{\text{Co}} < r_{\text{Fe}} < r_{\text{Mn}}$, and is in accordance with the stronger polarizing power of Co and the larger covalent character of the Co-N bond.

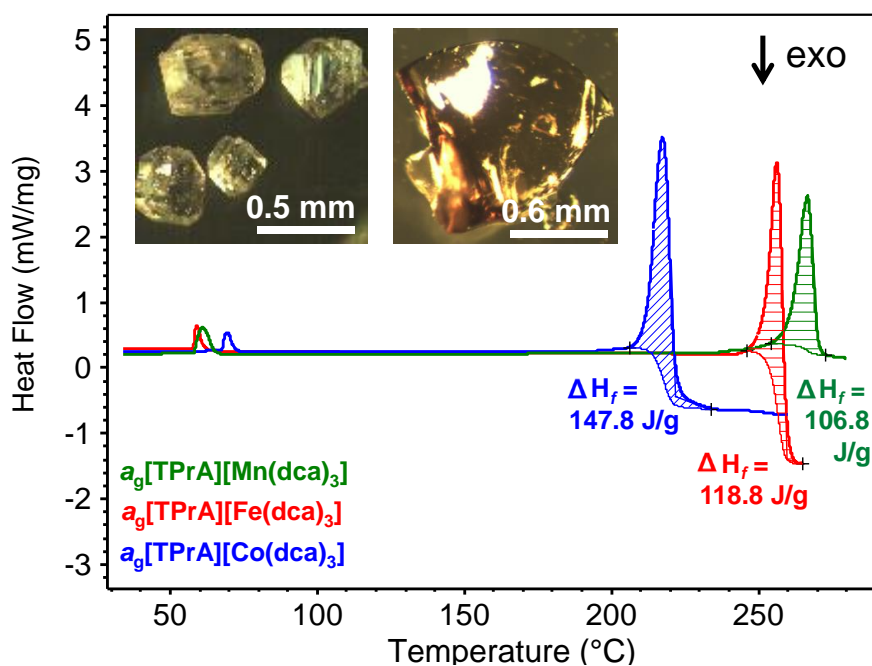


Figure 5.2. Glass formation from hybrid perovskites. Change in heat flow with increase in temperature for $[\text{TPrA}][\text{M}(\text{dca})_3]$ samples. Values for the enthalpy of fusion (ΔH_f) for the crystalline to liquid transition were extracted from the shaded sigmoidal areas, which were determined after subtracting sigmoidal baselines from the calorimetric data. Inset. Optical images of $[\text{TPrA}][\text{Mn}(\text{dca})_3]$ before heating (left) and after melt-quenching (right). DSC ran by Bikash Kumar Shaw.

5.5.2 Delineating Decoordination and Decomposition

^{13}C NMR double adiabatic echo (**Figure 5.3(a)**) spectra of $[\text{TPrA}][\text{Mn}(\text{dca})_3]$, $[\text{TPrA}][\text{Fe}(\text{dca})_3]$ and $[\text{TPrA}][\text{Co}(\text{dca})_3]$ before and after melt-quenching were obtained (**Figure 5.4**).¹⁵ Spectra of $[\text{TPrA}][\text{Fe}(\text{dca})_3]$ and $[\text{TPrA}][\text{Co}(\text{dca})_3]$ contain one resonance in the 200 to -100 ppm region per type of carbon in the TPrA cation and two (or more) poorly resolved resonances around 3900 ppm for the NCN carbon of the dca anions (see below and **Figure 5.5, 5.6** for spectral assignment). In contrast, in crystalline $[\text{TPrA}][\text{Mn}(\text{dca})_3]$ where the NMR lines are much narrower, resonances for each type of carbon in the TPrA and dca ions (*e.g.* the NCN resonance appears as two resolved shifts of 7 and 3 ppm in a 2:1 ratio) can be observed (**Figure 5.7**). These observations are consistent with the phases expected based on previous reports of phase transitions in the family.

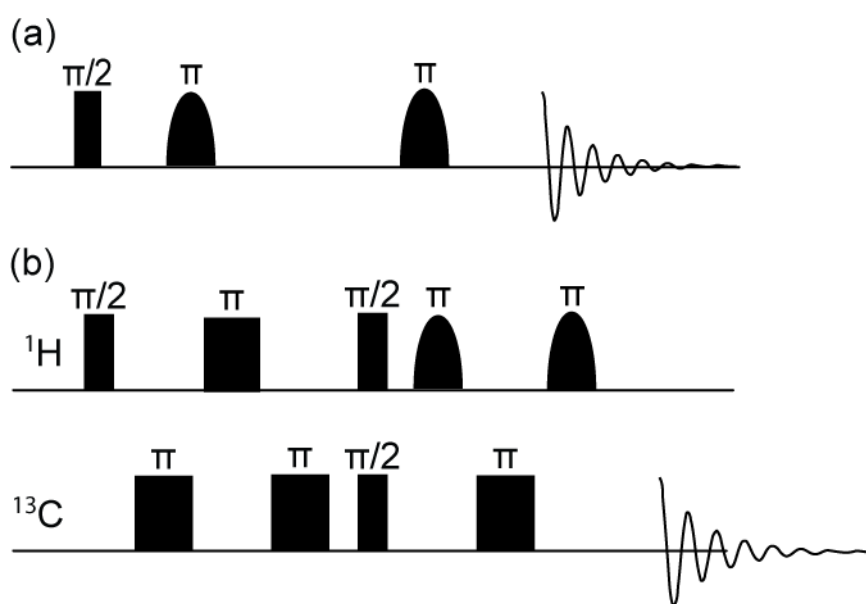


Figure 5.3. NMR pulse sequences used in this work. (a) Double adiabatic echo pulse sequences. (b) TEDOR pulse sequence. Hard pulses are shown as square whilst adiabatic pulses are denoted by shaped pulses above.

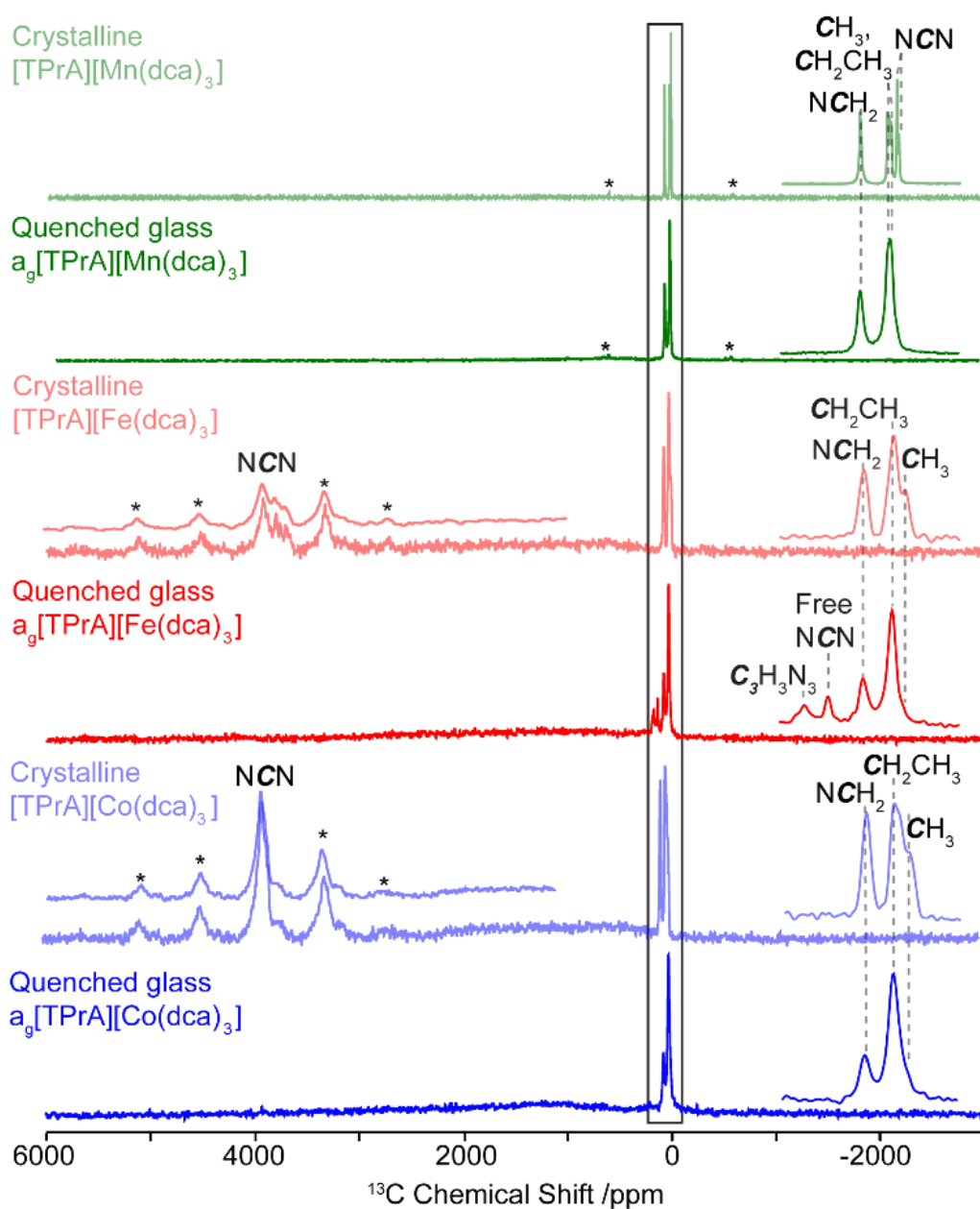


Figure 5.4. Structural insights into melting and glass structure. ^{13}C Double adiabatic echo MAS NMR spectra of crystalline $[\text{TPrA}][\text{Mn}(\text{dca})_3]$ before heating (pale green), after melt-quenching (green), crystalline $[\text{TPrA}][\text{Fe}(\text{dca})_3]$ (pale red), after melt-quenching (red), crystalline $[\text{TPrA}][\text{Co}(\text{dca})_3]$ before heating (pale blue) and after melt-quenching (blue). Magnified views of the 200 to -100 ppm region (within box) are shown on the right hand side with spectral assignments. Spectra were processed with exponential line broadenings (of 20 Hz), appropriate for the magnified views shown in order to capture the various spectral features, while the overlaid views in the 6000 to 1000 ppm paramagnetic shifts region show data processed with increased line broadenings (of 200 Hz) taking into account the larger linewidths of the NCN resonances of the dca ligand. $\text{C}_3\text{H}_3\text{N}_3$ corresponds to triazine-based structures. Asterisks (*) denote spinning sidebands.

Due to the paramagnetic nature of the metal centres within these perovskite structures, large changes in chemical shifts are expected and therefore the assignment was confirmed by using the TEDOR pulse scheme as illustrated in **Figure 5.3** above. This experiment provides detail concerning directly connected protons and carbons, enabling the differentiation between the dca ligand and the TPrA ligand. The absence of ^{13}C signal at *ca.* 3900 ppm in both $[\text{TPrA}][\text{Fe}(\text{dca})_3]$ and $[\text{TPrA}][\text{Co}(\text{dca})_3]$ TEDOR spectra (**Figure 5.5** and **5.6** below) strongly supports its assignment to the NCN carbon of the dca anions, which contains the only quaternary carbon amongst both TPrA and dca ions. It is therefore postulated that the very large paramagnetic shifts observed in dca result from its $\mu_{1,5}$ bonding mode to two metal centres (**Figure 5.4**).

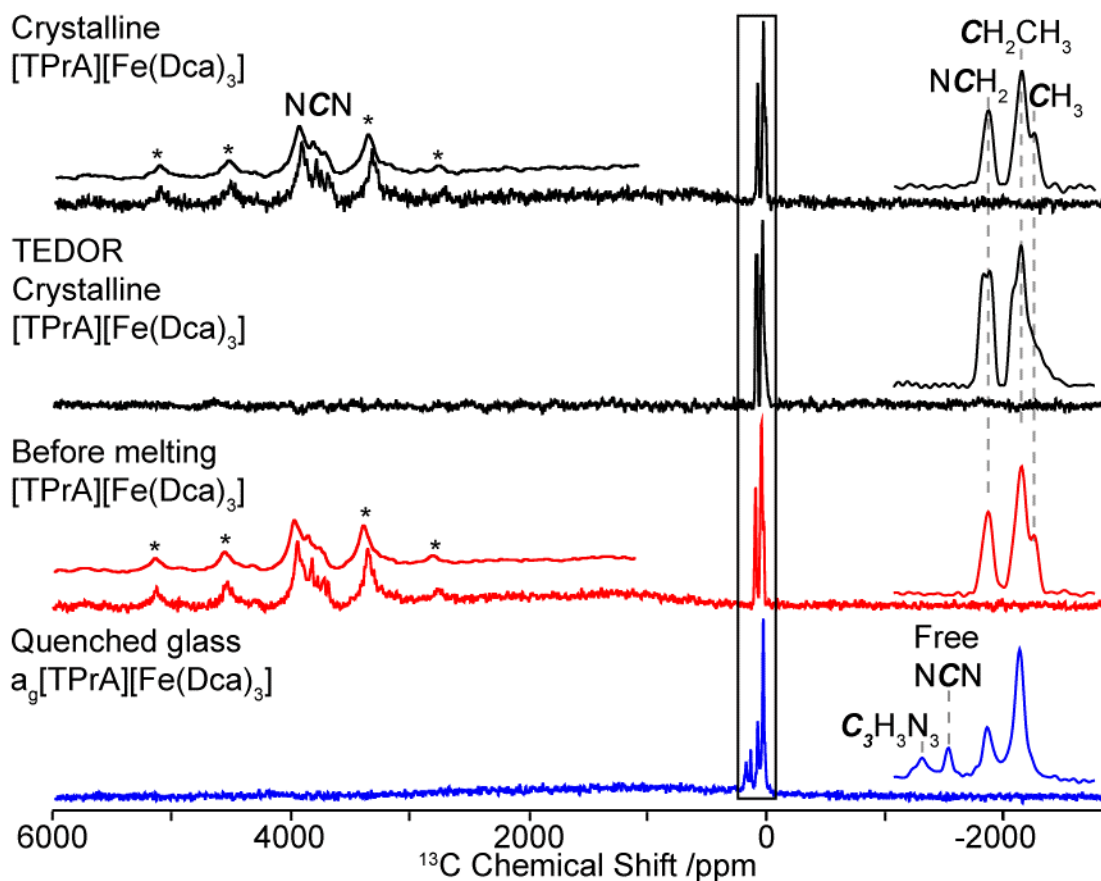


Figure 5.5. ¹³C Double adiabatic echo¹⁹ MAS NMR spectra of crystalline [TPrA][Fe(dca)₃] before heating (black), ¹³C edited TEDOR NMR spectrum of crystalline [TPrA][Fe(dca)₃] before heating (black), immediately prior to melting (red) and upon quenching (blue), a_g[TPrA][Fe(dca)₃]. Magnified views of the 200 to -100 ppm region (within box) are shown on the right hand side. Spectra were processed with exponential line broadenings (of 20 Hz), appropriate for the magnified views shown in order to capture the various spectral features, while the overlaid views in the 6000 to 1000 ppm paramagnetic shifts region show data processed with increased line broadenings (of 200 Hz) taking into account the larger linewidths of the NCN resonances of the dca ligand. C₃H₃N₃ corresponds to triazine-based structures. Asterisks (*) denote spinning sidebands.

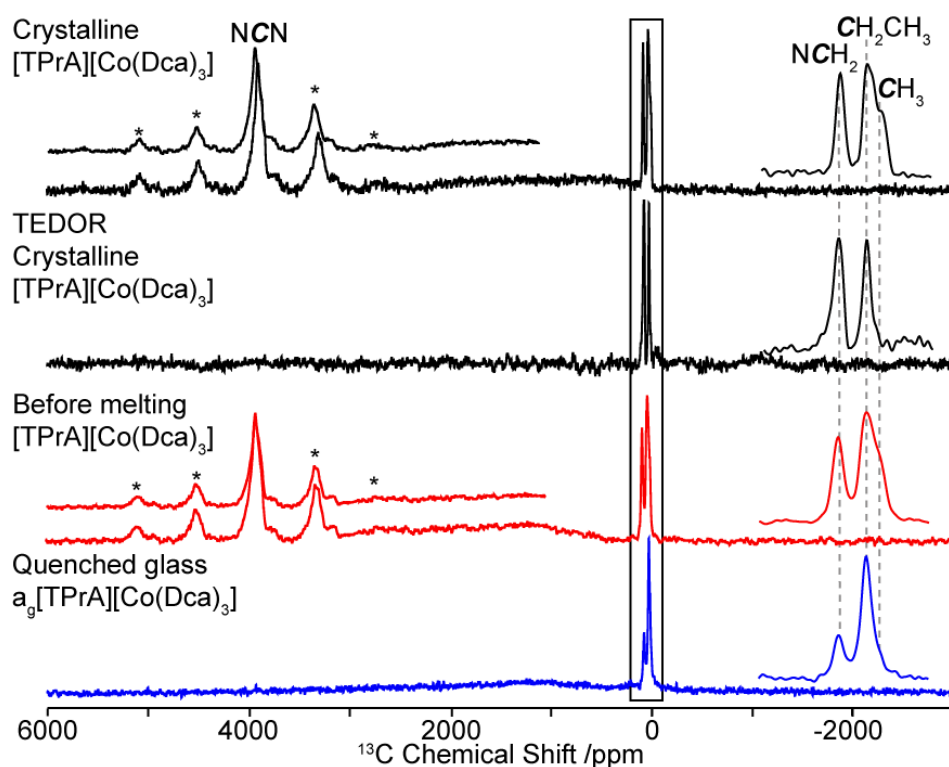


Figure 5.6. ^{13}C Double adiabatic echo- ^{19}F MAS NMR spectra of ground $[\text{TPrA}][\text{Co}(\text{dca})_3]$ before heating (top), ^{13}C edited TEDOR NMR spectrum of crystalline $[\text{TPrA}][\text{Co}(\text{dca})_3]$ before heating (black) immediately prior to melting (middle) and upon quenching (bottom), $a_g[\text{TPrA}][\text{Co}(\text{dca})_3]$. Magnified views of the 200 to -100 ppm region (within box) are shown on the right hand side Spectra were processed with exponential line broadenings (of 20 Hz), appropriate for the magnified views shown in order to capture the various spectral features, while the overlaid views in the 6000 to 1000 ppm paramagnetic shifts region show data processed with increased line broadenings (of 200 Hz) taking into account the larger linewidths of the NCN resonances of the dca ligand. Asterisks (*) denote spinning sidebands.

Notably, the NCN carbon within the $[\text{TPrA}][\text{Fe}(\text{dca})_3]$ and $[\text{TPrA}][\text{Co}(\text{dca})_3]$ materials appears at a very similar chemical shift, which is also seen elsewhere in literature.²⁷ The ^{13}C shifts of the TPrA cation are significantly less affected due to the greater distance of this species from the metal centres (**Figure 5.4**), whilst the different chemical shift of the dca ligand in crystalline $[\text{TPrA}][\text{Mn}(\text{dca})_3]$ (*ca.* 5 ppm, **Figure 5.7** and **Table 5.1**) is ascribed to the difference in magnetic susceptibility of Mn^{2+} , in comparison to Fe^{2+} and Co^{2+} . This yields smaller anisotropic bulk magnetic susceptibility broadening in the former, consistent with ^7Li MAS NMR of LiMPO_4 , $M = \text{Mn}, \text{Fe}, \text{Co}$.^{15,27}

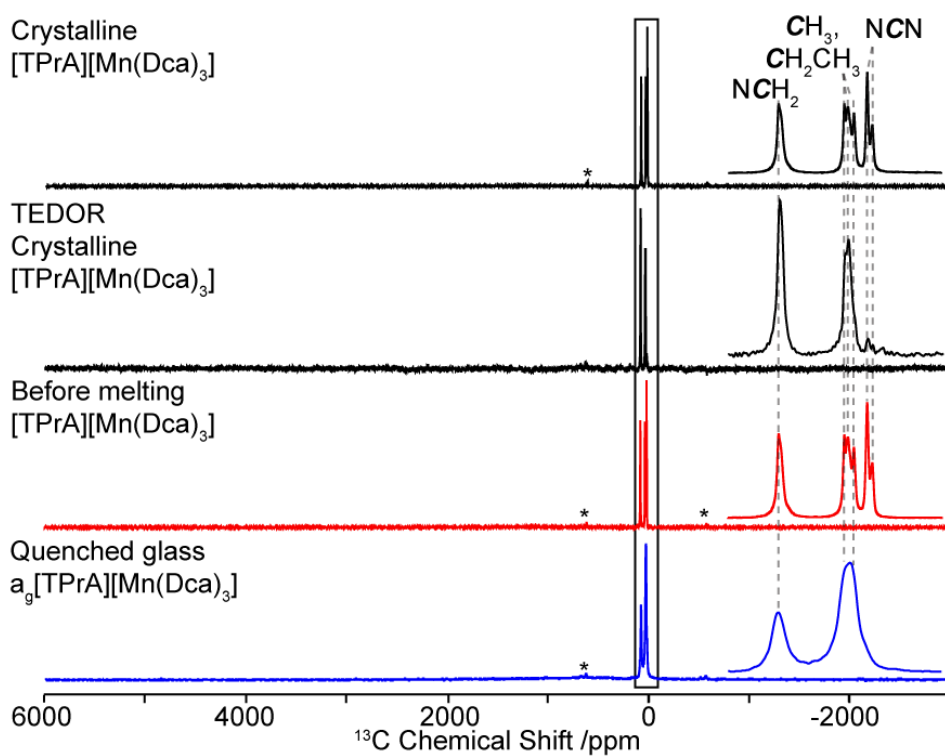


Figure 5.7. ^{13}C Double adiabatic echo¹⁹ MAS NMR spectra of crystalline $[\text{TPrA}][\text{Mn}(\text{dca})_3]$ before heating (black), ^{13}C edited TEDOR NMR spectrum of crystalline $[\text{TPrA}][\text{Mn}(\text{dca})_3]$ before heating (black), ^{13}C Double adiabatic echo MAS NMR spectra of crystalline $[\text{TPrA}][\text{Mn}(\text{dca})_3]$ immediately prior to melting (red) and after quenching (blue), $a_g[\text{TPrA}][\text{Mn}(\text{dca})_3]$. Magnified views of the 100 to -50 ppm region (within box) are shown on the right hand side with spectral assignments. Asterisks (*) denote spinning sidebands.

Table 5.1. ^{13}C NMR chemical shifts for crystalline and quenched glass phases of $[\text{TPrA}][\text{Mn}(\text{dca})_3]$, $[\text{TPrA}][\text{Fe}(\text{dca})_3]$ and $[\text{TPrA}][\text{Co}(\text{dca})_3]$.

Samples	Chemical Shift /ppm					
	CH_3	CH_2CH_3	NCH_2	NCN	Free NCN	$\text{C}_3\text{H}_3\text{N}_3$
$[\text{TPrA}][\text{Mn}(\text{dca})_3]$	16	20-23	66-69	3-7	N/A	N/A
$\alpha_g[\text{TPrA}][\text{Mn}(\text{dca})_3]$	15	20	67	Not observed	Not observed	Not observed
$[\text{TPrA}][\text{Fe}(\text{dca})_3]$	-8	10	60	3630-4020	N/A	N/A
$\alpha_g[\text{TPrA}][\text{Fe}(\text{dca})_3]$	-6	13	61	Not observed	119	158
$[\text{TPrA}][\text{Co}(\text{dca})_3]$	-10	13	61	3790-4020	N/A	N/A
$\alpha_g[\text{TPrA}][\text{Co}(\text{dca})_3]$	-12	10	59	Not observed	Not observed	N/A

Comparison of the spectra of crystalline and glass samples (**Figures 5.4-5.7**) shows similar chemical shifts in the TPrA region, suggesting that the 'A' site cation remains intact during the melt-quenching process. No resonances for dca are observed in their paramagnetic NMR regions for any of the quenched glasses due to a likely decrease in the T_2' upon vitrification and hence, an increase in paramagnetic broadening of the glasses.

Experimental evidence for the decoordination of dca ligands during the melting process arises from an additional resonance at 120 ppm in the spectra for $\alpha_g[\text{TPrA}][\text{Fe}(\text{dca})_3]$, which is assigned to a 'free' dca ligand.²⁸ A further peak at 159 ppm, combined with the appearance of two (weak) absorption bands at 1629-1634 cm^{-1} and 802-806 cm^{-1} in the infrared (IR) spectra for all glasses, may also indicate a small degree of ligand decomposition upon melting (**Figures 5.5 and 5.8**).²⁸⁻³⁰ This minimal decomposition has been confirmed by further liquid state NMR work conducted which is not presented in this thesis.

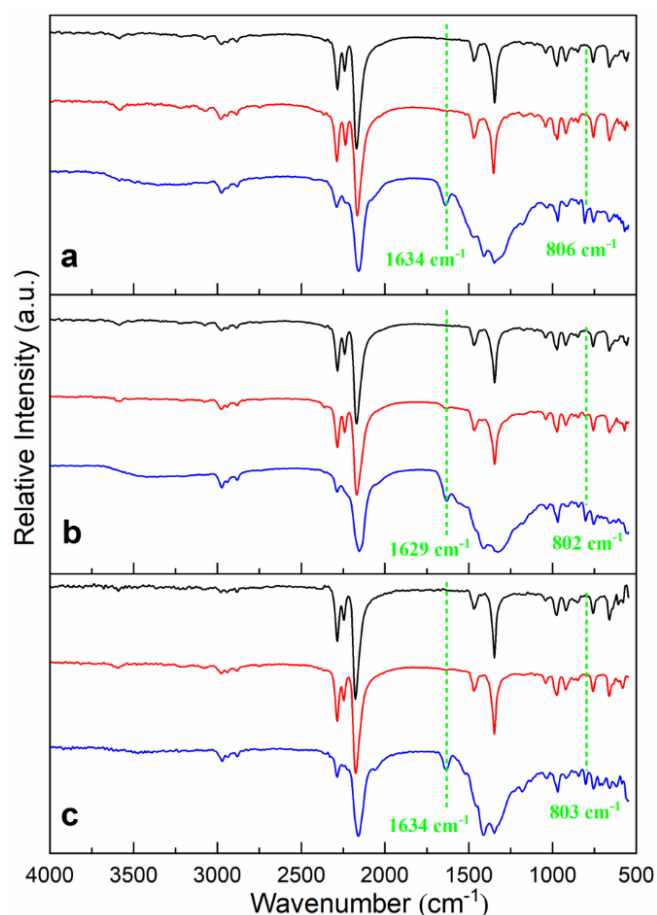


Figure 5.8. FT-IR spectra. (a) [TPrA][Mn(dca)₃], (b) [TPrA][Fe(dca)₃], (c) [TPrA][Co(dca)₃] at three different states, before heating (black), immediately prior to melting (red) and upon quenching from the liquid phase (blue). Dashed lines (green) appeared at 1629-1634 cm⁻¹ and 802-806 cm⁻¹ in all *a_g*[TPrA][M(dca)₃] spectra, indicates high temperature deformation of a portion of dca ligands (deformation vibration of δ_{C-N-C}) to triazine-based structures. Spectra ran by Bikash Kumar Shaw.

No ¹³C resonance outside the standard diamagnetic 200 to 0 ppm region was observed in crystalline [TPrA][Mn(dca)₃] (**Figure 5.4**) prompting us to explore the use of ¹³C-edited experiment to identify the dca carbon which is best achieved in these systems with a ¹H ¹³C double resonance TEDOR NMR experiment.^{19,25} In this experiment, only protonated carbons are observed and the corresponding ¹H-¹³C TEDOR NMR spectrum of [TPrA][Mn(dca)₃] unambiguously showed the disappearance of the 3-7 ppm signal which is therefore assigned to the carbon of the dca anion ligand.

The spectral deconvolution of [TPrA][Fe(dca)₃] and [TPrA][Co(dca)₃] in **Figures 5.9 and 5.10** shows three resonances in the 200 to -100 ppm region corresponding to three carbon environments within the TPrA molecule in the unit cell.²³ The spectral deconvolution of [TPrA][Mn(dca)₃] in **Figure 5.11** shows three resonances corresponding to the NCH₂ within the TPrA molecule and two resonances for the NCN at 7 and 3 ppm within the dca ligand in a 2:1 ratio. This is in agreement with the expected number of carbon environments in the unit cell for this compound.² The limited resolution does not permit the CH₂CH₃ and CH₃ groups to be distinguished from one another.

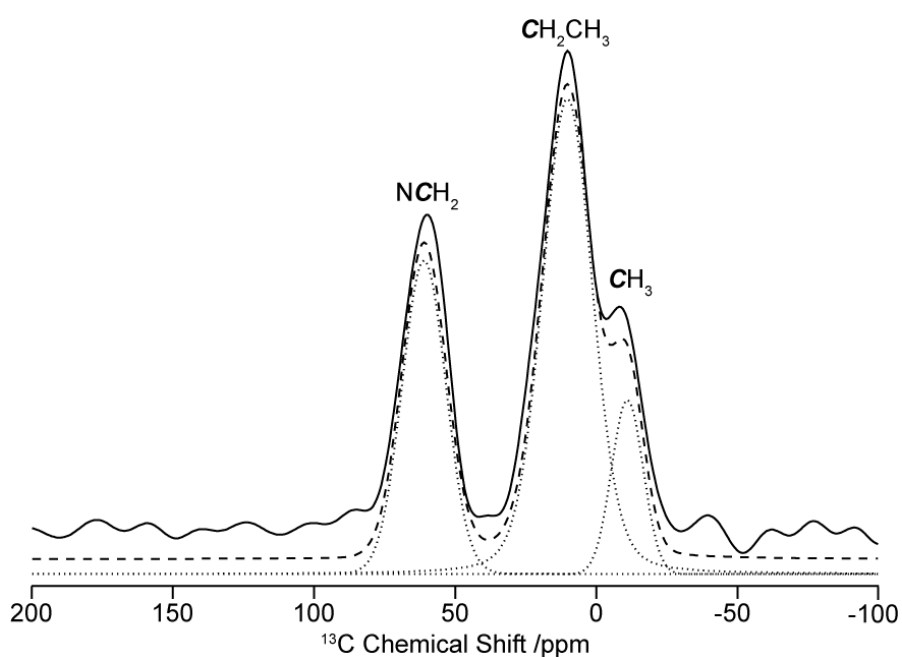


Figure 5.9. Deconvoluted ¹³C double adiabatic echo¹⁹ MAS NMR spectra of crystalline [TPrA][Fe(dca)₃] in the 200 to -100 ppm region. Experimental spectrum (solid line) with the spectral deconvolution (dotted lines) and total fit (dashed lines) shown.

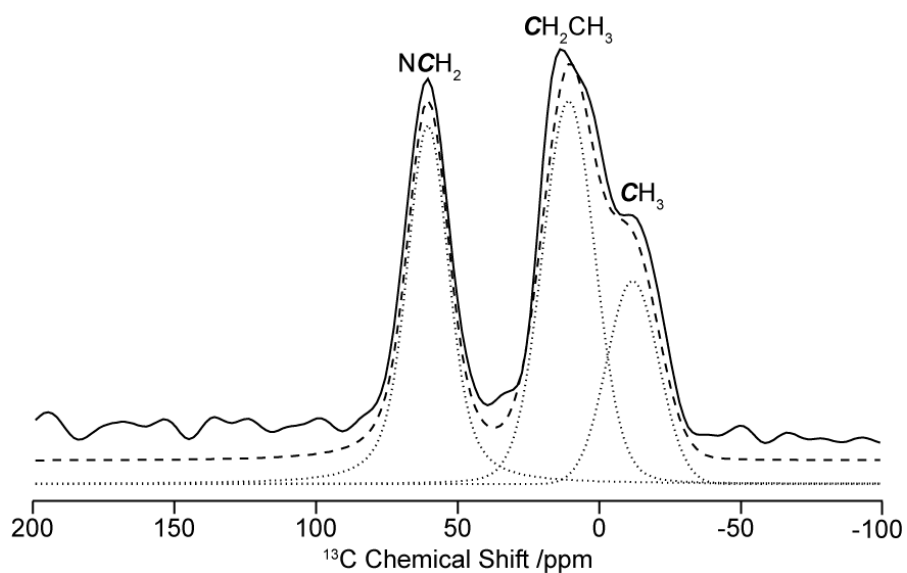


Figure 5.10. Deconvoluted ^{13}C double adiabatic echo- ^{19}F MAS NMR spectra of crystalline $[\text{TPrA}][\text{Co}(\text{dca})_3]$ in the 200 to -100 ppm region. Experimental spectrum (solid line) with the spectral deconvolution (dotted lines) and total fit (dashed lines) shown.

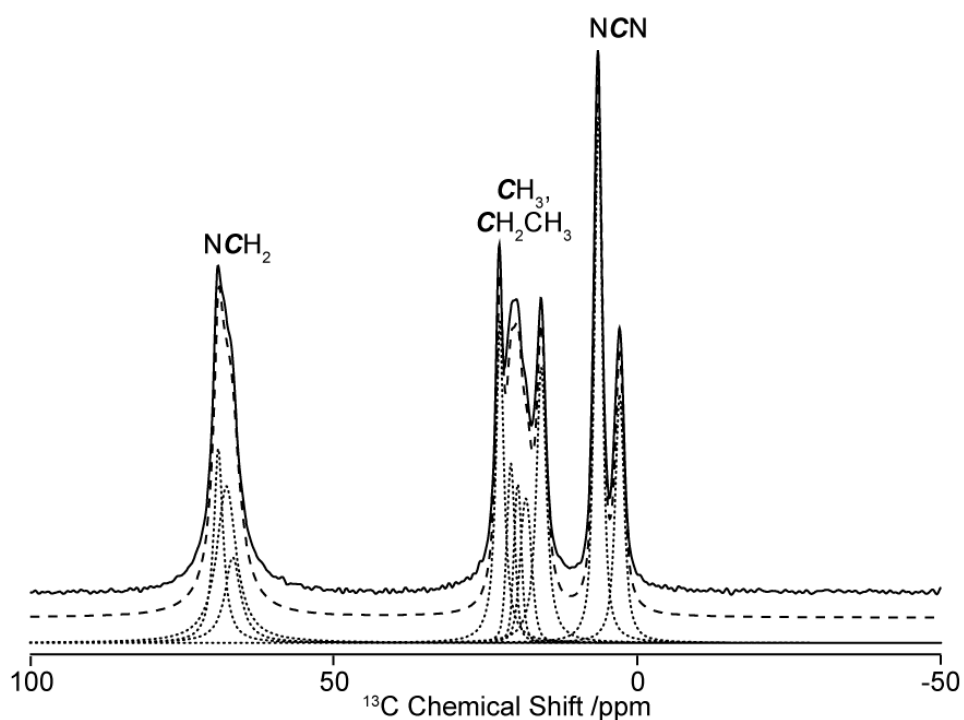


Figure 5.11. Deconvoluted ^{13}C double adiabatic echo- ^{19}F MAS NMR spectra of crystalline $[\text{TPrA}][\text{Mn}(\text{dca})_3]$ in the 100 to -50 ppm region. Experimental spectrum (solid line) with the spectral deconvolution (dotted lines) and total fit (dashed lines) shown.

5.6 Conclusion

The NMR of the crystalline compounds are consistent with the literature. Specifically, they support the existence of one TPrA cation and two dca anions in the asymmetric unit cell within the orthorhombic *Ibam* (centrosymmetric) space group of [TPrA][Fe(dca)₃] and [TPrA][Co(dca)₃],²³ and the presence of three independent ions in the tetragonal space group *P-42₁c* of [TPrA][Mn(dca)₃] at 45 °C.²¹ The spectra were assigned based on known chemical shift values for TPrA in diamagnetic systems,²⁷ spatial proximity to the metal centres and ¹³C-edited experiment using ¹H ¹³C TEDOR^{19,28} (transferred echo double resonance) experiments that filter out any non-protonated carbons (**Figures 5.5-5.7**). Unambiguous structural assignment is vital to aid in the interpretation of the change occurring through the melting process and solid state NMR is a key player in enabling this understanding.

The dca-containing family of perovskites themselves offer great potential for developing structure-property relationships by changing the 'A' site ammonium cation, or by utilizing different transition metals on the 'B' site(s), whilst the melting of HOIPs containing different organic linkers such as azides or hypophosphites will also be of interest.⁷ Studies of the effect of defects (near ubiquitous in the wider HOIP family) upon melting behaviour will also be important, whilst electrical conductivities may be raised further through precise control of partial decomposition processes to approach those of the best inorganic ($\sim [10^3-10^6] \text{ S m}^{-1}$)³¹ and organic ($\sim [10^{-3}-10^5] \text{ S m}^{-1}$)³² thermoelectrics. Such considerations and the enormous chemical variance possible within HOIPs family warrant further investigation into this new family of hybrid glass-formers.

5.7 References

1. B. Mitzi, D. Introduction: Perovskites. *Chem. Rev.* **119**, 3033–3035 (2019).
2. Li, W. *et al.* Chemically diverse and multifunctional hybrid organic–inorganic perovskites. *Nat. Rev. Mater.* **2**, 16099 (2017).
3. Li, W., A., S., Wang, Z.-M. & Gao, S. *Hybrid Organic-Inorganic Perovskites*. (Wiley, 2020).
4. Burschka, J. *et al.* Sequential deposition as a route to high-performance perovskite-sensitized solar cells. *Nature* **499**, 316–319 (2013).
5. Lee, M. M., Teuscher, J., Miyasaka, T., Murakami, T. N. & Snaith, H. J. Efficient Hybrid Solar Cells Based on Meso-Superstructured Organometal Halide Perovskites. *Science* **338**, 643 LP – 647 (2012).
6. Jain, P. *et al.* Multiferroic Behavior Associated with an Order–Disorder Hydrogen Bonding Transition in Metal–Organic Frameworks (MOFs) with the Perovskite ABX₃ Architecture. *J. Am. Chem. Soc.* **131**, 13625–13627 (2009).
7. Wu, Y. *et al.* [Am]Mn(H₂POO)₃: A New Family of Hybrid Perovskites Based on the Hypophosphite Ligand. *J. Am. Chem. Soc.* **139**, 16999–17002 (2017).
8. Bermúdez-García, J. M. *et al.* Giant barocaloric effect in the ferroic organic-inorganic hybrid [TPrA][Mn(dca)₃] perovskite under easily accessible pressures. *Nat. Commun.* **8**, 15715 (2017).
9. Saparov, B. & B. Mitzi, D. Organic–Inorganic Perovskites: Structural Versatility for Functional Materials Design. *Chem. Rev.* **116**, 4558–4596 (2016).
10. A. Egger, D., M. Rappe, A. & Kronik, L. Hybrid Organic–Inorganic Perovskites on the Move. *Acc. Chem. Res.* **49**, 573–581 (2016).
11. Wang, Y. *et al.* Pressure-Induced Phase Transformation, Reversible Amorphization, and Anomalous Visible Light Response in Organolead Bromide Perovskite. *J. Am. Chem. Soc.* **137**, 11144–11149 (2015).
12. Ou, T. *et al.* Visible light response, electrical transport, and amorphization in compressed organolead iodine perovskites. *Nanoscale* **8**, 11426–11431 (2016).

13. B. Mitzi, D. Synthesis, Crystal Structure, and Optical and Thermal Properties of $(C_4H_9NH_3)_2MI_4$ ($M = Ge, Sn, Pb$). *Chem. Mater.* **8**, 791–800 (1996).
14. Gaillac, R. *et al.* Liquid metal–organic frameworks. *Nat. Mater.* **16**, 1149–1154 (2017).
15. Pell, A. J., Pintacuda, G. & Grey, C. P. Progress in Nuclear Magnetic Resonance Spectroscopy Paramagnetic NMR in solution and the solid state. *Prog. Nucl. Magn. Reson. Spectrosc.* **111**, 1–271 (2019).
16. Bertmer, M. Paramagnetic solid-state NMR of materials. *Solid State Nucl. Magn. Reson.* **81**, 1–7 (2017).
17. Dawson, D. M. *et al.* High-resolution solid-state ^{13}C NMR spectroscopy of the paramagnetic metal–organic frameworks, STAM-1 and HKUST-1 †. *Phys. Chem. Chem. Phys.* **15**, 919–929 (2013).
18. Ishii, Y., Wickramasinghe, N. P. & Chimon, S. A New Approach in 1D and 2D ^{13}C High-Resolution Solid-State NMR Spectroscopy of Paramagnetic Organometallic Complexes by Very Fast Magic-Angle Spinning. *J. Am. Chem. Soc.* **125**, 3438–3439 (2003).
19. Kervern, G., Pintacuda, G. & Emsley, L. Fast adiabatic pulses for solid-state NMR of paramagnetic systems. *Chem. Phys. Lett.* **435**, 157–162 (2007).
20. Umeyama, D., Horike, S., Inukai, M., Itakura, T. & Kitagawa, S. Reversible Solid-to-Liquid Phase Transition of Coordination Polymer Crystals. *J. Am. Chem. Soc.* **137**, 864–870 (2015).
21. Bermúdez-García, J. M. *et al.* Role of Temperature and Pressure on the Multisensitive Multiferroic Dicyanamide Framework $[TPrA][Mn(dca)_3]$ with Perovskite-like Structure. *Inorg. Chem.* **54**, 11680–11687 (2015).
22. Schlueter, J. A., Manson, J. L. & Geiser, U. Structural and Magnetic Diversity in Tetraalkylammonium Salts of Anionic $M[N(CN)_2]_3$ - ($M = Mn$ and Ni) Three-Dimensional Coordination Polymers. *Inorg. Chem.* **44**, 3194–3202 (2005).
23. Bermúdez-García, J. M. *et al.* Multiple phase and dielectric transitions on a novel multi-sensitive $[TPrA][M(dca)_3]$ ($M: Fe^{2+}, Co^{2+}$ and Ni^{2+}) hybrid

- inorganic–organic perovskite family. *J. Mater. Chem. C* **4**, 4889–4898 (2016).
24. Thurber, K. R. & Tycko, R. Measurement of sample temperatures under magic-angle spinning from the chemical shift and spin-lattice relaxation rate of ⁷⁹Br in KBr powder. *J. Magn. Reson.* **196**, 84–87 (2009).
 25. Hing, A. W., Vega, S. & Schaefer, J. Transferred-Echo Double-Resonance NMR. *J. Magn. Reson.* **96**, 205–209 (1992).
 26. Morcombe, C. R. & Zilm, K. W. Chemical shift referencing in MAS solid state NMR. *J. Magn. Reson.* **162**, 479–486 (2003).
 27. Tucker, M. C. *et al.* Hyperfine Fields at the Li Site in LiFePO₄ -Type Olivine Materials for Lithium Rechargeable Batteries: A ⁷Li MAS NMR and SQUID Study. *J. Am. Chem. Soc.* **124**, 3832–3833 (2002).
 28. Täuber, K., Dani, A. & Yuan, J. Covalent Cross-Linking of Porous Poly(ionic liquid) Membrane via a Triazine Network. *ACS Macro Lett.* **6**, 1–5 (2017).
 29. Kroke, E. *et al.* Tri-s-triazine derivatives. Part I. From trichloro-tri-s-triazine to graphitic C₃N₄ structures. *New J. Chem.* **26**, 508–512 (2002).
 30. Bermúdez-García, J. M. *et al.* A simple in situ synthesis of magnetic M@CNTs by thermolysis of the hybrid perovskite [TPrA][M(dca)₃]. *New J. Chem.* **41**, 3124–3133 (2017).
 31. Gaultois, M. W. *et al.* Data-Driven Review of Thermoelectric Materials: Performance and Resource Considerations. (2013). doi:10.1021/cm400893e
 32. Russ, B., Gludell, A., Urban, J. J. & Chabiny, M. L. Organic thermoelectric materials temperature control. (2016). doi:10.1038/natrevmats.2016.50

Chapter 6: Conclusions and Further Work.

6.1 Conclusions.

Throughout this thesis the research presented utilises solid state NMR to monitor both the dynamics and structures of various supramolecular assemblies.

In **Chapter 3** a new family of tubular covalent cages was explored and found that TCC3-*R* was the fastest exclusively organic molecular rotor to date. The reorientation rates using experimental ^2H solid state NMR and simulation at variable temperature were probed, finding the low activation barriers for these materials. Subsequent iodine loading was also monitored by ^2H as well as ^{13}C spin lattice relaxation rates to show that iodine has been trapped within the voids, inhibiting rotation of the phenylene ring. Finally, upon monitoring iodine release a reorientation rate of the same order of magnitude to the pristine cage was observed, showing that these are smart materials which are responsive to external stimuli.¹

In **Chapter 4** the structure and dynamics of pillar[*n*]arenes, a relatively new class of macrocycles, were studied by solid state NMR. From the ^{13}C cross-polarisation magic angle spinning NMR spectra, deconvolutions and the 2D ^{13}C - ^{13}C through-bond connectivities INADEQUATE experiment, the NMR spectra of both **EtP5- α** and **EtP6- β** were fully assigned and confirmed the asymmetric unit cells of these phases.² The dynamics were studied utilising Proton Detected Local Field (PDLF) NMR and displayed small differences indicating faster motion for the OCH_2 groups in **EtP6- β** in comparison to **EtP5- α** that is attributed to the larger void space. Upon *para*-xylene loading, and at low temperature (100 K), additional dipolar spectra are observed indicating a host-guest interaction between the loaded xylene and the carbons within the core of the pillar[*n*]arene.

In **Chapter 5** spectral assignment is used to confirm the structures of various hybrid perovskites. The challenges of paramagnetic compounds were minimised by using Short High Adiabatic Pulses to sweep the frequency enabling detection of signal over

a larger chemical shift range. Transferred double echo rotation experiments confirmed the spectral assignment originally based on location to the paramagnetic centre with the aid of spectral deconvolution. In this work it was shown that this series of dicyanamide based hybrid organic inorganic perovskites melt below 300 °C, forming perovskite glasses which can be seen by the increase in width of the NMR resonances, indicating the amorphous nature of the glasses.

6.2 Further work

In both **Chapter 3** and **4** dynamics are studied, however different techniques are used. In **Chapter 3** the predominant technique utilised is static ^2H NMR line shape analysis and although touched on in **Chapter 3**, **Chapter 4** delves further into the use of relaxation rates to probe dynamics. **Chapter 4** also utilises the PDLF NMR technique which has not been applied to supramolecular assemblies before. Therefore, it is possible to build upon these chapters by re-assessing the molecular rotors using both variable temperature relaxation rates and PDLF NMR.

Further work expanding on **Chapter 4** could incorporate deuteration of the xylene guests. Performing ^{13}C CP on a deuterated xylene EtP6 adduct (where the EtP6 host is of natural abundance) would allow for a further confirmation of the signals arising from the host or guest molecule in the NMR spectrum. With deuterated xylene, ^2H NMR could also be utilised to determine the guest mobility in the guest loaded adducts. However, it should be noted that deuteration (in particular selective deuteration of certain parts of the molecule) can be a costly process and to provide a full analysis with minimal overlapping peaks could require analysis of adduct with differing degrees of deuteration. The time taken to complete this was therefore considered superfluous to this PhD project, however it does have a potential for progressing both the characterisation and understanding of dynamics of these materials.

In the literature review (**Chapter 2**) it was shown that spin diffusion techniques can be a useful tool to study interactions within supramolecular assemblies.³ Some preliminary work has been completed on the pillar[n]arenes used in **Chapter 3** applying this EXSY type pulse program and the resulting build up curves are shown in **Figure 6.1(c)** below. These curves show the typical decay of signal for the peaks which lie on the diagonal (shaded) and as mixing time increases, the polarisation transfer to the cross peaks typically increases. The increasing growth rate can be seen to have different rates dependent on the observed cross peak. Some negative cross peaks were also observed. Negative cross peaks have been hypothesised in solid state NMR literature to be due to a high-order spin diffusion process involving four spins.⁴

Although there is a significant increase in resolution upon spinning at 60 kHz and 20 T (**Figure 6.1(a)** and **(b)**), data from the spectrum is still difficult to extract with the current resolution. These pillar[n]arene molecules have a strong proton-proton dipolar coupling network, resulting in a large amount of homonuclear dipolar coupling occurring which is unable to be averaged out at these MAS rates. The potential use of homonuclear decoupling could aid in simplifying the ^1H spectra providing higher resolution spectra capable of complete analysis and interpretation.

The combined X-ray technique, DFT work and NMR crystallography work in **Chapter 4**² confirmed the molecular structure of **EtP6- β** . As spin diffusion curves are dependent on distance, with this confirmed molecular structure, spin diffusion curves and their rates could be simulated.⁵ The reverse is also possible, as we have the experimental spin diffusion curves the rate of growth of polarisation can give data corresponding to distance and therefore it is possible to provide details regarding the crystal structure.

To further expand on this spin diffusion work, this method could also be applied to the xylene loaded EtP6 adducts. The build-up curves would enable us to probe the ^1H dipolar interaction in the supramolecular assembly and we would expect to see a variation in ^1H dipolar coupling interactions *via* a difference in build-up curves observed depending on the guest present. This would then enable an enhanced crystal structure to be produced, providing further details regarding the guest positioning within the guest-host framework.

Chapter 5 has so far focused on the characterisation of hybrid perovskites. However, the materials have a wide range of applications most predominantly in photonics,⁶ which relates to both structure and dynamics. Therefore, we could also look into studying these materials and how the dynamics change upon loading using the techniques studied in this thesis or those suggested throughout literature and highlighted in **Chapter 2**.

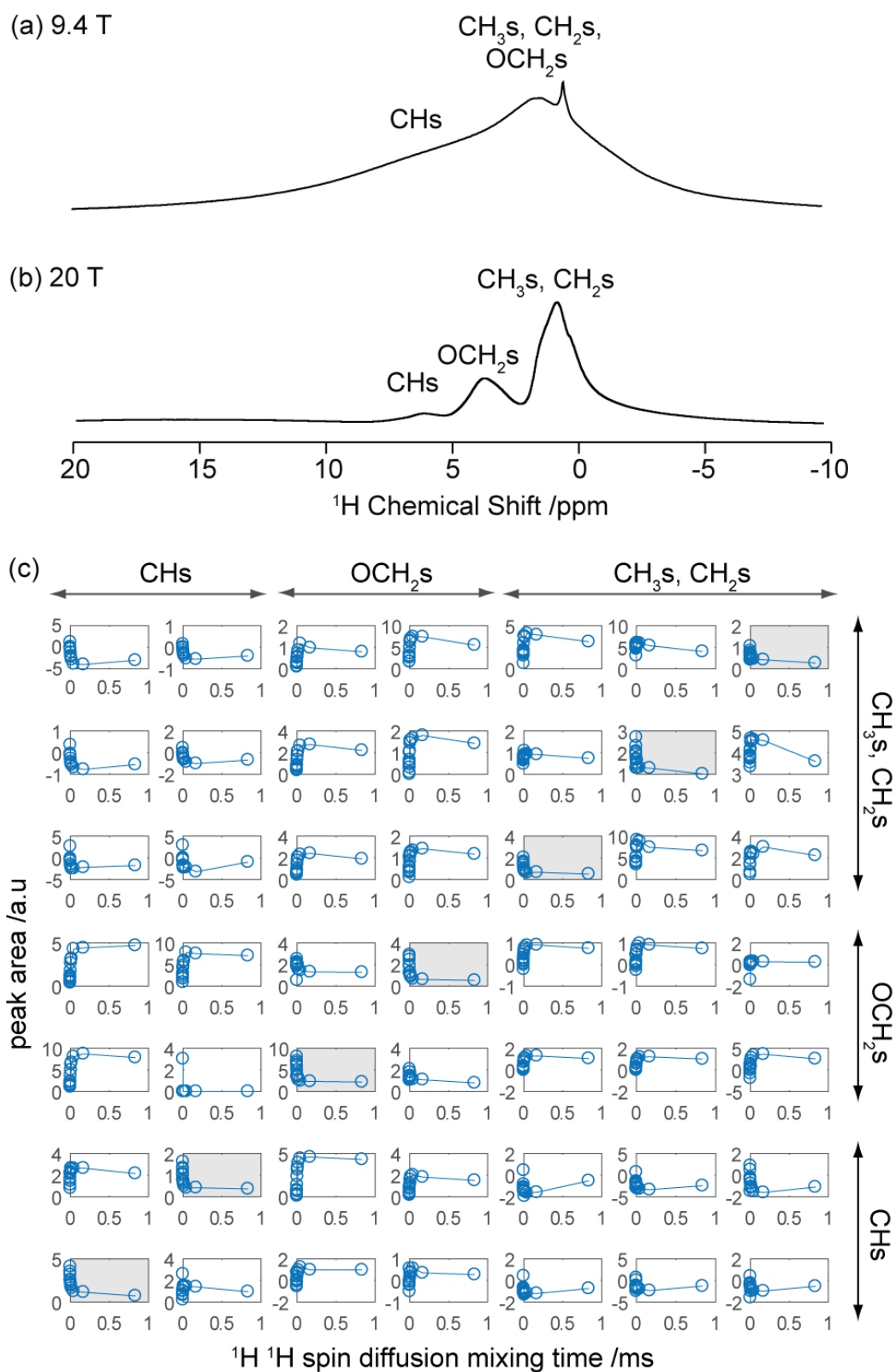


Figure 6.1. ¹H one pulse spectrum of EtP6- β obtained at (a) 9.4 T and $\nu_r = 12.5$ kHz, (b) 20 T and $\nu_r = 60$ kHz. (c) Spin diffusion build up curves of EtP6- β obtained from data collected with the incrementing spin diffusion mixing time until 1 ms was reached, under $\nu_r = 60$ kHz and 20 T.

6.3 References

- 1 A. R. Hughes, N. J. Brownbill, R. C. Lalek, M. E. Briggs, A. G. Slater, A. I. Cooper and F. Blanc, *Chem. - A Eur. J.*, 2017, **23**, 17217–17221.
- 2 K. Jie, M. Liu, Y. Zhou, M. A. Little, A. Pulido, S. Y. Chong, A. Stephenson, A. R. Hughes, F. Sakakibara, T. Ogoshi, F. Blanc, G. M. Day, F. Huang and A. I. Cooper, *J. Am. Chem. Soc.*, 2018, **140**, 6921–6930.
- 3 J. Wack, R. Siegel, T. Ahnfeldt, N. Stock, L. Mafra and J. Senker, *J. Phys. Chem. C*, 2013, **117**, 19991–20001.
- 4 V. Agarwal, *J. Magn. Reson.*, 2020, **311**, 106661.
- 5 B. Elena and L. Emsley, *J. Am. Chem. Soc.*, 2005, **127**, 9140–9146.
- 6 D. A. Egger, A. M. Rappe and L. Kronik, *Acc. Chem. Res.*, 2016, **49**, 573–581.